

Theoretical Interpretation of Experimental Data from Direct Dark Matter Detection

Dissertation

zur

Erlangung der Doktorgrades (Dr. rer. nat.)

der

Mathematisch-Naturwissenschaftlichen Fakultät

der

Rheinischen Friedrich-Wilhelms-Universität Bonn

vorgelegt von

CHUNG-LIN SHAN

aus Taipeh

Bonn 2007

Angefertigt mit Genehmigung der Mathematisch-Naturwissenschaftlichen
Fakultät der Universität Bonn

Referent: Prof. Manuel Drees
Korreferent: Prof. Herbert Dreiner

Tag der Promotion: 16. Oktober 2007

Ich versichere, dass ich diese Arbeit selbständig verfasst und keine anderen als die angegebenen Quellen und Hilfsmittel benutzt sowie die Zitate kenntlich gemacht habe.

Acknowledgments

First and foremost I would like to express my gratitude to my advisor Prof. Manuel Drees for the opportunity to work on the subject of Dark Matter. As a collaborator I have learned to appreciate his profound knowledge of the subject and intuition for the essential as well as his manner of researching and special unique point of views.

Next I would like to thank Mitsuru Kakizaki for discussing about our research, and especially for his help to correct this work.

I would also like to thank all colleagues in my office: Markus Bernhardt, Sascha Bornhauser, Sebastian Grab, Jong Soo Kim, Olaf Kittel, Ulrich Langenfeld, Anja Marold, and Federico von der Pahlen. I always enjoy the friendly atmosphere in our office and it is always being a pleasure to discuss about Physics together with something else with you.

My thanks also go to Prof. Herbert Dreiner, Prof. Hans-Peter Nilles, Kin-ya Oda and his wife Naoko, Saul-Noe Ramos-Sanchez, Patrick Vaudrevange, and all current and former colleagues in the theory group in the Physikalischen Institut. Moreover, I particularly want to thank the very helpful secretaries: Dagmar Fassbender, Sandra Heidbrink, Patricia Zündorf, and our computer and all-round specialist Andreas Wisskirchen. I am pleased to know you and thank for all your assistances.

My special thank goes to Prof. Andrzej Buras, Christoph Bobeth, Martin Gorbahn, Sebastian Jäger, Frank Krüger, Anton Poschenrieder, Andreas Weiler and his wife Laura as well as the other former colleagues in the Physics Department at the Technische Universität München. I was glad for the time spent with you at the beginning of my study in Germany.

Furthermore it is a great pleasure to thank the Deutschem Akademischem Austausch Dienst (DAAD), especially Ruth Eberlein, Petra Hagemann, Heike Schädlich, Elena Schmid, and all other members of the Referat 423, not only for the financial support, but also their thoughtful caring about the study and life.

In addition, I would also like to thank the following friends: Simone Müller, Dieter Rupp, Ritschi Spindler and Li-Chi Wu in Munich as well as the family of Kunkel, Hervé Barreteau, Chun-yi Chen, Piyada Dok-angkab, Marie Kubota, Hsiao-Yun Lee, Yin-Chen Lin, Yuka Nakajima, Naoko Teranishi, and Hsin-Tzu Wang in Bonn. You make my life in Germany more interesting and colorful.

My parents always respect my decisions, especially the long-time study in Germany, and support me for the whole time. I am very grateful to them.

Abstract

Weakly Interacting Massive Particles (WIMPs) are one of the leading candidates for Dark Matter. Currently, the most promising method to detect many different WIMP candidates is the direct detection of the recoil energy deposited in a low-background laboratory detector due to elastic WIMP-nucleus scattering. So far the usual procedure has been to predict the event rate of direct detection of WIMPs based on some model(s) of the Galactic halo from cosmology and of WIMPs from elementary particle physics.

The aim of this work is to invert this process. In this thesis I will present methods which allow to extract information on the WIMP velocity distribution function as well as on the WIMP mass from the recoil energy spectrum as well as from experimental data directly.

At first I will derive the expression that allow to reconstruct the normalized one-dimensional velocity distribution function of WIMPs from the recoil spectrum. I will also derive the formulae for determining the moments of the velocity distribution function. All these expressions are independent of the as yet unknown WIMP density near the Earth as well as of the WIMP-nucleus cross section. The only information about the nature of WIMPs which one needs is the WIMP mass.

Then I will present methods that allow to apply the expressions directly to experimental data, without the need to fit the recoil spectrum to a functional form. These methods are independent of the Galactic halo model. The reconstruction of the velocity distribution function will be further extended to take into account the annual modulation of the event rate.

Moreover, I will present a method for reconstructing the amplitude of the annual modulation of the velocity distribution. The only information which one needs is the measured recoil energies and their measuring times. An alternative, better way for confirming the annual modulation of the event rate will also be given.

Finally, I will present a method for determining the WIMP mass by combining two (or more) experiments with different detector materials. This method is not only independent of the model of Galactic halo but also of that of WIMPs. In addition, some meaningful information on the WIMP mass can already be extracted from less than one hundred events.

Contents

1	Dark Matter	1
1.1	Evidence for Dark Matter	1
1.1.1	Clusters of galaxies	1
1.1.2	Rotation curves of spiral galaxies	2
1.1.3	Escape velocity from the Milky Way	5
1.2	Cosmological density parameters	6
1.2.1	Cosmic microwave background (CMB)	7
1.2.2	Anisotropy of the CMB radiation	7
1.2.3	Age of the Universe	9
1.2.4	Present expansion rate of the Universe	10
1.2.5	Abundances of the light elements	10
1.2.6	Gas-to-total mass ratio	10
1.2.7	Mass-to-light ratio	12
1.2.8	Supernovae type Ia (SNe Ia) at high-redshift	13
1.2.9	Cosmological densities of different components	14
1.3	Galactic halo models	15
1.3.1	Standard assumptions of Dark Matter halo	15
1.3.2	Canonical isothermal spherical halo model	17
1.3.3	Alternative isothermal spherical halo model	19
1.3.4	Evans' power-law halo model	20
1.3.5	NFW halo model	24
1.3.6	Bulk rotation	25
2	Candidates for Dark Matter	26
2.1	Cold Dark Matter (CDM)	26
2.1.1	Minimal Supersymmetric Standard Model (MSSM)	27
2.1.2	Weakly Interacting Massive Particles (WIMPs)	29
2.1.3	Neutralinos	32
2.1.4	Sneutrinos	32
2.1.5	Heavy fourth-generation Dirac and Majorana neutrinos	32
2.1.6	Axions	33
2.1.7	Other possible SUSY candidates	34

2.2	Hot Dark Matter (HDM)	34
2.2.1	Massive neutrinos	35
2.3	Dark baryons	35
2.3.1	Massive astrophysical compact halo objects (MACHOs)	36
3	Direct Detection of WIMPs	37
3.1	Elastic WIMP-nucleus scattering	37
3.1.1	Rate for elastic WIMP-nucleus scattering	39
3.1.2	Nuclear form factor (for spin-independent coupling)	40
3.1.3	Simple isothermal Maxwellian halo	41
3.2	Annual modulation of the event rate	43
3.2.1	Shifted Maxwellian halo	44
3.3	Diurnal modulation of the event rate	45
3.4	Target material dependence	47
3.4.1	Spin-independent (SI) cross section	47
3.4.2	Spin-dependent (SD) cross section	48
3.4.3	Comparison of the SI and SD cross sections	48
3.4.4	Target mass	48
3.5	Measurement of recoil energy	49
3.5.1	A simple estimate	49
3.5.2	Induced signals	49
3.5.3	Quenching factor	50
3.5.4	Heat	50
3.5.5	Ionization	51
3.5.6	Scintillation	51
3.5.7	Combinations of two different signals	51
3.6	Background and background discrimination	52
3.6.1	Cosmic muons and underground laboratories	52
3.6.2	External natural radioactivity and (passive) shielding	53
3.6.3	Internal natural radioactivity and radiopure materials	53
3.6.4	Active background rejection	53
3.6.5	Neutron induced nuclear recoils	53
3.6.6	Multiple-scatter events and array of detectors	53
3.6.7	Electron recoils	54
3.6.8	Surface events and self shielding	54
3.6.9	Incomplete charge collection	55
3.6.10	Shape of the recoil energy spectrum	55
3.7	Cryogenic detectors	55
3.7.1	CDMS	55
3.7.2	CRESST	57

3.7.3	DAMA	58
3.7.4	EDELWEISS	60
3.7.5	Heidelberg-Moscow (HDMS)	60
3.7.6	KIMS	61
3.7.7	PICO-LON	61
3.8	Liquid noble gas detectors	61
3.8.1	ArDM	62
3.8.2	WARP	62
3.8.3	XENON	63
3.8.4	XMASS	63
3.8.5	ZEPLIN	63
3.9	Superheated droplet detectors (SDD)	65
3.9.1	DRIFT	65
3.9.2	MIMAC-He3	65
3.9.3	PICASSO	66
3.9.4	SIMPLE	66
3.10	Prospects	66
4	Reconstruction of the Velocity Distribution of WIMPs	69
4.1	From the scattering spectrum	70
4.2	From experimental data directly	72
4.2.1	Exponential ansatz for dR/dQ	73
4.2.2	Windowing the data set	77
4.2.3	Reconstructing the velocity distribution	80
4.2.4	Determining moments of the velocity distribution	82
4.3	Determining the WIMP mass	85
4.3.1	Neglecting Q_{thre}	86
4.3.2	With $Q_{\text{thre}} > 0$	91
5	Annual Modulated Event Rate	92
5.1	Taking into account the annual modulation	92
5.2	Reconstructing the modulated amplitude of $f_1(v)$	95
5.2.1	Criteria for the annual modulation	96
5.2.2	Reconstructing the modulated amplitude of $f_1(v)$	99
6	Summary and Conclusions	101
A	Expression of the Velocity Distribution of WIMPs	104
A.1	Properties of $F_1(v)$ defined in Eq.(4.1)	104
A.2	Derivations for $f_1(v)$ in Eq.(4.8)	105
A.3	Normalization constant and moments of $f_1(v)$	106

B	Moments of the Velocity Distribution of WIMPs	108
B.1	Calculating $\langle v \rangle$ and $\langle v^2 \rangle$ from $f_1(v)$	108
B.1.1	From $f_{1,\text{Gau}}(v)$ given in Eq.(3.20)	108
B.1.2	From $f_{1,\text{sh}}(v)$ given in Eq.(3.29)	109
B.2	Calculating $f_1(v)$, $\langle v \rangle$, and $\langle v^2 \rangle$ from dR/dQ	112
B.2.1	From $(dR/dQ)_{\text{Gau}}$ in Eq.(3.21)	112
B.2.2	From $(dR/dQ)_{\text{sh}}$ in Eq.(3.31)	113
C	Differential and Total Event Rates	118
C.1	Setting $F^2(Q) \approx 1$	118
C.1.1	Starting with $f_{1,\text{Gau}}(v)$ given in Eq.(3.20)	118
C.1.2	Starting with $f_{1,\text{sh}}(v)$ given in Eq.(3.29)	118
C.2	Using $F_{\text{ex}}^2(Q)$ given in Eq.(3.15)	119
C.2.1	Starting with $(dR/dQ)_{\text{Gau}}$ given in Eq.(3.21)	119
C.2.2	Starting with $(dR/dQ)_{\text{sh}}$ given in Eq.(3.31)	120
D	Some Old Attempts	121
D.1	Binning the data set	121
D.2	Reconstructing $f_1(v)$ without derivatives	122
D.3	Average logarithmic slope	123
D.4	Linear approximations of $(dQ/dR)_{Q \simeq Q_n}$	129
D.5	Using the exponential ansatz in Eq.(4.18)	130
D.6	Introducing the average value of $Q^\lambda/F^2(Q)$	133
E	Some Detailed Calculations	137
E.1	Derivations of covariances in Sec. 4.2	137
E.1.1	Covariances in Subsec. 4.2.2	137
E.1.2	Covariance in Eq.(4.61)	138
E.2	Derivation of the correction terms in Eq.(4.64)	139
E.3	Statistical error of $\mathcal{R}_n(Q_{\text{thre}})$ in Eq.(4.72)	139
E.4	Derivation of η_n in Eq.(5.24)	140

Chapter 1

Dark Matter

One of the most fundamental open questions in cosmology and elementary particle physics today is *what is the nature of Dark Matter*. Earlier the question was whether Dark Matter actually exists. But nowadays we have some strong evidence to believe that *something which we do not know exists*.

As introduction I review briefly the history of the discovery of (the existence of) Dark Matter in the Universe. It will be seen that, according to some astronomical observations and measurements, more than 80% of the total mass content of the Universe consists of Dark Matter. I will also present some models of Dark Matter halo in this chapter.

1.1 Evidence for Dark Matter

We call such *something* “dark” because it (*almost*) *neither emits nor absorbs electromagnetic radiation*. Historically the observational evidence for the existence of Dark Matter came only from galactic dynamics and are gravitational [1]. The following discussions in this section show that *the observed luminous objects* (stars, gas clouds, globular clusters, or even entire galaxies) *can not have enough mass to support the observed gravitational effects* [1].

1.1.1 Clusters of galaxies

Clusters of galaxies are the largest gravitationally-bound objects in the Universe. For example, our Milky Way and the M31 galaxy belong to the Local Group of Galaxies and are part of the Virgo Supercluster of Galaxies.

At the beginning of the 1930s, F. Zwicky and other astronomers measured the total mass of a few clusters of galaxies and the masses of the luminous objects in these clusters of galaxies [2], [3]. Their measurements showed that *the masses of these clusters of galaxies required to gravitationally bind their galaxies are much larger than the sum of the luminous masses of their individual galaxies*.

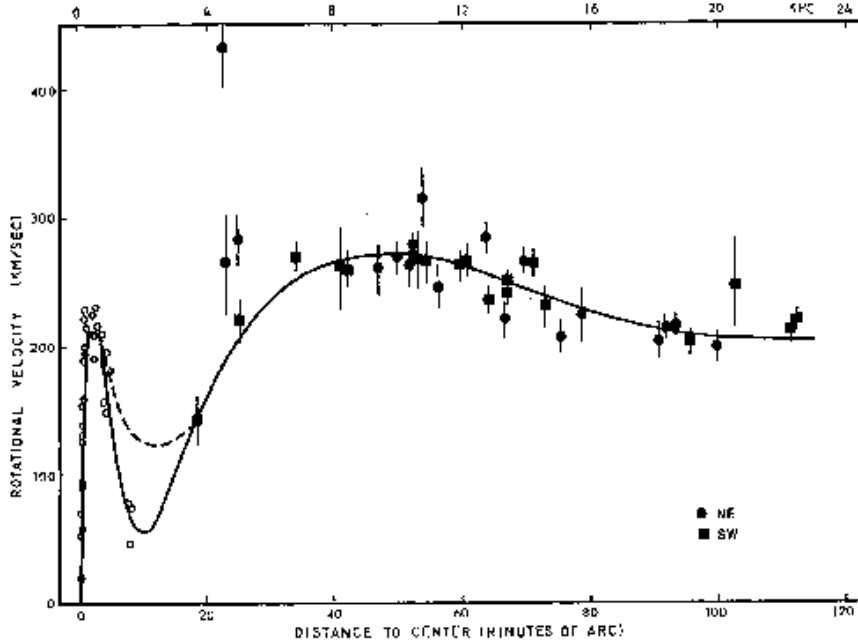


FIG. 9.—Rotational velocities for OB associations in M31, as a function of distance from the center. *Solid curve*, adopted rotation curve based on the velocities shown in Fig. 4. For $R \leq 12'$, curve is fifth-order polynomial; for $R > 12'$, curve is fourth-order polynomial required to remain approximately flat near $R = 120'$. *Dashed curve* near $R = 10'$ is a second rotation curve with higher inner minimum.

Figure 1.1: Rotation curve for OB associations in M31, as a function of distance from the galaxy center (figure from [4]).

1.1.2 Rotation curves of spiral galaxies

The most convincing evidence for the existence of Dark Matter came from the *measurement of the rotation curves of spiral galaxies* in the 1970s by V. C. Rubin and other astronomers [4]-[6].

According to Newton's Second Law, the rotational velocity v of an object on a stable orbit with radius r from the center of galaxy is ¹

$$\frac{v^2(r)}{r} = \frac{G_N M(r)}{r^2}, \quad (1.1)$$

namely,

$$v(r) \propto \sqrt{\frac{M(r)}{r}}, \quad (1.2)$$

where $M(r)$ is the mass inside the orbit. For an object outside the visible part of the galaxy, one would expect that

$$v(r) \propto \frac{1}{\sqrt{r}}. \quad (1.3)$$

¹Here the galaxy is assumed to be spherical symmetric.

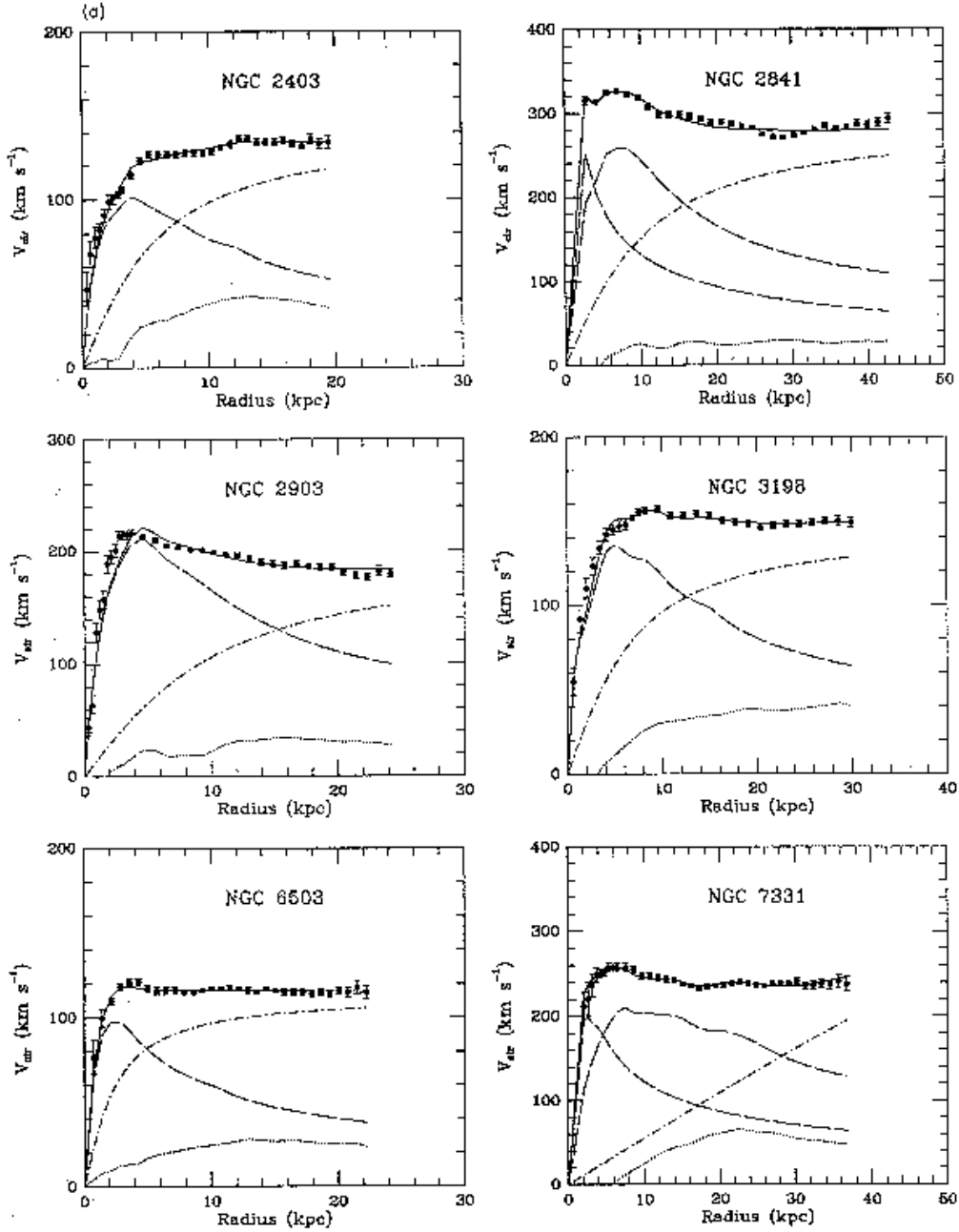


Figure 1. Three-parameter dark-halo fits (solid curves) to the rotation curves of sample galaxies. The rotation curves of the individual components are also shown: the dashed curves are for the visible components, the dotted curves for the gas, and the dash-dot curves for the dark halo. The fitting parameters are the mass-to-light ratio of the disc (M/L), the halo core radius (r_c), and the halo asymptotic circular velocity (V_h). The galaxies from the sample of Begeman are shown in (a) and the lower luminosity galaxies in (b). Best-fit values for the free parameters are given in columns 2, 3 and 4 of Table 2.

Figure 1.2a: Rotation curves for some simple spiral galaxies. The rotation curves of the individual components: visible component, gas, and dark halo, are also shown (figure from [7]).

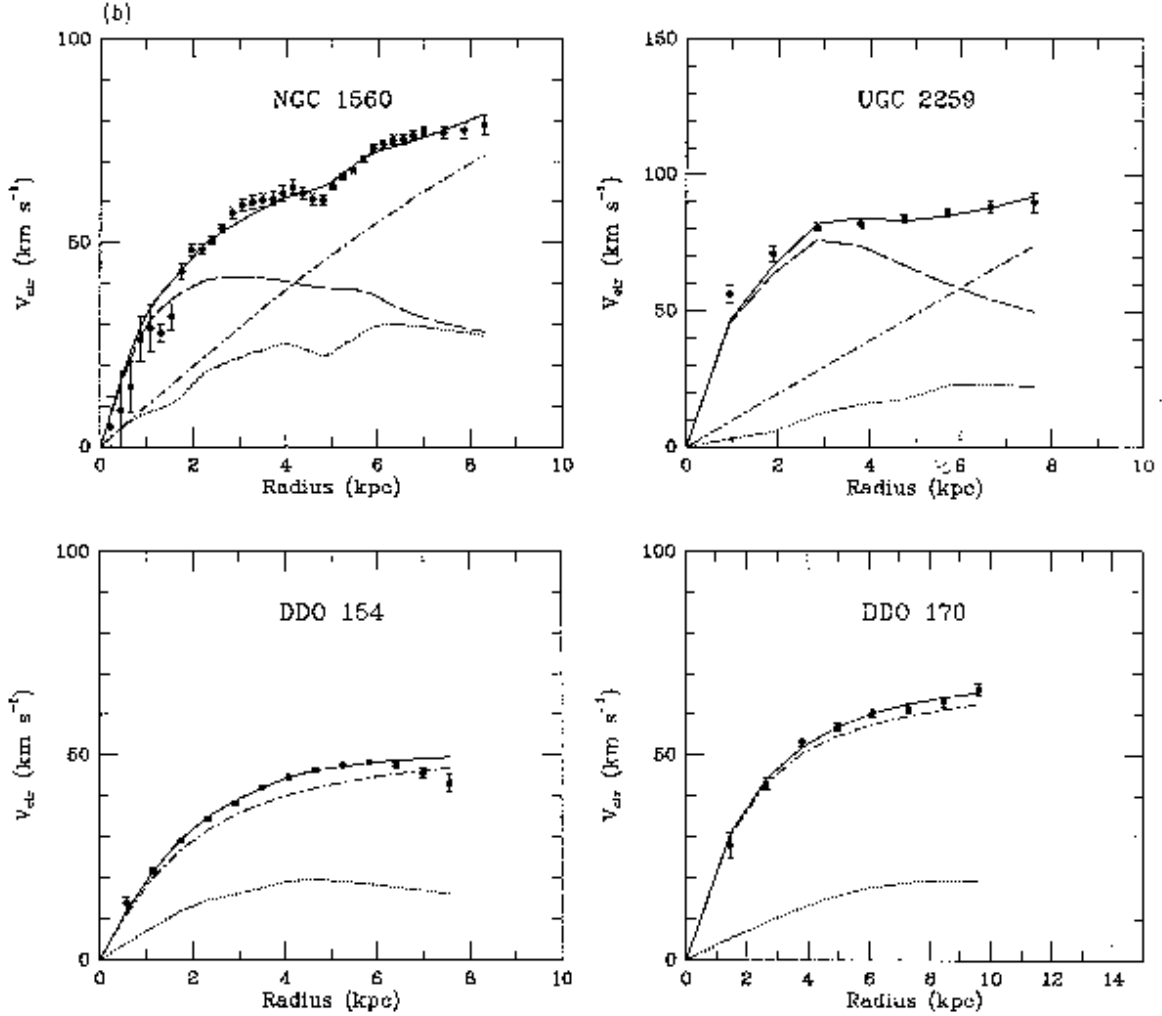


Figure 1 continued

Figure 1.2b: Rotation curves for some lower luminosity galaxies. The rotation curves of the individual components: visible component, gas, and dark halo, are also shown (figure from [7]).

However, measurements of the circular velocities of clouds of neutral hydrogen in galaxies by using their 21-cm emission [1] showed that the *rotation curves of spiral galaxies are flat* (see Figs. 1.1 and 1.2a) *or even rising* (see Fig. 1.2b) *at distances far away from their stellar and gaseous components* [4]-[8]. This implies the *existence of a “dark halo” around the galaxy* with a total mass profile:

$$M(r) \propto r, \tag{1.4}$$

i.e., the profile of the mass density should be

$$\rho(r) \propto \frac{1}{r^2}, \tag{1.5}$$

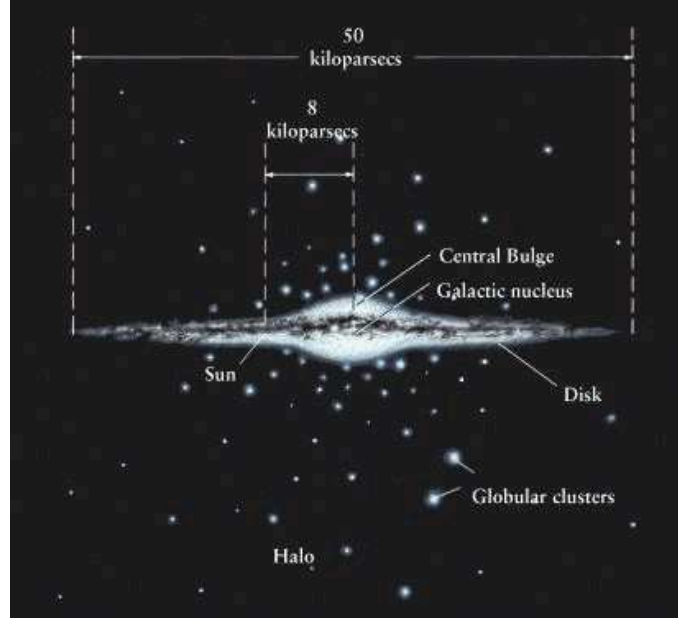


Figure 1.3: The position of the Sun in the Milky Way. The visible (luminous) component has been shown. It can be seen that our Solar system is already out of the Central Bulge of the Galaxy.

since

$$M(r) = 4\pi \int_0^r r'^2 \rho(r') dr'. \quad (1.6)$$

1.1.3 Escape velocity from the Milky Way

The escape velocity from the Milky Way at the position of our Solar system has been estimated as [9], [1]

$$v_{\text{esc}}^{\text{Galaxy}} \gtrsim 450 \text{ km/s}. \quad (1.7)$$

It is *much larger than can be accounted for by the luminous matter in our Galaxy*. It is not difficult to understand why this result so surprising if one thinks about the huge difference between the escape velocity from the Sun's surface [1]:

$$v_{\text{esc}}^{\odot} \cong 617.5 \text{ km/s}, \quad (1.8)$$

and that from the Solar system at the position of the Earth [10]:

$$v_{\text{esc}}^{\text{solar}} \cong 42.1 \text{ km/s}. \quad (1.9)$$

Recall that the gravitational well in our Solar system is essentially only caused by the Sun's mass which dominates the total mass of the Solar system. If the mass of the luminous matter in our Galaxy would also dominate the total mass of the Galaxy (see Fig. 1.3), the escape velocity from our Galaxy at the position of our Solar system would also be reduced (at least) one order of magnitude.

1.2 Cosmological density parameters

The cosmological density parameter of a given component of the total energy of the Universe i has been defined as the density of this component averaged over the Universe, ρ_i , in units of the *critical energy density* of the Universe, ρ_{crit} ,

$$\Omega_i \equiv \frac{\rho_i}{\rho_{\text{crit}}}. \quad (1.10)$$

The critical energy density of the Universe is the value that makes the geometry of the Universe flat (a more detailed explanation about the “flat Universe” will be given in Subsec. 1.2.2) [11]: ²

$$\begin{aligned} \rho_{\text{crit}} &= \frac{3H_0^2}{8\pi G_N} \simeq 2.775 \times 10^{11} h^2 M_{\odot}/\text{Mpc}^3 \\ &\simeq 1.878 \times 10^{-29} h^2 \text{ g/cm}^3. \end{aligned} \quad (1.11)$$

Here H is the expansion rate of the Universe (the time dependent Hubble parameter) defined as

$$H \equiv \frac{\dot{a}}{a} \quad (1.12)$$

with the scale factor of the Universe, $a(t)$, and H_0 denotes the expansion rate of the Universe “at the present epoch” (redshift $z = 0$),

$$H_0 \equiv 100h \text{ km/s/Mpc}, \quad (1.13)$$

with the dimensionless Hubble constant h . Moreover, the Newtonian gravitational constant, the mass of the Sun, and the parsec (pc) are given as [11]

$$G_N = 6.674 \times 10^{-11} \text{ m}^3/\text{kg/s}^2, \quad (1.14)$$

$$M_{\odot} = 1.988 \times 10^{30} \text{ kg}, \quad (1.15)$$

$$1 \text{ pc} \equiv \frac{1 \text{ AU}}{1 \text{ arc sec}} \simeq 3.0857 \times 10^{16} \text{ m} \simeq 3.262 c \cdot \text{yr}, \quad (1.16)$$

where the astronomical unit (AU), i.e., the mean distance between the Earth and the Sun, and the speed of light, c , are given as [11]

$$1 \text{ AU} = 1.4960 \times 10^{11} \text{ m}, \quad (1.17)$$

$$c \equiv 2.99792458 \times 10^8 \text{ m/s}. \quad (1.18)$$

In the rest of this section I present briefly some important astronomical measurements and their current results, by which the cosmological density parameters of different components of our Universe can be determined pretty exactly (to one or even two significant

²Note that ρ_{crit} here is the critical “energy density”. However, the factor c^2 in the expression has been usually neglected.

figure accuracy [12]). Particularly prominent are the measurement of the anisotropy of the cosmic microwave background (CMB) radiation, led by the three-year results from the Wilkinson Microwave Anisotropy Probe (WMAP) [13]. In the last subsection we will see that the cosmological density parameters also show the evidence for (or the necessity of) the existence of Dark Matter (and, more exactly, also of *Dark Energy*, both of them are “something which we do not know”). More details about theoretical explanations and experimental results of these measurements can be found in e.g., Refs. [14], [15], [12], and [16]-[18].

1.2.1 Cosmic microwave background (CMB)

The cosmic microwave background radiation (CMBR or CBR) discovered in 1965 provides the fundamental evidence for the hot Big-Bang model of the early Universe [14]. The spectrum of the CBR can be described very well by a blackbody function with the temperature T [18]. The energy density of “CMB photons” can then be obtained directly as [11]

$$\rho_\gamma = \frac{\pi^2 (k_B T)^4}{15 (\hbar c)^3}, \quad (1.19)$$

where the Boltzmann’s constant, k_B , and the Planck’s constant, \hbar , have been given as [14]

$$k_B = 1.3807 \times 10^{-23} \text{ J/K}, \quad (1.20)$$

$$\hbar = 1.0546 \times 10^{-34} \text{ J s}. \quad (1.21)$$

The present (mean) CBR temperature has been measured as [11]

$$T_0 = (2.725 \pm 0.001) \text{ K}. \quad (1.22)$$

1.2.2 Anisotropy of the CMB radiation

Another important observable quantity from the CMB is its anisotropy: tiny temperature difference (of order of 10^{-5} of the magnitude of the mean temperature T [18]) between two points on the sky (see Fig. 1.4). The measurement of the anisotropy of the CBR can be expanded in spherical harmonics as:

$$\delta T(\theta, \phi) = \sum_{l,m} a_{lm} Y_{lm}(\theta, \phi). \quad (1.23)$$

Here the multipole number l is given as

$$l \simeq \frac{200^\circ}{\theta}, \quad (1.24)$$

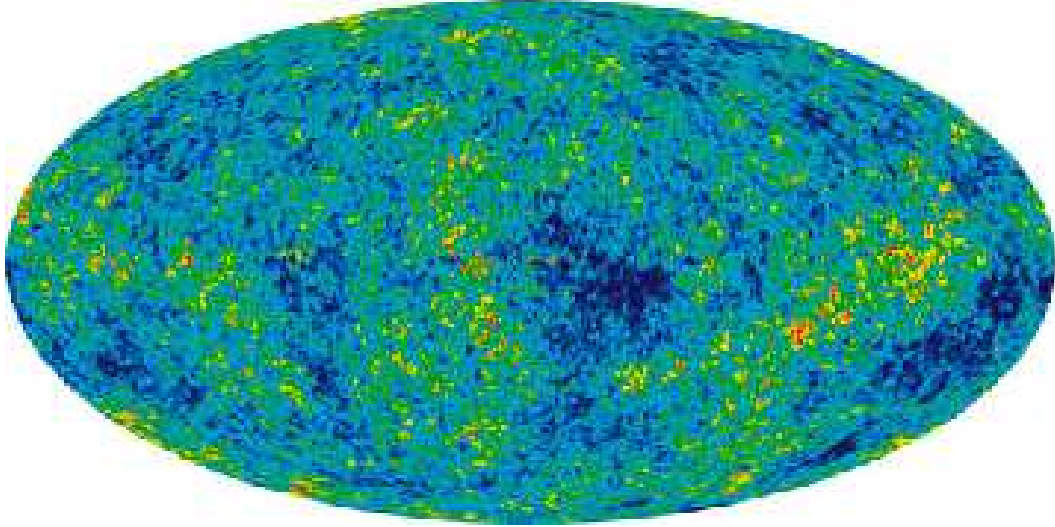


Figure 1.4: Anisotropy of the CMB radiation. The detailed, all-sky picture of the infant Universe from three years of WMAP data. The image reveals 13.7 billion year old temperature fluctuations (shown as color differences) which correspond to the seeds that grew to become the galaxies. The signal from our Galaxy was subtracted using the multi-frequency data. This image shows a temperature range of $\pm 200 \mu\text{K}$ (figure from NASA/WMAP Science Team).

and a useful quantity C_l has been defined as

$$C_l \equiv \langle |a_{lm}|^2 \rangle = \frac{1}{2l+1} \sum_{m=-l}^l |a_{lm}|^2. \quad (1.25)$$

The anisotropy of the CBR offers the best means for determining the curvature of the Universe, R_{curv} , [15] and thereby the “total matter/energy density” of the Universe, Ω_0 , according to the Friedmann equation [15], [12]:

$$\Omega_0 - 1 = \frac{k}{R_{\text{curv}}^2 H_0^2}, \quad (1.26)$$

where k is a curvature constant which can be chosen to take only three discrete values: ± 1 and 0. According to the Friedmann equation, when the total matter/energy density of our Universe is equal to 1, the Universe is “spatially flat” ($R_{\text{curv}} = \infty$, or, equivalently, $k = 0$). While, for $\Omega_0 > 1$ ($\Omega_0 < 1$), the constant k should be $+1$ (-1) and we call the Universe “closed” (“open”) [16]. In Fig. 1.5 one can find that the anisotropy power, sometimes shown as $l(l+1)C_l/2\pi$, oscillates (the so-called “gravity-driven acoustic oscillations”) with some “acoustic peaks”. Roughly speaking, the angular position of these peaks is a sensitive probe of the spatial curvature of the Universe: if our Universe is open (close), these peaks should lie at higher (lower) l [18].

Moreover, according to standard Big-Bang Cosmology, the higher the primordial matter density, the shorter the duration of the epoch of structure formation and thereby the larger fluctuations in the CBR [1], or, equivalently, the stronger these acoustic oscillations

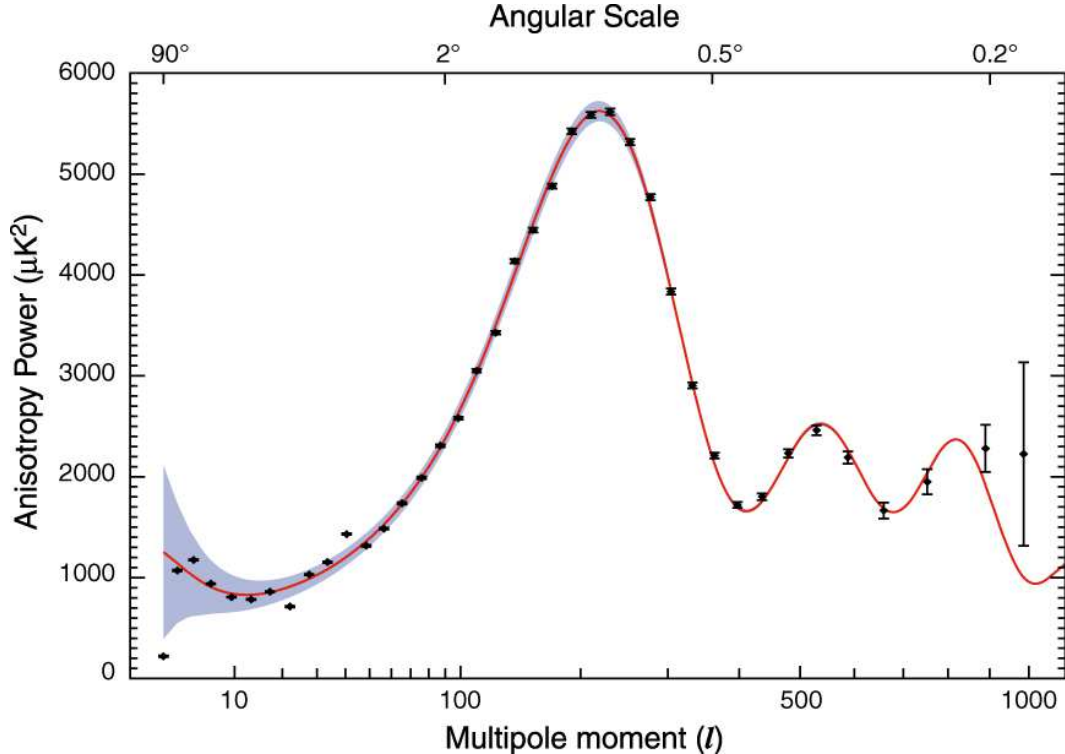


Figure 1.5: The angular power spectrum of the CMB temperature from three-year data of the WMAP satellite. The solid curve is the prediction from the best-fitting Λ CDM model. The error bars on the data points (which are tiny for most of them) indicate the observational errors, while the shaded region indicates the statistical uncertainty from being able to observe only one microwave sky, known as cosmic variance, which is the dominant uncertainty on large angular scales [12]. The first peak around $l \sim 200$ corresponds to $\theta \sim 1^\circ$ (figure from NASA/WMAP Science Team).

[15]. Hence, the relative height of the first acoustic peak can be used to determine the “primordial matter density”.

More details about the physics and the analyses of anisotropy of CBR can be found in Ref. [18].

1.2.3 Age of the Universe

As mentioned in the previous subsection, the higher the primordial matter density, the faster the Universe expanded and thus the shorter the age of the Universe reaching its present size. Hence, the measurements of the age of the Universe, T_U , and the expansion rate of the Universe, h , can give the upper and lower limits on the “matter density” in the Universe.

According to WMAP results combined with other astronomical measurements, the age of the Universe has been estimated as [13], [11]

$$T_U = 13.7_{-0.2}^{+0.1} \text{ Gyr}. \quad (1.27)$$

1.2.4 Present expansion rate of the Universe

According to the Hubble law [15]:

$$H_0 = \frac{v}{d}. \quad (1.28)$$

Here the velocity v can be determined by the redshift, thus the most accurate direct methods for measuring distances to distant objects d can be used to estimate the Hubble parameter H_0 [19]. Currently, there are two methods for measuring extra galactic distances [19]: time delays between luminosity variations in different gravitationally lensed images of distant quasars and the Sunyaev-Zel'dovich effect: Compton scattering of the CMB by the hot electrons in clusters of galaxies. Note that the error on the estimates of the Hubble parameter is dominated by one systematic uncertainty: the distance from our Galaxy to the Large Magellanic Cloud (LMC), which has been used to calibrate the Cepheid period-luminosity relationship [19].

The dimensionless Hubble constant has been estimated as [13], [11]

$$h = 0.73^{+0.03}_{-0.04}, \quad (1.29)$$

and the present expansion rate of the Universe can then be given as

$$H_0 = 73^{+3}_{-4} \text{ km/s/Mpc}. \quad (1.30)$$

1.2.5 Abundances of the light elements

BBN predicts the primordial abundances of the light elements. Thus measurements of the primordial abundances of the light elements produced in the Big Bang, such as deuterium (D), helium (^3He and ^4He), and lithium (^7Li), can also give the upper and lower limits of the “baryon density” in the Universe.

Moreover, among these four light elements, because the primordial abundance of deuterium depends strongly on the baryon density ($\propto \rho_b^{-1.7}$), and it can only be destroyed by the astrophysical processes, deuterium becomes the most powerful “baryometer” [15].

Fig. 1.6 shows the theoretically predicted abundances of the four lightest elements and the observational results.

1.2.6 Gas-to-total mass ratio

The clusters of galaxies formed due to density perturbations with a co-moving size of the order of 10 Mpc and gathered material from such a large region of the Universe [15]. Meanwhile, most of the baryons in the clusters of galaxies reside not in the galaxies themselves but in form of hot intercluster, x-ray emitting gas [15]. Hence, by measuring the gas-to-total mass ratio of the cluster, $f_{\text{gas/total}}$, and combining with the (measured)

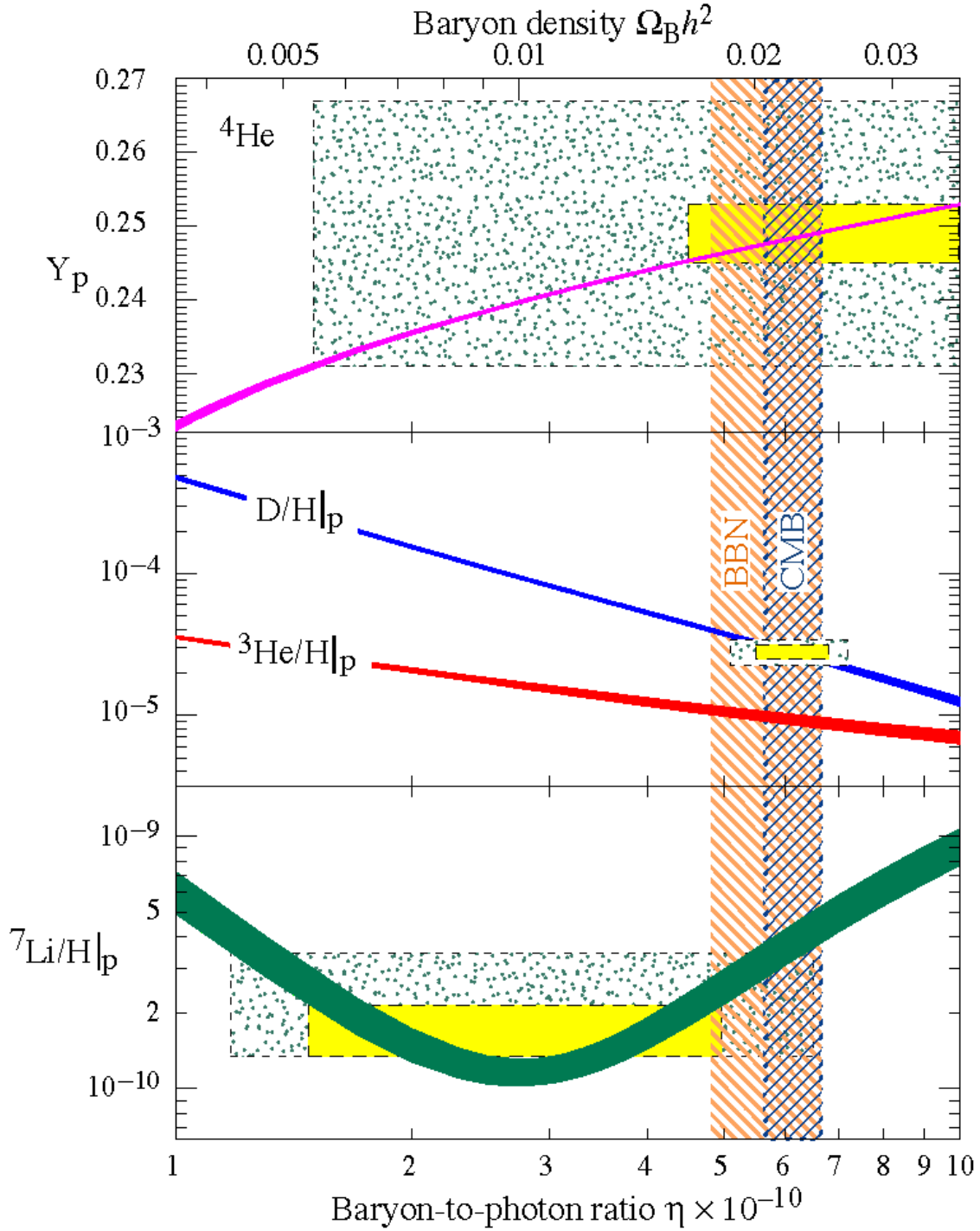


Figure 1.6: The predicted abundances of ${}^4\text{He}$ (mass fraction), D , ${}^3\text{He}$, and ${}^7\text{Li}$ (number relative to hydrogen) by the standard model of the BBN as a function of the baryon density. $Y_p \equiv 2n_n n_p / (n_n + n_p) \simeq 0.25$, where n_n and n_p are the neutron and proton number densities. Widths of the curves indicate 2σ theoretical uncertainty. Boxes indicate the observed light element abundances (smaller boxes: 2σ statistical errors; larger boxes: $\pm 2\sigma$ statistical and systematic errors). The narrow vertical band indicates the CMB measurement of the cosmic baryon density (figure from [17]).

baryon density in the Universe, Ω_b , we can determine the “matter density” in the Universe [15]:

$$\Omega_m = \frac{\Omega_b}{f_{\text{gas/total}}}. \quad (1.31)$$

There are two methods for determining the mass of the intercluster gas: the x-ray flux emitted from the intercluster gas or the Sunyaev-Zel’dovich CBR distortion caused by CMB photons scattering off hot electrons in the intracluster gas [15]. While, there are also three independent methods for estimating the total mass of a cluster: the motions of cluster galaxies with the virial theorem, assuming that the gas is in hydrostatic equilibrium and using it to infer the underlying mass distribution, or mapping the cluster mass directly by gravitational lensing [15], [20]. Within their uncertainties and where comparisons can be made, the two methods for determining the mass of the intercluster gas and the three methods for estimating the total mass of a cluster are consistent with each other, respectively [15].

1.2.7 Mass-to-light ratio

One other method for estimating the “matter density” of the Universe is using the mass-to-light ratios [15]:

$$\rho_m = \left(\frac{M}{L}\right) \mathcal{L}, \quad (1.32)$$

where \mathcal{L} is the averaged luminosity density of the Universe [1], [15]. In V-band [1] and in B-band [15], we have, respectively,

$$\mathcal{L}_V = (1.7 \pm 0.6) \times 10^8 h L_\odot/\text{Mpc}^3, \quad (1.33a)$$

and

$$\mathcal{L}_B = 2.4 \times 10^8 h L_\odot/\text{Mpc}^3, \quad (1.33b)$$

where L_\odot is the luminosity of the Sun [11],

$$L_\odot = (3.846 \pm 0.008) \times 10^{26} \text{ W}. \quad (1.34)$$

Once we have estimated the mass-to-light ratios of some systems, i.e.,

$$\Upsilon_x \equiv \frac{M}{L_x}, \quad x = \text{V, B}. \quad (1.35)$$

Then, combining Eqs.(1.10), (1.11), (1.32) and (1.33a) or (1.33b), the total matter density can be obtained as

$$\Omega_{m,x} = \frac{C_x}{10^4 h} \left(\frac{\Upsilon_x}{\Upsilon_\odot}\right), \quad x = \text{V, B}. \quad (1.36)$$

Here

$$C_V = 6.1, \quad C_B = 8.6, \quad (1.37)$$

and Υ_\odot is the mass-to-light ratio of the Sun,

$$\Upsilon_\odot = 5.169 \times 10^3 \text{ kg/W}, \quad (1.38)$$

where I have used Eqs.(1.15) and (1.34).

1.2.8 Supernovae type Ia (SNe Ia) at high-redshift

If we could measure the present extra galactic distances d_0 and velocities v_0 , they should obey the Hubble law [15]:

$$\frac{v_0}{d_0} = H_0, \quad (1.39)$$

since the expansion of the Universe is simply a rescaling. But what we can actually measure are the distances d_z and velocities v_z at an earlier time (redshift z). If we suppose that the expansion of our Universe should slow down due to the attractive force of gravity, i.e., $H_z > H_0$, the measured galactic velocities should be larger than that expected by the Hubble law:

$$v_z = d_z H_z > d_z H_0, \quad (1.40)$$

or, equivalently, for the galaxies with known velocities, their distances should be shorter than that expected by the Hubble law:

$$d_z = \frac{v_z}{H_z} < \frac{v_z}{H_0}. \quad (1.41)$$

In 1998 two groups: the Supernova Cosmology Project and the High- z Supernova Search Team have published their “magnitude-redshift (Hubble) diagram for fifty-some type Ia supernovae (SNe Ia) out to redshifts of nearly 1” [15]. By using SNe Ia as standard candles for estimating the distances to faraway galaxies, the two groups concluded that *distant galaxies are moving slower than predicted by the Hubble law* and that *this implies an accelerated expansion of our Universe* [15].

In order to explain this observational indication, i.e., in order to find the discrepancy between the measured total matter(/energy) density, Ω_0 , and the matter density, Ω_m , (data given in the next subsection), a new term “Dark Energy”³ (or sometimes also called “quintessence”) has been introduced [15].

³Dark Energy is beyond the area of my research and thus will not be discussed in this work. Short reviews and summaries can be found in e.g., [15], [12], [16], and [21].

1.2.9 Cosmological densities of different components

According to the various astronomical measurements described above (and other measurements, e.g., the peculiar velocities of galaxies, the shape of the present power spectrum of density perturbations, and the opacity of the Lyman- α forest toward high-redshift quasars), we can conclude today the cosmological densities of different components as follows.

The total matter/energy density is [13], [11]

$$\Omega_0 = 1.003^{+0.013}_{-0.017}. \quad (1.42)$$

It can be separated into Dark Energy [11]:

$$\Omega_\Lambda \equiv \frac{\Lambda}{3H_0^2} = 0.76^{+0.04}_{-0.06}, \quad (1.43)$$

where we have used

$$\rho_\Lambda = \frac{\Lambda}{8\pi G_N}, \quad (1.44)$$

and total matter [13], [11]:

$$\Omega_m = 0.127^{+0.007}_{-0.009} h^{-2} = 0.24^{+0.03}_{-0.04}. \quad (1.45)$$

The total matter in the Universe can also be separated into baryons [13], [11]:

$$\Omega_b = 0.0223^{+0.0007}_{-0.0009} h^{-2} = 0.042^{+0.003}_{-0.005}, \quad (1.46)$$

and *non-baryonic Dark Matter* [11]:

$$\Omega_{\text{DM}} = \Omega_m - \Omega_b = 0.105^{+0.007}_{-0.010} h^{-2} = 0.20^{+0.02}_{-0.04}. \quad (1.47)$$

Among the baryons in the Universe there is luminous matter with a density of [1] [22]:

$$\Omega_{\text{lum}} \simeq 0.01, \quad (1.48)$$

including the density of the stars [23]:

$$\Omega_{\text{stars}} = (0.0023 \sim 0.0041) \pm 0.0004. \quad (1.49)$$

While, the non-baryonic Dark Matter can be separated into *Cold Dark Matter* (CDM) and *Hot Dark Matter* (HDM) (the definitions and some discussions about the CDM and HDM will be given in Secs. 2.1 and 2.2, respectively). Finally, among the relativistic particles (see Sec. 2.2), the density of the CMB photons can be estimated directly by inserting T_0 in Eq.(1.22) into Eq.(1.19) as [11]

$$\Omega_\gamma = (2.471 \pm 0.004) \times 10^{-5} h^{-2} = (4.6 \pm 0.5) \times 10^{-5}, \quad (1.50)$$

and the density of the neutrinos has been estimated as [11]

$$\Omega_\nu < 0.014 \text{ (95\% C. L.)}. \quad (1.51)$$

1.3 Galactic halo models

In this section I present some simple halo models. For estimating some characteristics of halo Dark Matter, such as the velocity dispersion of Dark Matter particles, \bar{v} , and the local Dark Matter density, ρ_0 , the rotation curve of our Galaxy is the most important observational quantity, since it measures the change in density and sets the scale for the depth of the Galactic potential well [1]. Essentially, all important direct information which has been obtained about the halo is provided by the rotation curve [24]. However, due to our location inside the Milky Way, it is more difficult to measure the accurate rotation curve of our own Galaxy than those of other galaxies (see Fig. 1.7). In addition, the “disk contribution” to the rotation curve must be known to infer the halo contribution, but precise determination of the disk contribution is also difficult.

1.3.1 Standard assumptions of Dark Matter halo

The velocity dispersion of Dark Matter particles ⁴ in the Solar neighborhood has been assumed as

$$\bar{v} = \langle v^2 \rangle^{1/2} \simeq 270 \text{ km/s}. \quad (1.52)$$

And the IAU standard value for the rotational velocity at the Sun’s distance from the Galactic center is [11]

$$v_0 \equiv v_{\text{rot}}(r_0) \simeq (220 \pm 20) \text{ km/s}, \quad (1.53)$$

where the distance from the Sun to the Galactic center is [11]

$$r_0 \simeq (8.0 \pm 0.5) \text{ kpc}. \quad (1.54)$$

On the other hand, the local Dark Matter density (the Dark Matter density near the Solar system) is given by [1]

$$\begin{aligned} \rho_0 \equiv \rho(r_0) &\approx 0.3 \text{ GeV}/c^2/\text{cm}^3 \\ &\approx 5 \times 10^{-25} \text{ g/cm}^3, \end{aligned} \quad (1.55)$$

with an uncertainty of slightly less than a factor of 2 [1], [15]. Here I have used [25]

$$1 \text{ GeV}/c^2 = 1.7827 \times 10^{-24} \text{ g}. \quad (1.56)$$

⁴ Strictly speaking, the velocity dispersion should be $\langle \mathbf{v}^2 \rangle - \langle \mathbf{v} \rangle^2$. However, since the major component of Dark Matter should be cold (a detailed discussion will be given in Sec. 2.1) and assumed to have negligibly small velocity average $\langle \mathbf{v} \rangle$ in the Galactic rest frame, its rms velocity $\langle v^2 \rangle$ has been called sometimes simply as the velocity dispersion.

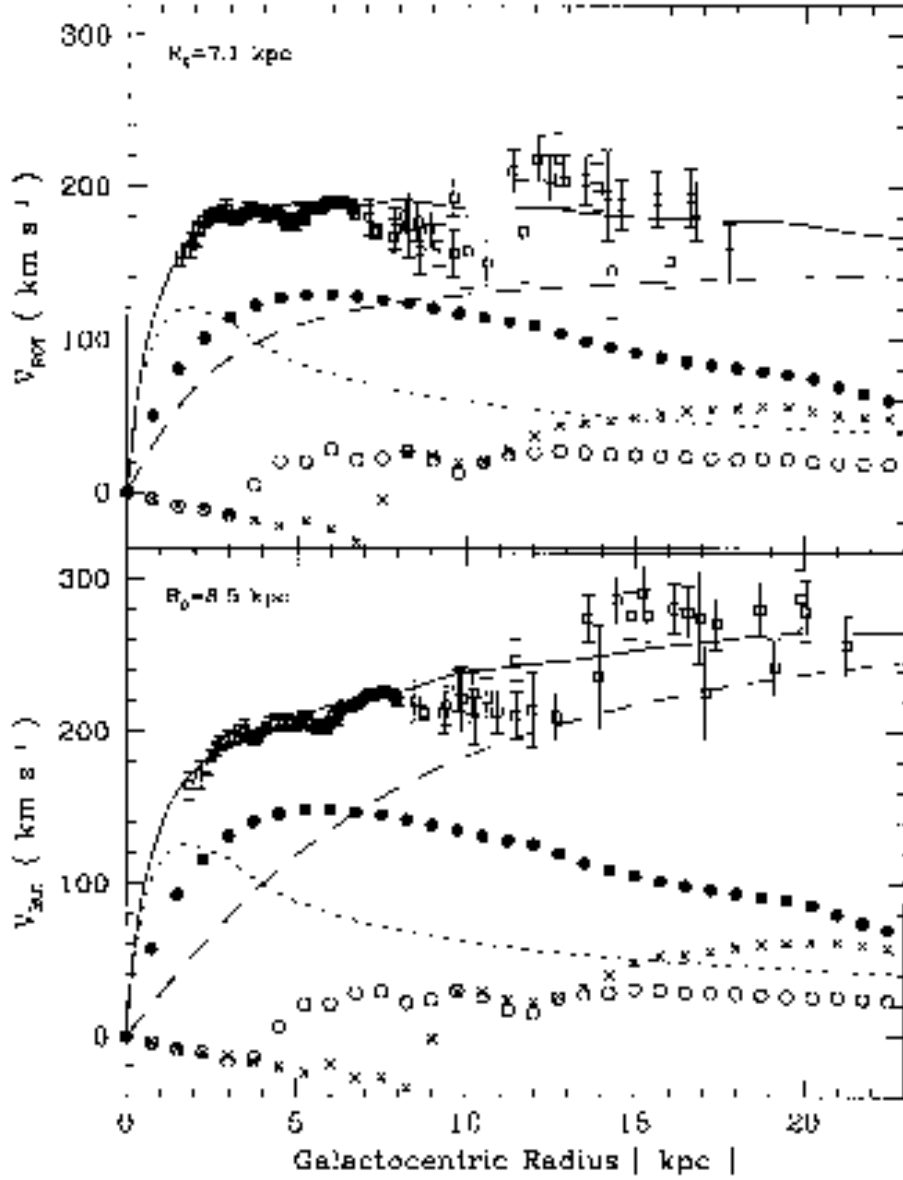


Figure 2. The rotation curve for the Milky Way for values of $R_{\odot} = 7.1$ kpc, $\Theta_{\odot} = 185 \text{ km s}^{-1}$, and $R_{\odot} = 8.5$ kpc, $\Theta_{\odot} = 220 \text{ km s}^{-1}$. The figure also shows one of the ways in which the rotation curve can be decomposed into the contributions from different mass components: the bulge (dotted line); the stellar disc (filled circles); the H I layer (crosses, where negative values mean that the force is directed outwards); the H₂ layer (circles); and the dark halo (dashed line). The best-fitting model, which is obtained by summing the individual components in quadrature, is shown as a full line.

Figure 1.7: Rotation curve for the Milky Way, as a function of distance from the Galactic center, with two different assumptions for the Sun's distance from the Galactic center, r_0 , and the rotation velocity at r_0 , $v_{\text{rot}}(r_0)$ (figure from [8]).

1.3.2 Canonical isothermal spherical halo model

The simplest halo model is an isothermal spherical halo. An empirically plausible radial profile for a spherical galactic halo is constrained only by its contribution to the galactic rotation curve. This means that the radial profile should approach to a constant near its core so that it gives rise to a linearly rising rotation curve at small radii, and it should fall as $1/r^2$ or eventually faster at large radii to provide a flat rotation curve [24]. The density profile of the cored isothermal spherical halo is given by [1]

$$\rho_{\text{IS}}(r) = \rho_0 \left(\frac{r_c^2 + r_0^2}{r_c^2 + r^2} \right), \quad (1.57)$$

where ρ_0 is the local halo density and r_c is the core radius of the isothermal spherical halo, within which the density $\rho_{\text{IS}}(r)$ behaves no longer as $1/r^2$, but goes to a constant as r approaches 0.

Substituting this expression into Eq.(1.6) and using Eq.(1.1), the rotational velocity at a radius r from the halo center can be found as

$$\begin{aligned} v_{\text{IS}}^2(r) &= 4\pi G_N \cdot \frac{1}{r} \int_0^r r'^2 \rho(r') dr' \\ &= 4\pi G_N \rho_0 (r_c^2 + r_0^2) \left[1 - \left(\frac{r_c}{r} \right) \tan^{-1} \left(\frac{r}{r_c} \right) \right], \end{aligned} \quad (1.58)$$

where I have used

$$\int \frac{x^2 dx}{a^2 + x^2} = x - a \tan^{-1} \left(\frac{x}{a} \right).$$

Define v_∞ as the (measured) rotational velocity as $r \rightarrow \infty$. One can find that

$$v_\infty^2 = v_{\text{IS}}^2(r \rightarrow \infty) = 4\pi G_N \rho_0 (r_c^2 + r_0^2), \quad (1.59)$$

thus the local halo density ρ_0 in Eq.(1.57) can be expressed as

$$\rho_0 = \frac{v_\infty^2}{4\pi G_N (r_c^2 + r_0^2)}. \quad (1.60)$$

Meanwhile, combining Eqs.(1.58) and (1.59), the core radius of the isothermal spherical halo in unit of r_0 , i.e., r_c/r_0 , can be solved (numerically) by [1]:

$$\left(\frac{r_c}{r_0} \right) \tan^{-1} \left(\frac{r_0}{r_c} \right) = 1 - \frac{v_{\text{IS}}^2(r_0)}{v_\infty^2}. \quad (1.61)$$

Eqs.(1.60) and (1.61) show how we can estimate the local halo density and the halo core radius in the isothermal spherical halo model once the rotational velocities v_0 and v_∞ have been measured.

Finally, substituting Eq.(1.60) into Eqs.(1.57) and (1.58) the density profile and the rotation curve of the isothermal spherical halo model can be rewritten as

$$\rho_{\text{IS}}(r) = \frac{v_\infty^2}{4\pi G_N} \left(\frac{1}{r_c^2 + r^2} \right), \quad (1.57')$$

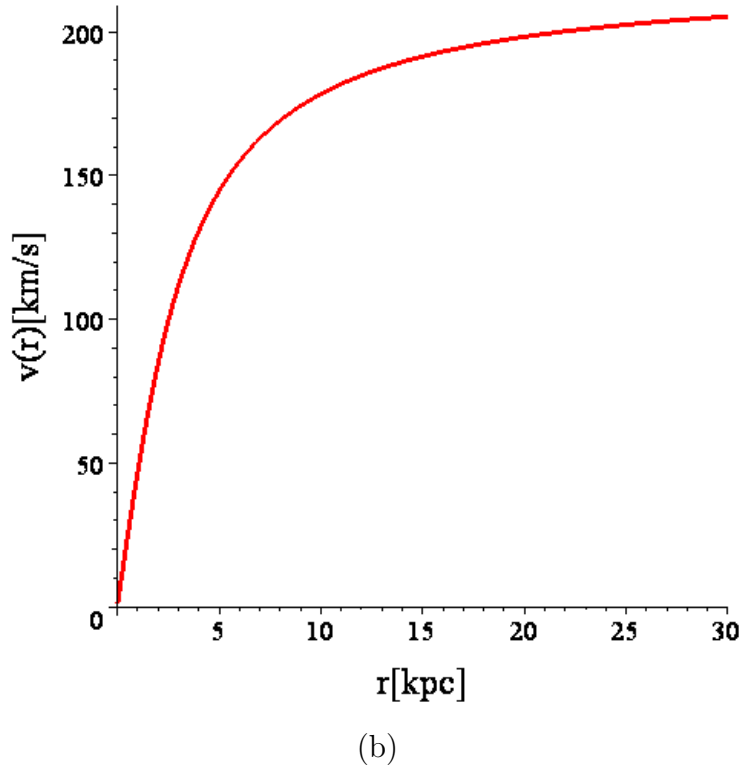
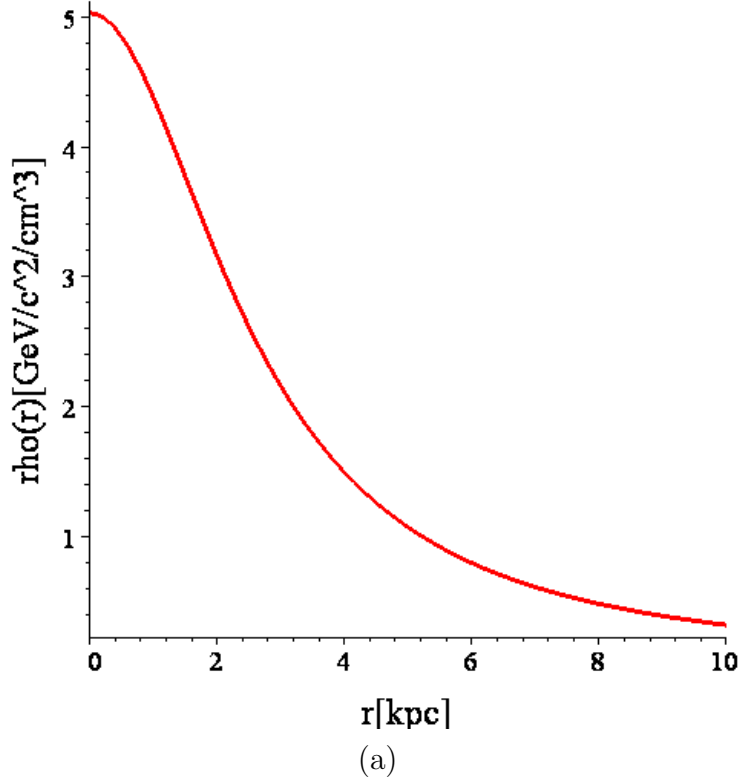


Figure 1.8: (a) The radial density profile $\rho_{\text{IS}}(r)$ given in Eq.(1.57') and (b) the rotation curve $v_{\text{IS}}(r)$ given in Eq.(1.58') of the canonical isothermal spherical halo model. Here I have used $v_{\infty} = 220$ km/s [24] and $r_c = 2.6$ kpc (see Subsec. 1.3.4).

and

$$v_{\text{IS}}(r) = v_{\infty} \left[1 - \left(\frac{r_c}{r} \right) \tan^{-1} \left(\frac{r}{r_c} \right) \right]^{1/2}, \quad (1.58')$$

Figs. 1.8 show the radial density profile (upper frame) and the rotation curve (lower frame) of the canonical isothermal spherical halo model given in Eqs.(1.57') and (1.58'), respectively.

1.3.3 Alternative isothermal spherical halo model

An alternative density profile for the isothermal spherical halo has been given by [24]

$$\rho_{\text{AIS}}(r) = \rho_0 \left(\frac{r_c + r_0}{r_c + r} \right)^2, \quad (1.62)$$

where ρ_0 is again the local halo density and r_c is the core radius of this alternative isothermal spherical halo mode.⁵ Using Eqs.(1.6) and (1.1), the rotation curve of this alternative isothermal spherical halo can be found as

$$v_{\text{AIS}}^2(r) = 4\pi G_N \rho_0 (r_c + r_0)^2 \left[1 + \frac{r_c}{r_c + r} - 2 \left(\frac{r_c}{r} \right) \ln \left(\frac{r_c + r}{r_c} \right) \right], \quad (1.63)$$

where I have used

$$\int \frac{x^2 dx}{(ax + b)^2} = \frac{1}{a^3} \left[(ax + b) - \frac{b^2}{ax + b} - 2b \ln(ax + b) \right].$$

Meanwhile, the core radius of this alternative halo model in unit of r_0 can be solved (numerically) by :

$$2\alpha_c \ln \left(\frac{\alpha_c + 1}{\alpha_c} \right) - \frac{\alpha_c}{\alpha_c + 1} = 1 - \frac{v_{\text{AIS}}^2(r_0)}{v_{\infty}^2}. \quad (1.64)$$

where I have defined

$$\alpha_c \equiv \frac{r_c}{r_0}. \quad (1.65)$$

Finally, from Eq.(1.63), one has

$$v_{\infty}^2 = v_{\text{AIS}}^2(r \rightarrow \infty) = 4\pi G_N \rho_0 (r_c + r_0)^2, \quad (1.66)$$

the density profile and the rotation curve of the alternative isothermal spherical halo model in Eqs.(1.62) and (1.63) can be rewritten as

$$\rho_{\text{AIS}}(r) = \frac{v_{\infty}^2}{4\pi G_N} \left(\frac{1}{r_c + r} \right)^2, \quad (1.62')$$

and

$$v_{\text{AIS}}(r) = v_{\infty} \left[1 + \frac{r_c}{r_c + r} - 2 \left(\frac{r_c}{r} \right) \ln \left(\frac{r_c + r}{r_c} \right) \right]^{1/2}. \quad (1.63')$$

Fig. 1.9 shows the equations for solving the ratios of the core radii of two cored isothermal spherical halo models to the distance from the Sun to the Galactic center, $\alpha_c \equiv r_c/r_0$, given in Eqs.(1.61) and (1.64).

⁵Here, for simplicity, I use the same notation as in Eq.(1.57), but r_c for these two halo models are not the same. The determination of these core radii will be given in Subsec. 1.3.4

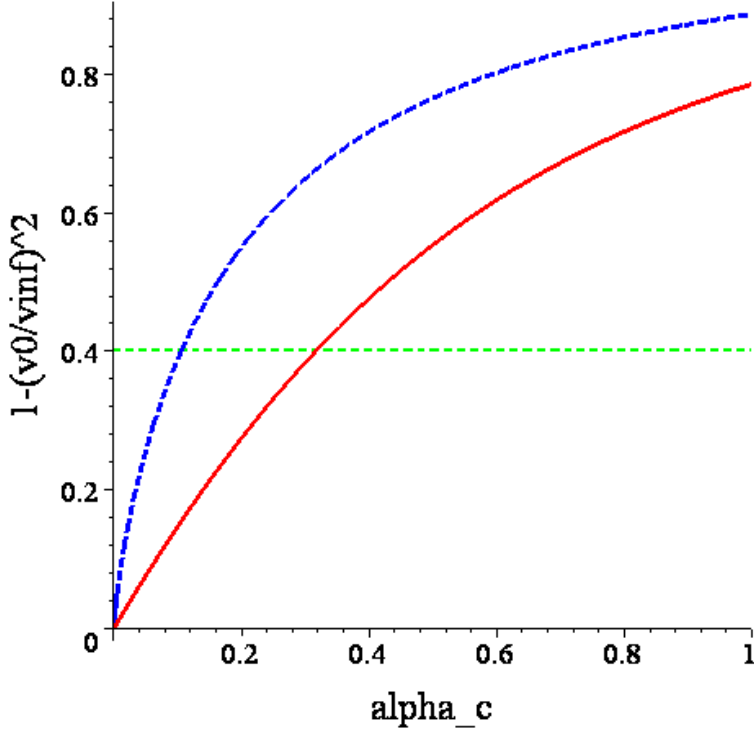


Figure 1.9: The equations for solving the ratios of the core radii of two cored isothermal spherical halo models to the distance from the Sun to the Galactic center, $\alpha_c \equiv r_c/r_0$. The solid (red) line shows Eq.(1.61) and the dash-dotted (blue) line shows Eq.(1.64). Here the dash (green) line denotes $v_{\text{IS}}(r_0) = v_{\text{AIS}}(r_0) = v_{\text{halo}}(r_0) = 170$ km/s [1], [24] and $v_\infty = 220$ km/s.

1.3.4 Evans' power-law halo model

Even if we consider only spherical halo distributions, there are still some latitudes in our choice for the precise form of the radial density profile of a halo model. Meanwhile, N-body simulations of gravitational collapse produce axisymmetric or triaxial halos [26], and other spiral galaxies appear to have flattened halos [27], [26].

The equipotentials of elliptical galaxies and the halos of spiral galaxies could be roughly stratified on similar concentric spheroids [28]. This suggests a useful approximation to their gravity field as [28]:

$$\psi(r, z) = \frac{\psi_a r_c^\beta}{(r_c^2 + r^2 + z^2/q^2)^{\beta/2}}, \quad \beta \neq 0, \quad (1.67)$$

where ψ_a is the central potential, r_c is the core radius of the halo, and q is the axis ratio of the equipotentials or the so-called flattening parameter. Note that I use here the cylindrical coordinates and r denotes the distance from the point which one considers to the rotation axis. The potential is just a power of the spheroidal radius r , thus this model has been called the power-law halo model [28].

Using the Poisson Equation: ⁶

$$\nabla^2 \psi = -4\pi G_N \rho, \quad (1.68)$$

the density distribution of the gravitational potential described in Eq.(1.67) can be obtained as [28]

$$\rho(r, z) = \frac{v_a^2}{4\pi G_N} \left(\frac{r_c^\beta}{q^2} \right) \left[\frac{(2q^2 + 1)r_c^2 + (1 - \beta q^2)r^2 + (2q^2 - \beta - 1)z^2/q^2}{(r_c^2 + r^2 + z^2/q^2)^{\beta/2+2}} \right], \quad (1.69)$$

where

$$v_a^2 \equiv \beta \psi_a. \quad (1.70)$$

Meanwhile, the velocity of the circular orbit in the equatorial plane with radius r can be obtained as [28]

$$v_{\text{circ}}(r) = v_a \left[\frac{r_c^\beta r^2}{(r_c^2 + r^2)^{\beta/2+1}} \right]^{1/2}, \quad (1.71)$$

since the central force

$$F_{\text{cen}}(r, z = 0) = -\nabla \psi(r, z) \cdot \hat{r} \Big|_{z=0} = \frac{v_{\text{circ}}^2(r)}{r}. \quad (1.72)$$

The rotational velocity in Eq.(1.71) is asymptotically falling if $\beta > 0$ and rising if $\beta < 0$ [28].

On the other hand, the model with spheroidal equipotentials and a completely flat rotation curve at large radii is well known as an axisymmetric logarithmic potential [29], [30], [28]:

$$\psi(r, z) = -\frac{v_a^2}{2} \ln \left(r_c^2 + r^2 + \frac{z^2}{q^2} \right), \quad (1.73)$$

where v_a is the rotational velocity at large radii (i.e., v_∞ used in the previous two subsections). Using the Poisson Equation, the density distribution can be found as [30]

$$\rho(r, z) = \frac{v_a^2}{4\pi G_N} \left[\frac{(2q^2 + 1)r_c^2 + r^2 + (2q^2 - 1)z^2/q^2}{q^2(r_c^2 + r^2 + z^2/q^2)^2} \right]. \quad (1.74)$$

Comparing this expression with the expression in Eq.(1.69), it can be seen that the logarithmic potential given in Eq.(1.73) has the properties corresponding to the missing $\beta = 0$ case in Eq.(1.67) [28]. The velocity of the circular orbit in the equatorial plane with radius r due to the potential given in Eq.(1.73) can be obtained as

$$v_{\text{circ}}(r) = v_a \left(\frac{r^2}{r_c^2 + r^2} \right)^{1/2}. \quad (1.75)$$

⁶Note that the Poisson Equation holds actually for the “total” potential and the “total” density distribution, i.e., for luminous baryonic matter and Dark Matter together, not for each component separately.

Furthermore, let $q = 1$ and use the replacement:

$$r^2 + z^2 \rightarrow r^2, \quad (1.76)$$

we can rewrite the potential in Eq.(1.73) to the potential for a spherical halo as [30]

$$\psi(r) = -\frac{v_a^2}{2} \ln(r_c^2 + r^2). \quad (1.77)$$

The density distribution and the velocity of the circular orbit of this spherical Evans model with radius r can be obtained as, respectively [30], [24],

$$\rho_{\text{PL}}(r) = \frac{v_a^2}{4\pi G_N} \left[\frac{3r_c^2 + r^2}{(r_c^2 + r^2)^2} \right], \quad (1.78)$$

and

$$v_{\text{circ}}(r) = v_a \left(\frac{r^2}{r_c^2 + r^2} \right)^{1/2}. \quad (1.79)$$

As done in Subsecs. 1.3.2 and 1.3.3, the core radius of the halo in unit of r_0 can be solved by means of the following equation [24]:

$$\frac{r_c}{r_0} = \left[\frac{v_a^2}{v_{\text{circ}}^2(r_0)} - 1 \right]^{1/2}. \quad (1.80)$$

Finally, using the local rotational velocity given in Eq.(1.53):

$$v_{\text{rot}}(r_0) \simeq 220 \text{ km/s}, \quad (1.53')$$

and the assumption for the disk contribution to the rotational velocity at $r = r_0$ [1], [24]:

$$v_{\text{disk}}(r_0) = 140 \text{ km/s}, \quad (1.81)$$

the local halo contribution can be found as

$$v_{\text{halo}}(r_0) \simeq 170 \text{ km/s}, \quad (1.82)$$

since,

$$v_{\text{rot}}(r_0) = \sqrt{v_{\text{disk}}^2(r_0) + v_{\text{halo}}^2(r_0)}. \quad (1.83)$$

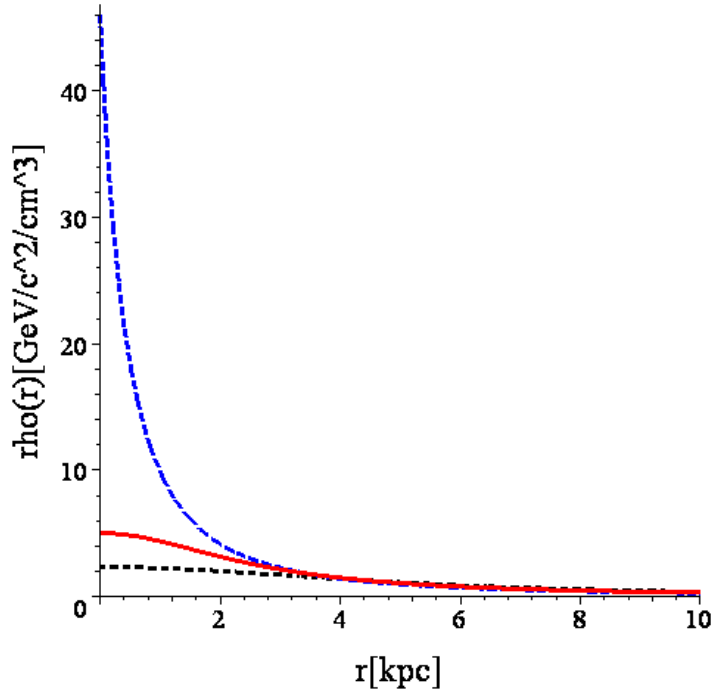
Then the core radii for the canonical, alternative, and Evans spherical halo models given in Eqs.(1.57'), (1.62'), and (1.78) can be found by means of Eqs.(1.61), (1.64), and (1.80) as

$$r_{c,\text{IS}} \simeq 2.6 \text{ kpc}, \quad (1.84)$$

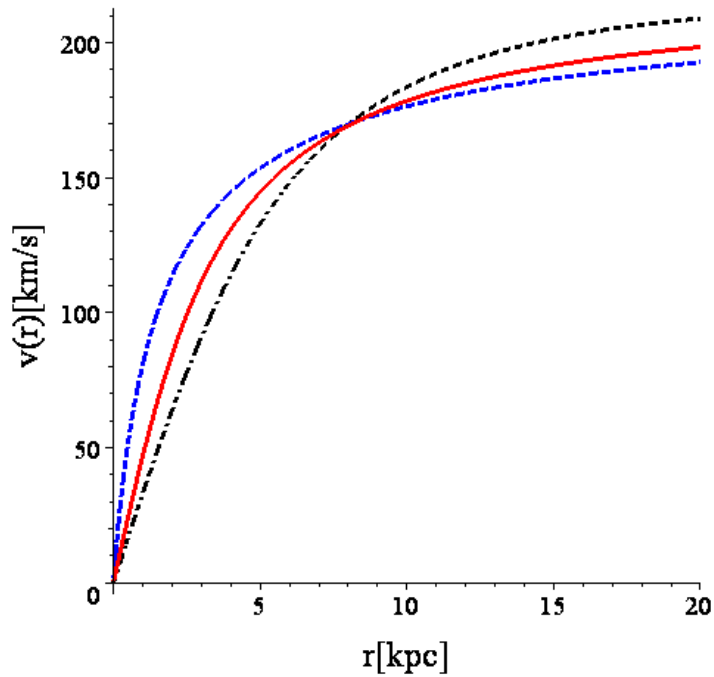
$$r_{c,\text{AIS}} \simeq 0.86 \text{ kpc}, \quad (1.85)$$

and

$$r_{c,\text{PL}} \simeq 6.6 \text{ kpc}, \quad (1.86)$$



(a)



(b)

Figure 1.10: (a) The radial density profiles and (b) the rotation curves of different isothermal spherical halo models. The solid (red) lines indicate the canonical halo model in Eq.(1.57') with $r_c \simeq 2.6$ kpc, the dash (blue) lines indicate the alternative halo model in Eq.(1.62') with $r_c \simeq 0.86$ kpc, and the dash-dotted (black) lines indicate the spherical Evans' halo model in Eq.(1.78) with $r_c \simeq 6.6$ kpc. Here I have used $v_\infty = 220$ km/s [24].

where I used

$$r_0 \simeq 8.0 \text{ kpc}, \quad (1.54')$$

and the rotational velocity at large radii as [24]

$$v_\infty = v_a = 220 \text{ km/s}. \quad (1.87)$$

Figs. 1.10 show the radial density profiles (upper frame) and the rotation curves (lower frame) of different isothermal spherical halo models with the core radii obtained above.

1.3.5 NFW halo model

Besides the three spherical halo models presented in the previous three subsections, there is also the well-known NFW density profile given as [31]-[33]:

$$\rho_{\text{NFW}}(r) = \frac{\rho_s}{(r/r_s)(1+r/r_s)^2}. \quad (1.88)$$

Here ρ_s is the characteristic density [33]:

$$\rho_s = \rho_{\text{crit}} \left(\frac{\lambda_s}{3} \right) \left[\frac{c_s^3}{\ln(1+c_s) - c_s/(1+c_s)} \right], \quad (1.89)$$

with the virial overdensity λ_s and the halo concentration parameter c_s , and r_s is the characteristic radius [33]:

$$r_s = \frac{r_{\text{vir}}}{c_s} = \frac{1.2 \times 10^2}{c_s} \left(\frac{M_{\text{vir}}}{10^{11} M_\odot} \right)^{1/3} \text{ kpc}. \quad (1.90)$$

The virial radius, r_{vir} , defined as the radius, inside which the average overdensity is λ_s times the critical density of the Universe, and the virial mass, M_{vir} is then the total mass within this virial radius r_{vir} [32]. Usually the average overdensity λ_s has been chosen as ≈ 200 , and the virial radius and the virial mass for $\lambda_s = 200$ have been then specially labeled as r_{200} and M_{200} , respectively [32]. However, for a flat Universe, i.e., $\Omega_0 = 1$, the average overdensity λ_s has been found to be [34]

$$\lambda_s = 18\pi^2 \simeq 178. \quad (1.91)$$

Note that there is a good correlation between c_s and M_{vir} in Eq.(1.90), which results from the fact that dark halo densities reflect the density of the Universe at the epoch of their formation and that halos of a given mass are preferentially assembled over a narrow range of redshifts [32]. Hence, as lower mass halos form earlier, at times when the Universe was significantly denser, they are more centrally concentrated [32].

Although the NFW density profile given in Eq.(1.88) doesn't approach the $1/r^2$ form for large r , high-resolution N-body simulations of structure formation and some observational results have shown that the NFW profile indeed provides a good description of the density distribution in clusters [34], [32].

Moreover, the NFW density profile given in Eq.(1.88) has been expanded to the following form [35]:

$$\rho_{\text{NFWE}}(r) = \frac{\rho_s}{(r/r_s)^\alpha (1 + r/r_s)^\nu}. \quad (1.92)$$

For the original NFW profile, one has $\alpha = 1$, $\nu = 2$; for a modified NFW profile, one can use $\alpha = \nu = 3/2$; and for a so-called Hernquist profile one has $\alpha = 1$, $\nu = 3$ [36], [35].

On the other hand, A. Burkert has suggested a Burkert density profile [32]:

$$\rho_{\text{B}}(r) = \frac{\rho_b}{(1 + r/r_b) [1 + (r/r_b)^2]}. \quad (1.93)$$

Some analyses show that density profiles of dwarfs and low surface brightness galaxies can be fitted by the Burkert profile much better than the NFW profile [34].

1.3.6 Bulk rotation

So far the halo models presented above are only classified by their density profiles or the gravity field, namely, their mass distribution. Because, as mentioned in the beginning of this section, what has been measured is just the rotation curve [24]. However, the rotation curve is determined by the halo mass distribution and is insensitive to its velocity distribution [24]. Thus, even though there are some theoretical arguments against a rotation-dominated velocity distribution, there is no empirical evidence to rule out a halo with bulk rotation [24]. Note that such bulk rotation can also affect the velocity distribution of WIMPs seen near the Earth [24].⁷

Halo models with bulk rotation can be constructed by taking linear combination of the velocity distribution function [26]:

$$\begin{aligned} f_{\text{rot}}(\mathbf{v}) &= a_{\text{rot}} f_+(\mathbf{v}) + (1 - a_{\text{rot}}) f_-(\mathbf{v}) \\ &= \begin{cases} a_{\text{rot}} f(\mathbf{v}), & \text{for } v_\phi > 0, \\ (1 - a_{\text{rot}}) f(\mathbf{v}), & \text{for } v_\phi < 0. \end{cases} \end{aligned} \quad (1.94)$$

A non-rotating halo has $a_{\text{rot}} = 0.5$, whereas a counter-rotating or a co-rotating one has $0 \leq a_{\text{rot}} < 0.5$ or $0.5 < a_{\text{rot}} \leq 1$, respectively [24], [26].

Moreover, a_{rot} is related to a dimensionless spin parameter λ_{rot} , which usually has been used to quantify the galactic angular momentum [24]:

$$\lambda_{\text{rot}} = 0.36 |a_{\text{rot}} - 0.5|. \quad (1.95)$$

Numerical studies of galaxy formation find that $|\lambda_{\text{rot}}| < 0.05$, corresponding to $0.36 < a_{\text{rot}} < 0.64$ [26].

⁷The velocity distribution of WIMPs will be discussed in Chap. 3.

Chapter 2

Candidates for Dark Matter

As defined in the Introduction, Dark Matter (almost) neither emits nor absorbs electromagnetic radiation. It is thus *non-luminous*.

Meanwhile, as described in Secs. 1.1 and 1.2, so far we can “observe” (or, actually, “feel”) the existence of Dark Matter only through its gravitational effects. Moreover, according to the observational results for the rotation curves of spiral galaxies (described in Subsec. 1.1.2), Dark Matter forms halos with an approximately spherical distribution around galaxies. Hence, Dark Matter (*almost*) *does not interact with ordinary matter* and is *collisionless*. Otherwise, if Dark Matter could interact with ordinary matter, it would dissipate its kinetic energy after the interactions, fall onto galaxies, settle deep into the galactic gravitational wells, and thus form the “galactic disks” with ordinary matter.

On the other hand, (the major part of) Dark Matter particles should *move non-relativistically* in the early Universe or, equivalently, *have sufficiently low primordial velocity dispersion*, in order to allow it to merge to galactic scale structures (e.g., galaxies and clusters of galaxies). In contrast, although neutrinos are also collisionless, they moved relativistically and have thus too large velocity dispersion to build galactic scale structures.

Therefore, Dark Matter should be some “non-luminous, non-baryonic, non-relativistic, and collisionless” elementary particles have not yet been discovered. In addition, the candidates for Dark Matter must satisfy the following cosmological conditions: they must be stable on cosmological time scales and have the right relic cosmological density [37].

In this chapter I present some most motivated and studied candidates for Dark Matter. Most of them are non-baryonic and non-relativistic particles. However, some relativistic particles and baryonic objects could also be (part of) Dark Matter.

2.1 Cold Dark Matter (CDM)

“Cold” has been used here to indicate that such Dark Matter particles moved *non-relativistically* at the matter-radiation decoupling time in the early Universe [22], i.e., at

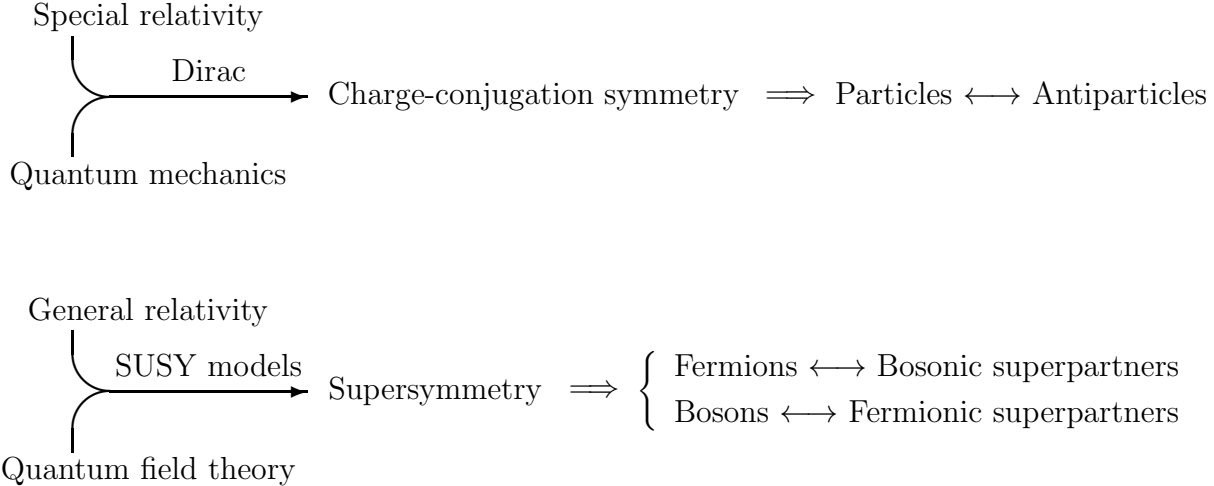


Figure 2.1: Extension of the Standard Model of particle physics to supersymmetric models

the time in which galaxies could just start to form. Due to their *relatively slower velocities* Cold Dark Matter would first form some relatively small galactic scale structures; large galaxies and clusters of galaxies are formed through “hierarchical merging” of these smaller structures.

2.1.1 Minimal Supersymmetric Standard Model (MSSM)

Supersymmetry has been considered to solve the hierarchy problem in the Standard Model (SM) of particle physics: Why is the electroweak scale ($E_{\text{EW}} \simeq \mathcal{O}(100 \text{ GeV})$) so small compared to the other known scales such as the grand unification scale ($E_{\text{GUT}} \simeq 10^{16} \text{ GeV}$ [1]) or the Planck scale ($E_{\text{Pl}} \simeq 10^{19} \text{ GeV}$ [1])?

As shown in Fig. 2.1, supersymmetry provides a natural framework for discussing theories with large hierarchies of scales and unification with gravity [1]. In supersymmetric models, *for every fermionic degree of freedom there is a bosonic degree of freedom and vice versa*. This means also that, for each “normal” particle, there will be a supersymmetric partner. Hence, the particle spectrum has been greatly extended in the MSSM.

The particles of typical supersymmetric models are given in Table 2.1. The spectrum of the normal particles is specified in the same manner as in non-supersymmetric models. Quark mass matrices determine the masses and the mixing angles, which are encoded in the Cabibbo-Kobayashi-Maskawa (CKM) matrix. The pattern of gauge-symmetry breaking is unchanged from the Standard Model, and gives the same tree-level relation between the masses of the W^\pm and Z^0 bosons. Quarks in the Standard Model have spin $\frac{1}{2}$, while their superpartners, squarks, are scalars [1]. There are two squarks (left-hand and right-hand) for each quark. In some models there is no mixing between different flavors, and each squark is associated with a given quark [1], for example, \tilde{u}_L and \tilde{u}_R , \tilde{d}_L and \tilde{d}_R . However, generally the three up-quarks can mix among themselves and similarly

Normal particles		SUSY partners	
Name	Symbol	Name	Symbol
up-quarks	$q = u, c, t$	up-squarks	$\tilde{u}_L, \tilde{u}_R, \tilde{c}_L, \tilde{c}_R, \tilde{t}_L, \tilde{t}_R$
down-quarks	$q = d, s, b$	down-squarks	$\tilde{d}_L, \tilde{d}_R, \tilde{s}_L, \tilde{s}_R, \tilde{b}_L, \tilde{b}_R$
leptons	e, μ, τ	sleptons	$\tilde{e}_L, \tilde{e}_R, \tilde{\mu}_L, \tilde{\mu}_R, \tilde{\tau}_L, \tilde{\tau}_R$
neutrinos	ν_e, ν_μ, ν_τ	sneutrinos	$\tilde{\nu}_e, \tilde{\nu}_\mu, \tilde{\nu}_\tau$
gluons	g	gluinos	\tilde{g}
photon	γ	photino $\tilde{\gamma}$	neutralinos $\tilde{\chi}_1^0, \tilde{\chi}_2^0, \tilde{\chi}_3^0, \tilde{\chi}_4^0$
Z boson	Z^0	Z-ino \tilde{Z}	
light scalar Higgs	h^0	neutral higgsinos \tilde{h}^0, \tilde{H}^0	
heavy scalar Higgs	H^0		
pseudoscalar Higgs	A^0		
charged Higgs	H^\pm	charged higgsinos \tilde{H}^\pm	charginos $\tilde{\chi}_1^\pm, \tilde{\chi}_2^\pm$
W bosons	W^\pm	gauginos, W-inos \tilde{W}^\pm	
graviton	G	gravitino	\tilde{G}
axion	a	axino	\tilde{a}

Table 2.1: Particles of typical supersymmetric models

for the three down-quarks, so there are totally six up-squarks and six down-squarks in the particle spectrum [1]. Similarly for the leptons. In these models, left-right sfermion mixing is proportional to the corresponding fermion mass [1]. Thus there is little left-right mixing for u, d , and s squarks or selectrons or smuons, but mixing of staus and c, b , and especially t squarks can be substantial [1].

A most important technical difference between the Standard Model and the MSSM occurs in the Higgs sector. Two weak isospin Higgs doublet fields are required in the MSSM, whereas only one is required in the SM [1]. This enrichment of the Higgs sector gives rise to five physical states and provides an important phenomenological window. The superpartners of the W^\pm and charged Higgs bosons, the gauginos and the charged higgsinos, carry the same $SU(3) \times U(1)$ quantum numbers. Thus they will generally mix after electroweak-symmetry breaking, and the two resulting mass eigenstates are linear combinations known as charginos [1]. Similarly for the superpartners of the photon, Z^0 boson, and neutral Higgs bosons. These fields generally mix to create four mass eigenstates called neutralinos [1]. In many supersymmetric models, constraints on the Higgs-higgsino sector are therefore an important area of supersymmetric phenomenology [1].

In Table 2.1, the tilde \sim has been used to denote a supersymmetric particle. However,

the tildes for neutralinos and charginos are sometimes omitted since there is no ambiguity for such particles. Moreover, the lightest neutralino is in most models the lightest supersymmetric particle (LSP) and usually just to be called as “the neutralino”. Note here that, although the lightest neutralino is the most studied LSP and some authors even use the LSP to indicate it, there are also some other candidates for LSP, e.g., the gravitino.

Furthermore, a R -parity should be also presented here [1]:

$$R = (-1)^{3(B-L)+2S}, \quad (2.1)$$

where B and L are the baryon and lepton number, S is the spin. For ordinary particles $R = +1$ (even) and for supersymmetric particles $R = -1$ (odd). If the R -parity is conserved, one SUSY particle (with $R = -1$) could only decay to a lighter SUSY particle (with $R = -1$) and any number of ordinary particles (with $R = +1$). Certainly, such decay can not happen with the “lightest” SUSY particle since no SUSY particle can be lighter than the lightest one. Hence, in models with strict R -parity conservation, the LSP must be absolutely stable and is then the best candidate for Dark Matter [1].

In contrast, if R -parity is broken, there is no special selection rule to prevent the decays of the supersymmetric particles in the spectrum with masses of order of a few GeV or larger [1]. In particular, there were no natural candidate for Cold Dark Matter [1]. Theories with broken R -parity also possess baryon- and lepton-number violating interactions with strengths controlled by the scale of R -parity violation [1].

2.1.2 Weakly Interacting Massive Particles (WIMPs)

Weakly Interacting Massive Particles (WIMPs) χ arise e.g., in supersymmetric extensions of the Standard Model of electroweak interactions and are the leading non-baryonic candidates for Cold Dark Matter [1]. They are *stable* particles and *interact with ordinary matter only via weak interactions*. Typically their masses have been presumed to be between 10 GeV and a few TeV [1], [37]. They could include neutralinos, sneutrinos, heavy fourth-generation Dirac and Majorana neutrinos, and non-minimal neutralinos (neutralinos in non-minimal supersymmetric models) [1].

Relic elementary particles are left over from the Big Bang. Stable or long-lived particles with very weak interactions can remain in sufficient numbers to account for a significant fraction of critical density [15]. Very weak interactions are necessary for their annihilations to cease before their numbers are too small [15].

WIMPs exist in thermal equilibrium and in abundance in the early Universe, when the temperature of the Universe T exceeds their masses m_χ ($T \gtrsim m_\chi$) [1]. The equilibrium abundance is maintained by pair annihilation of WIMPs with their antiparticles $\bar{\chi}$ into lighter particles l (quarks and leptons, or even gauge- and Higgs-bosons if their masses are heavy enough) and vice versa ($\chi\bar{\chi} \leftrightarrow l\bar{l}$) [1]. The rate of this reaction is proportional to the product of the WIMP number density n_χ and the WIMP pair annihilation cross

section into SM particles σ_A times the relative velocity between the two WIMPs in their center-of-mass system v [1], [37]:

$$\Gamma_\chi = n_\chi \langle \sigma_A v \rangle, \quad (2.2)$$

where $\langle \dots \rangle$ indicates the thermal averaging.

As the Universe cools to a temperature less than the masses of WIMPs ($T < m_\chi$), the equilibrium abundance (number density) of WIMPs drops exponentially until the rate for the annihilation reaction ($\chi\bar{\chi} \rightarrow l\bar{l}$) becomes smaller than the Hubble expansion rate of the Universe ($\Gamma_\chi \lesssim H$). At this point the interactions which maintain thermal equilibrium “freeze out” and the WIMPs cease to annihilate and drop out of thermal equilibrium [37]. Hence, a relic cosmological abundance “freezes in” [1], i.e., the density of the co-moving WIMPs remains essentially constant.

The time evolution of the number density of WIMPs $n_\chi(t)$ can be described by the Boltzmann equation [1]:

$$\frac{dn_\chi}{dt} + 3Hn_\chi = -\langle \sigma_A v \rangle \left[n_\chi^2 - (n_\chi^{\text{eq}})^2 \right]. \quad (2.3)$$

Here n_χ^{eq} is the number density of WIMPs in thermal equilibrium. The second term on the left-hand side accounts for the expansion of the Universe, the first term in the brackets on the right-hand side accounts for the depletion of WIMPs due to their pair-annihilation, and the second term arises from creation of WIMPs from the inverse reaction [1]. In the absence of number-changing interactions, the right-hand side would be zero and we would find $n \propto 1/a^3(t)$ [1], where $a(t)$ is the scale factor of the Universe in Eq.(1.12).

Note that Eq.(2.3) describes both Dirac particles ¹ as well as Majorana particles [1], which are particles that themselves are also their antiparticles, such as neutralinos ($\chi = \bar{\chi}$) [1]. For the case of Majorana particles (they are so-called “self-annihilating”), the annihilation rate in Eq.(2.2) should be modified to [1]

$$\Gamma_\chi = \left(\frac{n_\chi}{2} \right) \langle \sigma_A v \rangle. \quad (2.4)$$

However, in each annihilation, two particles are removed and the factor of 2 can be canceled. For Dirac particles with no particle-antiparticle asymmetry, i.e., $n_\chi = n_{\bar{\chi}}$, Eq.(2.2) is true. But the total number of particles plus antiparticles must be $2n_\chi$ [1]. In the case of Dirac particles with a particle-antiparticle asymmetry, the relic abundance is generally that given by the asymmetry [1]. For example, the relic proton density is fixed by the proton-antiproton asymmetry, i.e., the baryon number of the Universe [1].

The early Universe is radiation dominated and the Hubble expansion rate falls with temperature as [1]

$$H(T) = 1.66 \left(\frac{g_*^{1/2} T^2}{M_{\text{Pl}}} \right). \quad (2.5)$$

¹ n_χ^2 on the right-hand side should be modified to $n_\chi n_{\bar{\chi}}$ for Dirac particles, but often $n_\chi = n_{\bar{\chi}}$ has been assumed.

Here M_{Pl} is the Planck mass [11]

$$M_{\text{Pl}} \equiv \sqrt{\frac{\hbar c}{G_{\text{N}}}} = 1.2209 \times 10^{19} \text{ GeV}/c^2 = 2.1764 \times 10^{-5} \text{ g}, \quad (2.6)$$

and the quantity g_* is the effective number of relativistic degrees of freedom. It is approximately equal to the number of bosonic relativistic degrees of freedom plus $\frac{7}{8}$ times the number of fermionic relativistic degrees of freedom [1]. While, for very high temperature ($T \gtrsim m_\chi$) [1],

$$n_\chi^{\text{eq}} \propto T^3. \quad (2.7)$$

Hence, the expansion rate $H(T)$ in Eq.(2.5) decreases less rapidly than the number density of WIMPs. This means that, at early times, the expansion term in Eq.(2.3), $3Hn_\chi$, is negligible compared with the right-hand side, and the number density tracks its equilibrium abundance [1].

However, at later times or at low temperatures ($T \lesssim m_\chi$), the right-hand side in Eq.(2.3) becomes negligible compared with the expansion term, and the co-moving abundance of WIMPs remains unchanged [1]. It can be found that [1]

$$n_\chi^{\text{eq}} = g \left(\frac{m_\chi T}{2\pi} \right)^{3/2} e^{-m_\chi/T}, \quad (2.8)$$

where g is the number of internal degrees of freedom of the WIMPs and thus their density is Boltzmann suppressed [1]. If the expansion of the Universe were so slow that thermal equilibrium was always maintained, the number of WIMPs today would be exponentially suppressed (essentially, there would be no WIMPs) [1]. The temperature T_F at which the WIMPs freeze out is given by $\Gamma_\chi(T_F) = H(T_F)$ [1]. Using typical weak-scale numbers, the freeze-out temperature turns out to be [1]

$$T_F \simeq \frac{m_\chi}{20}. \quad (2.9)$$

There is a small logarithmic dependence on the mass and annihilation cross section here [1]. As stated above, after freeze out, the abundance of WIMPs per co-moving volume remains constant.

Finally, the present relic density of WIMPs is then approximately given by (ignoring logarithmic corrections) [1], [37]

$$\Omega_\chi h^2 \simeq \text{const.} \times \frac{T_0^3}{M_{\text{Pl}}^3 \langle \sigma_{Av} \rangle} \simeq \frac{0.1c \text{ pb}}{\langle \sigma_{Av} \rangle} = \frac{3 \times 10^{-27} \text{ cm}^3/\text{s}}{\langle \sigma_{Av} \rangle}, \quad (2.10)$$

where T_0 is the current CMB temperature given in Eq.(1.22), and c is the speed of light. It is inversely proportional to the annihilation cross section of WIMPs. Hence, as the annihilation cross section is increased, the WIMPs stay in equilibrium longer, and we are left with a smaller relic abundance [1]. The annihilation cross section is generally expected to decrease as the WIMP mass is increased, so the relic abundance should be also increased [1]. Therefore, heavier WIMPs should be more likely to contribute too much to the mass of the Universe, and then be cosmologically inconsistent [1].

2.1.3 Neutralinos

As introduced in Subsec. 2.1.1, neutralinos are linear combinations of photino, Z-ino and neutral higgsinos (the supersymmetric partners of the photon, Z^0 and neutral Higgs bosons, see Table 2.1):

$$\tilde{\chi}_i^0 = a_i \tilde{\gamma} + b_i \tilde{Z} + c_i \tilde{h}^0 + d_i \tilde{H}^0, \quad i = 1, 2, 3, 4. \quad (2.11)$$

In most SUSY models, the lightest neutralino is the lightest supersymmetric particle [37] and therefore the best motivated and the most widely studied candidate for WIMP Dark Matter, but not the unique candidate for LSP (e.g., sneutrinos) [37].

There are some theoretical reasons to believe that the lightest neutralino should be the LSP. First, suppose a charged uncolored SUSY particle, such as a chargino or a slepton, were the LSP. The relic number density of such particles can be given as roughly $10^{-6} n_b M / \text{GeV}$ [1], where n_b is the baryon number density and M is the mass of such particles. Then they would show up in searches for anomalously heavy protons [1]. Null results from such searches rule out such charged particles over a broad mass range [1]. Moreover, grand unified models predict relations between the masses of the SUSY particles. In most models the gluino is more massive than the neutralino, and the squarks are also heavier than the sleptons [1]. In addition, some detailed calculations show that the lightest neutralino has the desired thermal relic density, Ω_{DM} in Eq.(1.47), in at least four distinct regions of parameter space [37].

2.1.4 Sneutrinos

Sneutrinos are the spin-0 supersymmetric partner of the neutrinos (see Table 2.1). There are some reasons to rule out sneutrinos to be good candidate for Dark Matter. First, in most models, there is a slepton with mass similar to, but slightly smaller than, the sneutrino mass [1]. Meanwhile, their masses would have to exceed several hundred GeV for them to make good Dark Matter candidates. This is uncomfortably heavy for the lightest sparticle [37]. On the other hand, the annihilation cross sections of sneutrinos are expected to be quite large [37]. Hence, the negative outcome of various WIMP searches rules out ordinary sneutrinos as primary component of the Dark Matter halo of our Galaxy [37]. However, in models with gauge-mediated SUSY breaking the lightest messenger sneutrino could be a good candidate [37].

2.1.5 Heavy fourth-generation Dirac and Majorana neutrinos

They are the first proposed WIMP candidates for CDM [1]. They are heavy, but stable particles and assumed to have (weak) interactions with ordinary matter through Standard Model coupling to the Z^0 boson [1]. Such neutrinos could annihilate into light fermions via s-channel exchange of a Z^0 boson. For $m \ll M_Z$ the cross section is proportional to the square of their mass [1]. Because their interactions are fixed by gauge symmetry, the

only adjustable scale is then their masses [1]. The cosmological abundances of the heavy Dirac and Majorana neutrinos have been given as [1]

$$\Omega_{\nu,D}h^2 \simeq \left(\frac{m_{\nu,D}}{2 \text{ GeV}} \right)^{-2}, \quad (2.12)$$

and

$$\Omega_{\nu,M}h^2 \simeq \left(\frac{m_{\nu,M}}{5 \text{ GeV}} \right)^{-2}, \quad (2.13)$$

for neutrino masses in the range $\mathcal{O}(1 \text{ GeV}) \lesssim m_\nu \ll m_Z = 91.19 \text{ GeV}$.

However, there is no obvious reason why such massive neutrinos should not be allowed to decay [37]. Moreover, an SU(2) doublet neutrino will have a too small relic density if its mass exceeds $M_Z/2$, as required by LEP data [37].

On the other hand, for such neutrinos with masses greater than the electroweak gauge-boson masses, annihilations into gauge- and/or Higgs-boson pairs could occur. However, the cross section would not decrease as the neutrino mass increases [1], so the relic abundance of neutrinos with masses of the order of 100 GeV remains too small to account for the Dark Matter in the Galactic halo [1].

Dirac neutrinos interact with nuclei through a coherent vector interaction [1] (some details about the vector interaction with nuclei will be given in Subsec. 3.4.1). Thus the Dirac-neutrino-nucleus cross section is expected to be quite substantial [1], and this would lead to a significant event rate in a direct detection experiment. Null results from such experiments have ruled out Dirac neutrinos with masses in the range $12 \text{ GeV} \lesssim m_{\nu,D} \lesssim 1.4 \text{ TeV}$ as the primary component of the Dark Matter halo [1].

Meanwhile, Majorana neutrinos interact with nuclei only via an axial-vector interaction [1] (some details about the axial-vector interaction with nuclei will be given in Subsec. 3.4.2), and are therefore difficult to detect directly. However, such neutrinos would be captured in the Sun by scattering from hydrogen therein and their pair annihilations in the Sun would produce energetic neutrinos from the Sun [1]. Null results from searches for energetic neutrinos at e.g., Kamiokande have also ruled out Majorana neutrinos with mass less than a few hundred GeV [1].

2.1.6 Axions

Axion a is also one of the leading candidates for CDM. Axions have been introduced by Peccei and Quinn to solve the strong CP (charge-conjugation and parity) violation problem of QCD. They are pseudo Nambu-Goldstone bosons associated with the spontaneous breaking of a new global Peccei-Quinn (PQ) U(1) symmetry at scale f_a [37].

The present relic density of the axions can be given as [37]

$$\Omega_a = \kappa_a \left(\frac{f_a}{10^{12} \text{ GeV}} \right)^{1.175} \theta_a^2, \quad (2.14)$$

where κ_a is a numerical factor lying roughly between 0.5 and a few, θ_a is a “misalignment angle” which parameterizes the axion field. Suppose $\theta_a \sim \mathcal{O}(1)$, axions will have the required cosmological energy density in Eq.(1.47) to be Dark Matter, if $f_a \sim \mathcal{O}(10^{11} \text{ GeV})$. It is pretty comfortably above the laboratory and astrophysical constraints and this would correspond to an axion mass $m_a \sim 10^{-4} \text{ eV}$ [37].

Axions could be detected by looking for their conversion to microwave photons, $a \rightarrow \gamma$, in a strong magnetic field [37]. Such a conversion could proceed through the loop-induced $a\gamma\gamma$ coupling, whose strength $g_{a\gamma\gamma}$ is thus an important parameter of axion models [37]. Moreover, the conversion rate can be enhanced in a high quality cavity on resonance and, due to the equation $m_a c^2 = \hbar\omega_{\text{res}}$, varying this resonance frequency can give a range of m_a , or, equivalently, f_a [37].

2.1.7 Other possible SUSY candidates

Besides the neutralinos and the sneutrinos, some other supersymmetric particles are also (theoretically) possible to be candidates for Dark Matter. ²

Axino is the spin- $\frac{1}{2}$ superpartner of the axion. It may be the LSP or the next-lightest supersymmetric particle (NLSP) and may decay to the LSP [1]. When the axino is the lightest supersymmetric particle and has a mass of a few keV, it can be a good candidate for *Warm Dark Matter* (WDM) [1].

While, gravitino, the spin- $\frac{3}{2}$ superpartner of graviton, is also a possible candidate for Dark Matter. The gravitinos will decouple at temperatures of order of the Planck scale ($E_{\text{Pl}} \simeq 10^{19} \text{ GeV}$ [1]). Thus the physics of the gravitinos must be considered at energies and temperatures right up to this scale [1]. In addition, if gravitinos behave as standard stable thermal relics with an abundance determined by consideration of their decoupling, the mass of gravitinos should be less than a few keV [1]. However, in some models with gravitinos as LSP, the NLSP should decay to a gravitino plus ordinary particles [1]. Since the coupling to gravitinos is so weak, this NLSP will be very long-lived and the products of its decay will contain γ -ray with high energies [1].

2.2 Hot Dark Matter (HDM)

“Hot” has been used here to indicate that such Dark Matter particles moved *relativistically* in the early Universe. Due to their *fast velocities*, they would cover great distances and then form some very large scale structures. This means that the Hot Dark Matter forms the structure of our Universe from the top down, with superclusters fragmenting into clusters and galaxies [15]. It is in contrast to the observational evidence which indi-

²Besides the different supersymmetric extensions of the Standard Model, there are also some theories based on “flat universal extra dimensions (UED)”. The most studied candidate for CDM in these extra-dimension models is the first Kaluza-Klein (KK) mode of the hypercharge gauge boson (the lightest KK particle, LKP) $\gamma_{(1)}$.

cates that the structure of our Universe has been formed *from the bottom up* by merging dust to galactic scale structures [15].

However, there are still some suggestions in which part of Dark Matter is hot and the rest is cold. In these models the bulk of the Dark Matter (especially in galactic halos) is still cold.

2.2.1 Massive neutrinos

The leading candidates for Hot Dark Matter are the massive neutrinos. As shown in Subsec. 1.2.9, WMAP results combined with other astronomical measurements lead to a contribution for light (but massive) neutrino species [11]:

$$\Omega_\nu < 0.014. \tag{1.51}$$

They could include the electron-, muon-, and tauon-neutrinos in the Standard Model with non-zero masses ³ as well as the forth-generation Dirac and Majorana neutrinos (described in Subsec. 2.1.5) with extremely light masses.

2.3 Dark baryons

As mentioned above, some CDM particles, e.g., neutralinos and axions, could form galactic scale structures such as galaxies and clusters of galaxies, while, some HDM particles, e.g., massive neutrinos, could form larger structures of the Universe. This means that *on different scales Dark Matter might consist of different materials* [1]. ⁴

Moreover, in this chapter I presented some theoretically predicted (SUSY) particles as candidates for Dark Matter. However, *until now there is no direct accelerator evidence for the existence of supersymmetry* [1]. Actually, *it is not absolutely certain that Dark Matter is neither baryons nor neutrinos* [1]. There are also some conservative cosmological models which describe the Universe only in terms of baryons and perhaps neutrinos [1].

On the other hand, as shown in Subsec. 1.2.9, the baryonic matter density in the Universe is

$$\Omega_b \simeq 0.042, \tag{1.46'}$$

but only around 25% of the baryonic matter are luminous:

$$\Omega_{\text{lum}} \simeq 0.01. \tag{1.48}$$

Although, as mentioned in Subsec. 1.2.6, most of the baryons in the clusters of galaxies reside not in the galaxies themselves, but in form of hot intercluster, x-ray emitting gas

³At present we know from ν oscillations that at least two of these three SM neutrinos have small, but non-vanishing masses.

⁴However, some recent researches indicate that there should be only one species of Dark Matter in the Universe.

[15], such hot gas in the clusters of galaxies only accounts for around 10% of the baryons in the Universe [15]. Hence, there should (must) be some *baryonic Dark Matter*.⁵

Two most promising possibilities for such dark baryons are diffuse hot gas and dark stars, which include white dwarfs, neutron stars, black holes, or objects with masses around or below the hydrogen-burning limit [15].

2.3.1 Massive astrophysical compact halo objects (MACHOs)

Massive astrophysical compact halo objects include, for example, brown dwarfs which are balls of hydrogen and helium with masses $< 0.08M_{\odot}$ and therefore never begin nuclear fusion of hydrogen [1] (but they do burn deuterium), jupiters which are similar to brown dwarfs but have masses $\sim 0.001M_{\odot}$ [1] and do not burn anything, and white dwarfs [1]. Actually, objects with masses around or below the hydrogen-burning limit could be baryonic Dark Matter [15].

Meanwhile, neutron stars and stellar black-hole remnants are also candidates for baryonic Dark Matter [1]. Black holes with masses $\sim 100M_{\odot}$ could be remnants of an early generation of stars which were massive enough so that not many heavy elements were dispersed when they underwent their supernova explosions [1]. Primordial black holes which formed before the era of Big Bang could be counted for non-baryonic Dark Matter rather than baryonic one [37]. However, such an early creation of a large number of black holes is possible only in certain somewhat contrived cosmological models [37].

MACHOs might represent a large part of the galactic Dark Matter and could be detected through the microlensing effect [37]. The MACHO, EROS, OGLE collaborations have performed programs of observation of such objects by monitoring the luminosity of millions of stars in the Large and Small Magellanic Clouds [37]. They concluded that MACHOs contribute $\lesssim 40\%$ (MACHO) or even $\lesssim 20\%$ (EROS) to the mass of the galactic halo [37].

⁵However, some recent results of the measurement of the opacity of the Lyman- α forest toward high-redshift quasars indicate that there are probably enough baryons at $z \geq 3$, but it is not clear where they are now.

Chapter 3

Direct Detection of WIMPs

By definition, Dark Matter could neither emit nor absorb electromagnetic radiation. However, as described in Subsec. 2.1.2, WIMPs would have annihilated to some ordinary matter, e.g., quarks and leptons, in the early Universe. Otherwise, they would have unacceptable large abundance today. According to the crossing symmetry, the amplitude for WIMP annihilation to, for example, quarks is related to the amplitude for elastic scattering of WIMPs from quarks [1]. Therefore, *WIMPs should have some small, but non-zero couplings to ordinary matter.*

Due to this coupling to nucleus (through the coupling to quarks), WIMPs could scatter elastically from target nuclei of the detector material and produce nuclear recoils which deposit energy in the detector. Hence, one of the most promising methods of detecting Galactic Dark Matter is the direct detection of WIMPs [38]-[44]. Note that, although the lightest neutralino is the leading candidate for Dark Matter, such WIMP direct searches are not specialized to detect the neutralino but any particle with similar generic properties, e.g., a mass between a few GeV and a few TeV and weakly interacting with ordinary matter [45].¹

3.1 Elastic WIMP-nucleus scattering

Using the standard assumption of the WIMP density near the Earth

$$\rho_0 \approx 0.3 \text{ GeV}/c^2/\text{cm}^3, \tag{1.55}$$

and assuming a WIMP mass

$$m_\chi \approx 100 \text{ GeV}/c^2, \tag{3.1}$$

¹The lightest Kaluza-Klein particle arising in the extra-dimension models (mentioned as footnote in Subsec. 2.1.7) can also scatter elastically from the detector nuclei through KK-quark $q_{(1)}$ and Higgs exchange [46]. Thus such particles could also be detected from direct detection experiments. A brief description about the interaction between $q_{(1)}$ and Higgs and the analysis using recent experimental results can be found in Ref. [46].

the number density of WIMP can be found as

$$n = \frac{\rho_0}{m_\chi} \approx 3 \times 10^{-3} \text{ cm}^{-3}. \quad (3.2)$$

Meanwhile, by the assumption that the halo WIMPs are gravitationally bound to the Galaxy and its halo, the average velocity of WIMP wind is then approximately equal to the stellar velocity in the Solar neighborhood: ²

$$\langle v \rangle \approx 250 \text{ km/s}. \quad (3.3)$$

Therefore, the WIMP flux is $\sim 10^5$ WIMPs per square centimeter of the Earth's surface per second.

However, the very low cross section of WIMPs on ordinary material makes the elastic WIMP-nucleus scattering very rare. In typical SUSY models with neutralino WIMPs, WIMP-nucleus cross section is about $10^{-6} \sim 10^{-4}$ pb ($10^{-42} \sim 10^{-40}$ cm²) ³ and the expected event rate is then *at most 1 event/kg/day* [37], in some models it is even *less than 1 event/ton/yr* [47].

With expected WIMP mass in the range 10 GeV/ c^2 to 10 TeV/ c^2 [37], typical nuclear recoil energies are *of order of 1 to 100 keV*. However, as we can see in Fig. 4.1 in Subsec. 4.2.1, the event rate drops approximately exponentially and most events should be with energies less than 40 keV (a simple theoretical estimate will be given in Subsec. 3.5.1).

On the other hand, in the energy range from a few to a couple hundred keV, typical background noise due to cosmic rays and ambient radioactivity is much larger. Thus a underground laboratory and extensive shielding around the detector to protect against cosmic-ray induced backgrounds, and selection of extremely radiopure materials are necessary and important [37] (more details about background and its discrimination will be given in Sec. 3.6).

The event rate of elastic WIMP-nucleus scattering depends on various parameters coming from astrophysics, particle physics and nuclear physics: the WIMP density near the Solar system ρ_0 , the WIMP-nucleus cross section, the WIMP mass m_χ , and the velocity distribution of the incident WIMPs $f(v)$ in the Galactic halo near the Earth. However, by some standard assumptions about the halo model, e.g., the WIMP density profiles (have been presented in Sec. 1.3) and velocity distributions (will be discussed in Subsecs. 3.1.3 and 3.2.1), the expected event rate mainly depends on two unknowns: the mass of the incident WIMPs and the WIMP-nucleus cross section. Hence the experimental observable is usually expressed as a contour in the WIMP mass-cross section plane (e.g., Figs. 3.4 and 3.5), although it is basically the scattering rate and is a function of energy [37].

²Note that $\langle v \rangle \equiv \langle |\mathbf{v}| \rangle$ is $\mathcal{O}(v_0)$ even though $\langle \mathbf{v} \rangle = 0$ (see footnote on p.15).

³1 barn = 10^{-24} cm², 1 pb = 10^{-36} cm²

3.1.1 Rate for elastic WIMP-nucleus scattering

The direct detection experiment measures the number of events per unit time per unit mass of detector material as a function of the energy deposited in the detector Q . Qualitatively, the event rate of direct detection, R , can be simply expressed as [1]

$$R \approx \frac{n \langle v \rangle \sigma}{m_N}, \quad (3.4)$$

where $\langle v \rangle$ is the average velocity of the incident WIMPs relative to the Earth frame (i.e., to the target), σ is the WIMP-nucleus cross section, and m_N is the mass of the target nucleus. Here we multiply the factor $1/m_N$ to get the number of target nuclei per unit mass of the detector material.

More accurately, one should take into account the fact that the WIMPs move in the halo with velocities determined by their velocity distribution function $f(v)$, and that the differential cross section depends on $f(v)$ through an elastic nuclear form factor $F(q)$ [1]:

$$d\sigma = \frac{1}{v^2} \left(\frac{\sigma_0}{4m_{\text{r}}^2} \right) F^2(q) dq^2. \quad (3.5)$$

Here σ_0 is the total cross section ignoring the form factor suppression,

$$m_{\text{r}} = \frac{m_{\chi} m_N}{m_{\chi} + m_N} \quad (3.6)$$

is the reduced mass, q is the transferred 3-momentum:

$$q = \sqrt{2m_N Q}. \quad (3.7)$$

Therefore, in general, the differential scattering event rate (per unit detector mass) should be written as [1]

$$\begin{aligned} dR &= \frac{\rho_0}{m_{\chi} m_N} \int v f_1(v) d\sigma dv \\ &= \left(\frac{\rho_0 \sigma_0}{2m_{\chi} m_{\text{r}}^2} \right) F^2(Q) \int \left[\frac{f_1(v)}{v} \right] dv dQ, \end{aligned} \quad (3.8)$$

where $f_1(v)$ is the one-dimensional velocity distribution function of WIMPs impinging on the detector, v is the absolute value of the WIMP velocity in the Earth rest frame, and we have to integrate over all possible incoming velocities. By means of classical mechanics, the transferred momentum q can be expressed as

$$q = 2 \left[m_N \left(\frac{m_{\chi} v}{m_{\chi} + m_N} \right) \right] \sin \left(\frac{\theta_{\text{CM}}}{2} \right) = 2m_{\text{r}} v \sqrt{\frac{1 - \cos \theta_{\text{CM}}}{2}}, \quad (3.9)$$

where θ_{CM} is the scattering angle in the center-of-momentum frame. Since

$$0 \leq 1 - \cos \theta_{\text{CM}} \leq 2,$$

for a given deposited energy Q , we have

$$Q = \frac{(2m_{\text{r}}v_{\text{min}})^2}{2m_{\text{N}}} = \frac{2m_{\text{r}}^2v_{\text{min}}^2}{m_{\text{N}}},$$

i.e., the minimal incoming velocity of incident WIMPs that can deposit the energy Q in the detector can be expressed as

$$v_{\text{min}}(Q) = \sqrt{\frac{m_{\text{N}}}{2m_{\text{r}}^2}}\sqrt{Q} = \alpha\sqrt{Q}, \quad (3.10)$$

where I have defined

$$\alpha \equiv \sqrt{\frac{m_{\text{N}}}{2m_{\text{r}}^2}}. \quad (3.11)$$

Then the differential event rate for elastic WIMP-nucleus scattering, Eq.(3.8), can be rewritten as

$$\frac{dR}{dQ} = \mathcal{A}F^2(Q) \int_{v_{\text{min}}}^{\infty} \left[\frac{f_1(v)}{v} \right] dv, \quad (3.12)$$

where the constant coefficient \mathcal{A} is defined as

$$\mathcal{A} \equiv \frac{\rho_0\sigma_0}{2m_{\chi}m_{\text{r}}^2}. \quad (3.13)$$

Note that, first, α defined in Eq.(3.11) depends only on the WIMP mass m_{χ} (and the mass of the target material, m_{N} , which we can choose). The two as yet unknown parameters, i.e., the WIMP density ρ_0 and the total WIMP-nucleus cross section σ_0 , have been collected in the coefficient \mathcal{A} defined in Eq.(3.13). Second, I assumed here that the detector essentially only consists of nuclei of a single isotope. If the detector contains several different nuclei (e.g., NaI as in the DAMA detector [48]), the right-hand side of Eq.(3.12) has to be replaced by a sum of terms, each term describing the contribution of one isotope. For simplicity, in the remainder of this work I will focus on mono-isotopic detectors.

Finally, the total event rate per unit time per unit mass of detector material can be expressed as

$$R = \int_{Q_{\text{thre}}}^{\infty} \left(\frac{dR}{dQ} \right) dQ, \quad (3.14)$$

where Q_{thre} is the threshold energy of the detector.

3.1.2 Nuclear form factor (for spin-independent coupling)

Here I present two most commonly used parameterizations of the squared nuclear form factor $F^2(Q)$ in Eq.(3.12) for spin-independent coupling, which usually dominates the event rate (more details about WIMP-nucleus couplings will be given in Sec. 3.4). Moreover, the form factors for spin-dependent coupling are still only poorly understood.

The simplest form factor is the exponential one, first introduced by Ahlen *et al.* [49] and Freese *et al.* [42]:

$$F_{\text{ex}}^2(Q) = e^{-Q/Q_0}, \quad (3.15)$$

where Q is the recoil energy transferred from the incident WIMP to the target nucleus,

$$Q_0 = \frac{1.5}{m_N R_0^2} \quad (3.16a)$$

is the nuclear coherence energy and

$$R_0 = \left[0.3 + 0.91 \left(\frac{m_N}{\text{GeV}} \right)^{1/3} \right] \text{ fm} \quad (3.16b)$$

is the radius of the nucleus. The exponential form factor implies that the radial density profile of the nucleus has a Gaussian form. This Gaussian density profile is simple, but not very realistic. Engel has therefore suggested a more accurate form factor [50], inspired by the Woods-Saxon nuclear density profile,

$$F_{\text{WS}}^2(Q) = \left[\frac{3j_1(qR_1)}{qR_1} \right]^2 e^{-(qs)^2}. \quad (3.17)$$

Here $j_1(x)$ is a spherical Bessel function, q is the transferred 3-momentum given in Eq.(3.7), and

$$R_1 = \sqrt{R_A^2 - 5s^2} \quad (3.18a)$$

with

$$R_A \simeq 1.2 A^{1/3} \text{ fm}, \quad s \simeq 1 \text{ fm}, \quad (3.18b)$$

where A is the atomic mass number of the nucleus.

3.1.3 Simple isothermal Maxwellian halo

For the simplest halo model presented in Subsec. 1.3.2, the canonical isothermal spherical halo, with the assumption that the WIMPs trapped in the galactic field have attained thermal equilibrium with a Maxwellian velocity distribution [51], the velocity distribution function is given by [1]

$$f_{\text{Gau}}(v) = \left(\frac{1}{\pi^{3/2} v_0^3} \right) e^{-v^2/v_0^2}, \quad (3.19)$$

where v_0 is the orbital velocity of the Sun in the Galactic frame:

$$v_0 \simeq 220 \text{ km/s}, \quad (1.53')$$

which characterizes the velocity of all virialized objects in the Solar vicinity. Then, since

$$d^3v = v^2 dv d\Omega = 4\pi v^2 dv,$$

the normalized one-dimensional velocity distribution function has been obtained as [1]

$$f_{1,\text{Gau}}(v) = \frac{4}{\sqrt{\pi}} \left(\frac{v^2}{v_0^2} \right) e^{-v^2/v_0^2}. \quad (3.20)$$

According to Eq.(3.12), the scattering spectrum of the simplest theoretical velocity distribution given in Eq.(3.20) can be obtained as (a detailed calculation will be given in App. C.1.1)

$$\left(\frac{dR}{dQ} \right)_{\text{Gau}} = \mathcal{A} \left(\frac{2}{\sqrt{\pi}v_0} \right) F^2(Q) e^{-\alpha^2 Q/v_0^2}. \quad (3.21)$$

Meanwhile, the mean velocity and velocity dispersion of the halo WIMPs can be obtained as (detailed calculations will be given in App. B.1.1), respectively,

$$\langle v \rangle_{\text{Gau}} = \int_0^\infty v f_{1,\text{Gau}}(v) dv = \left(\frac{2}{\sqrt{\pi}} \right) v_0, \quad (3.22)$$

and

$$\langle v^2 \rangle_{\text{Gau}} = \int_0^\infty v^2 f_{1,\text{Gau}}(v) dv = \left(\frac{3}{2} \right) v_0^2. \quad (3.23)$$

For light WIMPs, the effect due to the form factor introduced in Eq.(3.5) can be neglected and we can use $F^2(Q) \approx 1$ [1]. Then the total event rate in Eq.(3.14) can be found directly as

$$R_{\text{Gau}}(Q_{\text{thre}}) = \frac{\rho_0 \sigma_0}{m_\chi m_N} \left(\frac{2v_0}{\sqrt{\pi}} \right) e^{-\alpha^2 Q_{\text{thre}}/v_0^2}. \quad (3.24)$$

For the case of $Q_{\text{thre}} = 0$, this result can be reduced to

$$R_{\text{Gau}}(Q_{\text{thre}} = 0) = \frac{\rho_0 \sigma_0 \langle v \rangle_{\text{Gau}}}{m_\chi m_N}, \quad (3.25)$$

which is exactly the naive estimate in Eq.(3.4). On the other hand, with the exponential form factor $F_{\text{ex}}^2(Q)$ given in Eq.(3.15), one can find that (a detailed calculation will be given in App. C.2.1)

$$R_{\text{Gau,ex}}(Q_{\text{thre}}) = \frac{\rho_0 \sigma_0 \langle v \rangle_{\text{Gau}}}{m_\chi m_N} \left(\beta^2 e^{-\alpha^2 Q_{\text{thre}}/v_0^2 \beta^2} \right), \quad (3.26)$$

and then

$$R_{\text{Gau,ex}}(Q_{\text{thre}} = 0) = \frac{\rho_0 \sigma_0 \langle v \rangle_{\text{Gau}}}{m_\chi m_N} \cdot \beta^2, \quad (3.27)$$

where I have defined

$$\beta \equiv \left(1 + \frac{v_0^2}{\alpha^2 Q_0} \right)^{-1/2}. \quad (3.28)$$

It can be seen that, for the case that the exponential form factor $F_{\text{ex}}^2(Q)$ can be neglected, or, equivalently, $Q_0 \rightarrow \infty$, i.e., $\beta \rightarrow 1$, $R_{\text{Gau,ex}}(Q_{\text{thre}})$ in Eqs.(3.26) and (3.27) will reduce to Eqs.(3.24) and (3.25).

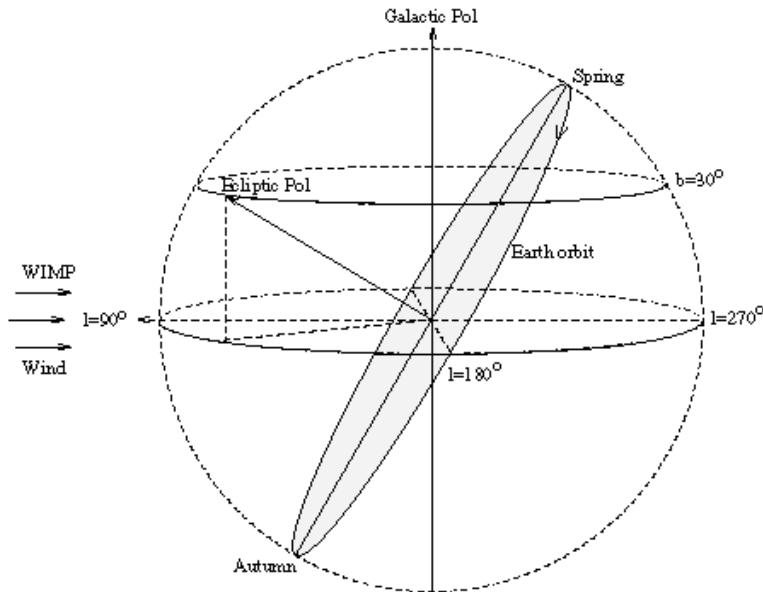


Figure 3.1: The Earth orbit in Galactic coordinates. The Sun moves to the left with about 220 km/s, inducing a WIMP wind (figure from [45]).

3.2 Annual modulation of the event rate

The one-dimensional velocity distribution function $f_{1,\text{Gau}}(v)$ given in Eq.(3.20) has been considered in the Galactic rest frame. More realistically, the orbital motion of the Solar system in the Galaxy as well as the motion of the Earth around the Sun must be considered [41]-[43]. As shown in Fig. 3.1, since the speed of the Earth adds to or subtracts from the speed of the Sun, the event rate for a given recoil energy (or energy range) in Eq.(3.12) should be a cosinusoidal function with a one-year period (see Figs. 3.3 and 5.1) and a peak around June 2nd [42]. The expected amplitude of this annual modulation is around 5%.⁴

Originally, such an annual modulation was only expected for the WIMP signal, not for the background. Thus this effect might serve a method to distinguish the WIMP signal from the background. And actually, the DAMA collaboration [48] has claimed that they have observed this annual modulation of the event rate [52]-[54] (more details about the DAMA result will be given in Subsec. 3.7.3). However, *the much larger background might also be subject to modulation* [37]. For example, the dependence of the cosmic muon flux on the atmospheric temperature, or the dependence of the background neutron flux on water in rock and concrete. Hence, the signal identification should also be performed.

⁴The ratio of a theoretically expected amplitude of this annual modulation to the time-averaged scattering spectrum as function of the recoil energy will be given in Fig. 5.2 in Subsec. 5.2.1. It can be seen that, for recoil energy between 0 and 50 keV, the modulated amplitude is around $-4\% \sim 5\%$. Some detailed discussions about the annual modulation of event rate will be given in Secs. 5.1 and 5.2.1.

3.2.1 Shifted Maxwellian halo

When we take into account the orbital motion of the Solar system around the Galaxy, as well as that of the Earth around the Sun, the velocity distribution function in Eq.(3.20) should be modified to [1]

$$f_{1,\text{sh}}(v, v_e) = \frac{1}{\sqrt{\pi}} \left(\frac{v}{v_e v_0} \right) \left[e^{-(v-v_e)^2/v_0^2} - e^{-(v+v_e)^2/v_0^2} \right] \quad (3.29)$$

with

$$v_e(t) = v_0 \left[1.05 + 0.07 \cos \left(\frac{2\pi(t - t_p)}{1 \text{ yr}} \right) \right], \quad (3.30)$$

where $t_p \simeq$ June 2nd is the date on which the velocity of the Earth relative to the WIMP halo is maximal [42]. Eq.(3.30) includes the effect of the rotation of the Earth around the Sun (second term), but does not allow for the possibility that the halo itself might rotate (some discussions about such bulk rotation has been given in Subsec. 1.3.6).

Substituting the shifted Maxwellian velocity distribution function in Eq.(3.29) into Eq.(3.12), the theoretically expected scattering spectrum can be obtained as (a detailed calculation will be given in App. C.1.2)

$$\left(\frac{dR}{dQ} \right)_{\text{sh}} = \mathcal{A} \left(\frac{1}{2v_e} \right) F^2(Q) \left[\text{erf} \left(\frac{\alpha\sqrt{Q}+v_e}{v_0} \right) - \text{erf} \left(\frac{\alpha\sqrt{Q}-v_e}{v_0} \right) \right]. \quad (3.31)$$

Here $\text{erf}(x)$ is the error function, defined as

$$\text{erf}(x) = \frac{2}{\sqrt{\pi}} \int_0^x e^{-t^2} dt.$$

Meanwhile, the mean velocity and velocity dispersion in Eqs.(3.22) and (3.23) should be modified to (detailed calculations will be given in App. B.1.2), respectively,

$$\langle v \rangle_{\text{sh}} = \left(\frac{v_0}{\sqrt{\pi}} \right) e^{-v_e^2/v_0^2} + \left(\frac{v_0^2}{2v_e} + v_e \right) \text{erf} \left(\frac{v_e}{v_0} \right), \quad (3.32)$$

and

$$\langle v^2 \rangle_{\text{sh}} = \left(\frac{3}{2} \right) v_0^2 + v_e^2. \quad (3.33)$$

As what I did in Subsec. 3.1.3, considering the light-WIMP case and using $F^2(Q) \approx 1$, the total event rate for the shifted Maxwellian distribution in Eq.(3.29) can be found as (a detailed calculation will be given in App. C.1.2)

$$R_{\text{sh}}(Q_{\text{thre}}) = \frac{\rho_0 \sigma_0}{m_\chi m_N} \left(\frac{v_0^2}{2v_e} \right) \left\{ \left(\frac{1}{2} - S_+ S_- \right) \left[\text{erf}(S_+) - \text{erf}(S_-) \right] + \frac{1}{\sqrt{\pi}} \left(S_+ e^{-S_-^2} - S_- e^{-S_+^2} \right) \right\}, \quad (3.34)$$

where I have defined

$$S_{\pm} \equiv \frac{\alpha\sqrt{Q_{\text{thre}} \pm v_e}}{v_0}. \quad (3.35)$$

For the case of $Q_{\text{thre}} = 0$, $R_{\text{sh}}(Q_{\text{thre}})$ in Eq.(3.34) can be reduced directly to

$$\begin{aligned} R_{\text{sh}}(Q_{\text{thre}} = 0) &= \frac{\rho_0\sigma_0}{m_{\chi}m_{\text{N}}} \left[\left(\frac{v_0^2}{2v_e} + v_e \right) \text{erf} \left(\frac{v_e}{v_0} \right) + \left(\frac{v_0}{\sqrt{\pi}} \right) e^{-v_e^2/v_0^2} \right] \\ &= \frac{\rho_0\sigma_0 \langle v \rangle_{\text{sh}}}{m_{\chi}m_{\text{N}}}, \end{aligned} \quad (3.36)$$

where I have used

$$\text{erf}(-x) = -\text{erf}(x).$$

Moreover, for the case with the exponential form factor $F_{\text{ex}}^2(Q)$ given in Eq.(3.15), I have (a detailed calculation will be given in App. C.2.2)

$$\begin{aligned} R_{\text{sh,ex}}(Q_{\text{thre}}) &= \frac{\rho_0\sigma_0}{m_{\chi}m_{\text{N}}} \left(\frac{v_0^2}{2v_e} \right) \left(\frac{\beta^2}{1-\beta^2} \right) \\ &\quad \times \left\{ e^{-(1-\beta^2)\alpha^2 Q_{\text{thre}}/v_0^2\beta^2} \left[\text{erf}(S_+) - \text{erf}(S_-) \right] \right. \\ &\quad \left. - \beta e^{-(1-\beta^2)v_e^2/v_0^2} \left[\text{erf}(T_+) - \text{erf}(T_-) \right] \right\}, \end{aligned} \quad (3.37)$$

where I have defined

$$T_{\pm} \equiv \frac{\alpha\sqrt{Q_{\text{thre}} \pm \beta^2 v_e}}{v_0\beta}. \quad (3.38)$$

For the case of $Q_{\text{thre}} = 0$, $R_{\text{sh,ex}}(Q_{\text{thre}})$ in Eq.(3.37) can be reduce to

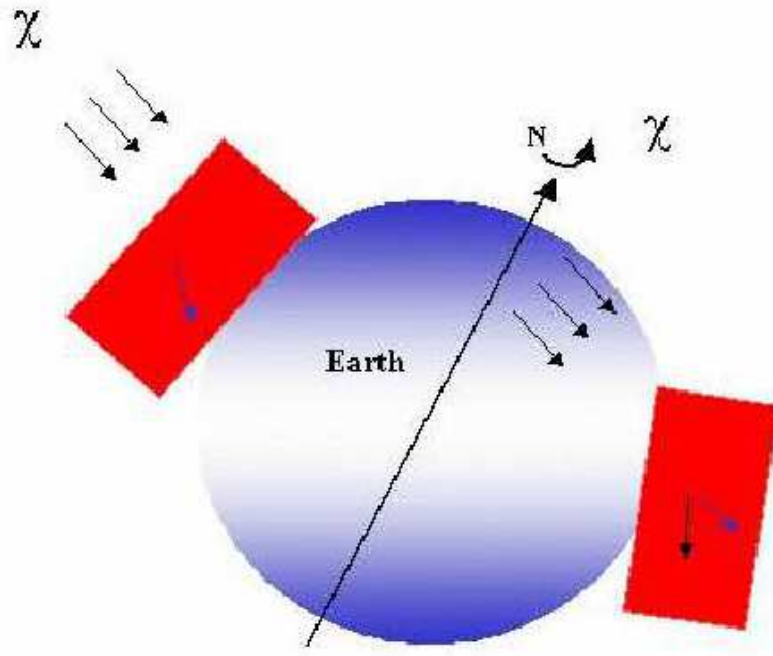
$$\begin{aligned} &R_{\text{sh,ex}}(Q_{\text{thre}} = 0) \\ &= \frac{\rho_0\sigma_0}{m_{\chi}m_{\text{N}}} \left(\frac{v_0^2}{v_e} \right) \left(\frac{\beta^2}{1-\beta^2} \right) \left[\text{erf} \left(\frac{v_e}{v_0} \right) - \beta e^{-(1-\beta^2)v_e^2/v_0^2} \text{erf} \left(\frac{\beta v_e}{v_0} \right) \right]. \end{aligned} \quad (3.39)$$

It is not difficult to check that $R_{\text{sh,ex}}(Q_{\text{thre}})$ in Eqs.(3.37) and (3.39) can be reduced to Eqs.(3.34) and (3.36) when one neglects the form factor $F_{\text{ex}}^2(Q)$, i.e., let $\beta \rightarrow 1$. On the other hand, as $v_e \ll v_0$, one can also prove that the results in Eqs.(3.32) to (3.34), and (3.36) can be reduced to Eqs.(3.22) to (3.25).

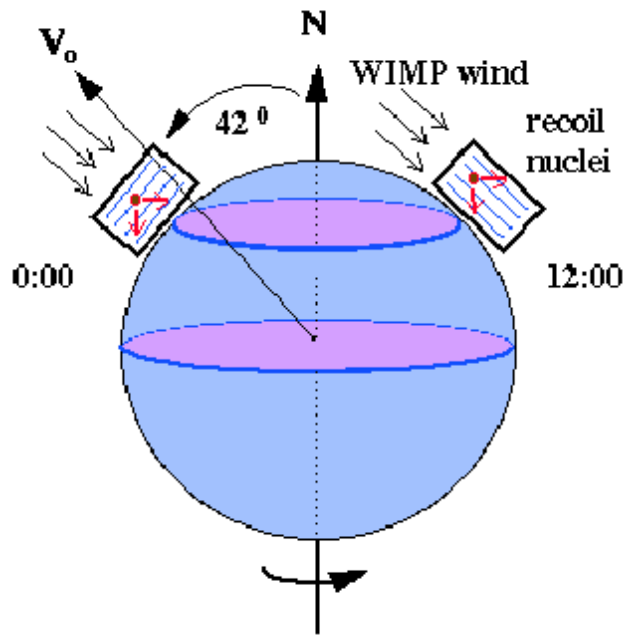
3.3 Diurnal modulation of the event rate

Similar to the annual modulation caused by the orbital motion of the Earth around the Sun, due to the rotation of the Earth, the event rate for a given energy (or energy range) should have a diurnal modulation [45], [22].

There are two different effects caused by this diurnal modulation. The first one is the shielding of the detector of the incident WIMP flux by the Earth [22] (illustrated



(a)



(b)

Figure 3.2: Two effects caused by the diurnal modulation: (a) shielding of the detector of the incident WIMP flux by the Earth (figure from [22]), and (b) directionality of the WIMP wind (figure from [45]).

in Figs. 3.2(a)). Some authors claimed that, for WIMP masses close to $50 \text{ GeV}/c^2$ and under certain assumptions, this diurnal modulation due to the shielding of the WIMP flux could be larger than the annual modulation [43], [22]. However, this requires a large WIMP-nucleus cross section and recent experimental results have (almost) excluded this possibility. Moreover, practically, it is still impossible for the detectors nowadays and should also be very difficult for the next-generation ones to get more than a few singles per day to prove this effect (more details about the status of the operated experiments and their results will be given in Secs. 3.7 to 3.9).

On the other hand, the second effect due to the rotation of the Earth is the directionality of the WIMP wind: a daily forward/backward asymmetry of the nuclear recoil direction (illustrated in Figs. 3.2(b)). A gaseous detector (e.g., DRIFT [55]) or anisotropic response scintillators should have the ability to measure this recoil direction [45], [37].

3.4 Target material dependence

The WIMP-nucleus cross section σ_0 in Eqs.(3.5) and (3.13) depends on the nature of the WIMP couplings to nucleons. For non-relativistic WIMPs, one in general has to distinguish spin-independent (SI) and spin-dependent (SD) couplings [37].

3.4.1 Spin-independent (SI) cross section

The total cross section for “scalar” coupling can be expressed as [1]

$$\sigma_{0,\text{scalar}} = \frac{4m_r^2}{\pi} [Zf_p + (A - Z)f_n]^2. \quad (3.40)$$

Here m_r is the reduced mass of the WIMP and the target nucleus in Eq.(3.6), Z is the atomic number, i.e., the number of protons, $A - Z$ is then the number of neutrons, f_p and f_n are the effective couplings of WIMPs to protons and neutrons, respectively.

Here we have to sum over the couplings to each nucleon before squaring because the wavelength associated with the momentum transfer is comparable to or larger than the size of the nucleus [51], the so-called “coherence effect”. In most cases, the couplings to protons and neutrons are approximately equal [1],

$$f_n \simeq f_p. \quad (3.41)$$

Then the cross section for scalar interaction in Eq.(3.40) can be reduced to

$$\sigma_{0,\text{scalar}} \propto A^2. \quad (3.42)$$

This means that, due to the coherence effect with the entire nucleus, the cross section for scalar interaction scales approximately as the square of the atomic mass of the target nucleus. Hence, *higher mass nuclei, e.g., Ge or Xe, are preferred for the search for the scalar interaction* [37].

On the other hand, WIMPs could also have a “vector” coupling to protons and neutrons [1]:

$$\sigma_{0,\text{vector}} = \frac{m_{\text{r}}^2}{64\pi} [2Zb_{\text{p}} + (A - Z)b_{\text{n}}]^2, \quad (3.43)$$

where b_{p} and b_{n} are the effective couplings to protons and neutrons. However, for Majorana WIMPs ($\chi = \bar{\chi}$), e.g., the neutralino, there is no such vector interaction [37].

3.4.2 Spin-dependent (SD) cross section

WIMPs could also couple to the spin of the target nucleus, an “axial-vector” (spin-spin) interaction. For this spin-spin coupling, only unpaired nucleons contribute significantly to the interaction, as the spins of the A nucleons in a nucleus are systematically anti-aligned [51]. And it is obvious that this spin-dependent interaction exists only if the incident WIMPs carry spin [37].

The total cross section for spin coupling can be expressed as [1]

$$\sigma_{0,\text{axial}} = \frac{32m_{\text{r}}^2}{\pi} [\Lambda^2 J(J + 1)], \quad (3.44)$$

where J is the total angular momentum of the nucleus and Λ ($\propto 1/J$) depends on the axial couplings of WIMPs to the quarks.

Because of the dependence on the nuclear spin factor, *the useful target nuclei for search for spin interaction are ^{19}F and ^{127}I* [37].

3.4.3 Comparison of the SI and SD cross sections

Generally speaking, a WIMP could have both scalar and spin-dependent interactions with the nucleus. Thus the WIMP-nucleus cross section σ_0 in Eqs.(3.5) and (3.13) should be the sum of the scalar cross section, $\sigma_{0,\text{scalar}}$, in Eq.(3.40) and the spin cross section, $\sigma_{0,\text{axial}}$, in Eq.(3.44).

For the scalar interaction, an analytic nuclear form factor, e.g., the exponential and the Woods-Saxon form factors presented in Subsec. 3.1.2, can be used. For the spin interaction, the form factor will differ from nucleus to nucleus and no simple analytic form factor can provide a very good approximation [1]. Fortunately, *for nuclei with $A \gtrsim 30$, the scalar interaction almost always dominates the spin interaction* [1].

3.4.4 Target mass

The scattering event rate depends also on the atomic mass of the target material directly.

First, according to Eq.(3.10), the smaller α the lower the incoming velocity with which the incident WIMPs can deposit energy larger than the threshold energy. Meanwhile, according to the definitions of α and m_{r} in Eqs.(3.11) and (3.6), it can be found that, for

WIMPs with a given mass and detector with a given threshold energy, α will be smallest if the mass of the target nucleus m_N is equal to the WIMP mass m_χ .

Second, for a given total mass of detector material, a larger target mass means also a smaller number density of the nucleus which can interact with the incident WIMPs. It will certainly reduce the total event number.

3.5 Measurement of recoil energy

3.5.1 A simple estimate

As an example, we assume a WIMP mass

$$m_\chi \approx 100 \text{ GeV}/c^2, \quad (3.1)$$

and use the standard theoretical WIMP rms velocity

$$\langle v^2 \rangle^{1/2} \simeq 270 \text{ km/s}. \quad (1.52)$$

then the average kinetic energy of the incident WIMPs can be estimated as

$$\langle E_\chi \rangle \approx 40 \text{ keV}. \quad (3.45)$$

On the other hand, by means of classical mechanics, the recoil energy of the target nucleus due to the elastic scattering can be expressed as

$$Q = \left[\frac{4m_\chi m_N}{(m_\chi + m_N)^2} \cos^2 \theta_{\text{Lab}} \right] E_\chi, \quad (3.46)$$

where θ_{Lab} is the recoil angle in the laboratory frame. This expression shows that the maximum recoil energy is obtained when $m_N = m_\chi$. This is also why this search should be more efficient for target material with a mass comparable to the WIMP mass.

3.5.2 Induced signals

When a WIMP scatters off a nucleus, the nucleus will at first obtain a few tens of keV kinetic energy and then dissipate this energy in the detector via three main processes: the electrons can be stripped by the scattered nucleus and an ionized nucleus-electrons system will be produced, this electronic activity can emit light, and the movement of the recoiling nucleus in the lattice can also induce vibrational phonons. Moreover, the ionization and scintillation energy will convert into phonons that will eventually thermalize and produce a tiny elevation of the temperature in the detector.

Hence, generally speaking, due to the elastic WIMP-nucleus scattering, the nuclear recoil can induce three different signals: ionization (charges), scintillation (light), and heat (phonons).

3.5.3 Quenching factor

When a photon with energy between keV and MeV enters a detector, it will induce an electron recoil with a range of the order of the μm and transfer most of its energy to the electron. However, the range of a nuclear recoil is only of the order of the nm and the nucleus will lose a substantial part of its energy directly into phonons associated with atom vibrations as the nucleus is stopped in the lattice [51].

Hence, the quenching factor (the nuclear recoil relative efficiency) for the ionization detectors has been defined as the ratio of the number of charge carriers produced by a nuclear recoil due to the WIMP interaction to that produced by an electron recoil with the same kinetic energy (energy calibrated with a γ -source, called “electron equivalent energy” or “eee”). Meanwhile, for scintillating detectors, the quenching factor is defined as the ratio between the light produced by a nuclear recoil and by an electron recoil. For conventional detectors, this factor is usually lower than 0.3 [22], [51]: ~ 0.3 for Ge or Si, ~ 0.25 for Na, ~ 0.09 for I, and ~ 0.2 for Xe. While, for cryogenic detectors measuring heat, the quenching factor has been measured to be around one for recoiling nuclei independently of the energy [22].

Note that, due to this quenching factor, the measured recoil energies are often quoted practically in keV_{ee} instead of true recoil energies in unit of keV.

3.5.4 Heat

Basically a cryogenic detector has been made of a crystal with a thermometer glued on it, and operated at very low temperature (around 20 mK).

When the detectors have been cooled to the operating temperature in a dilution refrigerator, the heat capacity ($\propto T^3$) is so low that even a few keV of deposited energy raises the temperature of one of the detectors by a measurable amount, allowing the amount of energy deposited to be determined [1].

Moreover, a superconducting-normal phase transition due to the elevation of the temperature has been used by the CRESST collaboration [56]. A thin film of tungsten (W) can be grown on a silicon detector and held just below the critical temperature. Phonons created by a WIMP-nucleus scattering would heat the superconducting film, causing it to go normal, and the change in resistance could be measured [1]. A very low threshold energy ($\simeq 500$ eV) of such detector were reached by the CRESST-I experiment with a 262 g sapphire detector [22], [57] (more details about the CRESST experiments and their results will be given in Subsec. 3.7.2).

Similarly, it is also possible to use some small superconducting granules in a magnetic field as detector, when one of such detectors is heated by a nuclear recoil, it would go normal and thereby cause a measurable change in the magnetic flux [1].

3.5.5 Ionization

A small voltage is placed across the crystal of the detector, and when several atoms have been ionized, the freed electrons will drift to one side, the collected charges can be used as a measure of the energy deposited in ionization [1].

Germanium ^{76}Ge used initially in the neutrino-less double- β ($0\nu 2\beta$) decay experiments has been used as the first detector material for direct WIMP detection experiments by the Heidelberg-Moscow (HDMS) collaboration [58] (more details about the HDMS experiments and their results will be given in Subsec. 3.7.5). Thanks to the high intrinsic purity achieved by the semiconductor industries and the technique developed for the $0\nu 2\beta$ decay experiments, Ge ionization detectors have nowadays very low thresholds and very good resolutions ($Q_{\text{thre}} \simeq 4 \sim 10 \text{ keV}_{ee}$, equivalent to $\simeq 15 \sim 30 \text{ keV}$ recoil energy, for HDMS [22]). Moreover, silicon (Si) has also been used by e.g., CDMS collaboration [59] as detector material (more details about the CDMS experiments and their results will be given in Subsec. 3.7.1). However, the size of such ionization detectors are limited.

3.5.6 Scintillation

Scintillation detectors, e.g., sodium iodine (NaI) or liquid xenon (LXe), are the solution to accumulate large mass of detector material ($\approx 100 \text{ kg}$). However, it is more difficult to achieve radiopurity comparable to Ge detectors [51].

Moreover, as mentioned in Subsec. 3.5.2, scintillation detectors do not measure the elevation of the temperature in the crystal, but the light emitted by the electrons produced due to the ionization, thus the energy threshold for these detectors may be substantially higher than the thermal calorimeters [1].

Meanwhile, the NaI-based experiments, such as DAMA [48], NaIAD [55], and EL-EGANT, originally attempted to use a pulse shape discrimination to statistically identify the WIMP signals from their observed events (detailed discussions about the background discrimination will be given in Sec. 3.6). It was found that the low number of detected scintillation photons per keV of incident energy (called “photo-electron per keV” or “p.e./keV $_{ee}$ ”) restricts the usefulness of this method at low energy [51]. This means that the background may be problematic. The technique is now being investigated for CsI or CaF scintillator, where the difference in time constants between scintillations induced by electron- and nuclear-recoils are larger than in the NaI detectors [51].

3.5.7 Combinations of two different signals

Actually, most of the direct WIMP detection experiments use detectors with mixed techniques and measure simultaneously two signals. For example, for cryogenic detectors, the CDMS and EDELWEISS collaborations [59], [60] investigate the heat-ionization signals (more details will be given in Subsecs. 3.7.1 and 3.7.4), and the CRESST col-

laboration [56] explores the heat-scintillation channel (more details will be given in Subsec. 3.7.2).

Combining information measuring from two different channels can offer a powerful event-by-event rejection method for the background discrimination down to 5 to 10 keV recoil energy [37]. As mentioned in Subsec. 3.5.3, due to the quenching effect of the detector material, the ratio of the ionization or the scintillation signal to the heat signal is significantly different for the nuclear recoils and for the electron recoils. Similarly, nuclear recoils due to WIMP or neutron interactions have a much higher characteristic light over charge ratio than electron recoils due to electron and γ -ray interactions [61]. Thus simultaneous measurements of two of the heat, the ionization, or the scintillation signals can be used to distinguish nuclear recoils induced by WIMPs from electron recoils induced by electron or γ -ray interactions (more details about different methods for background discrimination will be given in Sec. 3.6).

3.6 Background and background discrimination

As mentioned in the beginning of this chapter, due to the very low cross section of WIMPs on ordinary material, the event number of the elastic WIMP-nucleus scattering is very rare and the backgrounds coming from different sources are much larger.

For example, cosmic rays and cosmic-ray induced γ -rays with energies in the keV to MeV range, radioactive isotopes in and around the detector (in the equipment) should be considered. Moreover, neutrons induced by cosmic muons can produce nuclear recoil events similar to the real events induced by WIMPs. And electron recoils from photons (x-ray and γ -ray radiations) and electrons are also a major background.

3.6.1 Cosmic muons and underground laboratories

At ground level, approximately 10^3 cosmic muons pass through per square centimeter of the Earth's surface per day [51]. They can induce nuclear transmutations to unstable isotopes throughout the detector volume [51].

In order to protect from the penetrating cosmic muon flux, it is necessary to place the detector in deep underground. In underground laboratories such as the Soudan Underground Laboratory (the CDMS collaboration) in Minnesota in the USA, the Gran Sasso National Laboratory (the CRESST and DAMA collaborations) in Italy, or the Laboratoire Souterrain de Modane (LSM, the EDELWEISS collaboration) in the Fréjus Tunnel in the French-Italian Alps, the muon flux can be reduced by a factor of $10^5 \sim 10^7$ [51].

3.6.2 External natural radioactivity and (passive) shielding

External sources of radioactivity mean the radioactive isotopes in the rock around the underground laboratory and in the walls of the laboratory.

A shielding from external natural radioactivity can be achieved by surrounding the detector with thick absorbing material [51]: high- Z materials like lead are very effective for stopping γ -rays with MeV energy, while low- Z materials are sufficient for stopping low energy γ -rays as well as α - and β -radiations.

3.6.3 Internal natural radioactivity and radiopure materials

Beyond a thickness of 15 to 25 cm of lead shielding [51], one has to consider the internal radioactivity of the equipment, of the contamination near the detector or in the target material, and even of the lead shielding itself.

Internal radioactivity can be reduced very well by using detectors (and the other experimental equipment) made of radiopure materials. Archeological lead has also often been used since it has already been shielded from cosmic rays for 2000 years.

3.6.4 Active background rejection

Except passive shielding around the detector, most experiments use also some different techniques for active background rejection.

Generally there are two different types of background discrimination. Statistical rejections are used to ascertain which fraction of the total event sample comes from a well-defined type of background, but cannot tell for one individual event [51]. Moreover, this kind of rejections depends strongly on the theoretical predictions about the true signals induced by WIMPs and the background events.

On the other hand, the event-by-event rejections check each recorded event in the detector independently of the others (“blind”) and can be used to reject background events with an almost 100% certainty. Note that, however, in practice there is always a small probability that some background event may fake the signals induced by WIMPs.

3.6.5 Neutron induced nuclear recoils

Cosmic muons can induce neutrons in the inner lead shielding and such fast neutrons can induce nuclear recoils similar to those induced by WIMPs.

Fast neutron shielding consists of moderators made of material with a high density of hydrogen, such as polyethylene or water [51].

3.6.6 Multiple-scatter events and array of detectors

The interaction between WIMPs and ordinary material is too weak, or, equivalently, the mean free path of a WIMP in ordinary matter is too long (of the order of a light-year

[51]), so that WIMPs could never interact more than once in a single detector or two adjacent detectors. In contrast, the mean free path of a neutron or a high energy photon is of the order of cm, thus multiple-scatter events produced by neutrons are more common [51].

Hence, an array of closely packed detectors (e.g., the tower with six detectors used by the CDMS experiment, see Subsec. 3.7.1 and their web page [59]) can efficiently identify these multiple-scatter events [51].

3.6.7 Electron recoils

Theoretically WIMPs interact only with the nuclei (through the coupling to quarks) and produce nuclear recoils, while, due to the electromagnetic interaction, the dominant radioactive backgrounds interact usually with the electrons and produce electron recoils. Therefore, the experiments which can discriminate between the events due to nuclear recoils and events due to electron recoils can reject most radioactive background [62].

There are three ways to distinguish nuclear recoils from electron recoils. First, as mentioned in Subsec. 3.5.3, due to the quenching effect of the detector material, the ratio of the ionization or the scintillation signal to the heat signal is significantly different for nuclear recoils and for electron recoils. Thus one can measure simultaneously the heat signal and the ionization or the scintillation signal to distinguish the nuclear recoil events from the electron recoil events.

Second, the decay times of pulses for nuclear recoils may be different than that for electron recoils [62]. Thus some experiments use only a scintillation detector, but measure also the timing of the signals [62]. However, due to the limited resolution and discrimination power of this pulse shape analysis at low energies, this effect allows only a statistical background rejection [37]. This technique has been used by e.g., the DAMA/NaI and NaIAD experiments (NaI(Tl) detector) [48], [55] and ZEPLIN-I experiment (liquid xenon detector) [55].

Third, as mentioned in Subsec. 3.5.3, the range of a electron recoil is of the order of μm and that of a nuclear recoil is only of the order of nm. Thus the nuclear recoils have a much larger energy loss per unit length, dQ/dx , or, equivalently, produce a much higher energy density, than the electron recoils. Therefore, some experiments are actually immune to electron recoils because the energy they deposit is not dense enough to trigger [62].

3.6.8 Surface events and self shielding

Due to their very long mean free path, WIMPs will interact uniformly throughout the detector volume. In contrast, due to the short mean free path of the high-energy photons and neutrons, for a detector with a large volume, the interactions induced by radiations originating from the surrounding material and surface contamination will occur mostly

at the detector surface [51].

This “self-shielding” effect leads to the incentive of building large position-sensitive detectors in order to reject the surface events. Moreover, low-energy photons, α - and β -rays have very short mean free path ($< \text{mm}$), and can be rejected even if the position sensitivity is limited [51].

3.6.9 Incomplete charge collection

Some electromagnetic events occurring very near the detector surface can also mimic nuclear recoils because they produce less ionizations than expected from electron recoils [45]. But such surface events can also be rejected by the self-shielding effect.

3.6.10 Shape of the recoil energy spectrum

The shape of the recoil spectrum dR/dQ for a given WIMP mass in some simple halo models can be predicted numerically or even analytically (e.g., $(dR/dQ)_{\text{Gau}}$ in Eq.(3.21) and $(dR/dQ)_{\text{sh}}$ in Eq.(3.31)). The measured recoil spectrum should be consistent with the expectation.

However, first, the overall shape of the expected spectrum is (approximately) exponential, as is the case for many background sources; second, different velocity distribution functions in different halo models could predict totally different recoil spectrum (cf. $(dR/dQ)_{\text{Gau}}$ in Eq.(3.21) and $(dR/dQ)_{\text{sh}}$ in Eq.(3.31)). Moreover, the expected signal events measured by the currently operated detectors and even next-generation ones are at most only a few per day. Hence, as we will see in Sec. 4.2, at present a meaningful reconstruction of the recoil spectrum with a small statistical error is actually impossible.

3.7 Cryogenic detectors

As discussed above, a WIMP detector is constrained by three important requirements: low threshold, (ultra) low background, and high detector material mass [22].

In the following I will present some important collaborations worldwide and summarize their recent results and plans in the near future. More details about these collaborations and their experiments can be found in the references.

3.7.1 CDMS

The Cryogenic Dark Matter Search (CDMS) collaboration [59] uses the Berkeley Center for Particle Astrophysics (CfPA) germanium cryogenic detector [1]. Their first test run was at the Stanford University Underground Facility [1], and now moved to the deep Soudan Underground Laboratory (Soudan mine) in Minnesota in the USA [63]. The Soudan mine has 780 m rock overburden (2090 meters water equivalent, m.w.e.) [63], the

surface muon flux is then reduced by a factor of 5×10^4 [63], and the neutron background is also reduced by a factor of 400 [22] ($\sim 4 \times 10^{-4}$ /kg/day [64]).

It was the first experiment to operate a detector measuring simultaneously ionization and heat signals with a germanium/silicon crystal as the target material [22]. They developed Z(depth)-sensitive Ionization and Phonon (ZIP) detectors. The principle of their ZIP detector is basically the same as that discussed in Subsec. 3.5.5, except that the heat sensor is replaced by a thin film sensor and thus able to detect phonons before their complete thermalization [51].

Their “tower(s)” with mixed Ge and Si detectors are powerful for subtracting the neutron background [63]. Except the neutron multiple-scatter events discussed in Subsec. 3.6.6, while Ge and Si have similar scattering rates per nucleon for neutrons, the WIMP-nucleon scattering rate is expected to be 5-7 times greater in Ge than in Si for all but the lowest-mass WIMPs. Moreover, the kinematics of neutron elastic scattering gives a recoil energy spectrum scaled in energy by a factor of ~ 2 in Si compared to Ge, whereas the factor would be ~ 1 or less for WIMP elastic scattering. All of these three methods can be used (together), in conjunction with Monte Carlo simulations, to statistically subtract any neutron background.

In addition, because the athermal phonons from electron recoils are faster than those from nuclear recoils, particularly if the electron recoils occur near a detector surface, by collecting such fast, athermal phonons with thousands of thin-film sensors, their ZIP detector can discriminate very well against the surface electron recoils [62].

According to Ref. [63], for recoil energies above 10 keV, events due to the background photons can be almost perfectly rejected, and more than 96% of the incomplete charge collection events can also be rejected by using additional information from the shape, timing, and energy partition of the phonon pulses (namely, only events with both slow phonon pulses and low ionization have been accepted), while over half of the nuclear-recoil events should be kept [62].

In the first Soudan run of the CDMS-II experiment (from October 11, 2003 to January 11, 2004) [63], one tower with 4 Ge (each 250 g) and 2 Si (each 100 g) ZIP detectors has been operated for 52.6 live days, the recoil energy thresholds of these six detectors were between 10 and 20 keV, *only one candidate event* with a recoil energy of 64 keV in one Ge detector has been measured. For a WIMP mass of $60 \text{ GeV}/c^2$, a 4×10^{-7} pb upper limit on the spin-independent WIMP-nucleon cross section ⁵ from Ge as been achieved. Meanwhile, thanks to the ^{73}Ge (spin- $\frac{9}{2}$) and ^{29}Si (spin- $\frac{1}{2}$) content of natural germanium and silicon, a 0.2 pb upper limit on the spin-dependent WIMP-neutron cross section for a WIMP mass of $50 \text{ GeV}/c^2$ has also been achieved. These were the world’s lowest limits on the WIMP-nucleon cross-section in the case of spin-independent interactions and spin-dependent interactions with neutrons.

⁵Here the cross-section σ_0 shown in Eqs.(3.5) and (3.13) is normalized to a single nucleon $\sigma_{\chi n}$ in order to allow comparisons between different target nuclei.

In the second Soudan run (from March 25 to August 8, 2004) [65], [66], and [46], two towers (one tower with 4 Ge and 2 Si detectors and the other one with 2 Ge and 4 Si detectors) have been operated for 74.5 live days and the recoil energy thresholds have been improved to be only 7 keV, *one more candidate event* with a recoil energy of 10.5 keV in one Ge detector has been measured. For a WIMP mass of $60 \text{ GeV}/c^2$, the upper limit on the spin-independent WIMP-nucleon cross section has been given as $1.6 \times 10^{-7} \text{ pb}$ from Ge and $3.4 \times 10^{-6} \text{ pb}$ from Si (see Fig. 3.4). These limits are a factor of 6 lower than those given by the ZEPLIN-I experiment [55] (see Subsec. 3.8.5) and an order of magnitude lower than those of the CRESST and EDELWEISS collaborations [62]. Moreover, their results excluded the overlap between the CDMS and DAMA/NaI allowed regions at WIMP masses $\gtrsim 25 \text{ GeV}/c^2$, though compatible regions at lower masses remain [66] (see Fig. 3.4).

Now the CDMS collaboration is preparing for five towers with totally 19 Ge (4.75 kg) and 11 Si (1.1 kg) ZIP detectors, and will improve their sensitivity a factor of ≈ 10 [46]. Furthermore, they also planned a SuperCDMS project which will start with a total mass of 25 kg (Phase A, each detector will be 640 g) and be improved to 150 kg (Phase B) and eventually 1000 kg (Phase C) [46], in order to achieve $\sim 10^{-9} \text{ pb}$ sensitivity (for a WIMP mass of $60 \text{ GeV}/c^2$, Phase A, see Fig. 3.5) [46], corresponding to $\mathcal{O}(10^{-4})$ events/kg/day event rate in the energy range between 15 and 45 keV [64]. They will also move to the SNO Underground Laboratory at the Sudbury mine in Canada. The $\sim 6000 \text{ m.w.e.}$ overburden at this site results in over two orders of magnitude suppression in the neutron background compared to Soudan [64].

3.7.2 CRESST

The Cryogenic Rare Event Search using Superconducting Phase Transition Thermometers (CRESST) collaboration [56] uses heat-scintillation detectors with CaWO_4 crystal in the Gran Sasso National Laboratory in Italy. Their detector provides a good rejection of surface events as of photons due to the much larger light yield from all electron recoils relative to nuclear recoils [62].

As mentioned in Subsec. 3.5.4, their detector uses the superconducting-normal phase transition due to the difference of the temperature. A thin superconducting film of tungsten (W) has been grown on a silicon detector and held just below the critical temperature. Heat produced by WIMP-nucleus scatterings will change the film to its normal state and the change in resistance could be measured [1]. However, as mentioned in Subsec. 3.5.6, the threshold energy of such a scintillation detector is relatively higher than for an ionization detector. Thus a disadvantage of the CRESST heat-scintillation detector is that an event measured by the phonon channel but producing no light may mimic a WIMP signal [62].

In 2003 CRESST ran two prototype detectors for a couple of months without neutron shielding. A significant neutron background on the oxygen in their CaWO_4 detectors was

observed [62] and the light yield for W recoils is significantly less than for Ca or O recoils. This result indicates that WIMPs are expected to interact primarily with W nuclei, while neutrons will interact relatively more often with O and Ca nuclei [51].

In early 2004 they operated two 300 g CRESST-II prototype detector modules, 16 events have been recorded and a rate for nuclear recoil energy between 12 and 40 keV of (0.87 ± 0.22) events/kg/day has been obtained [67]. However, this is compatible with the rate expected from neutron background, and most of these events lie in the region of the phonon-light plane anticipated for neutron-induced recoils [67]. Moreover, a particularly strong limit for WIMPs with coherent scattering results from selecting a region of the phonon-light plane corresponding to tungsten recoils, where the best module shows zero events [67]. The sensitivity achieved by the CRESST-II experiment is given in Fig. 3.4.

Now they are preparing the scientific run of the CRESST-II experiment with 33 detectors (each 300 g) and totally ~ 10 kg target material (see Fig. 3.5).

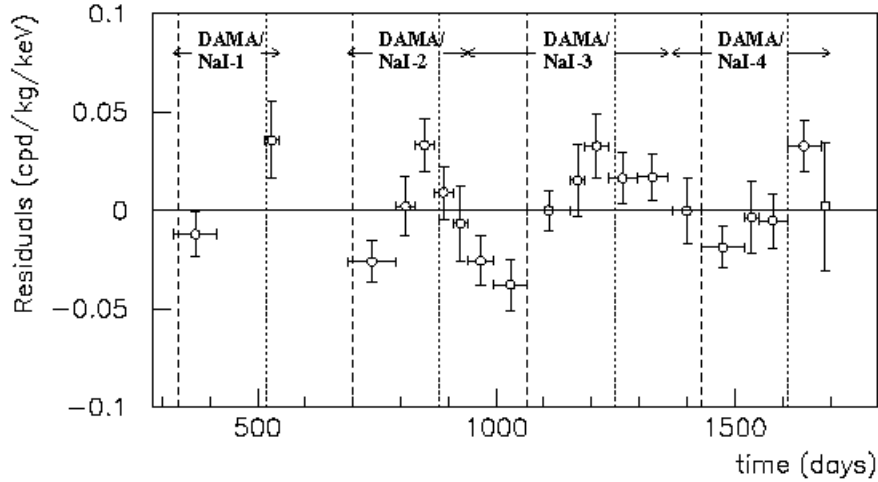
3.7.3 DAMA

The DARK MATTER (DAMA) collaboration [48] uses a scintillation detector with ~ 100 kg NaI(Tl) in the Gran Sasso National Laboratory (Laboratori Nazionali del Gran Sasso, LNGS) in Italy [52]. With 1400 m rock overburden (3500 m.w.e.), the total muon flux is reduced to $\sim 1/\text{m}^2/\text{hr}$ (one order of magnitude lower than that of CDMS), the external γ -ray flux is reduced by a factor of 10^5 .

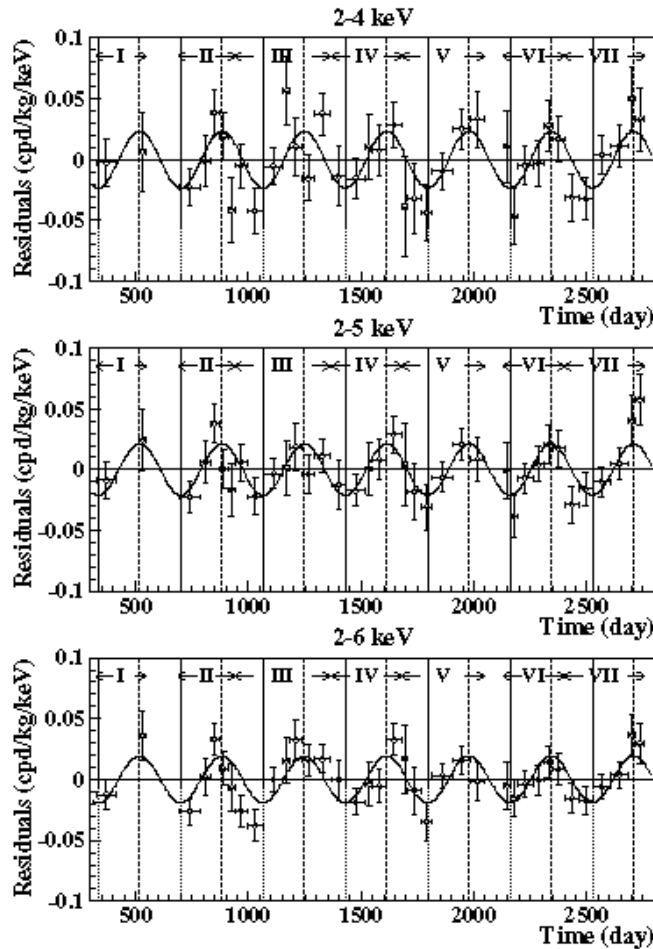
They are the only collaboration which claimed to detect the signal of halo Dark Matter due to the annual modulation effect discussed in Sec. 3.2. Figs. 3.3 show the 4-year and the 7-year results of the DAMA/NaI experiment [53], [54], their threshold energy is about 2 keV_{ee} , corresponding to approximately 22 keV recoil energy [51]. Meanwhile, they published a WIMP mass $m_\chi \simeq 52 \text{ GeV}/c^2$ and a WIMP-proton cross section $\sigma_{\chi p} \simeq 7.2 \times 10^{-6} \text{ pb}$ [52] under the standard assumptions of WIMP halo described in Subsec. 1.3.1 (see Fig. 3.4).

However, the DAMA collaboration uses the pulse shape discrimination (PSD) technique (see Subsec. 3.6.7) to statistically (not event-by-event) discriminate the measured events [51]. On the other hand, the CDMS results [68], [63], [65] and [66] are clearly incompatible with the signal claimed by DAMA under the standard assumptions of the WIMP halo and spin-independent WIMP-nucleus coupling [62].

But these two experiments might still be compatible in some exotic scenarios. One possibility is to postulate rather light ($m_\chi < 10 \text{ GeV}/c^2$) and fast WIMPs with large scattering cross section [69]. Since for this case $m_I \gg m_\chi$, the maximal recoil energy induced by the scattering on iodine will then be smaller than the threshold energy of the DAMA's detector and the recorded events have thus been induced by the scattering on sodium (see Eq.(3.46)). Similarly, the Ge nuclei used by the CDMS experiment could also be too heavy to deposit recoil energy large enough to be measured. However, the null results from the Si detector used by CDMS (see Subsec. 3.7.1) should (almost) rule



(a)



(b)

Figure 3.3: The published results of the DAMA/NaI experiment. (a) In the 2-6 keV_{ee} cumulative energy interval over 4 annual cycles, since January 1st of the first year of data taking. Theoretically expected minimum (dashed line), maximum (dotted line) (figure from [53]). (b) In the 2-4 keV_{ee}, 2-5 keV_{ee}, and 2-6 keV_{ee} cumulative energy intervals over 7 annual cycles and end of data taking in July 2002 (figure from [54]).

out this possibility. Another possible way out is to postulate that the detected events are actually inelastic, leading to the production of a second particle that is almost, but not exactly, degenerate with the WIMP [70].

They are running now the DAMA/LIBRA (Large sodium Iodide Bulk for RAre processes) experiment with totally ~ 250 kg NaI(Tl) [53].

3.7.4 EDELWEISS

The Expérience pour DETecter Les WIMPs En Site Souterrain (EDELWEISS, EDW) collaboration [60] is in the Laboratoire Souterrain de Modane (LSM) in the Fréjus Tunnel in the French-Italian Alps. With ~ 1800 m rock overburden (~ 4800 m.w.e.), the muon flux can be reduced to $\sim 4/\text{m}^2/\text{day}$, the fast neutron flux can be reduced to $\sim 1.6 \times 10^{-6}/\text{cm}^2/\text{s}$ [71].

The EDELWEISS-I experiment has used 3 (each 320 g) cryogenic heat-and-ionization Ge detector [51]. Their calibrations indicate that the larger ionization/recoil energy ratio of electron recoils results in very good discrimination ability against photon backgrounds down to the 20 keV threshold energy [62].

In 2000 to 2002 [47], the EDELWEISS-I experiment has been operated for an exposure of 13.6 kg-day. The energy threshold was 13 keV and *no event* has been recorded. In 2003 [47], the second run of the EDELWEISS-I has been operated for an exposure of 48.4 kg-day (totally 62 kg-day) and *40 nuclear recoil candidate events* have been recorded in the energy range 15 to 200 keV: 18 events between 15 and 20 keV, 16 events between 20 and 30 keV, 3 events between 30 and 100 keV, 3 events between 100 and 200 keV, and *more 19 events* have been observed below 15 keV; most likely due to remaining background neutrons and surface electrons. According to these results, they gave exclusion limits for WIMP masses above $25 \text{ GeV}/c^2$ [47] (see Fig. 3.4).

Now they are preparing the EDELWEISS-II experiment with 120 detectors [71] (see Fig. 3.5).

3.7.5 Heidelberg-Moscow (HDMS)

The Heidelberg-Moscow collaboration [58] uses a ~ 2 kg ^{76}Ge semiconductor ionization detector in the Gran Sasso National Laboratory in Italy and achieved a very low background count rate (< 0.2 event/kg/day) in the interval $10 \sim 40$ keV, and a threshold energy $Q_{\text{thre}} \simeq 4 \sim 10 \text{ keV}_{ee}$ (equivalent to $\simeq 15 \sim 30$ keV recoil energy) [22].

They produced the first limits on WIMP searches and until recently had the best performance. However, without positive identification of nuclear recoil events, these experiments could only set limits, e.g., excluding sneutrinos as major component of the galactic halo [37].

3.7.6 KIMS

The Korea Invisible Mass Search (KIMS) collaboration [72] in the Yangyang Underground Laboratory (Y2L, ~ 700 m rock overburden) in South Korea developed a CsI(Tl) crystal scintillation detector and uses an improved pulse shape discrimination to discriminate nuclear recoil events induced by WIMPs from electron recoil events induced by γ -ray background [73].

They have operated 4 detectors with an exposure of 3407 kg-day in the temperature 0°C and *null signals* have been observed [73]. Due to their ^{133}Cs and ^{127}I target nuclei this result has been used to give the lowest upper limits on the spin-dependent WIMP-proton cross section for WIMP masses $\gtrsim 30 \text{ GeV}/c^2$ [73] (the lowest upper limit on the spin-dependent WIMP-neutron cross section has been obtained by the CDMS collaboration, see Subsec. 3.7.1). Moreover, although several experiments have already given exclusion limits rejecting the DAMA signal region, it is the first time that such a limit obtained by the crystal scintillation detector containing ^{127}I , which has been usually assumed to be the dominant nucleus for the spin-independent interaction in the NaI(Tl) crystal.

3.7.7 PICO-LON

The Planar Inorganic Crystals Observatory for LOw-background Neutr(al)ino (PICO-LON) collaboration in Japan uses detector with multilayer (3 layers for PICO-LON-0 and 16 layers for PICO-LON-I) thin NaI(Tl) crystals [74], [75].

A special advantage of their 0.05 cm thin and 5 cm \times 5 cm wide area NaI(Tl) crystals is the position sensitivity of the recoil events [75]. The position resolution for the thinner directions is as good as 0.05 cm due to the segmentation of the detector [75]; while, the position information in the wider area was obtained by analyzing the ratio of the number of photons collected on the opposite sides of the detector [75] and a circle with $\simeq 0.5$ cm radius has been reached [76]. Moreover, they have also claimed that a very low threshold energy $\sim 2 \text{ keV}_{ee}$ has been measured [74], [76].

The PICO-LON-0 experiment has been run at the surface laboratory at Tokushima, and the PICO-LON detector will be installed into Oto Cosmo Observatory (100 km south from Osaka) covered by thick rock with ~ 1200 m.w.e. [75].

3.8 Liquid noble gas detectors

Liquid noble gas detectors have the advantage of easier scaling to large masses since it is based on liquids [62]. They can also be allowed to operate in higher temperatures: 165 K for xenon, 87 K for argon, and 27 K for neon [77].

Due to its high- A value, liquid xenon (LXe) has been used by the ZEPLIN collaboration [55] as the first liquid noble gas detector material (more details about the ZEPLIN experiments will be given Subsec. 3.8.5). Recoils in the liquid noble gas such as Xe can

induce both ionization and excitation of Xe atoms. An excitation produced by a nuclear recoil usually induces emission with a single photon, whereas that reduced by an electron recoil emits photons in form of a slow triplet, thus nuclear recoils have a faster pulse shape than electron recoils [62], [78].

Besides xenon, argon and neon are also suitable detector materials. The effect of faster pulse shape is particularly clear in Ar and Ne, leading to their extremely good discrimination based on timing [62]. In addition, due to the form factor effect introduced in Eq.(3.5) (two nuclear form factors for spin-independent cross section have been given in Subsec. 3.1.2), the event rate in e.g., argon is less sensitive to the energy threshold than in xenon [61].

Moreover, as discussed in Subsec. 3.5.7, the scintillation (light) over ionization (charge) ratio can be used additionally to discriminate the nuclear recoils from the electron recoils due to electron and γ -ray interactions.

However, discrimination of the radioactive contamination in the detector material, such as ^{85}Kr in liquid Xe (25 ppm Kr in natural Xe) or especially ^{39}Ar in liquid Ar [62] as well as of the surface radioactivity from the liquid container [51], and relatively larger threshold energies could be primary challenges for detectors using liquid noble gases.

3.8.1 ArDM

The Argon Dark Matter (ArDM) experiment at CERN [79] uses a ton-scale detector with liquid argon (LAr), which measures simultaneously the scintillation and the ionization signals [80], [61], and [81].

With a recoil energy threshold of 30 keV and a sensitivity of 10^{-6} pb WIMP-nucleon cross section, the ArDM experiment has been expected to yield approximately 100 events per day per ton [61]. By improving the background rejection power and further limiting the background sources, a sensitivity of 10^{-8} pb (1 event per day per ton) would become reachable [61].

3.8.2 WARP

Similar to the ArDM experiment, the WIMP ARgon Programme (WARP) experiment [82] uses also a dual-phase (gas-liquid) argon detector [62] in the Gran Sasso Underground Laboratory in Italy [77]. By using a strong electric field, ionization electrons are drifted out of the liquid argon into gaseous phase, where they are detected via the secondary luminescence [51], [62]. The discrimination technique is based on both of the pulse shape of the photon emissions and on the ratio of the scintillation to ionization energies [62] described in Subsec. 3.5.7.

Their first run of a 2.6 kg (1.87 ℓ) prototype with a 96.5 kg-day exposure resulted in *no candidate events* above the threshold energy 55 keV [77] (see Fig. 3.4). Later they will upgrade the detector to totally 140 kg ($> 100 \ell$) [77].

3.8.3 XENON

The XENON collaboration [83] uses also a dual-phase xenon time projection chamber (XeTPC) with 3D position sensitivity in the Gran Sasso Underground Laboratory in Italy [84].

The XENON10 experiment uses 15 kg liquid xenon, the background rate from ^{85}Kr contamination is reduced by a factor of 5000 by using a commercially available low-Kr (5 ppb) xenon, the self-shielding effect (see Subsec. 3.6.8) of LXe can reduce the background events in the central region of the LXe target by more than one order of magnitude for recoil energy below 50 keV_{ee} , (5 to 15 keV_{ee} corresponds to roughly 15 to 40 keV recoil energy) [84].

By measuring simultaneously the scintillation and the ionization produced by radiation in pure liquid xenon, the detector can discriminate signals from background down to 4.5 keV_{ee} [85]. Between October 6, 2006 and February 14, 2007 the XENON experiment has been run for 58.6 live days and 10 events have been observed in the energy range 4.5 to 26.9 keV_{ee} . However, none of these events are likely WIMP interactions. [85]

Their newest result gives a 90% C. L. upper limit on the spin-independent WIMP-nucleon cross section of $8.8 \times 10^{-8} \text{ pb}$ for a WIMP mass of $100 \text{ GeV}/c^2$ [85], a factor of 2.3 lower than the limit achieved by CDMS-II experiment (see Subsec. 3.7.1). For a WIMP mass of $30 \text{ GeV}/c^2$, the limit is $4.5 \times 10^{-8} \text{ pb}$ [85] (see Fig. 3.4).

The XENON10 experiment will be upgraded to $\sim 100 \text{ kg}$ [51] and a WIMP-nucleon sensitivity of $2 \times 10^{-8} \text{ pb}$ in 2008 [86] (see Fig. 3.5).

3.8.4 XMASS

The Xenon Neutrino MASS Detector (XMASS) experiment uses a 100 kg (intend to ultimately 800 kg) [37] single-phase Xe detector [62] at the SuperKamiokande site in Japan.

Because of their 100 kg total mass of target material, XMASS has a good position sensitivity and has demonstrated the self-shielding effect (see Subsec. 3.6.8) to reduce the background events induced by multiple scattering (see Subsec. 3.6.6) and surface contamination [37].

Besides the XMASS experiment with liquid Xe, CLEAN (Cryogenic Low-Energy Astrophysics with Neon) and DEAP are also single-phase experiments. They use Ar or Ne as detector material in order to take advantage of the much larger timing difference between nuclear recoils and electron recoils described above [62], [87].

3.8.5 ZEPLIN

The Zoned Proportional Scintillation in Liquid Noble Gases (ZEPLIN) collaboration [55] first used a liquid xenon scintillation detector in the Boulby Laboratory (1070 m underground) in the United Kingdom.

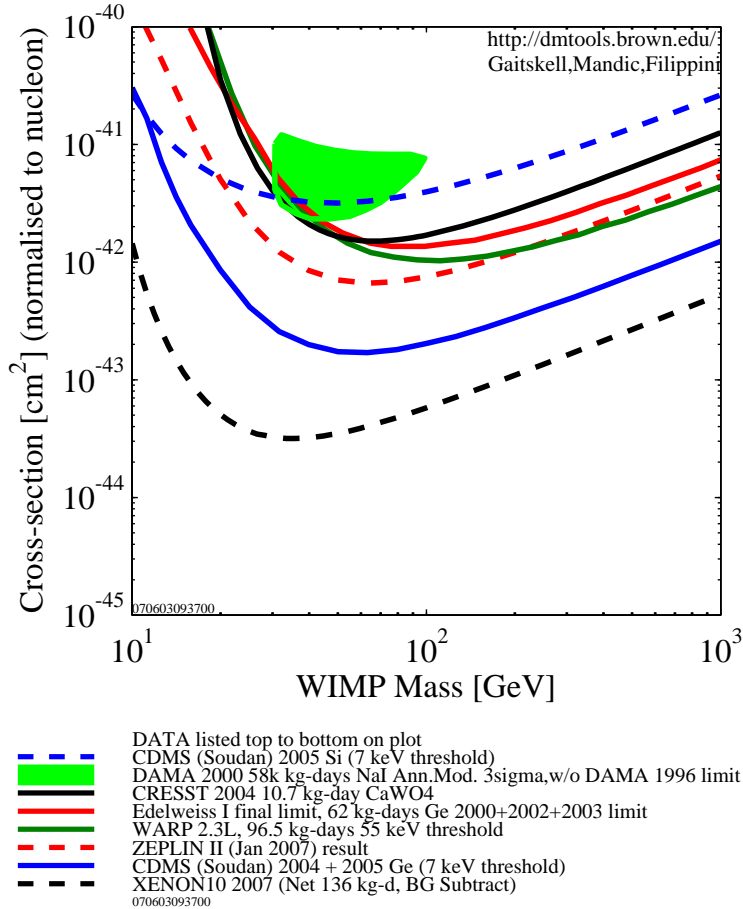


Figure 3.4: The curves show the sensitivities of (the exclusion limits on) the spin-independent WIMP-nucleon cross section versus WIMP mass achieved by the CDMS [65] (the blue solid and the blue dashed lines, for Ge and Si, respectively), the CRESST [67] (the black solid line), the DAMA [52] (the green area), the EDELWEISS [47] (the red solid line), the WARP [77] (the dark green solid line), the XENON [85] (the black dashed line), and the ZEPLIN [78] (the red dashed line) collaborations (plot generated by <http://dmtools.berkeley.edu/limitplots/>).

ZEPLIN-I was a single-phase experiment with 6 kg (3.1 kg fiducial) Xe, so it could not collect the ionization signals, but depended solely on the pulse shape discrimination [62]. In an exposure of 293 kg-day, *no excess consistent with nuclear recoils* was seen [62]. However, the published limits are somewhat controversial, because their calibration results of the neutron recoil discrimination do not appear to be convincing enough to consider the limits set on the WIMP signal to be as reliable as the ones set by the cryogenic experiments [37]. Actually, with only 1.5 photo-electron per keV and a three-fold coincidence, searching for the WIMP signal in the 2-10 keV_{ee} region is for ZEPLIN-I quite challenging [37].

ZEPLIN-II has been upgraded to a dual-phase experiment with 31 kg Xe [78]. In the first run with 225 kg-day exposure, *29 events* have been observed in an acceptance window

defined between 5 keV_{ee} and 20 keV_{ee}. With a summed expectation of 28.6 ± 4.3 γ -ray and radon progeny induced background events, these figures provide a 90% C. L. upper limit to the number of nuclear recoils of 10.4 events in this acceptance window, which converts to a spin-independent WIMP-nucleon cross-section of 6.6×10^{-7} pb for a WIMP mass of 65 GeV/ c^2 (see Fig. 3.4). For the second run a sensitivity of 2×10^{-7} pb has been expected (see Fig. 3.5).

3.9 Superheated droplet detectors (SDD)

Metastable liquid droplets immersed in a gel expand (explode) due to a phase transition to the gaseous phase, when a particle or nucleus with sufficiently high energy density (energy deposited over unit length, dQ/dx) interacts in the liquid [45]. A broad range of detector materials could be used and inexpensively scaled to large masses [62].

The main (best) advantage of such integrating detectors is that, by tuning pressure and temperature, the threshold energy of the detector can be adjusted so that the detector could be insensitive to the low energy density [62]. Thus electron recoils and α -radiation events can be rejected automatically.

3.9.1 DRIFT

The Directional Recoil Identification From Tracks (DRIFT) experiment [55] uses a low pressure Xe-CS₂ gas mixture TPC [22]. Using the negative CS₂ ions instead of usual e^- as charge carriers can reduce the diffusion and thus achieve millimetric track resolution [22]. The ionization tracks will be measured with a multi-wire proportional chamber in a low-pressure gas [45], this offers the most convincing technique to measure the direction of nuclear recoils [37], [87].

However, one disadvantage of the DRIFT's detector is the very low target mass and/or the need of a huge detector volume.

3.9.2 MIMAC-He3

The Micro-tpc (temporal projection chambers) MAtrix of Chambers of Helium 3 (MIMAC-He3) experiment [88] uses an ultra cold pure ³He detector [37]. The use of ³He as target material is motivated by its privileged features for Dark Matter search compared with other target nuclei. First, ³He being a spin- $\frac{1}{2}$ nucleus with a single neutron, a detector made of such material will be sensitive to the “neutron spin-dependent” interaction, leading to a natural complementarity to most existing or planned Dark Matter detectors as well as proton based spin-dependant detectors [90]. Moreover, the mass of the ³He atom is 2.81 GeV/ c^2 , the recoil energy range is expected less than 10 keV [89]. Hence, MIMAC-He3 could be used to measure events with low recoil energies as well as detect low-mass WIMPs ($6 \text{ GeV}/c^2 \leq m_\chi \leq 40 \text{ GeV}/c^2$ [90]).

There are several more advantages for a detector using ^3He [89], [90]: first, there are no intrinsic x-rays; second, a very low Compton cross section to γ -ray (two orders of magnitude weaker than in Ge) can reduce the natural radioactive background by several orders of magnitude; third, the neutron signature due to the capture process: $n + ^3\text{He} \rightarrow p + ^3\text{H} + 764 \text{ keV}$, will be very useful for discrimination of neutron background. On the other hand, the double detection of the ionization energy and the track projection by means of the TPC chambers can assure the electron-recoil discrimination.

However, similar to the DRIFT experiment, one disadvantage of their detector is the very low target mass and/or the need of a huge detector volume.

3.9.3 PICASSO

The Project In CANada to Search for Supersymmetric Objects (PICASSO) experiment in the Sudbury Neutron Observatory (SNO) in Canada uses ^{19}F (spin- $\frac{1}{2}$ isotope) as detector material and search for spin-dependent Dark Matter particles (see Subsec. 3.4.2)[22].

The principle of the PICASSO detector is as follows: Small superheated freon droplets imbedded in a gel matrix at room temperature. The nuclear recoil of ^{19}F induces the explosion of a droplet, creating an acoustic shock wave which will be measured with piezoelectric transducers [22].

3.9.4 SIMPLE

The Superheated Instrument for Massive ParticLe Experiments (SIMPLE) collaboration in the Laboratoire Souterrain à Bas Bruit (LSBB, $\sim 1500 \text{ m.w.e.}$) in France uses C_2ClF_5 and CF_3I and searches also for spin-dependent Dark Matter interaction [91], [92]. Their results exclude the spin-dependent WIMP-proton cross section above 1.14 pb for a WIMP mass of $50 \text{ GeV}/c^2$ [93] (an upper limit of 0.2 pb on the spin-dependent WIMP-neutron cross section has been given by the CDMS collaboration, see Subsec. 3.7.1).

3.10 Prospects

So far we did not obtain any convincing signal from experiments searching for Dark Matter particles. In the future, detector technique, better sensitivities as well as better background discrimination, will be improved. We need also some new ideas for detector building as well as application of experimental data.

As described in Subsec. 3.7.1, the CDMS collaboration has achieved a (so far the best) sensitivity of $\sim 10^{-7} \text{ pb}$ for spin-independent WIMP-nucleon cross section and of $\sim 10^{-1} \text{ pb}$ for spin-dependent WIMP-neutron cross section. Together with the other collaborations described above, direct WIMP detection experiments have started to probe some possible regions in the parameter space predicted by some supersymmetric models. For next-generation detectors, sensitivities will be upgraded down to $\sim 10^{-8} \text{ pb}$ (see Fig. 3.5)

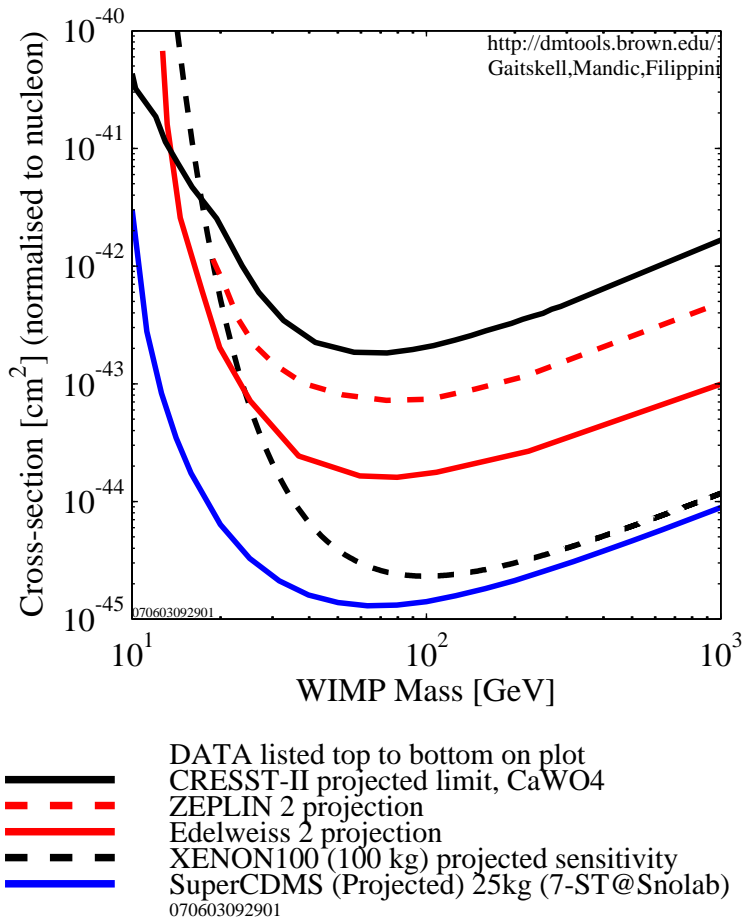


Figure 3.5: The curves show the sensitivities of the spin-independent WIMP-nucleon cross section versus WIMP mass projected by the SuperCDMS (25 kg), the CRESST-II (with CaWO_4), the EDELWEISS-II, the XENON100 (100 kg), and the ZEPLIN-II experiments. The indications of the lines as in Fig. 3.4 (plot generated by <http://dmttools.berkeley.edu/limitplots/>).

and, in long term, even $\sim 10^{-10}$ pb, and the corresponding WIMP-nucleus scattering event rate is then ~ 5 events/ton/yr for Ge [37], as needed to probe large regions of MSSM parameter space. The total mass of detector material will also be improved to the ton scale. For example, the ~ 100 kg Xe detector of the XENON and XMASS collaborations. The CDMS collaboration is also preparing for their SuperCDMS projects with maximum 1100 kg target mass, while the CRESST and the EDELWEISS collaborations will also build to a larger collaboration “EURECA” (European Underground Rare Event search with Calorimeter Array).

A nearly perfect background discrimination capability for next-generation detectors is also necessary. The ultimate neutron background will only be identified by the multiple interactions in a finely segmented or multiple interaction sensitive detector, and/or by operating detectors containing different target materials within the same setup [37].

Furthermore, the measurement of the recoil directions of the target nuclei would provide additional information on the distribution of WIMPs in our Galaxy [62]. As described in Subsec. 3.9.1, the most convincing way for determining the recoil direction is by drifting negative ions in a temporal projection chamber to accurately record the tiny recoil distance. The DRIFT experiment has provided a proof of the principle, but it remains to be seen if such gas detectors with enough target material can detect some signals [62].

By the way, in order to present the WIMP-nucleon cross sections and the detector sensitivities in the future more conveniently and also suitably, we may consider to use “zepto” (10^{-21}) or even “yocto” (10^{-24}) [94] barn instead of 10^{-9} pb (10^{-45} cm²) or 10^{-12} pb (10^{-48} cm²).

Chapter 4

Reconstruction of the Velocity Distribution of WIMPs

So far most theoretical analyses of direct detection of halo WIMPs, as discussed in Subsecs. 3.1.3 and 3.2.1, have predicted the detection rate for a given (class of) WIMPs, based on a specific model of the galactic halo (e.g., [24], [26], and [95]). The goal of my work is to invert this process. That is, I wish to study, as *model-independently* as possible, *what future direct detection experiments can teach us about the WIMP halo*.

In this chapter I will use a *time-averaged recoil spectrum*, and assume that *no directional information exists*. One can thus only reconstruct the (time-averaged) *one-dimensional velocity distribution*, $f_1(v)$. In the first section I will show how to derive the velocity distribution of WIMPs from the functional form of the recoil spectrum; the assumption here is that this functional form has been determined by fitting the data of some (future) experiment(s). I will also derive formulae for moments of the velocity distribution function, such as the mean velocity and the velocity dispersion of WIMPs, which can be compared with model predictions.

Then I will present the method for reconstructing the velocity distribution of WIMPs *directly from recorded signal events*. This allows statistically meaningful tests of predicted distribution functions. I will also discuss how to estimate the moments of the velocity distribution directly from these data.

Finally, I will show how to determine the mass of halo WIMPs, which one needs for the reconstruction of (the moments of) the velocity distribution, from experimental data directly. This allows also a useful comparison of the detected WIMPs with the new particle(s) produced at colliders, e.g., the Large Hadron Collider (LHC).

4.1 From the scattering spectrum

In this section I will start with the differential rate for elastic WIMP-nuclues scattering given in Eq.(3.12)

$$\frac{dR}{dQ} = \mathcal{A}F^2(Q) \int_{v_{\min}}^{\infty} \left[\frac{f_1(v)}{v} \right] dv, \quad (3.12)$$

and show how to find an expression for the one-dimensional velocity distribution function $f_1(v)$ for given (as yet only hypothetical) measured recoil spectrum dR/dQ . To that end, I first define

$$\frac{dF_1(v)}{dv} = \frac{f_1(v)}{v}, \quad (4.1)$$

i.e., $F_1(v)$ is the primitive of $f_1(v)/v$. Then Eq.(3.12) can be rewritten as

$$\frac{1}{\mathcal{A}F^2(Q)} \left(\frac{dR}{dQ} \right) = \int_{v_{\min}}^{\infty} \left[\frac{f_1(v)}{v} \right] dv = F_1(v \rightarrow \infty) - F_1(v_{\min}). \quad (4.2)$$

Since WIMPs (as candidate for CDM) in today's Universe move quite slowly, $f_1(v)$ must vanish as v approaches infinity,

$$f_1(v \rightarrow \infty) \rightarrow 0. \quad (4.3)$$

Hence

$$\left. \frac{dF_1(v)}{dv} \right|_{v \rightarrow \infty} = \left. \frac{f_1(v)}{v} \right|_{v \rightarrow \infty} \rightarrow 0. \quad (4.4)$$

This means that $F_1(v \rightarrow \infty)$ approaches a finite value.¹ Differentiating both sides of Eq.(4.2) with respect to v_{\min} and using Eq.(3.10), one can find that (detailed derivations will be given in App. A.2)

$$\begin{aligned} \frac{dF_1(v_{\min})}{dv_{\min}} &= -\frac{1}{\mathcal{A}} \left\{ \frac{d}{dv_{\min}} \left[\frac{1}{F^2(Q)} \left(\frac{dR}{dQ} \right) \right]_{Q=v_{\min}^2/\alpha^2} \right\} \\ &= \frac{1}{v_{\min}} \cdot \frac{1}{\mathcal{A}} \left\{ -2Q \cdot \frac{d}{dQ} \left[\frac{1}{F^2(Q)} \left(\frac{dR}{dQ} \right) \right] \right\}_{Q=v_{\min}^2/\alpha^2}. \end{aligned} \quad (4.5)$$

Since this expression holds for arbitrary v_{\min} , one can write down the following result directly:

$$\frac{f_1(v)}{v} = \frac{dF_1(v)}{dv} = \frac{1}{v} \cdot \frac{1}{\mathcal{A}} \left\{ -2Q \cdot \frac{d}{dQ} \left[\frac{1}{F^2(Q)} \left(\frac{dR}{dQ} \right) \right] \right\}_{Q=v^2/\alpha^2}. \quad (4.6)$$

The right-hand side of Eq.(4.6) depends on the as yet unknown constant \mathcal{A} . Recall, however, that $f_1(v)$ is the *normalized* velocity distribution, i.e., it is defined to satisfy

$$\int_0^{\infty} f_1(v) dv = 1. \quad (4.7)$$

¹The other properties of $F_1(v)$ will be discussed in App. A.1.

Therefore, the normalized one-dimensional velocity distribution function can be expressed as

$$f_1(v) = \mathcal{N} \left\{ -2Q \cdot \frac{d}{dQ} \left[\frac{1}{F^2(Q)} \left(\frac{dR}{dQ} \right) \right] \right\}_{Q=v^2/\alpha^2}, \quad (4.8)$$

with the normalization constant \mathcal{N} (a detailed derivation will be given in App. A.3)

$$\mathcal{N} = \frac{2}{\alpha} \left\{ \int_0^\infty \frac{1}{\sqrt{Q}} \left[\frac{1}{F^2(Q)} \left(\frac{dR}{dQ} \right) \right] dQ \right\}^{-1}. \quad (4.9)$$

Note that the integral here starts at $Q = 0$.

In the next step I want to compute the moments of the velocity distribution function:

$$\langle v^n \rangle = \int_{v_{\min}(Q_{\text{thre}})}^\infty v^n f_1(v) dv. \quad (4.10)$$

Here I have introduced a threshold energy Q_{thre} . This is needed experimentally, since at very low recoil energies, the signal is swamped by electronic noise. Moreover, later we will meet expressions that (formally) diverge as $Q \rightarrow 0$. $v_{\min}(Q_{\text{thre}})$ is calculated as in Eq.(3.10). Inserting Eq.(4.8) into Eq.(4.10) and integrating by parts, one can find that (a detailed derivation will be given in App. A.3)

$$\langle v^n \rangle = \mathcal{N} \left(\frac{\alpha^{n+1}}{2} \right) \left[\frac{2Q_{\text{thre}}^{(n+1)/2}}{F^2(Q_{\text{thre}})} \left(\frac{dR}{dQ} \right)_{Q=Q_{\text{thre}}} + (n+1)I_n(Q_{\text{thre}}) \right], \quad (4.11)$$

with

$$I_n(Q_{\text{thre}}) = \int_{Q_{\text{thre}}}^\infty Q^{(n-1)/2} \left[\frac{1}{F^2(Q)} \left(\frac{dR}{dQ} \right) \right] dQ. \quad (4.12)$$

Physically, $\langle v \rangle$ is the average WIMP velocity, while $\langle v^2 \rangle$ gives the velocity dispersion.² One emphasis here is that *Eqs.(4.11) and (4.12) can be evaluated directly once the recoil spectrum is known; knowledge of the functional form of $f_1(v)$ in Eq.(4.8) is not required.* Note that the first term in Eq.(4.11) vanishes for $n \geq 0$ if $Q_{\text{thre}} \rightarrow 0$. In the same limit, $\langle v^0 \rangle \rightarrow \mathcal{N} \alpha I_0(0)/2 \rightarrow 1$ by virtue of Eq.(4.9). On the other hand, as written in Eqs.(4.8) and (4.9), the velocity distribution integrated over the experimentally accessible range of WIMP velocities gives a value smaller than unity. Using only quantities that can be measured in the presence of a non-vanishing energy threshold Q_{thre} , Eq.(4.9) can be replaced by

$$\mathcal{N}(Q_{\text{thre}}) = \frac{2}{\alpha} \left[\frac{2Q_{\text{thre}}^{1/2}}{F^2(Q_{\text{thre}})} \left(\frac{dR}{dQ} \right)_{Q=Q_{\text{thre}}} + I_0(Q_{\text{thre}}) \right]^{-1}. \quad (4.13)$$

Using $\mathcal{N}(Q_{\text{thre}})$ in Eq.(4.8) ensures that the velocity distribution integrated over $v \geq v_{\min}(Q_{\text{thre}})$ gives unity.

²The dispersion of the function $f_1(v)$ in the statistical sense is given by $\langle v^2 \rangle - \langle v \rangle^2$.

From Eqs.(4.8), (4.9), and (4.11) to (4.13), it can be found that the (unrealistic) “reduced” spectrum (i.e., the recoil spectrum divided by the squared nuclear form factor) is more useful than the recoil spectrum itself. Meanwhile, note that the reduced spectrum from $(dR/dQ)_{\text{Gau}}$ in Eq.(3.21):

$$\frac{1}{F^2(Q)} \left(\frac{dR}{dQ} \right)_{\text{Gau}} \propto e^{-\alpha^2 Q/v_0^2} \quad (3.21')$$

is exactly exponential. This remains approximately true for the potentially quasi-realistic spectrum in Eq.(3.31) as well:

$$\frac{1}{F^2(Q)} \left(\frac{dR}{dQ} \right)_{\text{sh}} \propto \text{erf}\left(\frac{\alpha\sqrt{Q}+v_e}{v_0}\right) - \text{erf}\left(\frac{\alpha\sqrt{Q}-v_e}{v_0}\right). \quad (3.31')$$

In order to test these formulae, I have substituted the spectra in Eqs.(3.21') and (3.31') into Eqs.(4.8) and (4.11), taking $Q_{\text{thre}} = 0$. They reproduced the normalized velocity distribution functions in Eqs.(3.20) and (3.29), as well as the results in Eqs.(3.22), (3.23), (3.32), and (3.33). The detailed calculations will be given in Apps. B.2.1 and B.2.2, respectively.

One emphasis here is that *the final results in Eqs.(4.8) and (4.11) are independent of the as yet unknown quantity \mathcal{A} defined in Eq.(3.13)*. They do, however, depend on the WIMP mass m_χ through the coefficient α defined in Eq.(3.11). This mass can be extracted from a *single* recoil spectrum *only if* one makes some assumptions about the velocity distribution $f_1(v)$. In the kind of model-independent analysis pursued here, m_χ can be determined by requiring that the recoil spectra *using two different target nuclei* lead to the same moments of the velocity distribution, $\langle v^n \rangle$, through Eq.(4.11). This method will be discussed in Sec. 4.3. Note that this can be done *independent of the detailed particle physics model*, which determine the value of σ_0 for two target nuclei. But, one will need to know both form factors of the target nuclei, which strongly depend on whether spin-dependent or spin-independent interactions dominate (see Subsecs. 3.4.1 to 3.4.3). On the other hand, within a given particle physics model, the best determination of m_χ should eventually come from experiments at high-energy colliders. However, we need also an alternative method as cross-check to prove whether the particle produced at colliders is the same particle detected by the direct WIMP detection.

4.2 From experimental data directly

In the previous section I have derived formulae for the normalized one-dimensional velocity distribution function of WIMPs, $f_1(v)$, and for its moments $\langle v^n \rangle$, from the recoil-energy spectrum, dR/dQ . In order to use these expressions, one would need a functional form for dR/dQ . In practice this might result from a fit to experimental data. Note that the expression for $f_1(v)$ in Eq.(4.8) requires knowledge not only of dR/dQ , but also of

its derivative with respect to Q , i.e., we need to know both the spectrum and its slope. This will complicate the error analysis considerably, if dR/dQ is the result of a fit.

In this section I therefore go one step further, and derive expressions that allow to reconstruct $f_1(v)$ and its moments *directly from the data*. The assumption we have to make is that the sample to be analyzed only contains signal events, i.e., is free of background. This should be possible for the modern (next-generation) detectors (detailed discussions about the background and its discrimination have been given in Sec. 3.6). Having a sample of pure signal events, we can proceed with a complete statistical analysis of the precision with which we can reconstruct $f_1(v)$ and its moments.

However, in the absence of a true experimental sample of this kind, I had to resort to Monte Carlo experiments with an unweighted event generator written by M. Drees. Since detectors without directional sensitivity have been assumed, a single event is uniquely characterized by the measured recoil energy Q . Existing experiments such as CDMS [59] and CRESST [56] can determine the recoil energy quite accurately (some details about their detectors and experiments have been given in Subsecs. 3.7.1 and 3.7.2). We will see later that the statistical errors on the reconstructed velocity distribution $f_1(v)$ will be quite sizable even for next-generation experiments, given existing bounds on the scattering rate. It should therefore be a good approximation to ignore the error of Q in the analyses.

In the following I do not distinguish between the recoil spectrum dR/dQ and the actual differential counting rate dN/dQ . Since dR/dQ is usually given per unit detector mass and unit time, the two quantities differ only by a multiplicative constant. This constant can be canceled in Eq.(4.8), since it will also appear in the normalization constant \mathcal{N} in Eq.(4.9).

4.2.1 Exponential ansatz for dR/dQ

I divide the total energy range into B bins with central points Q_n and widths b_n , $n = 1, 2, \dots, B$. In each bin, N_n signal events will be recorded. The simulated data set can therefore be described by

$$Q_n - \frac{b_n}{2} \leq Q_{n,i} \leq Q_n + \frac{b_n}{2}, \quad i = 1, 2, \dots, N_n, \quad n = 1, 2, \dots, B. \quad (4.14)$$

The standard estimate for dR/dQ at $Q = Q_n$ is then

$$r_n = \frac{N_n}{b_n}, \quad n = 1, 2, \dots, B. \quad (4.15)$$

The squared statistical error on dR/dQ is accordingly

$$\sigma^2(r_n) = \frac{N_n}{b_n^2}, \quad (4.16)$$

since

$$\sigma^2(N_n) = N_n. \quad (4.17)$$

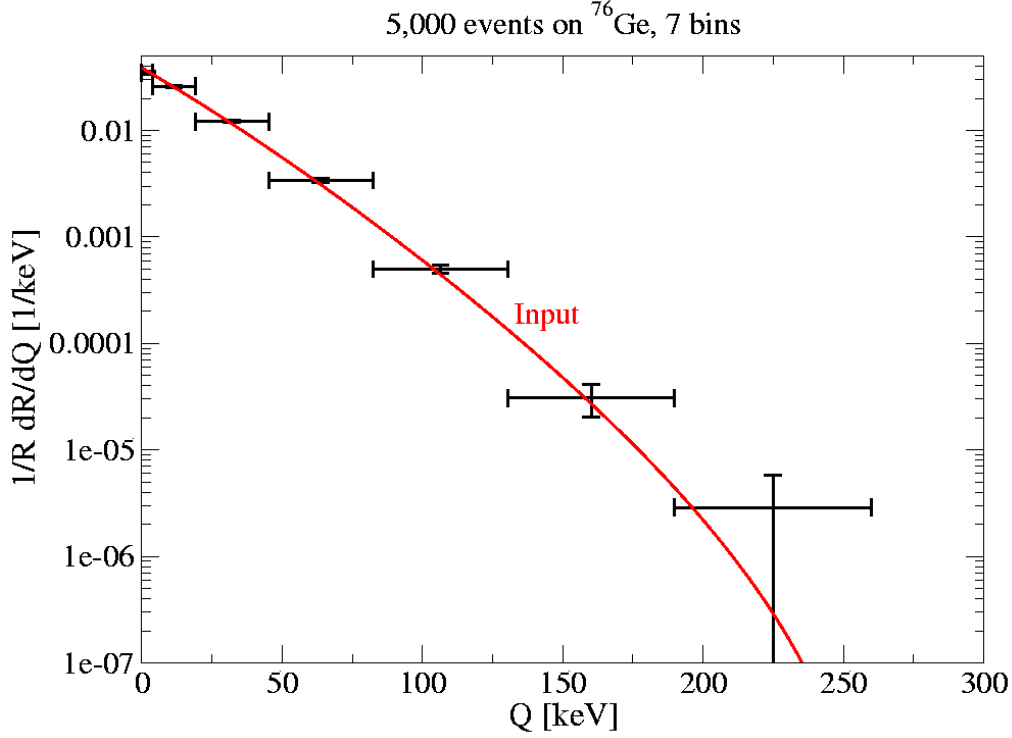


Figure 4.1: The curve shows the theoretical predicted recoil energy spectrum for the shifted Maxwellian velocity distribution $f_{1,\text{sh}}(v, v_e)$ in Eq.(3.29) with the Woods-Saxon form factor $F_{\text{WS}}^2(Q)$ in Eq.(3.17). The data points with error bars show simulated experimental data produced from this spectrum (5,000 total events, $m_\chi = 100 \text{ GeV}/c^2$, $m_N = 70.6 \text{ GeV}/c^2$ for ^{76}Ge , $v_0 = 220 \text{ km/s}$, $v_e = 231 \text{ km/s}$, and the Galactic escape velocity $v_{\text{esc}} = 700 \text{ km/s}$ as the cut-off velocity of the velocity distribution in Eq.(3.12)). The vertical error bars show the statistical uncertainties of the measurements, while the horizontal error bars indicate the bin widths.

As mentioned at the end of the previous section, the predicted recoil spectrum resembles a falling exponential (see Eqs.(3.21') and (3.31') in Sec. 4.1). This is confirmed in Fig. 4.1, which shows the predicted recoil spectrum of a $100 \text{ GeV}/c^2$ WIMP on ^{76}Ge by means of the shifted Maxwellian velocity distribution $f_{1,\text{sh}}(v, v_e)$ in Eq.(3.29) and the Woods-Saxon form factor $F_{\text{WS}}^2(Q)$ in Eq.(3.17). This figure also shows the result of a simulated experiment, where the exposure time and cross section are chosen such that the expected number of events is 5,000; these have been collected in seven bins in recoil energy. Note that, in practice the velocity distribution in Eq.(3.12) should be cut off at a velocity v_{esc} , since WIMPs with $v > v_{\text{esc}}$ can escape the gravitational well of our Galaxy. The cut-off velocity has been taken to be $v_{\text{esc}} = 700 \text{ km/s}$.

While an approximately exponential function can be approximated by a linear ansatz only over a narrow range, i.e., for small bin widths, the *logarithm* of this function can be approximated by a linear ansatz for much wider bins (some detailed discussions about

linear approximations can be found in App. D.4). This corresponds to the ansatz

$$\left(\frac{dR}{dQ}\right)_n \equiv \left(\frac{dR}{dQ}\right)_{Q \approx Q_n} \simeq \tilde{r}_n e^{k_n(Q-Q_n)} \equiv r_n e^{k_n(Q-Q_{s,n})}. \quad (4.18)$$

Here r_n is the standard estimator for dR/dQ at $Q = Q_n$ given in Eq.(4.15), \tilde{r}_n is the real value of the recoil spectrum at the point $Q = Q_n$,

$$\tilde{r}_n \equiv \left(\frac{dR}{dQ}\right)_{Q=Q_n}, \quad (4.19)$$

and k_n is the *logarithmic slope* of the recoil spectrum in the n -th Q -bin.

Now our task is to find estimators for \tilde{r}_n and k_n in Eq.(4.18) using (simulated) data. Note that, for $k_n \neq 0$, $\tilde{r}_n \neq r_n = N_n/b_n$ and cannot be estimated from the number of events N_n in the n -th bin alone. Instead, from the first part of Eq.(4.18), one has

$$N_n = \int_{Q_n-b_n/2}^{Q_n+b_n/2} \left(\frac{dR}{dQ}\right)_n dQ = \int_{Q_n-b_n/2}^{Q_n+b_n/2} \tilde{r}_n e^{k_n(Q-Q_n)} dQ = b_n \tilde{r}_n \left(\frac{\sinh \kappa_n}{\kappa_n}\right), \quad (4.20)$$

where, for simplicity, I have introduced the dimensionless quantities

$$\kappa_n \equiv \frac{b_n k_n}{2}. \quad (4.21)$$

Hence, it can be found that

$$\tilde{r}_n = \frac{N_n}{b_n} \left(\frac{\kappa_n}{\sinh \kappa_n}\right) \quad (4.22)$$

depends on k_n . Moreover, using the first and second moments of the recoil spectrum in the n -th bin, one can find that

$$\overline{Q - Q_n}|_n = \frac{1}{N_n} \int_{Q_n-b_n/2}^{Q_n+b_n/2} (Q - Q_n) \left(\frac{dR}{dQ}\right)_n dQ = \frac{b_n}{2} \left(\coth \kappa_n - \frac{1}{\kappa_n}\right), \quad (4.23)$$

and

$$\begin{aligned} \overline{(Q - Q_n)^2}|_n &= \frac{1}{N_n} \int_{Q_n-b_n/2}^{Q_n+b_n/2} (Q - Q_n)^2 \left(\frac{dR}{dQ}\right)_n dQ \\ &= \left(\frac{b_n}{2}\right)^2 \left[1 - 2 \left(\frac{\coth \kappa_n}{\kappa_n}\right) + \frac{2}{\kappa_n^2}\right], \end{aligned} \quad (4.24)$$

where $\overline{\dots}|_n$ denotes the average value in the n -th bin. κ_n , or, equivalently, k_n can not be solved analytically by only using Eq.(4.23). They can, however, be found numerically once

$$\overline{Q - Q_n}|_n = \frac{1}{N_n} \sum_{i=1}^{N_n} (Q_{n,i} - Q_n) \quad (4.25)$$

is known. Alternatively, multiplying both sides of Eq.(4.23) with b_n/κ_n and adding to Eq.(4.23), one can calculate the logarithmic slopes as

$$k_n = \frac{8 \overline{Q - Q_n}|_n}{b_n^2 - 4 \overline{(Q - Q_n)^2}|_n}, \quad (4.26)$$

where

$$\overline{(Q - Q_n)^2}|_n = \frac{1}{N_n} \sum_{i=1}^{N_n} (Q_{n,i} - Q_n)^2 \quad (4.27)$$

is now estimated from the data directly. Note that k_n determined either from Eq.(4.23) or from Eq.(4.26) is independent of the normalization r_n or \tilde{r}_n .

On the other hand, the second, equivalent expression in Eq.(4.18) means that we can still use the quantities $r_n = N_n/b_n$ as normalization. However, the logarithmic slopes, k_n , solved by either Eq.(4.23) or Eq.(4.26) describes the spectrum dR/dQ at the *shifted points* $Q_{s,n}$. Equivalence of the two expressions in Eq.(4.18) implies

$$Q_{s,n} = Q_n + \frac{1}{k_n} \ln \left(\frac{\sinh \kappa_n}{\kappa_n} \right). \quad (4.28)$$

Note that, while Q_n is simply the midpoint of the n -th Q -bin and can thus be chosen at will, $Q_{s,n}$ here is a derived quantity and depends on the logarithmic slope k_n . However, the second expression in Eq.(4.18) combined with $Q_{s,n}$ in Eq.(4.28) has two advantages. First, the prefactor r_n can be computed more easily than \tilde{r}_n in Eq.(4.22). Second, according to a detailed analysis [96], it has been found that, for a given bin width, one can minimize the leading systematic error by interpreting the estimator of k_n as logarithmic slope of the recoil spectrum, not at the center of the bin Q_n , but at the shifted point $Q_{s,n}$. Note that $Q_{s,n}$ itself depends on k_n . However, this *does not* introduce any additional error, if we simply interpret Eq.(4.28) as an - admittedly somewhat complicated - prescription for the determination of the Q -values where we wish to estimate the logarithmic slope of the recoil spectrum.

In the rest of this section I use only $\overline{Q - Q_n}|_n$ from Eq.(4.23) to estimate the logarithmic slope k_n , since it simplifies the error analysis somewhat. Note that, for using both $\overline{Q - Q_n}|_n$ and $\overline{(Q - Q_n)^2}|_n$ from Eq.(4.26) to estimate k_n , the statistical errors of them are correlated.³ Using standard error propagation, we have

$$\sigma^2(k_n) = \left[\frac{dk_n}{d\overline{Q - Q_n}|_n} \right]^2 \sigma^2(\overline{Q - Q_n}|_n). \quad (4.29)$$

The first factor above can be calculated straightforwardly from Eq.(4.23) as

$$\frac{d\overline{Q - Q_n}|_n}{dk_n} = \frac{1}{k_n^2} \left[1 - \left(\frac{\kappa_n}{\sinh \kappa_n} \right)^2 \right] = \frac{g(\kappa_n)}{k_n^2}, \quad (4.30)$$

where I have defined the auxiliary function

$$g(x) \equiv 1 - \left(\frac{x}{\sinh x} \right)^2. \quad (4.31)$$

The error on the average energy transfer $\sigma^2(\overline{Q - Q_n}|_n)$ in Eq.(4.29) can be estimated directly from the data, using

$$\sigma^2(\overline{Q - Q_n}|_n) = \frac{1}{N_n - 1} \left[\overline{(Q - Q_n)^2}|_n - \overline{Q - Q_n}|_n^2 \right]. \quad (4.32)$$

³In contrast, I will use Eq.(4.26) in Subsec. 5.2.2 due to some other reasons.

4.2.2 Windowing the data set

From two naive linear approximations discussed in App. D.4, one can find an important observation that the statistical error of both estimators of the slope of the recoil spectrum given in Eqs.(D.34) and (D.38) scale like the bin width to the power -1.5 (see Eqs.(D.39) and (D.40)). This can intuitively be understood from the argument that the variation of dR/dQ will be larger for larger bins (see Fig. 4.1). Moreover, a detailed analysis for the relation between the statistical error of k_n given in Eq.(4.29) and the bin width b_n [96] shows that, for small bins, the expected error again scales like $b_n^{-1.5}$ and if the bin width is large, the statistical error decreases even faster with increasing bin width. One would therefore naively conclude that the errors of the estimated slopes would be minimized by choosing very large bins.

However, as mentioned above and discussed in Ref. [96], neither a linear approximation of the recoil spectrum nor the linear ansatz of the logarithm of the spectrum can describe the real (but as yet unknown) recoil spectrum exactly. The neglected terms of higher powers of $Q - Q_n$ will certainly induce some uncontrolled systematic errors which increase quickly with increasing bin width b_n .

Using large bins has a second, obvious disadvantage: the number of bins scales inversely with their size, i.e., by using large bins we would be able to estimate $f_1(v)$ only at a small number of velocities. Fortunately, this can be alleviated by using overlapping bins, or, equivalently, *by combining several relatively small bins into overlapping “windows”*. This means that a given data point $Q_{n,i}$ may well contribute to several different windows, and hence to the estimate of $f_1(v)$ at several values of v . This can increase the total amount of information about $f_1(v)$ since the only information we use about the data points in a given window is encoded in the average recoil energy in this window (through the estimating of k_n by Eq.(4.23)). This averaging effectively destroys information. By letting a given data point contribute to several overlapping windows, this loss of information can be reduced.

One other obvious disadvantage of using large bins or windows is that it would lead to a quite large minimal value of v where $f_1(v)$ can be reconstructed, simply because the central value Q_1 , and also the shifted point $Q_{s,1}$, of a large first bin would be quite large. This can be again be alleviated by first collecting our data in relatively small bins, and then combining varying numbers of bins into overlapping windows. In particular, the first window would be identical with the first bin.

A final consideration concerns the size of the bins. Choosing fixed bin sizes, and therefore also mostly fixed window sizes, would lead to errors on the estimated logarithmic slopes, and hence also on the estimates of $f_1(v)$, which increase quickly with increasing Q or v . This is due to the essentially exponential form of the recoil spectrum, which would lead to a quickly falling number of events in equal-sized bins. A try-error analysis shows that the errors are roughly equal in all bins if the bin widths increase linearly (some different variations of binning of the data set will be given in App. D.1).

These considerations motivate the following set-up for the mock experimental analysis. One starts by binning the data, as in Eq.(4.14), where the bin widths satisfy

$$b_n = b_1 + (n - 1)\delta, \quad (4.33)$$

i.e.,

$$Q_n = Q_{\min} + \left(n - \frac{1}{2}\right) b_1 + \left[\frac{(n - 1)^2}{2}\right] \delta. \quad (4.34)$$

Here the increment δ satisfies

$$\delta = \frac{2}{B(B - 1)} (Q_{\max} - Q_{\min} - Bb_1), \quad (4.35)$$

B being the total number of bins, and $Q_{\max, \min}$ being the (kinematical or instrumental) extrema of the recoil energy. Then I collect up to n_W bins into a window, with smaller windows at the borders of the range of Q . In the rest of this section and the next chapter I use Latin indices n, m, \dots to label bins, and Greek indices μ, ν, \dots to label windows. For $1 \leq \mu \leq n_W$, the μ -th window simply consists of the first μ bins; for $n_W \leq \mu \leq B$, the μ -th window consists of bins $\mu - n_W + 1, \mu - n_W + 2, \dots, \mu$; and for $B \leq \mu \leq B + n_W - 1$, the μ -th window consists of the last $n_W - \mu + B$ bins. This can also be described by introducing the indices $n_{\mu-}$ and $n_{\mu+}$ which label the first and last bin contributing to the μ -th window, with

$$n_{\mu-} = \begin{cases} 1, & \mu \leq n_W \\ \mu - n_W + 1, & \mu \geq n_W \end{cases}, \quad (4.36a)$$

and

$$n_{\mu+} = \begin{cases} \mu, & \mu \leq B \\ B, & \mu \geq B \end{cases}. \quad (4.36b)$$

The total number of windows defined through Eqs.(4.36a) and (4.36b) is evidently $W = B + n_W - 1$, i.e., $1 \leq \mu \leq B + n_W - 1$.

As shown in the previous subsection, the basic observables needed for the reconstruction of $f_1(v)$ in Eq.(4.8) are the number of events in the n -th bin, N_n , as well as the averages $\overline{Q - Q_n|_n}$ in Eq.(4.25). Once N_n and $\overline{Q - Q_n|_n}$ can be obtained, we can then use Eqs.(4.15), (4.23) and (4.28) to get r_n, k_n and $Q_{s,n}$ as well as Eq.(4.29) to get the statistical error of k_n . One can easily calculate the number of events per window as

$$N_\mu = \sum_{n=n_{\mu-}}^{n_{\mu+}} N_n, \quad (4.37)$$

as well as the averages

$$\overline{Q - Q_\mu|_\mu} = \frac{1}{N_\mu} \left(\sum_{n=n_{\mu-}}^{n_{\mu+}} N_n \overline{Q|_n} \right) - Q_\mu, \quad (4.38)$$

where Q_μ is the central point of the μ -th window.

One drawback of the use of overlapping windows in the analysis is that the observables defined in Eqs.(4.37) and (4.38) are all correlated (for $n_W \neq 1$). The slope in the μ -th window, k_μ , will again be calculated as in Eq.(4.23) with “bin” quantities replaced by “window” quantities. We thus need the covariance matrix for the $\overline{Q - Q_\mu}|_\mu$, which follows directly from the definition in Eq.(4.38) (detailed deviations for the covariances in this subsection will be given in App. E.1.1):

$$\begin{aligned} & \text{cov} \left(\overline{Q - Q_\mu}|_\mu, \overline{Q - Q_\nu}|_\nu \right) \\ &= \frac{1}{N_\mu N_\nu} \sum_{n=n_{\nu-}}^{n_{\mu+}} \left[N_n \left(\overline{Q}|_n - \overline{Q}|_\mu \right) \left(\overline{Q}|_n - \overline{Q}|_\nu \right) + N_n^2 \sigma^2 \left(\overline{Q - Q_n}|_n \right) \right], \end{aligned} \quad (4.39)$$

where $\sigma^2 \left(\overline{Q - Q_n}|_n \right)$ is defined as in Eq.(4.32). In Eq.(4.39) I have assumed $\mu \leq \nu$; the covariance matrix is, of course, symmetric. Moreover, the sum is understood to vanish if the two windows μ, ν do not overlap, i.e., if $n_{\mu+} < n_{\nu-}$.

The ansatz in Eq.(4.18) is now assumed to hold over an entire window. We again can estimate the prefactor as

$$r_\mu = \frac{N_\mu}{w_\mu}, \quad (4.40)$$

w_μ being the width of the μ -th window. This implies

$$\text{cov}(r_\mu, r_\nu) = \frac{1}{w_\mu w_\nu} \sum_{n=n_{\nu-}}^{n_{\mu+}} N_n, \quad (4.41)$$

where I have again taken $\mu \leq \nu$. Finally, the mixed covariance matrix is given by

$$\text{cov} \left(r_\mu, \overline{Q - Q_\nu}|_\nu \right) = \frac{1}{w_\mu N_\nu} \sum_{n=n_-}^{n_+} N_n \left(\overline{Q}|_n - \overline{Q}|_\nu \right). \quad (4.42)$$

Note that this sub-matrix is not symmetric under the exchange of μ and ν . In the definition of n_- and n_+ we therefore have to distinguish two cases:

$$\begin{aligned} & \text{If } \mu \leq \nu : n_- = n_{\nu-}, n_+ = n_{\mu+}; \\ & \text{If } \mu \geq \nu : n_- = n_{\mu-}, n_+ = n_{\nu+}. \end{aligned} \quad (4.43)$$

As before, the sum in Eq.(4.42) is understood to vanish if $n_- > n_+$.

The covariance matrices involving the estimators of the logarithmic slopes k_μ , derived from Eq.(4.23) with $n \rightarrow \mu$ everywhere, can be calculated in terms of the covariance matrices in Eqs.(4.39) and (4.42):

$$\text{cov} (k_\mu, k_\nu) = \left[\frac{k_\mu^2 k_\nu^2}{g(\kappa_\mu) g(\kappa_\nu)} \right] \text{cov} \left(\overline{Q - Q_\mu}|_\mu, \overline{Q - Q_\nu}|_\nu \right), \quad (4.44)$$

and

$$\text{cov} (r_\mu, k_\nu) = \left[\frac{k_\nu^2}{g(\kappa_\nu)} \right] \text{cov} \left(r_\mu, \overline{Q - Q_\nu}|_\nu \right), \quad (4.45)$$

where κ_μ is as in Eq.(4.21) with $n \rightarrow \mu$, and the function $g(x)$ has been defined in Eq.(4.31).

4.2.3 Reconstructing the velocity distribution

Now we are ready to put all pieces together to reconstruct the velocity distribution and compute its statistical error. Substituting the ansatz in Eq.(4.18) (with the replacement $n \rightarrow \mu$) into Eq.(4.8), the reconstructed normalized one-dimensional velocity distribution function can be expressed as

$$f_{1,r}(v_{s,\mu}) = \mathcal{N} \left[\frac{2Q_{s,\mu}r_\mu}{F^2(Q_{s,\mu})} \right] \left[\frac{d}{dQ} \ln F^2(Q) \Big|_{Q=Q_{s,\mu}} - k_\mu \right], \quad (4.46)$$

for $\mu = 1, 2, \dots, B + n_W - 1$. Here $Q_{s,\mu}$ is given by Eq.(4.28) with $n \rightarrow \mu$, and,

$$v_{s,\mu} = \alpha \sqrt{Q_{s,\mu}}, \quad (4.47)$$

as in Eq.(3.10). Finally, the normalization constant \mathcal{N} defined in Eq.(4.9) can be estimated directly from the data:

$$\mathcal{N} = \frac{2}{\alpha} \left[\sum_a \frac{1}{\sqrt{Q_a} F^2(Q_a)} \right]^{-1}, \quad (4.48)$$

where the sum runs over all events in the sample.

Since neighboring windows overlap, the estimates of $f_1(v)$ at adjacent values of v_μ are correlated. This is described by the covariance matrix

$$\begin{aligned} & \text{cov} \left(f_{1,r}(v_{s,\mu}), f_{1,r}(v_{s,\nu}) \right) \\ &= \left[\frac{f_{1,r}(v_{s,\mu}) f_{1,r}(v_{s,\nu})}{r_\mu r_\nu} \right] \text{cov} (r_\mu, r_\nu) + (2\mathcal{N})^2 \left[\frac{Q_{s,\mu} Q_{s,\nu} r_\mu r_\nu}{F^2(Q_{s,\mu}) F^2(Q_{s,\nu})} \right] \text{cov} (k_\mu, k_\nu) \\ & \quad - \mathcal{N} \left\{ \left[\frac{f_{1,r}(v_{s,\mu})}{r_\mu} \right] \left[\frac{2Q_{s,\nu} r_\nu}{F^2(Q_{s,\nu})} \right] \text{cov} (r_\mu, k_\nu) + (\mu \longleftrightarrow \nu) \right\}, \end{aligned} \quad (4.49)$$

where the covariance matrices involving the normalized counting rates r_μ and logarithmic slopes k_μ have been given in Eqs.(4.41), (4.44), and (4.45). In principle Eq.(4.49) should also include contributions involving the statistical error of the estimator for \mathcal{N} in Eq.(4.48). However, this error and its correlations with the errors of the r_μ and k_μ has been found to be negligible compared to the errors included in Eq.(4.49).

Figs. 4.2 are results for the reconstructed velocity distribution, for “typical” simulated experiments with 500 (top) and 5,000 (bottom) events. In the top frame $B = 5$ bins has been chosen, the first bin having a width $b_1 = 8$ keV, and up to three bins have been combined into a window. Since the last bin is in fact empty, this leaves us with $W = 6$ windows, i.e., we can determine $f_{1,r}$ for six discrete values of the WIMP velocity v ; recall that these “measurements” of $f_{1,r}$ are correlated, as indicated by the horizontal bars in the figure. In the lower frame $B = 10$ bins with $b_1 = 10$ keV have been chosen, and up to four bins have been combined into one window. The bins are thus significantly smaller than in the upper frame. As a result, the last two bins are now (almost) empty, leaving us with $W = 11$ windows. Figs. 4.2 indicate that one will need *at least a few hundred events* for a meaningful direct reconstruction of $f_1(v)$.

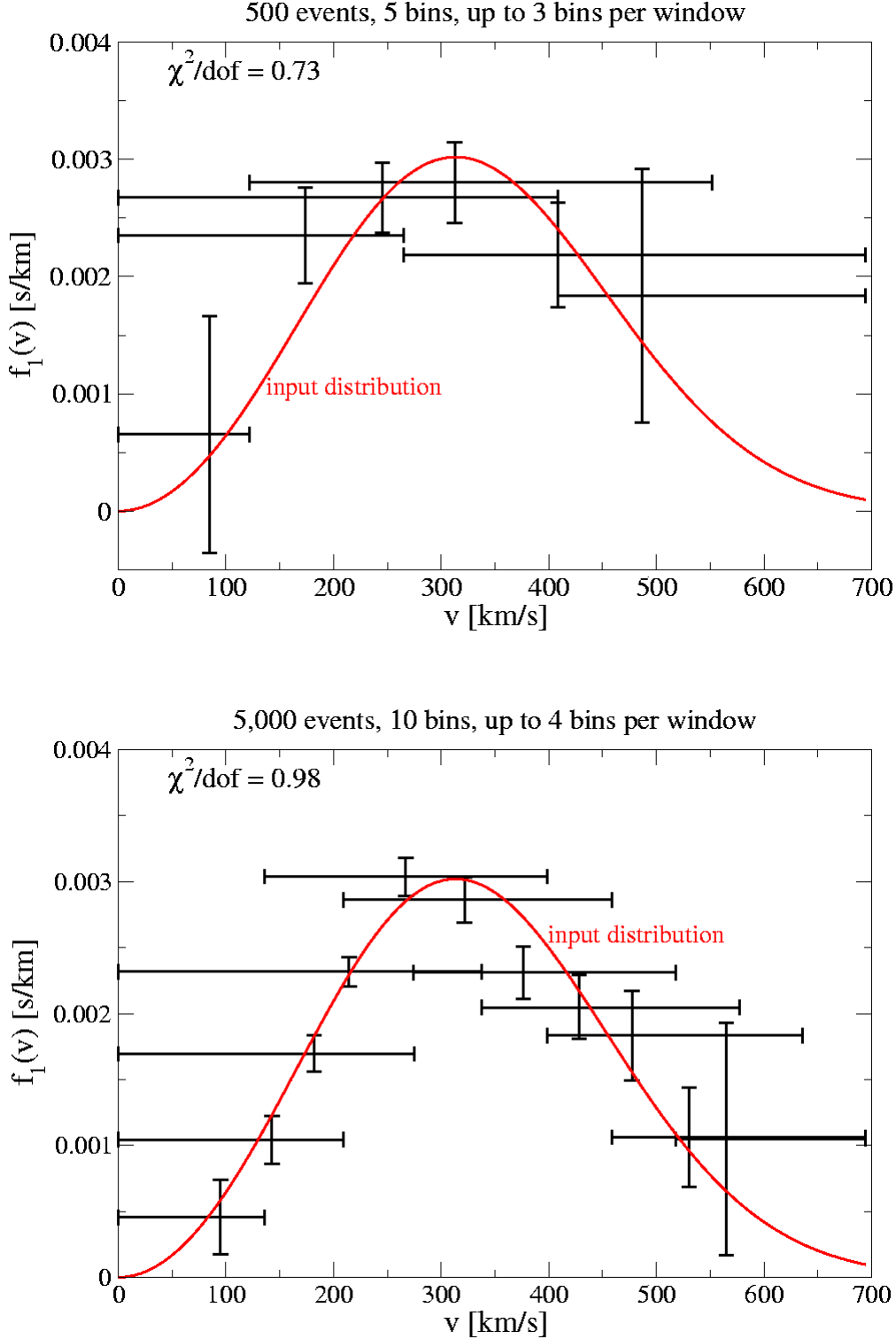


Figure 4.2: The WIMP velocity distribution reconstructed from a “typical” experiment with 500 (top) and 5,000 (bottom) events. The smooth curves show the input distributions, which are based on Eq.(3.29). The vertical error bars show the square roots of the diagonal entries of the covariance matrix given in Eq.(4.49); the horizontal bars show the size of the window used in deriving the given value of $f_{1,r}$. The overlap of these horizontal bars thus shows the range over which the values of $f_{1,r}$ are correlated. Parameters as in Fig. 4.1.

Furthermore, a χ_f^2 distributions has been defined by

$$\chi_f^2 \equiv \frac{1}{W} \sum_{\mu,\nu} \mathcal{C}_{\mu\nu} [f_{1,r}(v_{s,\mu}) - f_{1,\text{th}}(v_{s,\mu})] [f_{1,r}(v_{s,\nu}) - f_{1,\text{th}}(v_{s,\nu})]. \quad (4.50)$$

Here $f_{1,r}$ is the estimate in Eq.(4.46) of the velocity distribution, $f_{1,\text{th}}$ is a theoretical predicted velocity distribution (e.g., the input distributions in Figs. 4.2), and \mathcal{C} is the inverse of the covariance matrix of Eq.(4.49). This χ_f^2 distribution allows statistically meaningful tests of the predicted velocity distribution function.

More details about this χ_f^2 distribution and some applications can be found in Ref. [96].

4.2.4 Determining moments of the velocity distribution

As mentioned in the previous subsection, a direct reconstruction of the WIMP velocity distribution $f_1(v)$ will only be possible once several hundred nuclear recoil events have been collected. This is a tall order, given that not a single such event has so far been detected (barring the possible DAMA observation and a few candidate signals, see Secs. 3.7 to 3.9). The basic reason for the large required event sample is that, $f_1(v)$ being a normalized distribution, only information on the *shape* of $f_1(v)$ is meaningful. In order to obtain such shape information via direct reconstruction, we have to separate the events into several bins or windows. Moreover, each window should contain sufficiently many events to allow an estimate of the *slope* of the recoil spectrum in this window.

On the other hand, at the end of Sec. 4.1 I have also given expressions for the *moments* of $f_1(v)$ in Eqs.(4.11) to (4.13). With the exception of the moment with $n = -1$, these are entirely inclusive quantities, i.e., each moment is sensitive to the entire data set; no binning is required, nor do we need to determine any slope (with one possible minor exception; see below). It thus seems reasonable to expect that one can obtain meaningful information about these moments with fewer events.

The experimental implementation of Eq.(4.11) is quite straightforward. For $Q_{\text{thre}} = 0$, the normalization \mathcal{N} has already been given in Eq.(4.48). The case of non-vanishing threshold energy Q_{thre} can be treated straightforwardly, using Eq.(4.13). To that end one needs to estimate the recoil spectrum at the threshold energy. One possibility would be to choose an artificially high value of Q_{thre} , and simply count the events in a bin centered on Q_{thre} . However, in this case the events with $Q < Q_{\text{thre}}$ would be left out of the determination of the moments. We therefore should keep Q_{thre} as small as experimentally possible, and to estimate the counting rate at threshold using the ansatz in Eq.(4.18). Since we need the recoil spectrum only at this single point, we only have to determine the quantities r_1 and k_1 parameterizing dR/dQ in the first bin; this can be done as described in Subsec. 4.2.1, without the need to distinguish between bins and “windows”. Introduce the shorthand notation

$$r_{\text{thre}} \equiv \left(\frac{dR}{dQ} \right)_{Q=Q_{\text{thre}}} = r_1 e^{k_1(Q_{\text{thre}} - Q_{s,1})}. \quad (4.51)$$

Then, combining Eqs.(4.11) and (4.13), the n -th moment of the velocity distribution function can be rewritten as

$$\langle v^n \rangle = \alpha^n \left[\frac{2Q_{\text{thre}}^{1/2} r_{\text{thre}}}{F^2(Q_{\text{thre}})} + I_0 \right]^{-1} \left[\frac{2Q_{\text{thre}}^{(n+1)/2} r_{\text{thre}}}{F^2(Q_{\text{thre}})} + (n+1)I_n \right], \quad (4.52)$$

where the integral I_n defined in Eq.(4.12) can be estimated through the sum:

$$I_n = \sum_a \frac{Q_a^{(n-1)/2}}{F^2(Q_a)}, \quad (4.53)$$

as Eq.(4.48). Since all I_n are determined from the same data, they are correlated with

$$\text{cov}(I_n, I_m) = \sum_a \frac{Q_a^{(n+m-2)/2}}{F^4(Q_a)}. \quad (4.54)$$

This can e.g., be seen by writing Eq.(4.53) as a sum over narrow bins, such that the recoil spectrum within each bin can be approximated by a constant. Each term in the sum would then have to be multiplied with the number of events in this bin; Eq.(4.54) then follows from standard error propagation. Note that, when re-converted into an integral, the expression for $\text{cov}(I_0, I_0)$ will diverge logarithmically for $Q_{\text{thre}} \rightarrow 0$. Equivalently, the numerical estimate of this entry can become very large if the sample contains events with very small Q -values. But, according to some numerical simulations, there should be no problem for samples with $Q_{\text{thre}} > 1$ keV. Many existing experiments in fact require significantly larger energy transfers in their definition of a WIMP signal.

In order to calculate the statistical error of $\langle v^n \rangle$ in Eq.(4.52), one needs at first the error of r_{thre} which can be obtained from Eq.(4.51) as

$$\sigma^2(r_{\text{thre}}) = r_{\text{thre}}^2 \left\{ \frac{\sigma^2(r_1)}{r_1^2} + \left[Q_{\text{thre}} - Q_{s,1} - k_1 \left(\frac{\partial Q_{s,1}}{\partial k_1} \right) \right]^2 \sigma^2(k_1) \right\}. \quad (4.55)$$

Here the squared errors for r_1 and k_1 are simply the corresponding diagonal entries of the respective covariance matrices given in Eqs.(4.41) and (4.44), and the definition of $Q_{s,1}$ in Eq.(4.28) implies

$$Q_{s,1} + k_1 \left(\frac{\partial Q_{s,1}}{\partial k_1} \right) = Q_1 - \frac{1}{k_1} + \left(\frac{b_1}{2} \right) \coth \left(\frac{b_1 k_1}{2} \right), \quad (4.56)$$

where Q_1 is the central Q -value in the first bin. It should be noted that the first term in Eq.(4.11) is negligible for all $n \geq 1$ if $Q_{\text{thre}} \simeq 1$ keV. However, even for this low threshold energy it contributes significantly to the normalization constant \mathcal{N} , as described by Eq.(4.13). Of course, the first term in Eq.(4.11) always dominates for $n = -1$. This is not surprising, since the very starting point of this analysis, Eq.(3.12), already shows that the counting rate at Q_{thre} is proportional to the “minus first” moment of the velocity distribution.

One needs also the correlation between the errors on the estimate of the recoil spectrum at $Q = Q_{\text{thre}}$ and the integrals I_n . It is clear that these quantities are correlated,

since the former is estimated from all events in the first bin, which of course also contribute to the latter. These correlations can be estimated by using the ansatz in Eq.(4.18), which makes the following prediction for the contribution of the first bin to the integrals:

$$I_{n,1} = r_1 \int_{Q_{\text{thre}}}^{Q_{\text{thre}}+b_1} \left[\frac{Q^{(n-1)/2}}{F^2(Q)} \right] e^{k_1(Q-Q_{s,1})} dQ. \quad (4.57)$$

This immediately implies

$$\frac{\partial I_{n,1}}{\partial r_1} = \frac{I_{n,1}}{r_1}, \quad (4.58a)$$

and

$$\frac{\partial I_{n,1}}{\partial k_1} = I_{n+2,1} - \left[Q_{s,1} + k_1 \left(\frac{\partial Q_{s,1}}{\partial k_1} \right) \right] I_{n,1}. \quad (4.58b)$$

Note that $I_{n,1}$ and $I_{n+2,1}$ in Eqs.(4.58a) and (4.58b) can be evaluated as in Eq.(4.53), with the sum extending only over events in the first bin:

$$I_{n,1} = \sum_{i=1}^{N_1} \frac{Q_{1,i}^{(n-1)/2}}{F^2(Q_{1,i})}. \quad (4.59)$$

The correlation between r_{thre} and I_n is then given by

$$\begin{aligned} & \text{cov}(r_{\text{thre}}, I_n) \\ &= r_{\text{thre}} I_{n,1} \left\{ \frac{\sigma^2(r_1)}{r_1^2} + \left[Q_{\text{thre}} - Q_{s,1} - k_1 \left(\frac{\partial Q_{s,1}}{\partial k_1} \right) \right] \right. \\ & \quad \left. \times \left[\frac{I_{n+2,1}}{I_{n,1}} - Q_{s,1} - k_1 \left(\frac{\partial Q_{s,1}}{\partial k_1} \right) \right] \sigma^2(k_1) \right\}. \end{aligned} \quad (4.60)$$

Finally, these ingredients allow us to compute the covariance matrix for the estimates of the moments of the velocity distribution:

$$\begin{aligned} & \text{cov}(\langle v^n \rangle, \langle v^m \rangle) \\ &= \mathcal{N}_m^2 \left[\langle v^n \rangle \langle v^m \rangle \text{cov}(I_0, I_0) + \alpha^{n+m} (n+1)(m+1) \text{cov}(I_n, I_m) \right. \\ & \quad - \alpha^m (m+1) \langle v^n \rangle \text{cov}(I_0, I_m) - \alpha^n (n+1) \langle v^m \rangle \text{cov}(I_0, I_n) \\ & \quad + D_n D_m \sigma^2(r_{\text{thre}}) - (D_m \langle v^n \rangle + D_n \langle v^m \rangle) \text{cov}(r_{\text{thre}}, I_0) \\ & \quad \left. + \alpha^m (m+1) D_n \text{cov}(r_{\text{thre}}, I_m) + \alpha^n (n+1) D_m \text{cov}(r_{\text{thre}}, I_n) \right]. \end{aligned} \quad (4.61)$$

Here I have introduced the modified normalization constant:

$$\mathcal{N}_m \equiv \left(\frac{\alpha}{2} \right) \mathcal{N}, \quad (4.62)$$

which exploits the partial cancellation of the α factors between Eqs.(4.11) and (4.13), and the quantities

$$D_n \equiv \frac{1}{\mathcal{N}_m} \left(\frac{\partial \langle v^n \rangle}{\partial r_{\text{thre}}} \right) = \frac{2}{F^2(Q_{\text{thre}})} \left(\alpha^n Q_{\text{thre}}^{(n+1)/2} - \sqrt{Q_{\text{thre}}} \langle v^n \rangle \right). \quad (4.63)$$

Note that, in practice, one can determine $\langle v^n \rangle$ by a single experiment with a large number of events, or by averaging over many experiments with a relatively small number of events. However, numerical simulations [96] show that in the second case the average values of the reconstructed moments do not exactly converge to the input (exact) values. In order to understand this, consider the simple case $Q_{\text{thre}} = 0$. The moments are then proportional to the ratio I_n/I_0 (see Eq.(4.52)). The distortion arises because $\langle I_n/I_0 \rangle \neq \langle I_n \rangle / \langle I_0 \rangle$, where the averaging is over many simulated experiments. The leading correction terms for small Q_{thre} and not very large first bin can be found as (a detailed calculation by using Taylor expansion to second order will be given in App. E.2)

$$\delta \langle v^n \rangle = \alpha^n \mathcal{N}_m^2 \left\{ (n+1) \left[\text{cov}(I_0, I_n) - \mathcal{N}_m I_n \text{cov}(I_0, I_0) \right] + 2 \left[\frac{Q_{\text{thre}}^{(n+1)/2}}{F^2(Q_{\text{thre}})} \right] \left[\text{cov}(r_{\text{thre}}, I_0) - r_{\text{thre}} \mathcal{N}_m \text{cov}(I_0, I_0) \right] \right\}, \quad (4.64)$$

where the second line in Eq.(4.60) is significant only for $n = -1$. Note that this correction becomes very small if the statistical errors on the I_n as well as on r_{thre} become small.

Meanwhile, according to some detailed numerical analyses [96], an ‘‘error on the error’’ should be added. The contribution to the diagonal entries of the covariance matrix given in Eq.(4.55) can be estimated as

$$\sigma^2(\text{cov}(I_n, I_n)) = \sum_a \frac{Q_a^{2n-2}}{F^8(Q_a)}, \quad (4.65)$$

the off-diagonal entries are then scaled up such that the correlation matrix remains unaltered. The numerical analyses show also that very rare events with large recoil energies contribute significantly more to the higher moments. Hence, an experiment with a small number of events will usually underestimate $\langle v^n \rangle$ and, especially, its error; the problem will become worse with increasing n . However, because this method uses whole experimental data together to determine the moments of $f_1(v)$, it has also been found that, based only on the first two or three moments, some non-trivial information can already be extracted from $\mathcal{O}(20)$ events.

More details and discussions about the reconstruction of the velocity distribution and determination of its moments can be found in Ref. [96].

4.3 Determining the WIMP mass

In the previous two sections I discussed how to use a recoil spectrum from direct Dark Matter detection as well as experimental data directly (i.e., the measured recoil energies) to reconstruct the velocity distribution function of WIMPs as well as to determine its moments. As noted earlier, for both of these reconstruction methods we need to know the mass of the incident WIMPs m_χ . In well-motivated WIMP models from elementary particle physics, m_χ can be determined with high accuracy from future collider experiment

data. However, one has to check experimentally that the particles produced at colliders are in fact the same ones seen in Dark Matter detection experiments which form the Galactic halo. In this section I present a method for (self-)determining the WIMP mass based on the determination of the moments of the velocity distribution function, $\langle v^n \rangle$, (presented in Sec. 4.2.4) from two (or more) experimental data sets with different target materials.⁴

4.3.1 Neglecting Q_{thre}

As mentioned in the end of Sec. 4.1, the basic idea for using two different detector materials to determine the WIMP mass is that, from independent direct WIMP detection experiments with different target nuclei, the measured recoil spectra should lead to the same (moments of the) velocity distribution function of incident WIMPs.

For the case that the threshold energy Q_{thre} can be neglected, the n -th moment of the velocity distribution function, $\langle v^n \rangle$, in Eq.(4.52) can be expressed simply as

$$\langle v^n \rangle = \alpha^n (n+1) \left(\frac{I_n}{I_0} \right), \quad (4.66)$$

where I_n and I_0 can be estimated by Eq.(4.53). Suppose X and Y are two target nuclei. Eq.(4.66) implies

$$\alpha_X^n \left(\frac{I_{n,X}}{I_{0,X}} \right) = \alpha_Y^n \left(\frac{I_{n,Y}}{I_{0,Y}} \right). \quad (4.67)$$

Note that the form factor $F^2(Q)$ in Eq.(4.53) for estimating $I_{n,X}$ and $I_{n,Y}$ are different. Then, according to the definition of α in Eq.(3.11) with the expression of the reduced mass m_r in Eq.(3.6) and using some simple algebra, one can find the WIMP mass as

$$m_\chi = \frac{\sqrt{m_X m_Y} - m_X \mathcal{R}_n}{\mathcal{R}_n - \sqrt{m_X/m_Y}}, \quad (4.68)$$

where I have defined

$$\mathcal{R}_n \equiv \frac{\alpha_Y}{\alpha_X} = \left(\frac{I_{n,X}}{I_{0,X}} \cdot \frac{I_{0,Y}}{I_{n,Y}} \right)^{1/n}, \quad n \neq 0, -1. \quad (4.69)$$

Fig. 4.3 shows the ratios of the reproduced WIMP masses estimated by Eq.(4.68) with different combinations of target nuclei to the input (true) one as functions of the input WIMP mass. ^{28}Si , ^{40}Ar , and ^{76}Ge have been chosen as three target nuclei and thus three combinations for \mathcal{R}_n defined in Eq.(4.69) with $n = 1$ are shown. \mathcal{R}_n has been estimated by the integral form of I_n in Eq.(4.12) with a maximal measuring energy of 200 keV. The theoretical predicted recoil spectrum for the shifted Maxwellian velocity distribution

⁴Note that the ansatz here is quite different from that used in Ref. [97], which assumes different WIMP velocity distributions with two input parameters: the WIMP mass and the WIMP-nucleon cross section, and then analyses with which precision in the usual WIMP mass-cross section plane the WIMP mass can be reproduced from the direct detection experiment.

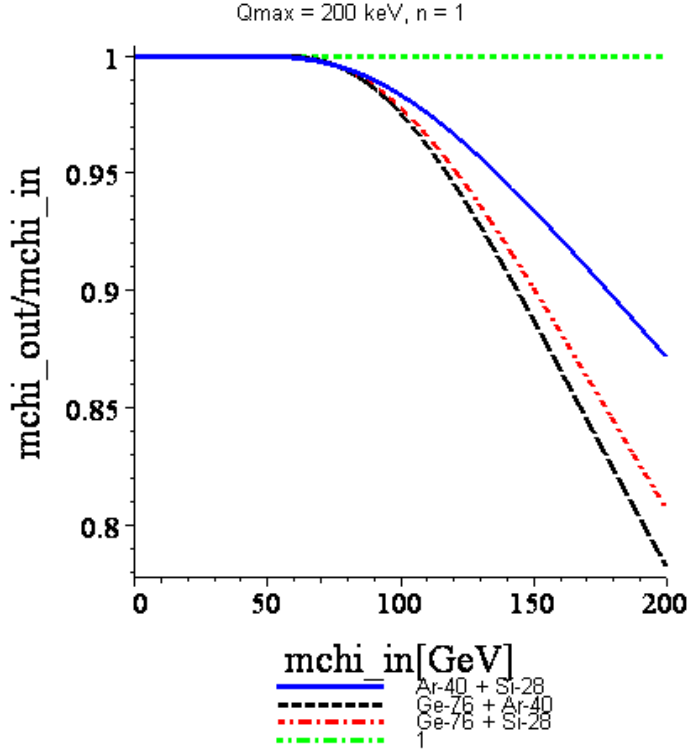


Figure 4.3: The curves show the ratios of the reproduced WIMP masses estimated by Eq.(4.68) with different combinations of target nuclei to the input (true) one as functions of the input WIMP mass. \mathcal{R}_n with $n = 1$ has been estimated by the integral form of I_n with a maximal measuring energy of 200 keV. The recoil energy spectrum for a shifted Maxwellian velocity distribution with the Woods-Saxon form factor has been used (parameters as in Fig. 4.1). The solid (blue) line, the dashed (black) line, and the dash-dotted (red) line are for $^{40}\text{Ar} + ^{28}\text{Si}$, $^{76}\text{Ge} + ^{40}\text{Ar}$, and $^{76}\text{Ge} + ^{28}\text{Si}$ combination, respectively. The straight dash-dotted (green) line denotes 1.

function, $(dR/dQ)_{\text{sh}}$ in Eq.(3.31), with the Woods-Saxon form factor $F_{\text{WS}}^2(Q)$ in Eq.(3.17) has been used. In Fig. 4.3 one can see obviously a deviation of the reproduced WIMP mass from the input (true) one as input $m_\chi \gtrsim 60 \text{ GeV}/c^2$. The heavier the nuclear masses of two target nuclei, e.g., $^{76}\text{Ge} + ^{28}\text{Si}$, the larger the deviation from the true WIMP mass. This is caused by introducing the maximal measuring energy for estimating I_n . As discussed in Subsec. 4.2.4, the heavier the nuclear mass m_N , or, equivalently, the larger α , and the larger n , the more the contribution to I_n comes from the high Q region, and, for a fixed maximal measuring energy, the smaller the value for \mathcal{R}_n and then for m_χ will be estimated. As shown in Fig. 4.3, for $n = 1$ and input $m_\chi = 200 \text{ GeV}/c^2$, the deviation with $Q_{\text{max}} = 200 \text{ keV}$ is around 20%. However, according to the numerical analysis, with $Q_{\text{max}} = 250 \text{ keV}$ or 300 keV , this deviation will be reduced to around 10% or even only 5%. Later we will see, due to a quite large statistical error with very few events, a deviation around 10% for input $m_\chi = 200 \text{ GeV}/c^2$ is not very bad. Moreover, for input $m_\chi \lesssim 120 \text{ GeV}/c^2$, the deviation should be less than 5% or even 1% for $Q_{\text{max}} = 200 \text{ keV}$

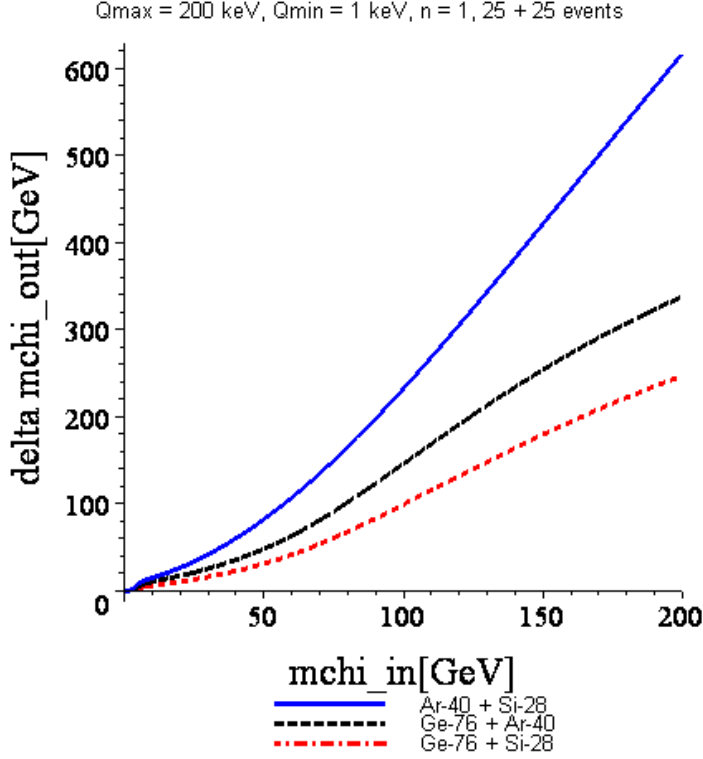


Figure 4.4: The curves show the statistical errors estimated by Eq.(4.70) with different combinations of target nuclei as functions of the input WIMP mass. Each experiment has 25 events, i.e., totally 50 events. Parameters and indications of the lines as in Fig. 4.3.

or 250 keV.

Furthermore, the statistical error on the reproduced WIMP mass can be obtained from Eq.(4.68) directly as

$$\begin{aligned}
 \sigma(m_X) &= \frac{\sqrt{m_X/m_Y} |m_X - m_Y|}{\left(\mathcal{R}_n - \sqrt{m_X/m_Y}\right)^2} \cdot \sigma(\mathcal{R}_n) \\
 &= \frac{\mathcal{R}_n \sqrt{m_X/m_Y} |m_X - m_Y|}{\left(\mathcal{R}_n - \sqrt{m_X/m_Y}\right)^2} \\
 &\quad \times \frac{1}{|n|} \left[\frac{\sigma^2(I_{n,X})}{I_{n,X}^2} + \frac{\sigma^2(I_{0,X})}{I_{0,X}^2} - \frac{2\text{cov}(I_{0,X}, I_{n,X})}{I_{0,X} I_{n,X}} + (X \rightarrow Y) \right]^{1/2}, \quad (4.70)
 \end{aligned}$$

where $\sigma^2(I_{n,X}) = \text{cov}(I_{n,X}, I_{n,X})$ and $\text{cov}(I_{0,X}, I_{n,X})$ and so on can be estimated from Eq.(4.54).

Fig. 4.4 shows the statistical errors estimated by Eq.(4.70) with three different combinations of target nuclei as functions of the input (true) WIMP mass. Each experiment has 25 events, i.e., totally 50 events. Note that, in order to use the integral form of $\text{cov}(I_n, I_m)$ in Eq.(4.54), a threshold energy $Q_{\min} = 1$ keV has been given. In Fig. 4.4 one can observe that *the larger the mass difference between two detector nuclei, the smaller*

the statistical error will be. Hence, the combination with the largest mass difference, e.g., $^{76}\text{Ge} + ^{28}\text{Si}$ will have the smallest statistical error. In principle one other combination: $^{131}\text{Xe} + ^{40}\text{Ar}$ has larger mass difference and should have an even smaller statistical error. However, because the Woods-Saxon form factor has been used here, the integral form of $\text{cov}(I_n, I_m)$ in Eq.(4.54) has a pole at $Q \sim 100$ keV! Thus ^{131}Xe has been not used for this simulation. On the other hand, despite of the factor $1/|n|$ in Eq.(4.70), it has been found that the statistical errors increase with increasing n , except the $^{40}\text{Ar} + ^{28}\text{Si}$ combination. For this combination, the statistical error with $n = 2$ is a little smaller than with $n = 1$; but, with $n = 3$, the statistical error is significantly larger (and, as discussed above, the deviation of the reproduced WIMP mass should also be larger). Hence, $n = 1$ should be the best choice for m_χ and $\sigma(m_\chi)$ in Eqs.(4.68) and (4.70), respectively.

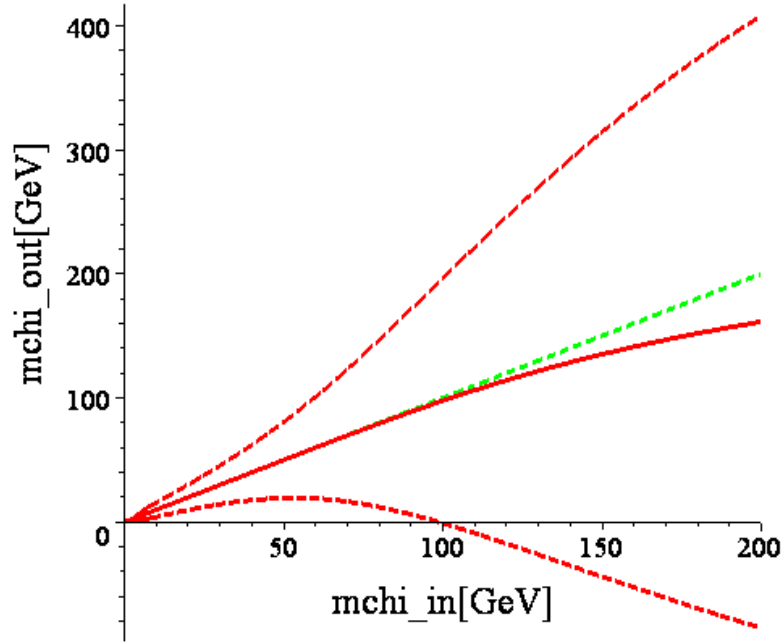
Figs. 4.5 show the reproduced WIMP mass with the statistical error by using ^{76}Ge and ^{28}Si as two target nuclei as a function of the input (true) WIMP mass. From the upper frame, it can be found that, despite of the very few ($25 + 25$, totally 50) events and correspondingly very large statistical error, for $m_\chi \leq 100$ GeV/c^2 , one can already extract some meaningful information on the WIMP mass. For example, for $m_\chi = 25$ GeV/c^2 and $m_\chi = 50$ GeV/c^2 , we will reproduce $m_\chi \simeq (25 \pm 13)$ GeV/c^2 and $m_\chi \simeq (50 \pm 31)$ GeV/c^2 . For the case with 500 ($250 + 250$) total events, the statistical error will be reduced to less than 5 and 10 GeV/c^2 , respectively! Certainly, as shown in the lower frame of Figs. 4.5, for the case with 500 total events, the deviation of the reproduced WIMP mass from the input one becomes important. Nevertheless, in practice, an experiment with more than 200 events should have a larger maximal measuring energy, and, as discussed above, the deviation can (should) be strongly reduced.

For the simplified simulations with the integral form of I_n presented above, the event numbers from both experiments have been considered to be equal. Practically, as described in Subsecs. 3.4.1 to 3.4.3, experiments with the higher mass nuclei, e.g., Ge or Xe, are expected to measure (much) more signal events. However, according to the expression for $\sigma(m_\chi)$ in Eq.(4.70) and the definition of \mathcal{R}_n in Eq.(4.69), it can be found that only the terms in the brackets depends on the event number and the contributions from the two experiments are independent of each other. Moreover, a detailed analysis of contributions from different terms of $\sigma(m_\chi)$ shows that the prefactor

$$\frac{\mathcal{R}_n \sqrt{m_X/m_Y} |m_X - m_Y|}{\left(\mathcal{R}_n - \sqrt{m_X/m_Y}\right)^2} \quad (4.71)$$

which depends practically only on the choice of the combination of the two target nuclei is very large for every combination, while the terms in the brackets with the factor $1/|n|$ are actually quite small. This implies that one *can not* reduce the statistical error of m_χ estimated by Eq.(4.70) by *improving only one experiment* with even very large event number, since the contribution from the other (poor) experiment will dominate the error.

$Q_{\max} = 200 \text{ keV}$, $Q_{\min} = 1 \text{ keV}$, $n = 1, 25 + 25 \text{ events}$, Ge-76 + Si-28



$Q_{\max} = 200 \text{ keV}$, $Q_{\min} = 1 \text{ keV}$, $n = 1, 250 + 250 \text{ events}$, Ge-76 + Si-28

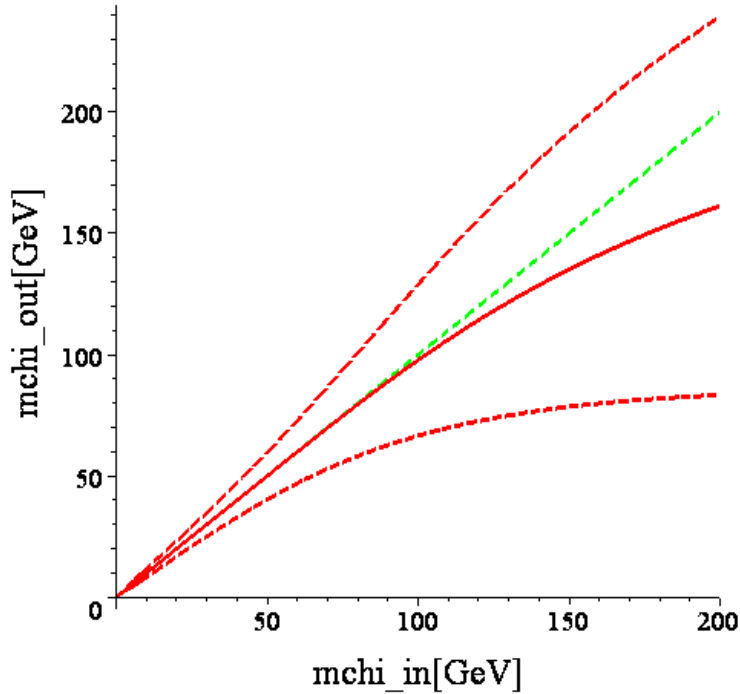


Figure 4.5: The reproduced WIMP mass with the statistical error by using ^{76}Ge and ^{28}Si as two target nuclei as a function of the input WIMP mass. The solid (red) line indicates the reproduced WIMP mass estimated by Eq.(4.68), the dashed (red) lines indicate the $1\text{-}\sigma$ statistical error estimated by Eq.(4.70). The straight dash-dotted (green) line indicates the input (true) WIMP mass. Each experiment has 25 (250) events, i.e., totally 50 (500) events, in the upper (lower) frame. Parameters as in Fig. 4.3.

4.3.2 With $Q_{\text{thre}} > 0$

For the case that Q_{thre} in Eq.(4.52) can not be neglected, \mathcal{R}_n defined in Eq.(4.69) should be modified to the following general form:

$$\mathcal{R}_n(Q_{\text{thre}}) = \left[\frac{2Q_{\text{thre},X}^{(n+1)/2} r_{\text{thre},X} + (n+1)I_{n,X} F_X^2(Q_{\text{thre},X})}{2Q_{\text{thre},X}^{1/2} r_{\text{thre},X} + I_{0,X} F_X^2(Q_{\text{thre},X})} \right]^{1/n} \times \left[\frac{2Q_{\text{thre},Y}^{1/2} r_{\text{thre},Y} + I_{0,Y} F_Y^2(Q_{\text{thre},Y})}{2Q_{\text{thre},Y}^{(n+1)/2} r_{\text{thre},Y} + (n+1)I_{n,Y} F_Y^2(Q_{\text{thre},Y})} \right]^{1/n}, \quad (4.72)$$

where $r_{\text{thre},X}$ and $r_{\text{thre},Y}$ should be determined by Eq.(4.51) (practically) with different r_1 , k_1 , $Q_{s,1}$, and Q_{thre} . In this general form of $\mathcal{R}_n(Q_{\text{thre}})$ there are totally six variables: $r_{\text{thre},X}$, $I_{n,X}$, $I_{0,X}$ and the other three for nucleus Y . This should generally produce a larger statistical error than that estimated by Eq.(4.70) due to the contribution from r_{thre} (the statistical error of $\mathcal{R}_n(Q_{\text{thre}})$ will be given in App. E.3). However, one can practically reduce the number of variables by choosing $n = -1$:

$$\mathcal{R}_{-1}(Q_{\text{thre}}) = \frac{r_{\text{thre},Y}}{r_{\text{thre},X}} \left[\frac{2Q_{\text{thre},X}^{1/2} r_{\text{thre},X} + I_{0,X} F_X^2(Q_{\text{thre},X})}{2Q_{\text{thre},Y}^{1/2} r_{\text{thre},Y} + I_{0,Y} F_Y^2(Q_{\text{thre},Y})} \right]. \quad (4.73)$$

Then $\sigma(\mathcal{R}_n)$ in the first line of Eq.(4.70) should be replaced by

$$\begin{aligned} & \sigma(\mathcal{R}_{-1}(Q_{\text{thre}})) \\ &= \mathcal{R}_{-1}(Q_{\text{thre}}) \left\{ \left[\frac{I_{0,X} F_X^2(Q_{\text{thre},X})}{2Q_{\text{thre},X}^{1/2} r_{\text{thre},X} + I_{0,X} F_X^2(Q_{\text{thre},X})} \right]^2 \right. \\ & \quad \times \left[\frac{\sigma^2(r_{\text{thre},X})}{r_{\text{thre},X}^2} + \frac{\sigma^2(I_{0,X})}{I_{0,X}^2} - \frac{2\text{COV}(r_{\text{thre},X}, I_{0,X})}{r_{\text{thre},X} I_{0,X}} \right] \\ & \quad \left. + (X \rightarrow Y) \right\}^{1/2}, \end{aligned} \quad (4.74)$$

where $\sigma^2(r_{\text{thre},X})$ and $\text{cov}(r_{\text{thre},X}, I_{0,X})$ and so on can be calculated by Eqs.(4.55) and (4.60).

Chapter 5

Annual Modulated Event Rate

In the previous chapter I have presented methods for reconstructing the velocity distribution function and its moments from the *time-averaged* recoil energy spectrum fitted to experimental data as well as from data directly. The annual modulation of the event rate discussed in Sec. 3.2 has been ignored. As shown in Sec. 4.2, in the foreseeable future with rare signal events, the statistical errors will remain large and thus this is a reasonable first approximation. However, for the future detectors with strongly improved sensitivity and (very) large target mass (large exposure), the formulae and methods have to be extended to allow for an annual modulation of the event rate.

In the first section of this chapter I extend the method developed in the previous chapter by considering *an arbitrary, but cosine-like time-dependent recoil spectrum with a one-year period*. In the second section I present the method for *reconstructing the amplitude of the (possible) annual modulation of the velocity distribution function*. An alternative, better way for *checking the annual modulation of the event rate* will also be described.

5.1 Taking into account the annual modulation

For simplicity, in this chapter I take $t_p = 0$ in Eq.(3.30) and rewrite it as

$$v_e(t) = v_0 [1.05 + 0.07 \cos(\omega t)], \quad (3.30')$$

with

$$\omega \equiv \frac{2\pi}{365}. \quad (5.1)$$

This means that in the following analyses experiments (data) have been assumed to be started (collected), i.e., $t = 0$, when v_e is maximal (around June 2nd, theoretically predicted) and the time t will be measured in unit of “day”.

As discussed in Secs. 3.1 and 3.2, roughly speaking, the differential event rate for direct WIMP detection is proportional to the WIMP flux, or, equivalently, the velocity of the Earth relative to the WIMP halo. And, due to the motion of the Earth on an elliptical

orbit around the Sun, the projection of the Earth's orbital speed on the orbital speed of the Sun around the Galactic center is *approximately* a cosine function. Therefore, as shown in Eqs.(3.30) and (3.30') above, the differential event rate should theoretically be a cosinusoidal function (c.f. the DAMA results in Figs. 3.3). On the other hand, substituting $v_e(t)$ in Eq.(3.30') into Eq.(3.31), it can be found that $(dR/dQ)_{\text{sh}}$ are not exact cosine but *cosine-like* functions with a period of 365 days (shown in Figs. 5.1). According to this observation, I assume generally *an arbitrary, but cosine-like time-dependent recoil spectrum with a one-year period* and then expand this spectrum and its corresponding velocity distribution function as *Fourier cosine series* as:

$$\left(\frac{dR}{dQ}\right)_t = \left(\frac{dR}{dQ}\right)_{(0)} + \left(\frac{dR}{dQ}\right)_{(1)} \cos(\omega t) + \left(\frac{dR}{dQ}\right)_{(2)} \cos(2\omega t) + \dots, \quad (5.2)$$

and

$$f_1(v, t) = f_{1,(0)}(v) + f_{1,(1)}(v) \cos(\omega t) + f_{1,(2)}(v) \cos(2\omega t) + \dots. \quad (5.3)$$

According to Eq.(3.12), $(dR/dQ)_t$ and $f_1(v, t)$ must satisfy the equation for the *time-dependent* WIMP-nucleus scattering spectrum:

$$\left(\frac{dR}{dQ}\right)_t = \mathcal{A}F^2(Q) \int_{v_{\min}}^{\infty} \left[\frac{f_1(v, t)}{v} \right] dv, \quad (5.4)$$

and, consequently, each pair of their Fourier coefficients must satisfy a time-independent equation:

$$\left(\frac{dR}{dQ}\right)_{(m)} = \mathcal{A}F^2(Q) \int_{v_{\min}}^{\infty} \left[\frac{f_{1,(m)}(v)}{v} \right] dv, \quad m = 0, 1, 2, \dots. \quad (5.5)$$

Moreover, if we neglect (due to the very low detection rate discussed in Sec. 3.1 and the tiny difference shown in Figs. 5.1, we can practically neglect) the terms with $m \geq 2$ in Eqs.(5.2) and (5.3), $(dR/dQ)_{(0)}$ and $f_{1,(0)}(v)$ above are the time-averaged scattering spectrum and the time-averaged velocity distribution function of WIMPs, which we considered in Chap. 4, and $(dR/dQ)_{(1)}$ and $f_{1,(1)}(v)$ are the amplitudes of the annual modulations of the scattering spectrum and its corresponding velocity distribution. In addition, since $(dR/dQ)_{(m)}$ are Fourier coefficients of $(dR/dQ)_t$, we have

$$\left(\frac{dR}{dQ}\right)_{(0)} = \frac{1}{365} \int_0^{365} \left(\frac{dR}{dQ}\right)_t dt, \quad (5.6)$$

and

$$\left(\frac{dR}{dQ}\right)_{(m)} = \frac{2}{365} \int_0^{365} \left(\frac{dR}{dQ}\right)_t \cos(m\omega t) dt, \quad m = 1, 2, \dots. \quad (5.7)$$

Now, as mentioned in Subsec. 4.2.2, the important elements needed for the reconstruction of $f_{1,r}$ in Eq.(4.46) are the number of events N_μ in the μ -th window given in

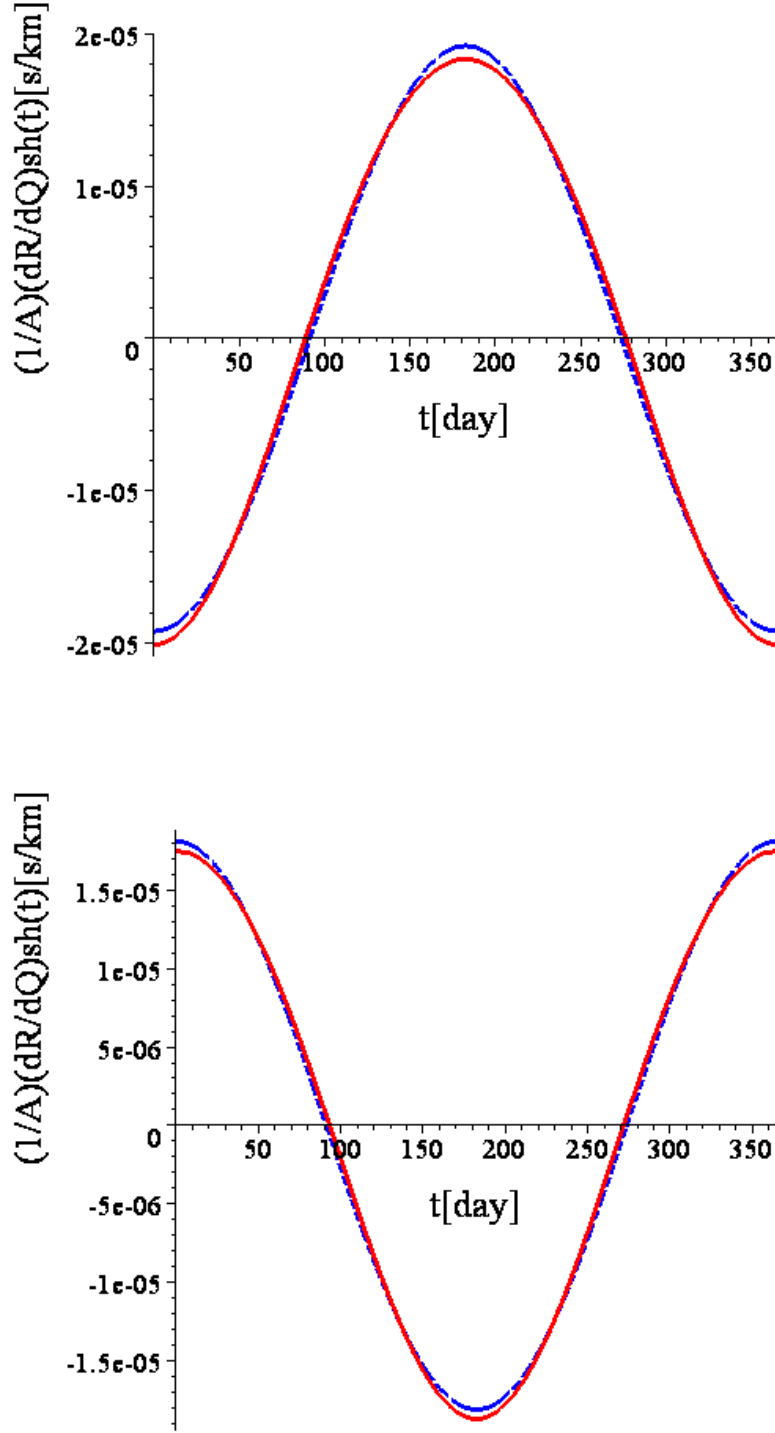


Figure 5.1: The solid (red) curves are the predicted modulations of the recoil energy spectrum for the shifted Maxwellian WIMP velocity distribution, $(dR/dQ)_{\text{sh}}$ in Eq.(3.31), with the Woods-Saxon form factor $F_{\text{WS}}^2(Q)$ in Eq.(3.21); the dashed (blue) curves are cosine functions with an amplitude $[(dR/dQ)_{\text{sh}}(t=0) - (dR/dQ)_{\text{sh}}(t=\pi/2)]/2$. Here I have used $m_\chi = 100 \text{ GeV}/c^2$, $m_N = 70.6 \text{ GeV}/c^2$ for ^{76}Ge , $v_0 = 220 \text{ km/s}$. The upper and lower frames are drawn for $Q = 15 \text{ keV}$ and $Q = 30 \text{ keV}$, respectively.

Eq.(4.37), as well as the averages $\overline{Q - Q_\mu}|_\mu$ given in Eq.(4.38), which are theoretically defined as, respectively,

$$N_\mu \equiv \int_{Q_\mu - w_\mu/2}^{Q_\mu + w_\mu/2} \left(\frac{dR}{dQ} \right)_{(0)} dQ, \quad (5.8)$$

and

$$\overline{(Q - Q_\mu)^\lambda}|_\mu \equiv \frac{1}{N_\mu} \int_{Q_\mu - w_\mu/2}^{Q_\mu + w_\mu/2} (Q - Q_\mu)^\lambda \left(\frac{dR}{dQ} \right)_{(0)} dQ, \quad (5.9)$$

where I have used generally the λ -th moment of the averaged recoil spectrum $(dR/dQ)_{(0)}$. Substituting Eq.(5.6) into Eqs.(5.8) and (5.9), it can be found easily that, for a time-dependent recoil spectrum with a one-year period,

$$N_\mu = \frac{1}{365} \int_0^{365} \int_{Q_\mu - w_\mu/2}^{Q_\mu + w_\mu/2} \left(\frac{dR}{dQ} \right)_t dQ dt = \frac{N_{\mu,1 \text{ yr}}}{365}, \quad (5.10)$$

and

$$\begin{aligned} \overline{(Q - Q_\mu)^\lambda}|_\mu &= \frac{1}{N_\mu} \left[\frac{1}{365} \int_0^{365} \int_{Q_\mu - w_\mu/2}^{Q_\mu + w_\mu/2} (Q - Q_\mu)^\lambda \left(\frac{dR}{dQ} \right)_t dQ dt \right] \\ &= \frac{1}{N_{\mu,1 \text{ yr}}} \sum_{i=1}^{N_{\mu,1 \text{ yr}}} (Q_{\mu,i} - Q_\mu)^\lambda, \end{aligned} \quad (5.11)$$

where $Q_{\mu,i}$, $i = 1, 2, \dots, N_{\mu,1 \text{ yr}}$, are the measured recoil energies from the direct WIMP detection experiment in the μ -th window *in one year*. Note that the “=” sign in the second line of Eq.(5.11) denotes not mathematically equal but an experimental estimator for $\overline{(Q - Q_\mu)^\lambda}|_\mu$.

Comparing these results with the expressions in Eqs.(4.25) and (4.27), Eqs.(5.10) and (5.11) show that, for an *arbitrary time-dependent* recoil spectrum with a one-year period (even though it is not cosine-like), we just have to take the experimental data *over some whole years* to find out the average event number (per day) and the annual average value of the energy transfer $(Q - Q_\mu)^\lambda$ in the μ -th window (or bin). Then we can reconstruct the time-averaged velocity distribution by means of the method presented in the previous chapter directly. Moreover, the results above show also that it is actually *not necessary* to know when v_e is maximal but only use all events collected in these (whole) years.

5.2 Reconstructing the modulated amplitude of $f_1(v)$

In this section I follow the trick used with $(dR/dQ)_{(0)}$ in the previous section and develop a method for reconstructing the (annual) modulated amplitude of $f_1(v)$. Meanwhile, I will also introduce two criteria for checking the annual modulation of the event rate.

5.2.1 Criteria for the annual modulation

Replacing $(dR/dQ)_{(0)}$ in Eq.(5.9) by $(dR/dQ)_{(1)}$ in Eq.(5.7), it can be found that ¹

$$\begin{aligned}
& \frac{1}{N_n} \int_{Q_n-b_n/2}^{Q_n+b_n/2} (Q - Q_n)^\lambda \left(\frac{dR}{dQ} \right)_{(1)} dQ \\
&= \frac{1}{N_n} \left[\frac{2}{365} \int_0^{365} \int_{Q_n-b_n/2}^{Q_n+b_n/2} (Q - Q_n)^\lambda \cos(\omega t) \left(\frac{dR}{dQ} \right)_t dQ dt \right] \\
&= \frac{2}{N_{n,1 \text{ yr}}} \sum_{i=1}^{N_{n,1 \text{ yr}}} (Q_{n,i} - Q_n)^\lambda \cos(\omega t_{n,i}), \tag{5.12}
\end{aligned}$$

where $t_{n,i}$, $i = 1, 2, \dots, N_{n,1 \text{ yr}}$, $n = 1, 2, \dots, B$, are the ‘‘measuring times’’ at which we measure the recoil energies $Q_{n,i}$ in the n -th bin in one year. Note that, first, the ‘‘=’’ sign in the second line of Eq.(5.12) denotes again an experimental estimator; second, the factor $\cos(\omega t_{n,i})$ comes from the integral in Eq.(5.7) (not from the second term of $v_e(t)$ in Eq.(3.30)!). On the other hand, by substituting $v_e(t)$ in Eq.(3.30) into $(dR/dQ)_{\text{sh}}$ in Eq.(3.31), it can be found that the ratio of the modulated amplitude of the recoil spectrum, $(dR/dQ)_{(1)}$, to the time-averaged recoil spectrum, $(dR/dQ)_{(0)}$, increases monotonically with the recoil energy Q and is approximately a linear function of Q (shown in Fig. 5.2). Hence, I introduce an ansatz for the modulated amplitude of the recoil spectrum in the n -th bin:

$$\left(\frac{dR}{dQ} \right)_{(1),n} = \left(\frac{dR}{dQ} \right)_{(0)} \cdot [l_n(Q - Q_n) + h_n], \quad n = 1, 2, \dots, B. \tag{5.13}$$

Note that $(dR/dQ)_{(0)}$ here indicates generally a time-averaged recoil spectrum, not specified to the exponential ansatz in Eq.(4.18). Substituting the ansatz for $(dR/dQ)_{(1),n}$ into the left-hand side of the Eq.(5.12), it can be found that

$$\frac{1}{N_n} \int_{Q_n-b_n/2}^{Q_n+b_n/2} (Q - Q_n)^\lambda \left(\frac{dR}{dQ} \right)_{(1),n} dQ = l_n \overline{(Q - Q_n)^{\lambda+1}}|_n + h_n \overline{(Q - Q_n)^\lambda}|_n. \tag{5.14}$$

Setting $\lambda = 0$ and 1 and combining Eqs.(5.12) and (5.14), l_n and h_n in Eq.(5.13) can be solved as

$$l_n = \frac{2 \overline{(Q - Q_n) \cos(\omega t)}|_n - 2 \overline{\cos(\omega t)}|_n \overline{Q - Q_n}|_n}{\overline{(Q - Q_n)^2}|_n - \overline{Q - Q_n}|_n^2}, \tag{5.15}$$

and

$$h_n = \frac{2 \overline{\cos(\omega t)}|_n \overline{(Q - Q_n)^2}|_n - 2 \overline{(Q - Q_n) \cos(\omega t)}|_n \overline{Q - Q_n}|_n}{\overline{(Q - Q_n)^2}|_n - \overline{Q - Q_n}|_n^2}, \tag{5.16}$$

where I have defined

$$\overline{(Q - Q_n)^\lambda \cos^\rho(\omega t)}|_n \equiv \frac{1}{N_{n,1 \text{ yr}}} \sum_{i=1}^{N_{n,1 \text{ yr}}} (Q_{n,i} - Q_n)^\lambda \cos^\rho(\omega t_{n,i}). \tag{5.17}$$

¹For simplicity and clarity, I discuss in this section the case with bins, thus μ and w_μ in Eq.(5.9) have been replaced here by n and b_n , respectively. However, all formulae given in this section can be used for the case with windows by substituting n and b_n by μ and w_μ .

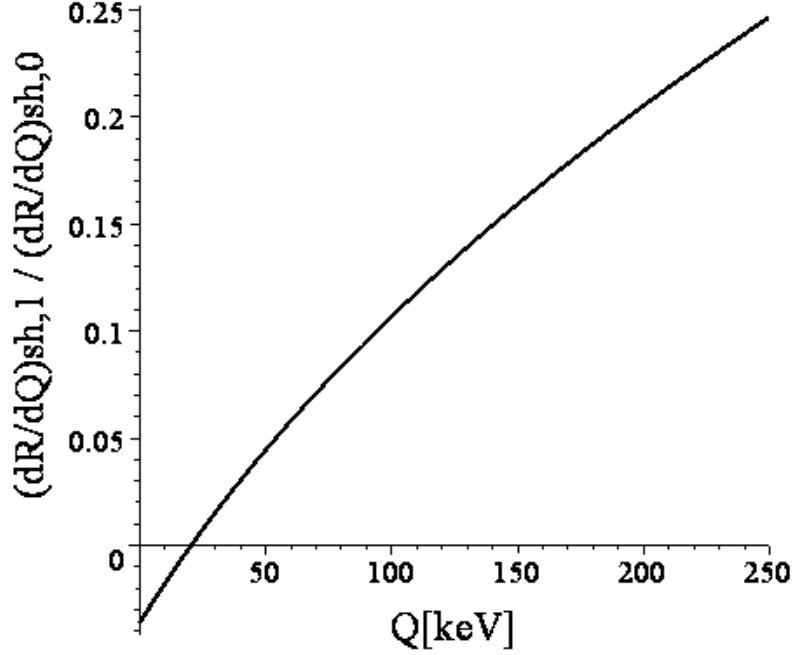


Figure 5.2: The curve shows the ratio of the modulated amplitude of the recoil spectrum, $(dR/dQ)_{(1)}$, to the time-averaged recoil spectrum, $(dR/dQ)_{(0)}$, as a function of the recoil energy Q . Parameters as in Figs. 5.1.

Due to the annual modulation effect, around $t = 0$ we should get more events than around $t = \pi$. Recall that I have assumed that experiments start when v_e is maximal. Thus, even though $\int_0^{2\pi} \cos(\omega t) dt = 0$, $\overline{\cos(\omega t)}|_n$ above are generally not equal to 0. Moreover, l_n in Eq.(5.15) can be rewritten as

$$l_n = \frac{2 \operatorname{cov}(\overline{Q - Q_n}|_n, \overline{\cos(\omega t)}|_n)}{\sigma^2(Q - Q_n|_n)}, \quad (5.15')$$

where $\operatorname{cov}(\overline{Q - Q_n}|_n, \overline{\cos(\omega t)}|_n)$ is the covariance between the average value of the measured recoil energies $Q_{n,i} - Q_n$ and that of $\cos(\omega t_{n,i})$ in the n -th bin. According to Fig. 5.2 and the ansatz in Eq.(5.14), l_n should be generally > 0 and this means that $\overline{Q - Q_n}|_n$ and $\overline{\cos(\omega t)}|_n$ should be positively correlated. This result offers a better way to test the annual modulation effect! Traditionally, in order to confirm the annual modulation of the event rate, one has to collect the recoil events in a given energy range in several short time intervals (a few days to a couple weeks) and then compare the numbers of collected events in the different time intervals in one year (e.g., the DAMA 4-year and 7-year results shown in Figs. 3.3). As mentioned in Sec. 3.2, the annual modulation of event rate is expected to be only a few percent (about $-4\% \sim 5\%$ in the energy range between 0 and 50 keV, see Fig. 5.2) and this method can be used once more than one hundred events (in a few days!) have been accumulated. However, according to the discussion above, one can now collect all recoil events in a relatively larger energy range (since the calculation

with bins can be extended directly to that with windows) in one year (or even several years) and then only has to check the following quantities:

$$\Delta_t \equiv \overline{\cos(\omega t)} = \frac{1}{N_{tot}} \sum_a \cos(\omega t_a), \quad (5.18)$$

and

$$\Delta_{Q,t} \equiv \text{cov} \left(\overline{Q}, \overline{\cos(\omega t)} \right) = \frac{1}{N_{tot} - 1} \left[\overline{Q \cos(\omega t)} - \overline{Q} \overline{\cos(\omega t)} \right], \quad (5.19)$$

where the averages are over all events in the energy range which one concerns and N_{tot} is the total event number in this energy range. If the annual modulation of event rate exists, one should than get $\Delta_t \neq 0$ and $\Delta_{Q,t} > 0$. Note that, for the case that some time-independent background events mixed into the true signals, the two quantities above will be *underestimated* through the averaging; or even worse, if most of the background events have been discriminated, then the contribution from the rest events can not cancel each other any more. However, for the case that the time-independent background events dominate the whole data set, one can use a quantity modified from Δ_t in Eq.(5.18):

$$\Delta'_t \equiv \sum_a \cos(\omega t_a). \quad (5.20)$$

The quantity Δ'_t defined here is not the average but the sum of the cosine values of the measuring times. Hence, the contributions from background events will cancel each other and not change the value of Δ'_t (too much). But in the statistical error of Δ'_t :²

$$\sigma^2(\Delta'_t) = \sum_a \cos^2(\omega t_a), \quad (5.21)$$

there can not be any cancellation, i.e., $\sigma^2(\Delta'_t)$ will increase with the total event number N_{tot} . In addition, for a “time-dependent” background the quantity in Eq.(5.20) can not be used any more.

Furthermore, for the check of the quantities in Eqs.(5.18) and (5.19), it is important to know when v_e is maximal. This offers in practice a possibility to determine (to check theoretically predicted) t_p in Eq.(3.30). One sets the starting date of the experiment on January 1st, inserts a phase φ into Eqs.(5.18) and (5.19), and then finds out when the quantity

$$\Delta_{t-\varphi} = \overline{\cos \omega(t - \varphi)} \quad (5.18')$$

is (almost) equal to 0, which corresponds to $t_p \pm \pi/2\omega$, and when the quantity

$$\Delta_{Q,t-\varphi} = \text{cov} \left(\overline{Q}, \overline{\cos \omega(t - \varphi)} \right) \quad (5.19')$$

has a maximal value (positive), a minimal value (negative), or is (almost) equal to 0, which correspond to t_p , $t_p \pm \pi/\omega$, or $t_p \pm \pi/2\omega$, respectively. Certainly, for the case that such annual modulation of the event rate does not exist, one will find that Δ_t and $\Delta_{Q,t}$ are independent of φ and always (approximately) equal to 0.

²Here I have assumed that $N_{tot} \gg 1$ and then used $\sigma^2(\overline{\cos(\omega t)}) = \left[\overline{\cos^2(\omega t)} - \overline{\cos(\omega t)}^2 \right] / N_{tot}$.

5.2.2 Reconstructing the modulated amplitude of $f_1(v)$

According to Eq.(4.8), each coefficient of the time-dependent velocity distribution function, $f_1(v, t)$, in Eq.(5.3), can be solved from Eq.(5.5) as

$$f_{1,(m)}(Q) = \mathcal{N} \left\{ -2Q \cdot \frac{d}{dQ} \left[\frac{1}{F^2(Q)} \left(\frac{dR}{dQ} \right)_{(m)} \right] \right\}, \quad m = 0, 1, 2, \dots, \quad (5.22)$$

since, for all m ,

$$f_{1,(m)}(v \rightarrow \infty) \rightarrow 0, \quad (5.23)$$

see Eq.(4.3). Substituting the ansatz for $(dR/dQ)_{(1),n}$ in Eq.(5.14) at first and then the ansatz for $(dR/dQ)_{(0),n}$ in Eq.(4.18) into Eq.(5.22), the ratio of the modulated amplitude of the velocity distribution function to the time-averaged one at the point $Q = Q_n$ (not at $v = v_n!$) can be obtained as (a detailed derivation will be given in App. E.4)

$$\eta_n \equiv \frac{f_{1,(1),n}(Q_n)}{f_{1,(0),n}(Q_n)} = h_n - l_n \left[\frac{d}{dQ} \ln F^2(Q) \Big|_{Q=Q_n} - k_n \right]^{-1}. \quad (5.24)$$

Note that the first term in the brackets has been evaluated at $Q = Q_n$ (not at $Q = Q_{s,n}!$).

The result in Eq.(5.24) has three advantages. First, since η_n here is the *ratio* of the modulated amplitude of the velocity distribution function to the time-average one in the n -th Q -bin, it is not necessary to combine the data from all bins to get the normalization constant, each one of these η_n is independent of the others.³ Second, due to the same reason, one can estimate the η_n even if he can not obtain (enough) events in the high energy range (> 100 keV). It is, in contrast, necessary to collect enough events until high energy (≈ 200 keV for a WIMP mass ~ 100 GeV/ c^2 and ^{76}Ge as target nucleus) in order to determine the normalization constant \mathcal{N} in Eq.(4.48). Third, the η_n are independent of α defined in Eq.(3.11), or, equivalently, independent of the WIMP mass m_χ . Certainly, one can use the method described in Sec. 4.3 to determine the WIMP mass. But for the case with very rare total events or too few events in the energy range higher than e.g., 100 keV, the deviation of the estimation of the WIMP mass from the true one and the statistical error will be very large. However, due to the independence of the η_n of α , the reconstruction by Eq.(5.24) will not be affected by the (large) uncertainty of the estimation of the WIMP mass.

The statistical errors of η_n in Eq.(5.24) can be expressed as

$$\sigma^2(\eta_n) = \sum_{\nu=1}^4 \left(\frac{\partial \eta_n}{\partial y_{\nu,n}} \right)^2 \sigma^2(y_{\nu,n}) + \sum_{\substack{\nu,\tau=1 \\ \tau \neq \nu}}^4 \left(\frac{\partial \eta_n}{\partial y_{\nu,n}} \right) \left(\frac{\partial \eta_n}{\partial y_{\tau,n}} \right) \text{cov}(y_{\nu,n}, y_{\tau,n}). \quad (5.25)$$

Here I have defined

$$y_{\nu,n} = \overline{Q - Q_n}|_n, \quad \overline{(Q - Q_n)^2}|_n, \quad \overline{\cos(\omega t)}|_n, \quad \overline{(Q - Q_n) \cos(\omega t)}|_n, \quad (5.26)$$

³For the case with windows, the η_n are no more independent of each other. But the off-diagonal entries of the correlation matrix of the statistical error of the η_n are practically not important.

and one has

$$\sigma^2 (y_{\nu,n}) = \text{cov} (y_{\nu,n}, y_{\nu,n}) , \quad (5.27)$$

with

$$\begin{aligned} & \text{cov} \left(\overline{(Q - Q_n)^\lambda \cos^\rho(\omega t)}|_n, \overline{(Q - Q_n)^\nu \cos^\tau(\omega t)}|_n \right) \\ &= \frac{1}{N_n - 1} \left[\overline{(Q - Q_n)^{\lambda+\nu} \cos^{\rho+\tau}(\omega t)}|_n \right. \\ & \quad \left. - \overline{(Q - Q_n)^\lambda \cos^\rho(\omega t)}|_n \overline{(Q - Q_n)^\nu \cos^\tau(\omega t)}|_n \right] . \end{aligned} \quad (5.28)$$

According to Eqs.(4.26), ⁴ (5.15), (5.16), and (5.24), the derivatives of η_n with respect to each of the $y_{\nu,n}$ in Eq.(5.26) can be found easily as

$$\begin{aligned} \frac{\partial \eta_n}{\partial \overline{Q - Q_n}|_n} &= \frac{h_n}{\sigma_n} \left(\overline{Q - Q_n}|_n + K_n \right) - \frac{l_n}{\sigma_n} \left[\overline{(Q - Q_n)^2}|_n + \overline{Q - Q_n}|_n K_n \right] \\ & \quad - k_n \left(\frac{l_n K_n^2}{\overline{Q - Q_n}|_n} \right) , \end{aligned} \quad (5.29a)$$

$$\frac{\partial \eta_n}{\partial \overline{Q - Q_n}|_n} = \frac{l_n}{\sigma_n} \left(\overline{Q - Q_n}|_n + K_n \right) - \frac{k_n^2}{2} \left(\frac{l_n K_n^2}{\overline{Q - Q_n}|_n} \right) , \quad (5.29b)$$

$$\frac{\partial \eta_n}{\partial \overline{\cos(\omega t)}|_n} = \frac{2}{\sigma_n} \left[\overline{(Q - Q_n)^2}|_n + \overline{Q - Q_n}|_n K_n \right] , \quad (5.29c)$$

$$\frac{\partial \eta_n}{\partial \overline{(Q - Q_n) \cos(\omega t)}|_n} = -\frac{2}{\sigma_n} \left(\overline{Q - Q_n}|_n + K_n \right) , \quad (5.29d)$$

where I have defined

$$\sigma_n \equiv \sigma^2 \left(\overline{Q - Q_n}|_n \right) = \frac{1}{N_n - 1} \left[\overline{(Q - Q_n)^2}|_n - \left(\overline{Q - Q_n}|_n \right)^2 \right] , \quad (5.30)$$

and

$$K_n \equiv \left[\frac{d}{dQ} \ln F^2(Q) \Big|_{Q=Q_n} - k_n \right]^{-1} . \quad (5.31)$$

⁴Since l_n and h_n are functions of both $\overline{Q - Q_n}|_n$ and $\overline{(Q - Q_n)^2}|_n$, for simplicity, I have used here the expression for k_n in Eq.(4.26).

Chapter 6

Summary and Conclusions

In this thesis I have presented methods which allow to extract information on the WIMP velocity distribution as well as on the WIMP mass from the recoil energy spectrum dR/dQ measured in elastic WIMP-nucleus scattering experiments. In the long term the information on the WIMP velocity distribution can be used to test or constrain models of the dark halo of our Galaxy; this information would complement the information on the density distribution of WIMPs, which can be derived e.g., from measurements of the Galactic rotation curve. Meanwhile, the information on the WIMP mass can be used to constrain e.g., SUSY models in the elementary particle physics and compare with information from future collider experiments.

In Sec. 4.1 I have derived the expression that allow to reconstruct the normalized one-dimensional velocity distribution function of WIMPs, $f_1(v)$, given an expression (e.g., a fit to data) for the recoil spectrum. I have also derived formulae for determining the moments of $f_1(v)$. All these expressions are independent of the as yet unknown WIMP density near the Earth as well as of the WIMP-nucleus cross section. The only information about the nature of WIMPs which one needs is the WIMP mass.

Then, in Sec. 4.2, I have presented methods that allow to apply the expressions derived in Sec. 4.1 directly to experimental data, without the need to fit the recoil spectrum to a functional form. A good variable that allows direct reconstruction of $f_1(v)$ is the average recoil energy in a given bin (or “window”, introduced in Subsec. 4.2.2). This average energy is sensitive to the slope of the recoil spectrum, which is the quantity one needs to reconstruct $f_1(v)$. The statistical error of the reconstruction of $f_1(v)$ has been analyzed. Unfortunately it has been found that several hundred events will be needed for the method to be able to extract meaningful information on $f_1(v)$. This is partly due to the fact that $f_1(v)$ is normalized, i.e., only the shape of this distribution contains meaningful information, and partly because this shape depends on the slope of the recoil spectrum, which is intrinsically difficult to determine.

Meanwhile, a method for determining the moments of $f_1(v)$ has also been presented in Subsec. 4.2.4. Numerical simulation shows that very rare events with large recoil energies contribute significantly more to the higher moments. Nevertheless, because this method

uses the whole experimental data together to determine the moments of $f_1(v)$, it has been found that, based only on the first two or three moments, some non-trivial information can already be extracted from $\mathcal{O}(20)$ events.

As noted earlier, one needs to know the WIMP mass m_χ for the reconstruction of (the moments of) the velocity distribution. Moreover, although in well-motivated WIMP models m_χ can be determined with high accuracy from future collider data, we will have to check experimentally that the particles produced at colliders are in fact the same ones seen in direct Dark Matter detection experiments which form the Galactic halo.

In Sec. 4.3 I have developed a method for (self-)determining m_χ based on the determination of the moments of $f_1(v)$ by combining two (or more) experiments with different detector materials. The numerical analysis shows that, the larger the mass difference between two target nuclei, the smaller the statistical error will be. Hence, the combinations of two semiconductor detectors: Si and Ge and of two liquid noble gas detectors: Ar and Xe should be good choices. Meanwhile, due to the maximal measuring energy of the detector, there will be a deviation of the reproduced WIMP mass from the true one as WIMP masses $\gtrsim 60 \text{ GeV}/c^2$. However, the numerical analysis shows also that, for WIMP masses $\leq 100 \text{ GeV}/c^2$ some meaningful information on the WIMP mass can already be extracted from $\mathcal{O}(50)$ total (each experiment $\mathcal{O}(25)$) events.

At the first step I have ignored the annual modulation of the WIMP flux. Given the large statistical errors expected in the foreseeable future, this is a reasonable first approximation. However, for the future detectors with strongly improved sensitivity and (very) large target mass (large exposure), the formulae and methods have to be extended to allow for an annual modulation of the event rate. Hence, in Sec. 5.1 I have discussed the extension of the reconstruction of the velocity distribution by taking into account the time dependence of the recoil spectrum. The analysis shows that the two important observables for reconstructing the velocity distribution function: the event number and the average recoil energy measured in a given bin (or window), can be obtained as the annual average of the total event number (per day) and the average value of the recoil energies measured in experiments operated over some whole years.

Moreover, in Subsec. 5.2.2 I have presented a method for reconstructing the ratio of the modulated amplitude of the velocity distribution to the time-averaged one. The only information which one needs is the measured recoil energies and their measuring times. This reconstruction is independent of the WIMP mass and can be done even if we can not obtain (enough) events in the high energy range. Hence, before the sensitivity of detectors can be improved to offer enough data until high energy range, reconstructing this ratio directly from experimental data and comparing it with the theoretical predictions might be the best possibility to test the different models of the halo Dark Matter.

Furthermore, in Subsec. 5.2.1, I have given an alternative, and also better way to check whether the annual modulation of the event rate exists and thereby test models of the Dark Matter halo. The main advantage of this test is that, instead of (traditionally)

comparing the numbers of collected signal events in different, short time intervals in one year, one can now use information, i.e., the measured recoil energies and their measuring times, from all signal events collected in one or even several years together. For the case that the background events dominate the whole data set, this test might be still useful, if one expects that the background is (almost) time independent.

The analyses of this work are based on several simplifying assumptions. First, all experimental systematic uncertainties, as well as the uncertainty on the measurement of the recoil energy Q have been ignored. This should be a quite good approximation, given that we will have to live with quite large statistical uncertainties in the foreseeable future. Recall that, as shown in Secs. 3.7 to 3.9, not a single WIMP event has as yet been unambiguously recorded.

I have also assumed that the detector consists of a single isotope. This is quite realistic for the current semiconductor (Si or Ge) detectors. On the other hand, for detectors containing more than one nucleus, by simultaneously measuring two signals, one might be able to tell on an event-by-event basis which kind of nucleus has been struck (see Subsec. 3.7.2). In this case, the methods can be applied straightforwardly to the separate sub-spectra.

The analyses treat each recorded event as signal, i.e., background has been ignored altogether. At least after introducing a lower cut Q_{thre} on the recoil energy, this may in fact not be unrealistic for modern detectors, which contain cosmic ray veto and neutron shielding systems (described in Subsec. 3.6). Background subtraction should be relatively straightforward when fitting some function to the data, which would allow to use the expressions given in Sec. 4.1. It should also be feasible in the method described in Sec. 4.2, if its effect on the average Q -values in the bins can be determined; in particular, an approximately flat (Q -independent) background would not change the slope of the recoil spectrum.

In summary, a theoretical exploration of studying what direct Dark Matter detection experiments can teach us about the properties of Dark Matter particles in our Galactic neighborhood, e.g., their velocity distribution and their mass, the so-called “WIMP astronomy”, has been started. However, the analyses show that this will require substantial data samples. Hopefully this work will encourage our experimental colleagues to plan future experiments well beyond the stage of “merely” detecting Dark Matter. On the other hand, due to the significantly reduced condition (less than 100 events) for extracting meaningful information on the WIMP mass by means of data from direct Dark Matter detection experiments, a championship for finding new particle(s) between the collaborations of direct Dark Matter detection and that of collider experiments has also been started.

Appendix A

Expression of the Velocity Distribution of WIMPs

In this chapter I discuss at first some properties of the auxiliary function $F_1(v)$ defined in Eq.(4.1). Then I show two different approaches to find out the expression of $f_1(v)$ in Eq.(4.8), and derive the normalization constant \mathcal{N} in Eq.(4.9) as well as the expression of moments of $f_1(v)$, $\langle v^n \rangle$, in Eq.(4.10).

A.1 Properties of $F_1(v)$ defined in Eq.(4.1)

First, according to the definition of $F_1(v)$ in Eq.(4.1) and noting that the velocity distribution function $f_1(v)$ can not be negative:

$$f_1(v) \geq 0, \tag{A.1}$$

I have

$$\frac{dF_1(v)}{dv} = \frac{f_1(v)}{v} \geq 0. \tag{A.2}$$

This means that $F_1(v)$ increases monotonically with v . Second, $f_1(v)$ must vanish as v approaches infinity:

$$f_1(v \rightarrow \infty) \rightarrow 0, \tag{4.3}$$

since WIMPs (as candidate for CDM) in today's Universe move quite slowly, then I have

$$\left. \frac{dF_1(v)}{dv} \right|_{v \rightarrow \infty} = \left. \frac{f_1(v)}{v} \right|_{v \rightarrow \infty} \rightarrow 0. \tag{4.4}$$

This means that $F_1(v)$ must approach a finite constant $F_{1,\infty}$ as $v \rightarrow \infty$. On the other hand, the three-dimensional velocity distribution function of WIMPs, $f(v)$, must be bounded:

$$f(v) \propto \frac{f_1(v)}{v^2} \neq \infty, \tag{A.3}$$

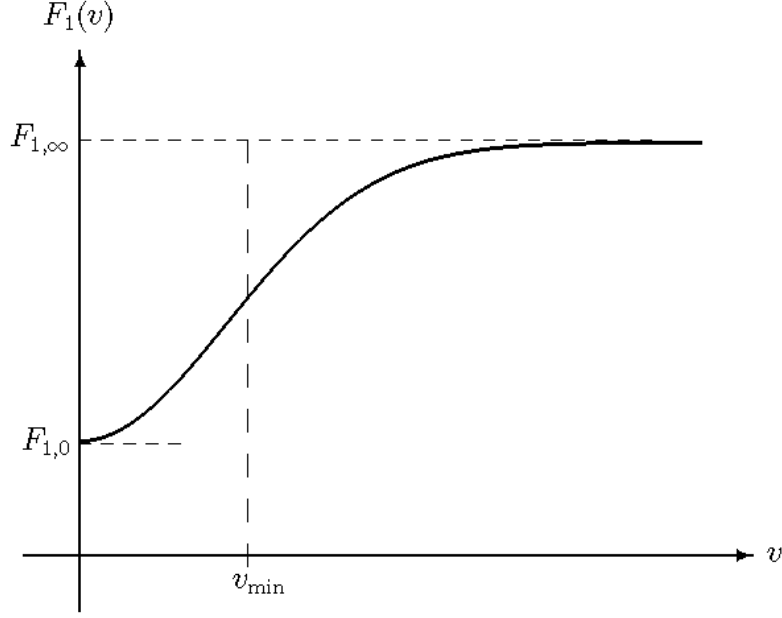


Figure A.1: Sketch of the auxiliary function $F_1(v)$ defined in Eq.(4.1).

where I have used

$$\int f(v) d^3v = \int f(v) v^2 dv d\Omega = \int f_1(v) dv.$$

Hence,

$$\left. \frac{dF_1(v)}{dv} \right|_{v=0} = \left. \frac{f_1(v)}{v} \right|_{v=0} = \left[v \cdot \frac{f_1(v)}{v^2} \right]_{v=0} = 0. \quad (\text{A.4})$$

This means that $F_1(v)$ also approaches a constant $F_{1,0}$ as $v \rightarrow 0$. Actually, $F_{1,0}$ can be set to 0 without loss of generality, since Eq.(4.1) defines $F_1(v)$ only up to an additional constant. A sketch of the auxiliary function $F_1(v)$ is given in Fig. A.1.

A.2 Derivations for $f_1(v)$ in Eq.(4.8)

According to Eq.(3.10), I have

$$\frac{dv_{\min}}{dQ} = \frac{\alpha}{2\sqrt{Q}} = \frac{v_{\min}}{2Q}, \quad (\text{A.5})$$

namely,

$$\frac{dQ}{dv_{\min}} = \frac{2Q}{v_{\min}}. \quad (\text{A.6})$$

Differentiating both sides of Eq.(4.2) and using Eq.(4.1), one can obtain that

$$\frac{f_1(v_{\min})}{v_{\min}} = \frac{dF_1(v_{\min})}{dv_{\min}} = -\frac{1}{\mathcal{A}} \left\{ \frac{d}{dv_{\min}} \left[\frac{1}{F^2(Q)} \left(\frac{dR}{dQ} \right) \right]_{Q=v_{\min}^2/\alpha^2} \right\}$$

$$\begin{aligned}
&= -\frac{1}{\mathcal{A}} \left\{ \frac{d}{dQ} \left[\frac{1}{F^2(Q)} \left(\frac{dR}{dQ} \right) \right] \cdot \left(\frac{dQ}{dv_{\min}} \right) \right\}_{Q=v_{\min}^2/\alpha^2} \\
&= \frac{1}{v_{\min}} \cdot \frac{1}{\mathcal{A}} \left\{ -2Q \cdot \frac{d}{dQ} \left[\frac{1}{F^2(Q)} \left(\frac{dR}{dQ} \right) \right] \right\}_{Q=v_{\min}^2/\alpha^2}, \quad (4.5)
\end{aligned}$$

namely,

$$\begin{aligned}
f_1(v_{\min}) &= \frac{1}{\mathcal{A}} \left\{ -2Q \cdot \frac{d}{dQ} \left[\frac{1}{F^2(Q)} \left(\frac{dR}{dQ} \right) \right] \right\}_{Q=v_{\min}^2/\alpha^2} \\
&= \frac{1}{\mathcal{A}} \left\{ \frac{2Q}{F^2(Q)} \left[\frac{2}{F(Q)} \left(\frac{dF}{dQ} \right) \left(\frac{dR}{dQ} \right) - \frac{d}{dQ} \left(\frac{dR}{dQ} \right) \right] \right\}_{Q=v_{\min}^2/\alpha^2}. \quad (A.7)
\end{aligned}$$

On the other hand, according to *Leibnitz's Rule for Differentiation of Integrals*:

$$\frac{d}{dt} \left[\int_{a(t)}^{b(t)} F(x, t) dx \right] = \int_{a(t)}^{b(t)} \left[\frac{\partial F(x, t)}{\partial t} \right] dx + \left[F(b, t) \left(\frac{db}{dt} \right) - F(a, t) \left(\frac{da}{dt} \right) \right], \quad (A.8)$$

one can also differentiate both sides in Eq.(3.12) with respect to Q directly and obtain

$$\begin{aligned}
&\frac{d}{dQ} \left(\frac{dR}{dQ} \right) \\
&= \frac{d}{dQ} \left\{ \mathcal{A} F^2(Q) \int_{v_{\min}}^{\infty} \left[\frac{f_1(v)}{v} \right] dv \right\} \\
&= \mathcal{A} \left[\frac{dF^2(Q)}{dQ} \right] \int_{v_{\min}}^{\infty} \left[\frac{f_1(v)}{v} \right] dv + \mathcal{A} F^2(Q) \left[-\frac{f_1(v_{\min})}{v_{\min}} \left(\frac{dv_{\min}}{dQ} \right) \right]_{v_{\min}=\alpha\sqrt{Q}} \\
&= \left[2F(Q) \left(\frac{dF}{dQ} \right) \right] \left[\frac{1}{F^2(Q)} \left(\frac{dR}{dQ} \right) \right] - \mathcal{A} F^2(Q) \left[\frac{f_1(v_{\min})}{v_{\min}} \left(\frac{v_{\min}}{2Q} \right) \right]_{v_{\min}=\alpha\sqrt{Q}} \\
&= \frac{2}{F(Q)} \left(\frac{dF}{dQ} \right) \left(\frac{dR}{dQ} \right) - \mathcal{A} \left[\frac{F^2(Q)}{2Q} \right] f_1 \left(v_{\min} = \alpha\sqrt{Q} \right).
\end{aligned}$$

Therefore, it can be also found that

$$f_1(v_{\min}) = \frac{1}{\mathcal{A}} \left\{ \frac{2Q}{F^2(Q)} \left[\frac{2}{F(Q)} \left(\frac{dF}{dQ} \right) \left(\frac{dR}{dQ} \right) - \frac{d}{dQ} \left(\frac{dR}{dQ} \right) \right] \right\}_{Q=v_{\min}^2/\alpha^2}. \quad (A.7)$$

A.3 Normalization constant and moments of $f_1(v)$

Since

$$v = \alpha\sqrt{Q}, \quad (A.9)$$

I have

$$dv = \left(\frac{\alpha}{2\sqrt{Q}} \right) dQ. \quad (A.10)$$

From Eq.(4.8) and according to the normalization condition in Eq.(4.7), I can get

$$\begin{aligned}
& \int_0^\infty f_1(v) dv \\
&= \mathcal{N} \int_0^\infty \left\{ -2Q \cdot \frac{d}{dQ} \left[\frac{1}{F^2(Q)} \left(\frac{dR}{dQ} \right) \right] \right\} \left(\frac{\alpha}{2\sqrt{Q}} \right) dQ \\
&= \mathcal{N} \cdot (-\alpha) \int_0^\infty \sqrt{Q} \cdot \frac{d}{dQ} \left[\frac{1}{F^2(Q)} \left(\frac{dR}{dQ} \right) \right] dQ \\
&= \mathcal{N} \cdot (-\alpha) \left\{ \sqrt{Q} \left[\frac{1}{F^2(Q)} \left(\frac{dR}{dQ} \right) \right]_0^\infty - \frac{1}{2} \int_0^\infty \frac{1}{\sqrt{Q}} \left[\frac{1}{F^2(Q)} \left(\frac{dR}{dQ} \right) \right] dQ \right\} \\
&= \mathcal{N} \left(\frac{\alpha}{2} \right) \int_0^\infty \frac{1}{\sqrt{Q}} \left[\frac{1}{F^2(Q)} \left(\frac{dR}{dQ} \right) \right] dQ \\
&= 1,
\end{aligned} \tag{A.11}$$

where I have used the conditions:

$$\left. \frac{dR}{dQ} \right|_{Q \rightarrow \infty} \rightarrow 0, \tag{A.12}$$

and

$$\left. \frac{dR}{dQ} \right|_{Q \rightarrow 0} \neq \infty. \tag{A.13}$$

Eq.(4.9) follows immediately from Eq.(A.11).

Using Eqs.(A.9), (A.10) and integration by parts, I can also find the moments of $f_1(v)$, defined in Eq.(4.10) with a lower cut-off Q_{thre} on the energy transfer, as follows:

$$\begin{aligned}
\langle v^n \rangle &= \int_{v_{\min}(Q_{\text{thre}})}^\infty v^n f_1(v) dv \\
&= \mathcal{N} \int_{Q_{\text{thre}}}^\infty (\alpha\sqrt{Q})^n \left\{ -2Q \cdot \frac{d}{dQ} \left[\frac{1}{F^2(Q)} \left(\frac{dR}{dQ} \right) \right] \right\} \left(\frac{\alpha}{2\sqrt{Q}} \right) dQ \\
&= \mathcal{N} \cdot (-\alpha^{n+1}) \int_{Q_{\text{thre}}}^\infty Q^{(n+1)/2} \cdot \frac{d}{dQ} \left[\frac{1}{F^2(Q)} \left(\frac{dR}{dQ} \right) \right] dQ \\
&= \mathcal{N} \alpha^{n+1} \left\{ \frac{Q_{\text{thre}}^{(n+1)/2}}{F^2(Q_{\text{thre}})} \left(\frac{dR}{dQ} \right) \right. \\
&\quad \left. + \frac{n+1}{2} \int_{Q_{\text{thre}}}^\infty Q^{(n-1)/2} \left[\frac{1}{F^2(Q)} \left(\frac{dR}{dQ} \right) \right] dQ \right\}.
\end{aligned} \tag{A.14}$$

This reproduces Eqs.(4.11) and (4.12) in Sec. 4.1.

Appendix B

Moments of the Velocity Distribution of WIMPs

In this chapter I derive at first the first and second moments of $f_1(v)$, i.e., the mean velocity and the velocity dispersion of WIMPs, for both of the two simplest semi-realistic halo models discussed in Subsecs. 3.1.3 and 3.2.1. Then, as tests of the formulae for reconstructing $f_1(v)$ and determining $\langle v^n \rangle$, I use the reduced spectra given in Eqs.(3.21') and (3.31') in Sec. 4.1 and the expressions for $f_1(v)$ in Eqs.(4.8) and (4.9) as well as for the moments of $f_1(v)$ in Eqs.(4.11) and (4.12) to obtain the same results.

B.1 Calculating $\langle v \rangle$ and $\langle v^2 \rangle$ from $f_1(v)$

B.1.1 From $f_{1,\text{Gau}}(v)$ given in Eq.(3.20)

For a simple isothermal Maxwellian halo, the normalized one-dimensional velocity distribution function has been given as

$$f_{1,\text{Gau}}(v) = \frac{4}{\sqrt{\pi}} \left(\frac{v^2}{v_0^3} \right) e^{-v^2/v_0^2}. \quad (3.20)$$

One can find directly that

$$\begin{aligned} \langle v^n \rangle_{\text{Gau}} &= \int_0^\infty v^n f_{1,\text{Gau}}(v) dv \\ &= \int_0^\infty v^n \left[\frac{4}{\sqrt{\pi}} \left(\frac{v^2}{v_0^3} \right) e^{-v^2/v_0^2} \right] dv \\ &= \frac{4}{\sqrt{\pi} v_0^3} \int_0^\infty v^{n+2} e^{-v^2/v_0^2} dv \\ &= \frac{4}{\sqrt{\pi} v_0^3} \left\{ \frac{\Gamma \left[\frac{1}{2}(n+3) \right]}{2} \cdot (v_0^2)^{(n+3)/2} \right\} \\ &= \left(\frac{2}{\sqrt{\pi}} \right) \Gamma \left[\frac{1}{2}(n+1) + 1 \right] v_0^n \\ &= \left(\frac{n+1}{\sqrt{\pi}} \right) \Gamma \left[\frac{1}{2}(n+1) \right] v_0^n, \end{aligned} \quad (\text{B.1})$$

where I have used

$$\int_0^\infty x^n e^{-ax^2} dx = \frac{\Gamma\left[\frac{1}{2}(n+1)\right]}{2a^{(n+1)/2}},$$

and

$$\Gamma(m+1) = m\Gamma(m),$$

for $m = 0, \frac{1}{2}, 1, \frac{3}{2}, 2, \dots$. Hence, using

$$\Gamma(n+1) = n!,$$

and

$$\Gamma\left(n + \frac{1}{2}\right) = \frac{1 \cdot 3 \cdots (2n-1)\sqrt{\pi}}{2^n},$$

for $n = 0, 1, 2, 3, \dots$, Eqs.(3.22) and (3.23) can be obtained directly.

B.1.2 From $f_{1,\text{sh}}(v)$ given in Eq.(3.29)

When we take into account the orbital motion of the Solar system around the Galaxy, the velocity distribution function should be modified to

$$f_{1,\text{sh}}(v, v_e) = \frac{1}{\sqrt{\pi}} \left(\frac{v}{v_e v_0} \right) \left[e^{-(v-v_e)^2/v_0^2} - e^{-(v+v_e)^2/v_0^2} \right]. \quad (3.29)$$

First, I have

$$\begin{aligned} \langle v \rangle_{\text{sh}} &= \int_0^\infty v f_{1,\text{sh}}(v, v_e) dv \\ &= \frac{1}{\sqrt{\pi} v_e v_0} \int_0^\infty v \cdot v \left[e^{-(v-v_e)^2/v_0^2} - e^{-(v+v_e)^2/v_0^2} \right] dv \\ &= \frac{1}{\sqrt{\pi} v_e} \left[\frac{1}{v_0} \int_0^\infty v^2 e^{-(v-v_e)^2/v_0^2} dv - \frac{1}{v_0} \int_0^\infty v^2 e^{-(v+v_e)^2/v_0^2} dv \right] \\ &= \frac{1}{\sqrt{\pi} v_e} (\mathbf{V}_{1,-} - \mathbf{V}_{1,+}). \end{aligned} \quad (B.2)$$

Define

$$u_\pm \equiv \frac{v \pm v_e}{v_0}, \quad (B.3a)$$

i.e.,

$$v = v_0 u_\pm \mp v_e, \quad (B.3b)$$

it can be found that

$$\begin{aligned}
\mathbf{V}_{1,-} &\equiv \frac{1}{v_0} \int_0^\infty v^2 e^{-(v-v_e)^2/v_0^2} dv \\
&= \frac{1}{v_0} \int_{-\tilde{v}_e}^\infty (v_0 u_- + v_e)^2 e^{-u_-^2} (v_0 du_-) \\
&= v_0^2 \int_{-\tilde{v}_e}^\infty u_-^2 e^{-u_-^2} du_- + 2v_e v_0 \int_{-\tilde{v}_e}^\infty u_- e^{-u_-^2} du_- + v_e^2 \int_{-\tilde{v}_e}^\infty e^{-u_-^2} du_- \\
&= v_0^2 \left(2 \int_0^{\tilde{v}_e} u_-^2 e^{-u_-^2} du_- + \int_{\tilde{v}_e}^\infty u_-^2 e^{-u_-^2} du_- \right) + 2v_e v_0 \int_{\tilde{v}_e}^\infty u_- e^{-u_-^2} du_- \\
&\quad + v_e^2 \left(2 \int_0^{\tilde{v}_e} e^{-u_-^2} du_- + \int_{\tilde{v}_e}^\infty e^{-u_-^2} du_- \right), \tag{B.4a}
\end{aligned}$$

and

$$\begin{aligned}
\mathbf{V}_{1,+} &\equiv \frac{1}{v_0} \int_0^\infty v^2 e^{-(v+v_e)^2/v_0^2} dv \\
&= \frac{1}{v_0} \int_{\tilde{v}_e}^\infty (v_0 u_+ - v_e)^2 e^{-u_+^2} (v_0 du_+) \\
&= v_0^2 \int_{\tilde{v}_e}^\infty u_+^2 e^{-u_+^2} du_+ - 2v_e v_0 \int_{\tilde{v}_e}^\infty u_+ e^{-u_+^2} du_+ + v_e^2 \int_{\tilde{v}_e}^\infty e^{-u_+^2} du_+, \tag{B.4b}
\end{aligned}$$

where I have defined

$$\tilde{v}_e \equiv \frac{v_e}{v_0}. \tag{B.5}$$

Combining Eqs.(B.4a) and (B.4b), one can get

$$\begin{aligned}
&\mathbf{V}_{1,-} - \mathbf{V}_{1,+} \\
&= 2v_0^2 \int_0^{\tilde{v}_e} u^2 e^{-u^2} du + 2v_e v_0 \int_{\tilde{v}_e}^\infty e^{-u^2} du^2 + 2v_e^2 \int_0^{\tilde{v}_e} e^{-u^2} du \\
&= 2v_0^2 \left[-\frac{1}{2} (\tilde{v}_e e^{-\tilde{v}_e^2}) + \left(\frac{\sqrt{\pi}}{4} \right) \text{erf}(\tilde{v}_e) \right] + 2v_e v_0 e^{-\tilde{v}_e^2} + 2v_e^2 \left[\left(\frac{\sqrt{\pi}}{2} \right) \text{erf}(\tilde{v}_e) \right] \\
&= v_e v_0 e^{-v_e^2/v_0^2} + \sqrt{\pi} \left(\frac{v_0^2}{2} + v_e^2 \right) \text{erf} \left(\frac{v_e}{v_0} \right), \tag{B.6}
\end{aligned}$$

where I have used the definition of error function

$$\text{erf}(x) = \frac{2}{\sqrt{\pi}} \int_0^x e^{-t^2} dt,$$

and

$$\int_0^x t^2 e^{-t^2} dt = -\frac{1}{2} (x e^{-x^2}) + \left(\frac{\sqrt{\pi}}{4} \right) \text{erf}(x).$$

Hence, the mean velocity of WIMPs for a shifted Maxwellian halo discussed in Sub-sec. 3.2.1 can be found as

$$\langle v \rangle_{\text{sh}} = \left(\frac{v_0}{\sqrt{\pi}} \right) e^{-v_e^2/v_0^2} + \left(\frac{v_0^2}{2v_e} + v_e \right) \text{erf} \left(\frac{v_e}{v_0} \right). \tag{3.32}$$

Meanwhile,

$$\begin{aligned}
\langle v^2 \rangle_{\text{sh}} &= \int_0^\infty v^2 f_{1,\text{sh}}(v, v_e) dv \\
&= \frac{1}{\sqrt{\pi} v_e v_0} \int_0^\infty v^2 \cdot v \left[e^{-(v-v_e)^2/v_0^2} - e^{-(v+v_e)^2/v_0^2} \right] dv \\
&= \frac{1}{\sqrt{\pi} v_e} \left[\frac{1}{v_0} \int_0^\infty v^3 e^{-(v-v_e)^2/v_0^2} dv - \frac{1}{v_0} \int_0^\infty v^3 e^{-(v+v_e)^2/v_0^2} dv \right] \\
&= \frac{1}{\sqrt{\pi} v_e} (\mathbf{V}_{2,-} - \mathbf{V}_{2,+}). \tag{B.7}
\end{aligned}$$

Using Eqs.(B.3a), (B.3b), and (B.5), it can be found that

$$\begin{aligned}
\mathbf{V}_{2,-} &\equiv \frac{1}{v_0} \int_0^\infty v^3 e^{-(v-v_e)^2/v_0^2} dv \\
&= \frac{1}{v_0} \int_{-\tilde{v}_e}^\infty (v_0 u_- + v_e)^3 e^{-u_-^2} (v_0 du_-) \\
&= v_0^3 \int_{-\tilde{v}_e}^\infty u_-^3 e^{-u_-^2} du_- + 3v_e v_0^2 \int_{-\tilde{v}_e}^\infty u_-^2 e^{-u_-^2} du_- \\
&\quad + 3v_e^2 v_0 \int_{-\tilde{v}_e}^\infty u_- e^{-u_-^2} du_- + v_e^3 \int_{-\tilde{v}_e}^\infty e^{-u_-^2} du_- \\
&= v_0^3 \int_{\tilde{v}_e}^\infty u_-^3 e^{-u_-^2} du_- + 3v_e v_0^2 \left(\int_0^{\tilde{v}_e} u_-^2 e^{-u_-^2} du_- + \int_0^\infty u_-^2 e^{-u_-^2} du_- \right) \\
&\quad + 3v_e^2 v_0 \int_{\tilde{v}_e}^\infty u_- e^{-u_-^2} du_- + v_e^3 \left(\int_0^{\tilde{v}_e} e^{-u_-^2} du_- + \int_0^\infty e^{-u_-^2} du_- \right), \tag{B.8a}
\end{aligned}$$

and

$$\begin{aligned}
\mathbf{V}_{2,+} &\equiv \frac{1}{v_0} \int_0^\infty v^3 e^{-(v+v_e)^2/v_0^2} dv \\
&= \frac{1}{v_0} \int_{\tilde{v}_e}^\infty (v_0 u_+ - v_e)^3 e^{-u_+^2} (v_0 du_+) \\
&= v_0^3 \int_{\tilde{v}_e}^\infty u_+^3 e^{-u_+^2} du_+ - 3v_e v_0^2 \int_{\tilde{v}_e}^\infty u_+^2 e^{-u_+^2} du_+ \\
&\quad + 3v_e^2 v_0 \int_{\tilde{v}_e}^\infty u_+ e^{-u_+^2} du_+ - v_e^3 \int_{\tilde{v}_e}^\infty e^{-u_+^2} du_+. \tag{B.8b}
\end{aligned}$$

Combining them, one can get

$$\begin{aligned}
\mathbf{V}_{2,-} - \mathbf{V}_{2,+} &= 6v_e v_0^2 \int_0^\infty u^2 e^{-u^2} du + 2v_e^3 \int_0^\infty e^{-u^2} du \\
&= 6v_e v_0^2 \left(\frac{\Gamma\left(\frac{3}{2}\right)}{2} \right) + 2v_e^3 \left(\frac{\sqrt{\pi}}{2} \right) \\
&= \left(\frac{3\sqrt{\pi}}{2} \right) v_e v_0^2 + \sqrt{\pi} v_e^3. \tag{B.9}
\end{aligned}$$

Therefore, the mean velocity of WIMPs for a shifted Maxwellian halo can be found as

$$\langle v^2 \rangle_{\text{sh}} = \left(\frac{3}{2} \right) v_0^2 + v_e^2. \tag{3.33}$$

Finally, according to Leibnitz's Rule for Differentiation of Integrals given in Eq.(A.8), one has

$$\frac{d}{dx} [\text{erf}(x)] = \frac{2}{\sqrt{\pi}} \left[\frac{d}{dx} \int_0^x e^{-t^2} dt \right] = \frac{2}{\sqrt{\pi}} e^{-x^2}. \quad (\text{B.10})$$

Then it is easily to prove that, for $v_e \ll v_0$, i.e., $\tilde{v}_e \ll 1$, Eqs.(3.32) and (3.33) will reduce to Eqs.(3.22) to (3.23).

B.2 Calculating $f_1(v)$, $\langle v \rangle$, and $\langle v^2 \rangle$ from dR/dQ

B.2.1 From $(dR/dQ)_{\text{Gau}}$ in Eq.(3.21)

Substituting Eq.(3.21') in Sec. 4.1 into Eq.(4.8), I have

$$\begin{aligned} f_{1,\text{Gau}}(v) &= \mathcal{N}_{\text{Gau}} \left\{ -2Q \cdot \frac{d}{dQ} \left[\frac{1}{F^2(Q)} \left(\frac{dR}{dQ} \right)_{\text{Gau}} \right] \right\}_{Q=v^2/\alpha^2} \\ &= \mathcal{N}_{\text{Gau}} \left[-2Q \cdot \frac{d}{dQ} \left(e^{-\alpha^2 Q/v_0^2} \right) \right]_{Q=v^2/\alpha^2} \\ &= \mathcal{N}_{\text{Gau}} \left[2 \left(\frac{v}{v_0} \right)^2 e^{-v^2/v_0^2} \right]. \end{aligned} \quad (\text{B.11})$$

Meanwhile, according to Eq.(4.9), the normalization constant \mathcal{N}_{Gau} can be found as

$$\begin{aligned} \mathcal{N}_{\text{Gau}} &= \frac{2}{\alpha} \left\{ \int_0^\infty \frac{1}{\sqrt{Q}} \left[\frac{1}{F^2(Q)} \left(\frac{dR}{dQ} \right)_{\text{Gau}} \right] dQ \right\}^{-1} \\ &= \frac{1}{\alpha} \left\{ \int_0^\infty \left[\frac{1}{F^2(Q)} \left(\frac{dR}{dQ} \right)_{\text{Gau}} \right]_{Q=q^2} dq \right\}^{-1} \\ &= \frac{1}{\alpha} \left(\int_0^\infty e^{-\alpha^2 q^2/v_0^2} dq \right)^{-1} \\ &= \frac{1}{\alpha} \left(\frac{v_0}{\alpha} \cdot \frac{\sqrt{\pi}}{2} \right)^{-1} \\ &= \frac{2}{\sqrt{\pi} v_0}. \end{aligned} \quad (\text{B.12})$$

Here, for simplicity, I have defined ¹:

$$Q = q^2, \quad (\text{B.13a})$$

and then

$$dQ = 2q dq. \quad (\text{B.13b})$$

Substituting Eq.(B.12) into Eq.(B.11), the normalized one-dimensional velocity distribution function $f_{1,\text{Gau}}(v)$ in Eq.(3.20) can be obtained directly. Moreover, substituting

¹I will use this definition in this section and the next chapter. Please do not confuse with the transferred 3-momentum in Eq.(3.7).

Eq.(3.21') into Eqs.(4.12) and (4.11) and using the normalization constant in Eq.(B.12), one can get

$$\begin{aligned}
\langle v^n \rangle_{\text{Gau}} &= \mathcal{N}_{\text{Gau}} \left(\frac{\alpha^{n+1}}{2} \right) \cdot (n+1) \int_0^\infty Q^{(n-1)/2} \left[\frac{1}{F^2(Q)} \left(\frac{dR}{dQ} \right)_{\text{Gau}} \right] dQ \\
&= \mathcal{N}_{\text{Gau}} (n+1) \left(\frac{\alpha^{n+1}}{2} \right) \int_0^\infty Q^{(n-1)/2} e^{-\alpha^2 Q/v_0^2} dQ \\
&= \mathcal{N}_{\text{Gau}} (n+1) \left(\frac{\alpha^{n+1}}{2} \right) \int_0^\infty q^{n-1} e^{-\alpha^2 q^2/v_0^2} (2q dq) \\
&= \left(\frac{2}{\sqrt{\pi} v_0} \right) (n+1) \alpha^{n+1} \left\{ \frac{1}{2} \left(\frac{v_0}{\alpha} \right)^{n+1} \Gamma \left[\frac{1}{2} (n+1) \right] \right\} \\
&= \left(\frac{n+1}{\sqrt{\pi}} \right) \Gamma \left[\frac{1}{2} (n+1) \right] v_0^n. \tag{B.1}
\end{aligned}$$

Note that I have set $Q_{\text{thre}} = 0$ here.

B.2.2 From $(dR/dQ)_{\text{sh}}$ in Eq.(3.31)

According to Eq.(B.10), one can obtain that

$$\frac{d}{dQ} \left[\text{erf} \left(\frac{\alpha \sqrt{Q} \pm v_e}{v_0} \right) \right] = \frac{1}{\sqrt{\pi}} \left(\frac{\alpha}{v_0} \right) \left[\frac{1}{\sqrt{Q}} e^{-[(\alpha \sqrt{Q} \pm v_e)/v_0]^2} \right]. \tag{B.14}$$

Then, substituting Eq.(3.31') in Sec. 4.1 into Eq.(4.8), I have

$$\begin{aligned}
&f_{1,\text{sh}}(v, v_e) \\
&= \mathcal{N}_{\text{sh}} \left\{ -2Q \cdot \frac{d}{dQ} \left[\frac{1}{F^2(Q)} \left(\frac{dR}{dQ} \right)_{\text{sh}} \right] \right\}_{Q=v^2/\alpha^2} \\
&= \mathcal{N}_{\text{sh}} \left\{ -2Q \cdot \frac{d}{dQ} \left[\text{erf} \left(\frac{\alpha \sqrt{Q} + v_e}{v_0} \right) - \text{erf} \left(\frac{\alpha \sqrt{Q} - v_e}{v_0} \right) \right] \right\}_{Q=v^2/\alpha^2} \\
&= \mathcal{N}_{\text{sh}} \left\{ -2Q \cdot \frac{1}{\sqrt{\pi}} \left(\frac{\alpha}{v_0} \right) \frac{1}{\sqrt{Q}} \left\{ e^{-[(\alpha \sqrt{Q} + v_e)/v_0]^2} - e^{-[(\alpha \sqrt{Q} - v_e)/v_0]^2} \right\} \right\}_{Q=v^2/\alpha^2} \\
&= \mathcal{N}_{\text{sh}} \cdot \frac{2}{\sqrt{\pi}} \left(\frac{v}{v_0} \right) \left[e^{-(v-v_e)^2/v_0^2} - e^{-(v+v_e)^2/v_0^2} \right]. \tag{B.15}
\end{aligned}$$

Meanwhile, as done for \mathcal{N}_{Gau} in Eq.(B.12), one can use Eqs.(B.13a) and (B.13b) and find that

$$\begin{aligned}
\mathcal{N}_{\text{sh}} &= \frac{1}{\alpha} \left\{ \int_0^\infty \left[\frac{1}{F^2(Q)} \left(\frac{dR}{dQ} \right)_{\text{sh}} \right]_{Q=q^2} dq \right\}^{-1} \\
&= \frac{1}{\alpha} \left\{ \int_0^\infty \left[\text{erf} \left(\frac{\alpha q + v_e}{v_0} \right) - \text{erf} \left(\frac{\alpha q - v_e}{v_0} \right) \right] dq \right\}^{-1} \\
&= \frac{1}{\alpha} \left[\mathbf{V}_0(\infty) - \mathbf{V}_0(0) \right]^{-1}, \tag{B.16}
\end{aligned}$$

where I have defined

$$\mathbf{V}_0(q) \equiv \int \left[\operatorname{erf} \left(\frac{\alpha q + v_e}{v_0} \right) - \operatorname{erf} \left(\frac{\alpha q - v_e}{v_0} \right) \right] dq \equiv \mathbf{V}_{0,+}(q) - \mathbf{V}_{0,-}(q). \quad (\text{B.17})$$

Define

$$s_{\pm} \equiv \frac{\alpha q \pm v_e}{v_0}, \quad (\text{B.18a})$$

i.e.,

$$q = \frac{v_0 s_{\pm} \mp v_e}{\alpha}, \quad (\text{B.18b})$$

it can be found that

$$\begin{aligned} \mathbf{V}_{0,\pm}(q) &\equiv \int \operatorname{erf} \left(\frac{\alpha q \pm v_e}{v_0} \right) dq \\ &= \int \operatorname{erf}(s_{\pm}) \left[\left(\frac{v_0}{\alpha} \right) ds_{\pm} \right] \\ &= \frac{v_0}{\alpha} \int \operatorname{erf}(s_{\pm}) ds_{\pm} \\ &= \frac{v_0}{\alpha} \left[s_{\pm} \operatorname{erf}(s_{\pm}) + \frac{1}{\sqrt{\pi}} e^{-s_{\pm}^2} \right] \\ &= \left(q \pm \frac{v_e}{\alpha} \right) \operatorname{erf}(s_{\pm}) + \frac{1}{\sqrt{\pi}} \left(\frac{v_0}{\alpha} \right) e^{-s_{\pm}^2}, \end{aligned} \quad (\text{B.19})$$

where I have used

$$\int \operatorname{erf}(x) dx = x \operatorname{erf}(x) + \frac{1}{\sqrt{\pi}} e^{-x^2}.$$

Substituting $\mathbf{V}_{0,\pm}(q)$ in Eq.(B.19) into Eq.(B.17), I can get

$$\mathbf{V}_0(q) = q [\operatorname{erf}(s_+) - \operatorname{erf}(s_-)] + \frac{v_e}{\alpha} [\operatorname{erf}(s_+) + \operatorname{erf}(s_-)] + \frac{1}{\sqrt{\pi}} \left(\frac{v_0}{\alpha} \right) (e^{-s_+^2} - e^{-s_-^2}). \quad (\text{B.20})$$

Now note that, as $q \rightarrow \infty$,

$$\mathbf{V}_0(q \rightarrow \infty) = \left(\frac{2}{\alpha} \right) v_e, \quad (\text{B.21})$$

since

$$s_{\pm}(q \rightarrow \infty) \rightarrow \infty, \quad (\text{B.22})$$

and

$$\operatorname{erf}(\infty) = \frac{2}{\sqrt{\pi}} \int_0^{\infty} e^{-t^2} dt = 1.$$

While, since as $q = 0$,

$$s_{\pm}(0) = \pm \frac{v_e}{v_0} = \pm \tilde{v}_e, \quad (\text{B.23})$$

where I have used the definition in Eq.(B.18a), and

$$\operatorname{erf}(-x) = -\operatorname{erf}(x),$$

it can be found that

$$\mathbf{V}_0(0) = 0. \quad (\text{B.24})$$

Substituting Eqs.(B.22) and (B.24) into Eq.(B.16), the normalization constant \mathcal{N}_{sh} can be found as

$$\mathcal{N}_{\text{sh}} = \frac{1}{\alpha} \left[\left(\frac{2}{\alpha} \right) v_e \right]^{-1} = \frac{1}{2v_e}. \quad (\text{B.25})$$

Then I can obtain the normalized velocity distribution function in Eq.(3.29) directly. Meanwhile, substituting Eq.(3.31') into Eq.(4.11) ($Q_{\text{thre}} = 0$) and using Eqs.(B.13a) and (B.13b), I have

$$\begin{aligned} \langle v \rangle_{\text{sh}} &= \mathcal{N}_{\text{sh}} \cdot \alpha^2 \int_0^\infty \left[\frac{1}{F^2(Q)} \left(\frac{dR}{dQ} \right)_{\text{sh}} \right]_{Q=q^2} (2q dq) \\ &= \frac{1}{2v_e} \cdot 2\alpha^2 \int_0^\infty q \left[\operatorname{erf} \left(\frac{\alpha q + v_e}{v_0} \right) - \operatorname{erf} \left(\frac{\alpha q - v_e}{v_0} \right) \right] dq \\ &= \frac{\alpha^2}{v_e} [\mathbf{V}_1(\infty) - \mathbf{V}_1(0)], \end{aligned} \quad (\text{B.26})$$

where I have defined

$$\mathbf{V}_1(q) \equiv \int q \left[\operatorname{erf} \left(\frac{\alpha q + v_e}{v_0} \right) - \operatorname{erf} \left(\frac{\alpha q - v_e}{v_0} \right) \right] dq \equiv \mathbf{V}_{1,+}(q) - \mathbf{V}_{1,-}(q). \quad (\text{B.27})$$

Using Eqs.(B.18a) and (B.18b), it can be found that

$$\begin{aligned} &\mathbf{V}_{1,\pm}(q) \\ &\equiv \int q \operatorname{erf} \left(\frac{\alpha q \pm v_e}{v_0} \right) dq \\ &= \frac{v_0}{\alpha} \int \left(\frac{v_0 s_\pm \mp v_e}{\alpha} \right) \operatorname{erf}(s_\pm) ds_\pm \\ &= \left(\frac{v_0}{\alpha} \right)^2 \int s_\pm \operatorname{erf}(s_\pm) ds_\pm \mp \frac{v_e v_0}{\alpha^2} \int \operatorname{erf}(s_\pm) ds_\pm \\ &= \frac{1}{2} \left(\frac{v_0}{\alpha} \right)^2 \left[\left(s_\pm^2 - \frac{1}{2} \right) \operatorname{erf}(s_\pm) + \frac{1}{\sqrt{\pi}} s_\pm e^{-s_\pm^2} \right] \mp \frac{v_e v_0}{\alpha^2} \left[s_\pm \operatorname{erf}(s_\pm) + \frac{1}{\sqrt{\pi}} e^{-s_\pm^2} \right] \\ &= \frac{1}{2} \left(\frac{v_0}{\alpha} \right)^2 \left\{ \left(s_\pm \mp \frac{2v_e}{v_0} \right) \left[s_\pm \operatorname{erf}(s_\pm) + \frac{1}{\sqrt{\pi}} e^{-s_\pm^2} \right] - \frac{1}{2} \operatorname{erf}(s_\pm) \right\} \\ &= \frac{1}{2} \left(\frac{v_0}{\alpha} \right)^2 \left[\left(s_+ s_- - \frac{1}{2} \right) \operatorname{erf}(s_\pm) + \frac{1}{\sqrt{\pi}} s_\mp e^{-s_\pm^2} \right], \end{aligned} \quad (\text{B.28})$$

where I have used

$$\int x \operatorname{erf}(x) dx = \frac{1}{2} \left[\left(x^2 - \frac{1}{2} \right) \operatorname{erf}(x) + \frac{1}{\sqrt{\pi}} x e^{-x^2} \right],$$

and

$$v_0 s_{\pm} \mp 2v_e = (\alpha q \pm v_e) \mp 2v_e = \alpha q \mp v_e = v_0 s_{\mp}. \quad (\text{B.29})$$

Hence, I can get

$$\mathbf{V}_1(q) = \frac{1}{2} \left(\frac{v_0}{\alpha} \right)^2 \left\{ \left(s_+ s_- - \frac{1}{2} \right) \left[\text{erf}(s_+) - \text{erf}(s_-) \right] + \frac{1}{\sqrt{\pi}} \left(s_- e^{-s_+^2} - s_+ e^{-s_-^2} \right) \right\}. \quad (\text{B.30})$$

From Eq.(B.22), it can be found easily that

$$\mathbf{V}_1(q \rightarrow \infty) = 0, \quad (\text{B.31})$$

and, from Eq.(B.23),

$$\mathbf{V}_1(0) = - \left(\frac{v_0}{\alpha} \right)^2 \left[\left(\tilde{v}_e^2 + \frac{1}{2} \right) \text{erf}(\tilde{v}_e) + \frac{1}{\sqrt{\pi}} \left(\tilde{v}_e e^{-\tilde{v}_e^2} \right) \right]. \quad (\text{B.32})$$

Therefore, substituting these results into Eq.(B.26), I can obtain that

$$\begin{aligned} \langle v \rangle_{\text{sh}} &= \frac{\alpha^2}{v_e} \left\{ \left(\frac{v_0}{\alpha} \right)^2 \left[\left(\tilde{v}_e^2 + \frac{1}{2} \right) \text{erf}(\tilde{v}_e) + \frac{1}{\sqrt{\pi}} \left(\tilde{v}_e e^{-\tilde{v}_e^2} \right) \right] \right\} \\ &= \left(v_e + \frac{v_0^2}{2v_e} \right) \text{erf} \left(\frac{v_e}{v_0} \right) + \left(\frac{v_0}{\sqrt{\pi}} \right) e^{-v_e^2/v_0^2}. \end{aligned} \quad (\text{3.32})$$

Similarly,

$$\begin{aligned} \langle v^2 \rangle_{\text{sh}} &= \mathcal{N}_{\text{sh}} \cdot \left(\frac{3}{2} \right) \alpha^3 \int_0^\infty q \left[\frac{1}{F^2(Q)} \left(\frac{dR}{dQ} \right)_{\text{sh}} \right]_{Q=q^2} (2q dq) \\ &= \frac{1}{2v_e} \cdot 3\alpha^3 \int_0^\infty q^2 \left[\text{erf} \left(\frac{\alpha q + v_e}{v_0} \right) - \text{erf} \left(\frac{\alpha q - v_e}{v_0} \right) \right] dq \\ &= \frac{3}{2} \left(\frac{\alpha^3}{v_e} \right) \left[\mathbf{V}_2(\infty) - \mathbf{V}_2(0) \right], \end{aligned} \quad (\text{B.33})$$

where I have defined

$$\mathbf{V}_2(q) \equiv \int q^2 \left[\text{erf} \left(\frac{\alpha q + v_e}{v_0} \right) - \text{erf} \left(\frac{\alpha q - v_e}{v_0} \right) \right] dq \equiv \mathbf{V}_{2,+}(q) - \mathbf{V}_{2,-}(q). \quad (\text{B.34})$$

Using Eqs.(B.18a) and (B.18b), it can be found that

$$\begin{aligned} \mathbf{V}_{2,\pm}(q) &\equiv \int q^2 \text{erf} \left(\frac{\alpha q \pm v_e}{v_0} \right) dq \\ &= \frac{v_0}{\alpha} \int \left(\frac{v_0 s_{\pm} \mp v_e}{\alpha} \right)^2 \text{erf}(s_{\pm}) ds_{\pm} \\ &= \left(\frac{v_0}{\alpha^3} \right) \int \left(v_0^2 s_{\pm}^2 \mp 2v_e v_0 s_{\pm} + v_e^2 \right) \text{erf}(s_{\pm}) ds_{\pm} \\ &= \left(\frac{v_0}{\alpha} \right)^3 \left[\int s_{\pm}^2 \text{erf}(s_{\pm}) ds_{\pm} \mp 2\tilde{v}_e \int s_{\pm} \text{erf}(s_{\pm}) ds_{\pm} + \tilde{v}_e^2 \int \text{erf}(s_{\pm}) ds_{\pm} \right] \end{aligned}$$

$$\begin{aligned}
&= \left(\frac{v_0}{\alpha}\right)^3 \left\{ \frac{1}{3} \left[s_{\pm}^3 \operatorname{erf}(s_{\pm}) + \frac{1}{\sqrt{\pi}} (s_{\pm}^2 + 1) e^{-s_{\pm}^2} \right] \right. \\
&\quad \mp \tilde{v}_e \left[\left(s_{\pm}^2 - \frac{1}{2} \right) \operatorname{erf}(s_{\pm}) + \frac{1}{\sqrt{\pi}} s_{\pm} e^{-s_{\pm}^2} \right] \\
&\quad \left. + \tilde{v}_e^2 \left[s_{\pm} \operatorname{erf}(s_{\pm}) + \frac{1}{\sqrt{\pi}} e^{-s_{\pm}^2} \right] \right\} \\
&= \left(\frac{v_0}{\alpha}\right)^3 \left\{ \left[\frac{1}{3} \left(\frac{\alpha}{v_0}\right)^3 q^3 \pm \left(\frac{\tilde{v}_e^3}{3} + \frac{\tilde{v}_e}{2}\right) \right] \operatorname{erf}(s_{\pm}) \right. \\
&\quad \left. + \frac{1}{\sqrt{\pi}} \left(\frac{s_{\pm}^2}{3} \mp \tilde{v}_e s_{\pm} + \tilde{v}_e^2 + \frac{1}{3} \right) e^{-s_{\pm}^2} \right\}, \tag{B.35}
\end{aligned}$$

where I have used

$$\int x^2 \operatorname{erf}(x) dx = \frac{1}{3} \left[x^3 \operatorname{erf}(x) + \frac{1}{\sqrt{\pi}} (x^2 + 1) e^{-x^2} \right],$$

and

$$\begin{aligned}
\frac{s_{\pm}^3}{3} \mp \tilde{v}_e s_{\pm}^2 + \tilde{v}_e^2 s_{\pm} &= \frac{1}{3} \left[(s_{\pm}^3 \mp 3\tilde{v}_e s_{\pm}^2 + 3\tilde{v}_e^2 s_{\pm} \mp \tilde{v}_e^3) \pm \tilde{v}_e^3 \right] \\
&= \frac{1}{3} \left(\frac{v_0 s_{\pm} \mp v_e}{v_0} \right)^3 \pm \frac{\tilde{v}_e^3}{3} \\
&= \frac{1}{3} \left(\frac{\alpha}{v_0} \right)^3 q^3 \pm \frac{\tilde{v}_e^3}{3}. \tag{B.36}
\end{aligned}$$

Hence, I can get

$$\begin{aligned}
\mathbf{V}_2(q) &= \left(\frac{v_0}{\alpha}\right)^3 \left\{ \frac{1}{3} \left(\frac{\alpha}{v_0}\right)^3 q^3 \left[\operatorname{erf}(s_+) - \operatorname{erf}(s_-) \right] + \left(\frac{\tilde{v}_e^3}{3} + \frac{\tilde{v}_e}{2}\right) \left[\operatorname{erf}(s_+) + \operatorname{erf}(s_-) \right] \right. \\
&\quad \left. + \frac{1}{\sqrt{\pi}} \left[\left(\frac{s_+}{3} - \tilde{v}_e \right) s_+ e^{-s_+^2} - \left(\frac{s_-}{3} + \tilde{v}_e \right) s_- e^{-s_-^2} \right] \right. \\
&\quad \left. + \frac{1}{\sqrt{\pi}} \left(\tilde{v}_e^2 + \frac{1}{3} \right) (e^{-s_+^2} - e^{-s_-^2}) \right\}. \tag{B.37}
\end{aligned}$$

From Eq.(B.22), it can be found easily that

$$\mathbf{V}_2(q \rightarrow \infty) = \left(\frac{v_0}{\alpha}\right)^3 \left[2 \left(\frac{\tilde{v}_e^3}{3} + \frac{\tilde{v}_e}{2} \right) \right] = \frac{v_e}{\alpha^3} \left[\left(\frac{2}{3} \right) v_e^2 + v_0^2 \right], \tag{B.38}$$

and, from Eq.(B.22),

$$\mathbf{V}_2(0) = 0. \tag{B.39}$$

Therefore, substituting these results into Eq.(B.33), I can obtain that

$$\langle v^2 \rangle_{\text{sh}} = \frac{3}{2} \left(\frac{\alpha^3}{v_e} \right) \left\{ \frac{v_e}{\alpha^3} \left[\left(\frac{2}{3} \right) v_e^2 + v_0^2 \right] \right\} = v_e^2 + \left(\frac{3}{2} \right) v_0^2. \tag{3.33}$$

Appendix C

Differential and Total Event Rates

In this chapter I derive the differential and total event rates for the simple and shifted isothermal Maxwellian halo models from their velocity distribution functions given in Eqs.(3.20) and (3.29). The case for $F^2(Q) \approx 1$ and the case with the exponential form factor $F_{\text{ex}}^2(Q)$ given in Eq.(3.15) will be considered.

C.1 Setting $F^2(Q) \approx 1$

C.1.1 Starting with $f_{1,\text{Gau}}(v)$ given in Eq.(3.20)

For a simple isothermal Maxwellian halo, the normalized one-dimensional velocity distribution function has been given as

$$f_{1,\text{Gau}}(v) = \frac{4}{\sqrt{\pi}} \left(\frac{v^2}{v_0^3} \right) e^{-v^2/v_0^2}. \quad (3.20)$$

I can get directly that

$$\begin{aligned} \int_{v_{\min}}^{\infty} \left[\frac{f_{1,\text{Gau}}(v)}{v} \right] dv &= \int_{v_{\min}}^{\infty} \frac{1}{v} \left[\frac{4}{\sqrt{\pi}} \left(\frac{v^2}{v_0^3} \right) e^{-v^2/v_0^2} \right] dv \\ &= \frac{4}{\sqrt{\pi} v_0^3} \int_{v_{\min}}^{\infty} v e^{-v^2/v_0^2} dv \\ &= \frac{2}{\sqrt{\pi} v_0^3} \int_{v_{\min}}^{\infty} e^{-v^2/v_0^2} dv^2 \\ &= \left(\frac{2}{\sqrt{\pi} v_0} \right) e^{-v_{\min}^2/v_0^2}. \end{aligned} \quad (C.1)$$

Using this result and Eqs.(3.10) and (3.12), one can obtain $(dR/dQ)_{\text{Gau}}$ in Eq.(3.21) and then $R_{\text{Gau}}(Q_{\text{thre}})$ in Eq.(3.24) easily when $F^2(Q)$ has been neglected.

C.1.2 Starting with $f_{1,\text{sh}}(v)$ given in Eq.(3.29)

When we take into account the orbital motion of the Solar system around the Galaxy, the velocity distribution function should be modified to

$$f_{1,\text{sh}}(v, v_e) = \frac{1}{\sqrt{\pi}} \left(\frac{v}{v_e v_0} \right) \left[e^{-(v-v_e)^2/v_0^2} - e^{-(v+v_e)^2/v_0^2} \right]. \quad (3.29)$$

First, using Eqs.(B.3a) and (B.3b), it can be found that

$$\begin{aligned}
\int_{v_{\min}}^{\infty} \left[\frac{f_{1,\text{sh}}(v)}{v} \right] dv &= \frac{1}{\sqrt{\pi} v_e v_0} \left[\int_{v_{\min}}^{\infty} e^{-(v-v_e)^2/v_0^2} dv - \int_{v_{\min}}^{\infty} e^{-(v+v_e)^2/v_0^2} dv \right] \\
&= \frac{1}{\sqrt{\pi} v_e v_0} \left[\int_{u_{-, \min}}^{\infty} e^{-u_-^2} (v_0 du_-) - \int_{u_{+, \min}}^{\infty} e^{-u_+^2} (v_0 du_+) \right] \\
&= \frac{1}{\sqrt{\pi} v_e} \cdot \frac{\sqrt{\pi}}{2} \left[\text{erfc}(u_{-, \min}) - \text{erfc}(u_{+, \min}) \right] \\
&= \frac{1}{2v_e} \left[\text{erf}(u_{+, \min}) - \text{erf}(u_{-, \min}) \right], \tag{C.2}
\end{aligned}$$

where I have used the definition

$$\text{erfc}(x) = \frac{2}{\sqrt{\pi}} \int_x^{\infty} e^{-t^2} dt = 1 - \text{erf}(x),$$

and

$$u_{\pm, \min} \equiv \frac{v_{\min} \pm v_e}{v_0}. \tag{C.3}$$

Combining Eqs.(C.2) and (C.3) with Eqs.(3.10) and (3.12), one can obtain $(dR/dQ)_{\text{sh}}$ in Eq.(3.31). Moreover, by using Eqs.(B.13a) and (B.13b), one can find that

$$\begin{aligned}
&\int_{Q_{\text{thre}}}^{\infty} \left[\text{erf}\left(\frac{\alpha\sqrt{Q}+v_e}{v_0}\right) - \text{erf}\left(\frac{\alpha\sqrt{Q}-v_e}{v_0}\right) \right] dQ \\
&= \int_{q_{\text{thre}}}^{\infty} \left[\text{erf}\left(\frac{\alpha q + v_e}{v_0}\right) - \text{erf}\left(\frac{\alpha q - v_e}{v_0}\right) \right] (2q dq) \\
&= 2 \left[\mathbf{V}_1(q \rightarrow \infty) - \mathbf{V}_1(q_{\text{thre}}) \right] \\
&= \left(\frac{v_0}{\alpha} \right)^2 \left\{ \left(\frac{1}{2} - S_+ S_- \right) \left[\text{erf}(S_+) - \text{erf}(S_-) \right] + \frac{1}{\sqrt{\pi}} \left(S_+ e^{-S_-^2} - S_- e^{-S_+^2} \right) \right\}. \tag{C.4}
\end{aligned}$$

Here I have defined

$$q_{\text{thre}} \equiv \sqrt{Q_{\text{thre}}}, \tag{C.5}$$

and used Eqs.(B.27), (B.31), (B.30), (B.18a), and (3.35). Hence, for $F^2(Q) \approx 1$, one can get $R_{\text{sh}}(Q_{\text{thre}})$ in Eq.(3.34) directly.

C.2 Using $F_{\text{ex}}^2(Q)$ given in Eq.(3.15)

C.2.1 Starting with $(dR/dQ)_{\text{Gau}}$ given in Eq.(3.21)

Substituting the exponential form factor $F_{\text{ex}}^2(Q)$ given in Eq.(3.15) into Eq.(3.21), one can get

$$\left(\frac{dR}{dQ} \right)_{\text{Gau,ex}} = \mathcal{A} \left(\frac{2}{\sqrt{\pi} v_0} \right) e^{-(\alpha^2/v_0^2 + 1/Q_0)Q} = \mathcal{A} \left(\frac{2}{\sqrt{\pi} v_0} \right) e^{-\alpha^2 Q/v_0^2 \beta^2}, \tag{C.6}$$

where β has been defined in Eq.(3.28). Then it is easy to find that

$$\begin{aligned} R_{\text{Gau,ex}}(Q_{\text{thre}}) &= \mathcal{A} \left(\frac{2}{\sqrt{\pi}v_0} \right) \int_{Q_{\text{thre}}}^{\infty} e^{-\alpha^2 Q/v_0^2 \beta^2} dQ \\ &= \frac{\rho_0 \sigma_0 \langle v \rangle_{\text{Gau}}}{m_\chi m_N} \left(\beta^2 e^{-\alpha^2 Q_{\text{thre}}/v_0^2 \beta^2} \right). \end{aligned} \quad (3.26)$$

C.2.2 Starting with $(dR/dQ)_{\text{sh}}$ given in Eq.(3.31)

Substituting the exponential form factor $F_{\text{ex}}^2(Q)$ into Eq.(3.31), one can get

$$\left(\frac{dR}{dQ} \right)_{\text{sh,ex}} = \mathcal{A} \left(\frac{1}{2v_e} \right) e^{-Q/Q_0} \left[\text{erf} \left(\frac{\alpha\sqrt{Q}+v_e}{v_0} \right) - \text{erf} \left(\frac{\alpha\sqrt{Q}-v_e}{v_0} \right) \right]. \quad (C.7)$$

Consider

$$\begin{aligned} &\int e^{-Q/Q_0} \text{erf} \left(\frac{\alpha\sqrt{Q}\pm v_e}{v_0} \right) dQ \\ &= -Q_0 e^{-Q/Q_0} \text{erf} \left(\frac{\alpha\sqrt{Q}\pm v_e}{v_0} \right) + \frac{Q_0}{\sqrt{\pi}} \left(\frac{\alpha}{v_0} \right) \int \frac{1}{\sqrt{Q}} e^{-Q/Q_0 - [(\alpha\sqrt{Q}\pm v_e)/v_0]^2} dQ, \end{aligned} \quad (C.8)$$

where I have used integration by parts and Eqs.(B.14). Using Eqs.(B.13a) and (B.13b), the integral of the second term on the right-hand side above can be found as

$$\begin{aligned} \int \frac{1}{\sqrt{Q}} e^{-Q/Q_0 - [(\alpha\sqrt{Q}\pm v_e)/v_0]^2} dQ &= 2 \int e^{-[(\alpha^2/v_0^2 + 1/Q_0)q^2 \pm (2\alpha v_e/v_0^2)q + v_e^2/v_0^2]} dq \\ &= \sqrt{\pi} \left(\frac{v_0\beta}{\alpha} \right) e^{-(1-\beta^2)\tilde{v}_e^2} \text{erf} \left(\frac{\alpha\sqrt{Q}}{v_0\beta} \pm \beta\tilde{v}_e \right), \end{aligned} \quad (C.9)$$

where I have used

$$\int e^{-(ax^2+bx+c)} dx = \frac{1}{2} \sqrt{\frac{\pi}{a}} e^{(b^2/4a-c)} \text{erf} \left(\sqrt{a}x + \frac{b}{2\sqrt{a}} \right),$$

and the definition in Eq.(B.5). Combining Eqs.(C.7) to (C.9), one can get

$$\begin{aligned} &R_{\text{sh,ex}}(Q_{\text{thre}}) \\ &= \mathcal{A} \left(\frac{Q_0}{2v_e} \right) \left\{ e^{-Q_{\text{thre}}/Q_0} \left[\text{erf} \left(\frac{\alpha\sqrt{Q_{\text{thre}}+v_e}}{v_0} \right) - \text{erf} \left(\frac{\alpha\sqrt{Q_{\text{thre}}-v_e}}{v_0} \right) \right] \right. \\ &\quad \left. - \beta e^{-(1-\beta^2)\tilde{v}_e^2} \left[\text{erf} \left(\frac{\alpha\sqrt{Q_{\text{thre}}+\beta^2 v_e}}{v_0\beta} \right) - \text{erf} \left(\frac{\alpha\sqrt{Q_{\text{thre}}-\beta^2 v_e}}{v_0\beta} \right) \right] \right\} \\ &= \frac{\rho_0 \sigma_0}{m_\chi m_N} \left(\frac{v_0^2}{2v_e} \right) \left(\frac{\beta^2}{1-\beta^2} \right) \\ &\quad \times \left\{ e^{-(1-\beta^2)\alpha^2 Q_{\text{thre}}/v_0^2 \beta^2} \left[\text{erf}(S_+) - \text{erf}(S_-) \right] \right. \\ &\quad \left. - \beta e^{-(1-\beta^2)v_e^2/v_0^2} \left[\text{erf}(T_+) - \text{erf}(T_-) \right] \right\}, \end{aligned} \quad (3.37)$$

where I have used the definitions in Eqs.(3.35) and (3.38) as well as

$$Q_0 = \frac{v_0^2}{\alpha^2} \left(\frac{\beta^2}{1-\beta^2} \right). \quad (3.28')$$

Appendix D

Some Old Attempts

In this chapter I present some old attempts for reconstructing the velocity distribution function, eventually also for determining its moments. I describe also their disadvantages and problems. However, these unsuccessful attempts could perhaps inspire some new ideas.

D.1 Binning the data set

The usually used choice for binning a data set is that every bin has that same width:

$$b_n = b = \frac{Q_{\max} - Q_{\min}}{B}, \quad (\text{D.1})$$

and thus

$$Q_n = Q_{\min} + \left(n - \frac{1}{2}\right) b. \quad (\text{D.2})$$

However, as discussed in Subsec. 4.2.2, using bins with linearly increasing widths can make the errors roughly equal:

$$b_n = b_1 + (n - 1)\delta, \quad (\text{D.33})$$

here the increment δ satisfies

$$\delta = \frac{2}{B(B-1)}(Q_{\max} - Q_{\min} - Bb_1). \quad (\text{D.35})$$

Hence, for the n -th Q -bin, one has

$$Q_{n,\min} = Q_{\min} + (n-1)b_1 + \left[\frac{(n-1)(n-2)}{2}\right]\delta, \quad (\text{D.3a})$$

and

$$Q_{n,\max} = Q_{\min} + nb_1 + \left[\frac{n(n-1)}{2}\right]\delta. \quad (\text{D.3b})$$

This means that

$$Q_n = Q_{\min} + \left(n - \frac{1}{2}\right) b_1 + \left[\frac{(n-1)^2}{2}\right]\delta. \quad (\text{D.34})$$

Moreover, one other choice for binning the data set is

$$b_n = b_1 \delta^{n-1}. \quad (\text{D.4})$$

It is more comfortable if we choose δ as the input parameter and then determine b_1 as

$$b_1 = \left(\frac{\delta - 1}{\delta^B - 1} \right) (Q_{\max} - Q_{\min}). \quad (\text{D.5})$$

Hence, for the n -th Q -bin, one has

$$Q_{n,\min} = Q_{\min} + \left(\frac{\delta^{n-1} - 1}{\delta - 1} \right) b_1, \quad (\text{D.6a})$$

and

$$Q_{n,\max} = Q_{\min} + \left(\frac{\delta^n - 1}{\delta - 1} \right) b_1. \quad (\text{D.6b})$$

This means that

$$Q_n = Q_{\min} + \left[\frac{\delta^n + \delta^{n-1} - 2}{2(\delta - 1)} \right] b_1. \quad (\text{D.7})$$

D.2 Reconstructing $f_1(v)$ without derivatives

According to the expression of the differential event rate in Eq.(3.12), I have

$$\left(\frac{dR}{dQ} \right)_{Q=Q_n} = \mathcal{A} F^2(Q_n) \int_{v_n}^{\infty} \left[\frac{f_1(v)}{v} \right] dv, \quad (\text{D.8})$$

where, from Eq.(3.10),

$$v_n = \alpha \sqrt{Q_n}. \quad (\text{D.9})$$

Then it can be found that

$$\begin{aligned} \int_{v_n}^{v_{n+1}} \left[\frac{f_1(v)}{v} \right] dv &= \frac{1}{\mathcal{A}} \left[\frac{1}{F^2(Q_n)} \left(\frac{dR}{dQ} \right)_{Q=Q_n} - \frac{1}{F^2(Q_{n+1})} \left(\frac{dR}{dQ} \right)_{Q=Q_{n+1}} \right] \\ &\equiv \Delta_n. \end{aligned} \quad (\text{D.10})$$

The mean value theorem of calculus implies

$$\frac{\Delta_n}{v_{n+1} - v_n} = \left[\frac{f_1(v)}{v} \right]_{v=\tilde{v}_n}, \quad (\text{D.11})$$

where $v_n \leq \tilde{v}_n \leq v_{n+1}$. Hence, I can let

$$\tilde{v}_n = \alpha_n v_{n+1} + (1 - \alpha_n) v_n = v_n + \alpha_n (v_{n+1} - v_n), \quad (0 \leq \alpha_n \leq 1), \quad (\text{D.12})$$

and rewrite Eq.(D.11) to

$$f_1(\tilde{v}_n) = \left(\frac{\tilde{v}_n}{v_{n+1} - v_n} \right) \Delta_n = \left[\frac{1}{(v_{n+1}/v_n) - 1} + \alpha_n \right] \Delta_n, \quad (0 \leq \alpha_n \leq 1). \quad (\text{D.13})$$

Therefore, the error of $f_1(\tilde{v}_n)$ can be given as

$$\sigma(f_1(\tilde{v}_n)) = \left[\frac{1}{(v_{n+1}/v_n) - 1} + \alpha_n \right] \sigma(\Delta_n). \quad (\text{D.14})$$

Usually, one sets $\alpha_n = \frac{1}{2}$ and then it can be reduced to

$$\sigma(f_1(\tilde{v}_n, \alpha_n = 1/2)) \equiv \sigma(f_1(v_{n+1/2})) = \frac{1}{2} \left(\frac{v_{n+1} + v_n}{v_{n+1} - v_n} \right) \sigma(\Delta_n). \quad (\text{D.15})$$

Here, from Eq.(D.10),

$$\begin{aligned} \sigma(\Delta_n) &= \frac{1}{\mathcal{A}} \left\{ \frac{1}{F^4(Q_n)} \sigma^2 \left[\left(\frac{dR}{dQ} \right)_{Q=Q_n} \right] + \frac{1}{F^4(Q_{n+1})} \sigma^2 \left[\left(\frac{dR}{dQ} \right)_{Q=Q_{n+1}} \right] \right\}^{1/2} \\ &= \frac{1}{\mathcal{A}} \left\{ \frac{1}{F^4(Q_n)} \left(\frac{N_n}{b_n^2} \right) + \frac{1}{F^4(Q_{n+1})} \left(\frac{N_{n+1}}{b_{n+1}^2} \right) \right\}^{1/2}, \end{aligned} \quad (\text{D.16})$$

where I have used the standard estimator for dR/dQ at the point $Q = Q_n$ in Eq.(4.15) and then its statistical error in Eq.(4.16).

This method is straightforward. However, neither $f_1(\tilde{v}_n)$ nor its statistical error is independent of the unknown constant \mathcal{A} . Moreover, this method has an *anti-correlation* problem: An upward fluctuation of the counting rate in the n -th Q -bin will lead to too small f_1 in the $n - 1$ -st v -bin, but tends to give too large f_1 in the n th v -bin.

D.3 Average logarithmic slope

As shown in Fig. 4.1, the theoretically predicted recoil spectrum is approximately exponential. And, as discussed in Subsec. 4.2.1, an exponential approximation can approximate the recoil spectrum for a wider bin. Hence, I have considered the exponential ansatz in Eq.(4.18), but at beginning only naively combined with the standard estimator for dR/dQ at the point $Q = Q_n$ as

$$\left(\frac{dR}{dQ} \right)_{Q \simeq Q_n} = r_n e^{k_n(Q-Q_n)}, \quad (\text{D.17})$$

where $r_n = N_n/b_n$ is the standard estimator given in Eq.(4.15). Define the slope of the straight line with two endpoints $(Q_n, \ln(dR/dQ)_{Q=Q_n})$ and $(Q_{n+1}, \ln(dR/dQ)_{Q=Q_{n+1}})$ as

$$k_{n,n+1} \equiv \frac{\ln r_{n+1} - \ln r_n}{Q_{n+1} - Q_n}, \quad n = 1, 2, \dots, B - 1. \quad (\text{D.18})$$

Then I can define an *average slope* for the function $\ln(dR/dQ)_{Q \simeq Q_n}$ at the point $Q = Q_n$, $n = 2, 3, \dots, B - 1$, as (see Fig. D.1)

$$k_{n,\text{ave}} \equiv \frac{k_{n-1,n} + k_{n,n+1}}{2} = \frac{1}{2} \left(\frac{\ln r_n - \ln r_{n-1}}{Q_n - Q_{n-1}} + \frac{\ln r_{n+1} - \ln r_n}{Q_{n+1} - Q_n} \right), \quad (\text{D.19a})$$

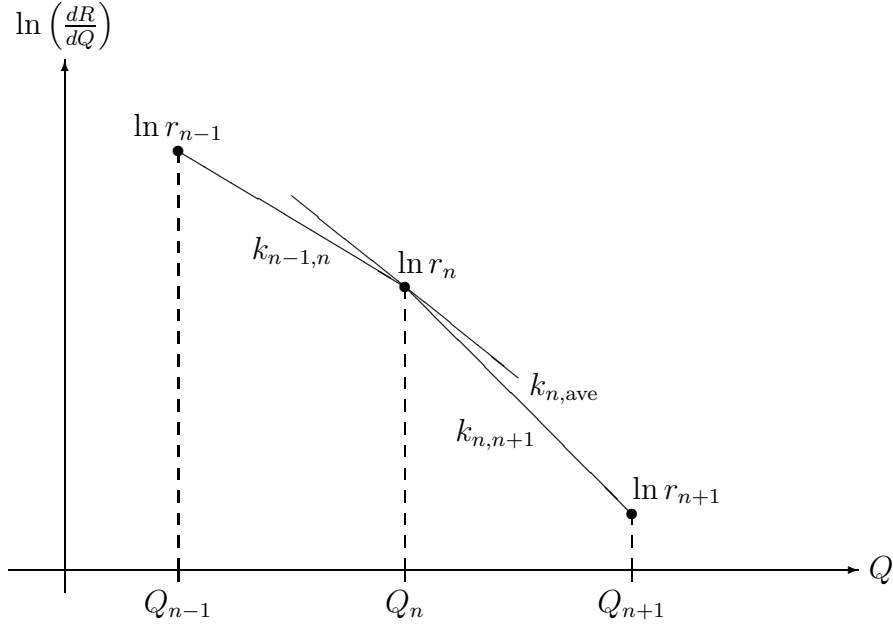


Figure D.1: Sketch of the average slope for the function $\ln(dR/dQ)_{Q \simeq Q_n}$ at $Q = Q_n$, $k_{n,\text{ave}}$, defined in Eq.(D.19a).

but, at the point $Q = Q_1$, I have defined

$$k_{1,\text{ave}} \equiv k_{1,2} = \frac{\ln r_2 - \ln r_1}{Q_2 - Q_1}. \quad (\text{D.19b})$$

The statistical errors on $k_{n,\text{ave}}$ can be obtained directly from Eqs.(D.19a) and (D.19b) as

$$\sigma^2(k_{n,\text{ave}}) = \frac{1}{4} \left[\left(\frac{1}{Q_n - Q_{n-1}} - \frac{1}{Q_{n+1} - Q_n} \right)^2 \frac{1}{N_n} + \left(\frac{1}{Q_n - Q_{n-1}} \right)^2 \frac{1}{N_{n-1}} + \left(\frac{1}{Q_{n+1} - Q_n} \right)^2 \frac{1}{N_{n+1}} \right], \quad (\text{D.20a})$$

for $n = 2, 3, \dots, B-1$, and

$$\sigma^2(k_{1,\text{ave}}) = \left(\frac{1}{Q_2 - Q_1} \right)^2 \left(\frac{1}{N_1} + \frac{1}{N_2} \right), \quad (\text{D.20b})$$

where I have used Eqs.(4.15) and (4.16) to get

$$\frac{\sigma^2(r_n)}{r_n^2} = \frac{1}{N_n}. \quad (\text{D.21})$$

Moreover, the $k_{n,\text{ave}}$ given in Eqs.(D.19a) and (D.19b) are correlated. Hence, for $k_{n,\text{ave}}$ in Eq.(D.19a), I have

$$\begin{aligned} & \text{COV}(k_{n,\text{ave}}, k_{n+1,\text{ave}}) \\ &= \frac{1}{4} \left[- \left(\frac{1}{Q_n - Q_{n-1}} - \frac{1}{Q_{n+1} - Q_n} \right) \left(\frac{1}{Q_{n+1} - Q_n} \right) \frac{1}{N_n} \right. \\ & \quad \left. + \left(\frac{1}{Q_{n+1} - Q_n} \right) \left(\frac{1}{Q_{n+1} - Q_n} - \frac{1}{Q_{n+2} - Q_{n+1}} \right) \frac{1}{N_{n+1}} \right], \end{aligned} \quad (\text{D.22a})$$

and

$$\text{COV}(k_{n,\text{ave}}, k_{n+2,\text{ave}}) = -\frac{1}{4} \left(\frac{1}{Q_{n+1} - Q_n} \right) \left(\frac{1}{Q_{n+2} - Q_{n+1}} \right) \frac{1}{N_{n+1}}, \quad (\text{D.22b})$$

while, for $k_{1,\text{ave}}$ in Eq.(D.19b), I have

$$\text{COV}(k_{1,\text{ave}}, k_{2,\text{ave}}) = \frac{1}{2} \left[\left(\frac{1}{Q_2 - Q_1} \right)^2 \frac{1}{N_1} + \frac{1}{Q_2 - Q_1} \left(\frac{1}{Q_2 - Q_1} - \frac{1}{Q_3 - Q_2} \right) \frac{1}{N_2} \right], \quad (\text{D.22c})$$

and

$$\text{COV}(k_{1,\text{ave}}, k_{3,\text{ave}}) = -\frac{1}{2} \left(\frac{1}{Q_2 - Q_1} \right) \left(\frac{1}{Q_3 - Q_2} \right) \frac{1}{N_2}. \quad (\text{D.22d})$$

Now I can begin to reconstruct the recoil spectrum. The basic idea is that I approximate the function $\ln(dR/dQ)$ in each bin by a straight line $\ln r_{n,\text{ave}}(Q)$ which has the slope $k_{n,\text{ave}}$ and passes through the point $(Q_n, \ln r_n)$ (see Fig. D.2):

$$\frac{\ln r_{n,\text{ave}}(Q) - \ln r_n}{Q - Q_n} = k_{n,\text{ave}}. \quad (\text{D.23})$$

Hence, I have

$$\left(\frac{dR}{dQ} \right)_{Q \simeq Q_n} = r_{n,\text{ave}}(Q) = r_n e^{k_{n,\text{ave}}(Q - Q_n)}, \quad n = 2, 3, \dots, B-1, \quad (\text{D.24a})$$

in the n -th Q -bin:

$$\frac{Q_{n-1} + Q_n}{2} \equiv Q_{n-} \leq Q \leq Q_{n+} \equiv \frac{Q_n + Q_{n+1}}{2}, \quad (\text{D.25a})$$

and

$$\left(\frac{dR}{dQ} \right)_{Q \simeq Q_1} = r_{1,\text{ave}}(Q) = r_1 e^{k_{1,\text{ave}}(Q - Q_1)}, \quad (\text{D.24b})$$

in the first Q -bin:

$$Q_{\text{thre}} \equiv Q_{1-} \leq Q \leq Q_{1+} \equiv \frac{Q_1 + Q_2}{2}, \quad (\text{D.25b})$$

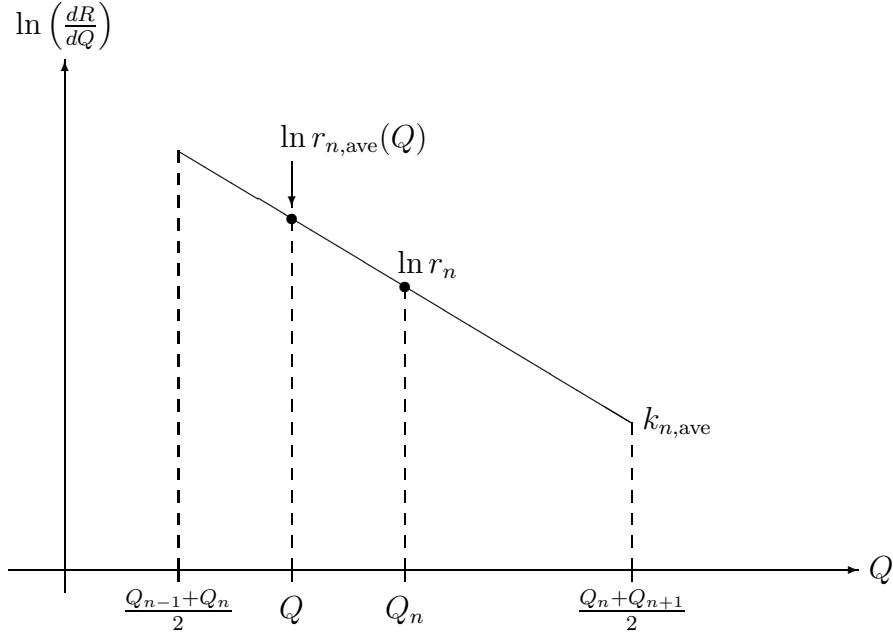


Figure D.2: Sketch of the reconstructed segment of the function $\ln(dR/dQ)$ between $(Q_{n-1} + Q_n)/2$ and $(Q_n + Q_{n+1})/2$, $\ln r_{n,\text{ave}}(Q)$.

where Q_{thre} is the threshold energy and the $k_{n,\text{ave}}$, $n = 1, 2, \dots, B-1$, are given in Eqs.(D.19a) and (D.19b), respectively. Then, similar to Eq.(4.46), the velocity distribution function $f_1(v)$ given in Eq.(4.8) can be reconstructed as

$$f_{1,\text{ave}}(v_n) = \mathcal{N}_{\text{ave}} \left[\frac{2Q_n r_n}{F^2(Q_n)} \right] \left[\frac{d}{dQ} \ln F^2(Q) \Big|_{Q=Q_n} - k_{n,\text{ave}} \right], \quad (\text{D.26})$$

for $n = 1, 2, \dots, B-1$. Here v_n is given in Eq.(D.9).

The first problem with the expression in Eq.(D.26) is estimating the normalization constant \mathcal{N}_{ave} . One possibility is inserting $r_{n,\text{ave}}(Q)$ given in Eqs.(D.24a) and (D.24b) into Eq.(4.9) directly:

$$\mathcal{N}_{\text{ave}} = \frac{2}{\alpha} \left\{ \sum_{i=1}^{B-1} \int_{Q_{i-}}^{Q_{i+}} \frac{1}{\sqrt{Q}} \left[\frac{r_{i,\text{ave}}(Q)}{F^2(Q)} \right] dQ \right\}^{-1}, \quad (\text{D.27})$$

where $Q_{i\pm}$ are given in Eqs.(D.25a) and (D.25b). Similarly, I_n defined in Eq.(4.12) and $(dR/dQ)_{Q=Q_{\text{thre}}}$ in Eq.(4.11) can also be estimated as

$$I_n = \sum_{i=1}^{B-1} \int_{Q_{i-}}^{Q_{i+}} Q^{(n-1)/2} \left[\frac{r_{i,\text{ave}}(Q)}{F^2(Q)} \right] dQ, \quad (\text{D.28})$$

and

$$\left(\frac{dR}{dQ} \right)_{\text{ave}, Q=Q_{\text{thre}}} = r_{1,\text{ave}}(Q_{\text{thre}}) = r_1 e^{k_{1,\text{ave}}(Q_{\text{thre}} - Q_1)}. \quad (\text{D.29})$$

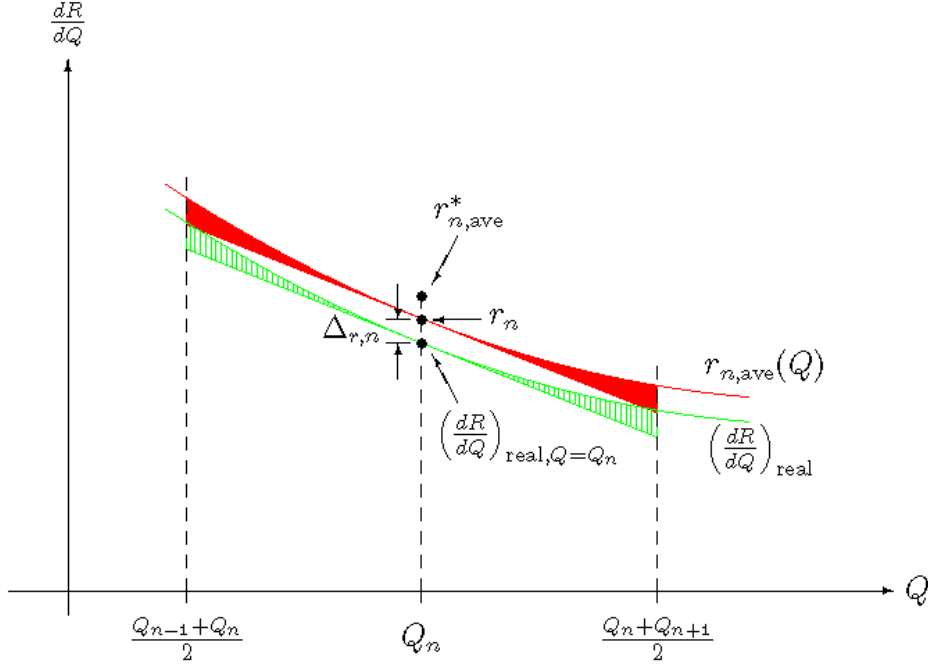


Figure D.3: Sketch of the elevation from $(dR/dQ)_{\text{real},Q=Q_n}$ to r_n and from r_n to $r_{n,\text{ave}}^*$ due to the concavity of the recoil curve, $(dR/dQ)_{\text{real}}$, and that of the reconstructed spectrum, $r_{n,\text{ave}}(Q)$, between $(Q_{n-1} + Q_n)/2$ and $(Q_n + Q_{n+1})/2$, respectively.

However, it should be pretty complicated to estimate the statistical errors of $f_{1,\text{ave}}(v_n)$ given in Eq.(D.26) with \mathcal{N}_{ave} estimated in Eq.(D.27).

The other serious problem with the ansatz in Eqs.(D.24a) and (D.24b) is that one must also consider a systematic error caused by using the exponential ansatz with the standard estimator $r_n = N_n/b_n$. Suppose that $(dR/dQ)_{\text{real}}$ is the real recoil spectrum and passes through the point $(Q_n, (dR/dQ)_{\text{real},Q=Q_n})$ (see Fig. D.3). During the experiment we measure deposited energies and count the event rate, which is proportional to the area under the real recoil spectrum (see Eq.(4.20)), in the n -th Q -bin, and then estimate $r_n = N_n/b_n$. However, because the recoil spectrum is concave, the estimator r_n is a little larger than the real value, $(dR/dQ)_{\text{real},Q=Q_n}$ (see \tilde{r}_n given in Eq.(4.22)). Define this elevation from $(dR/dQ)_{\text{real},Q=Q_n}$ to r_n as

$$\Delta_{r,n} \equiv r_{n,\text{ave}}(Q_n) - \left(\frac{dR}{dQ}\right)_{\text{real},Q=Q_n} \equiv r_n - r_{n,\text{real}}, \quad n = 1, 2, \dots, B-1. \quad (\text{D.30})$$

On the other hand, it is plausible to suppose that the reconstructed recoil spectrum $r_{n,\text{ave}}(Q)$ in Eq.(D.20a) and (D.20b) are approximately parallel to the real one $(dR/dQ)_{\text{real}}$, thus I can estimate the elevation by

$$\Delta_{r,n} \approx r_{n,\text{ave}}^* - r_n, \quad n = 1, 2, \dots, B-1. \quad (\text{D.31})$$

Here $r_{n,\text{ave}}^*$ can be calculated from $r_{n,\text{ave}}(Q_n)$ as

$$\begin{aligned}
r_{n,\text{ave}}^* &= \frac{2}{Q_{n+1} - Q_{n-1}} \int_{(Q_{n-1}+Q_n)/2}^{(Q_n+Q_{n+1})/2} r_{n,\text{ave}}(Q) dQ \\
&= \frac{2}{Q_{n+1} - Q_{n-1}} \int_{(Q_{n-1}+Q_n)/2}^{(Q_n+Q_{n+1})/2} \left[r_n e^{k_{n,\text{ave}}(Q-Q_n)} \right] dQ \\
&= r_n \left[\frac{2}{k_{n,\text{ave}}(Q_{n+1} - Q_{n-1})} \right] \left[e^{k_{n,\text{ave}}\left(\frac{Q_{n+1}-Q_n}{2}\right)} - e^{-k_{n,\text{ave}}\left(\frac{Q_n-Q_{n-1}}{2}\right)} \right], \quad (\text{D.32a})
\end{aligned}$$

for $n = 2, 3, \dots, B-1$, and for $n = 1$,

$$\begin{aligned}
r_{1,\text{ave}}^* &= \frac{2}{Q_1 + Q_2 - 2Q_{\text{thre}}} \int_{Q_{\text{thre}}}^{(Q_1+Q_2)/2} r_{1,\text{ave}}(Q) dQ \\
&= \frac{2}{Q_1 + Q_2 - 2Q_{\text{thre}}} \int_{Q_{\text{thre}}}^{(Q_1+Q_2)/2} \left[r_1 e^{k_{1,\text{ave}}(Q-Q_1)} \right] dQ \\
&= r_1 \left[\frac{2}{k_{1,\text{ave}}(Q_1 + Q_2 - 2Q_{\text{thre}})} \right] \left[e^{k_{1,\text{ave}}\left(\frac{Q_2-Q_1}{2}\right)} - e^{-k_{1,\text{ave}}(Q_1-Q_{\text{thre}})} \right]. \quad (\text{D.32b})
\end{aligned}$$

Combining Eqs.(D.30) to (D.32b), the real value of the recoil spectrum $(dR/dQ)_{\text{real}}$ at the point $Q = Q_n$, $n = 2, 3, \dots, B-1$, can be obtained (approximately) as

$$\begin{aligned}
r_{n,\text{real}} &\approx 2r_n - r_{n,\text{ave}}^* \\
&= 2r_n \left\{ 1 - \left[\frac{1}{k_{n,\text{ave}}(Q_{n+1} - Q_{n-1})} \right] \right. \\
&\quad \left. \times \left[e^{k_{n,\text{ave}}\left(\frac{Q_{n+1}-Q_n}{2}\right)} - e^{-k_{n,\text{ave}}\left(\frac{Q_n-Q_{n-1}}{2}\right)} \right] \right\}, \quad (\text{D.33a})
\end{aligned}$$

and at the point $Q = Q_1$,

$$\begin{aligned}
r_{1,\text{real}} &\approx 2r_1 - r_{1,\text{ave}}^* \\
&= 2r_1 \left\{ 1 - \left[\frac{1}{k_{1,\text{ave}}(Q_1 + Q_2 - 2Q_{\text{thre}})} \right] \right. \\
&\quad \left. \times \left[e^{k_{1,\text{ave}}\left(\frac{Q_2-Q_1}{2}\right)} - e^{-k_{1,\text{ave}}(Q_1-Q_{\text{thre}})} \right] \right\}. \quad (\text{D.33b})
\end{aligned}$$

Note that the correction of r_n here is essentially the same as the expression of \tilde{r}_n in Eq.(4.22).

Now one can replace r_n in Eqs.(D.19a) and (D.19b) by $r_{n,\text{real}}$ estimated by Eqs.(D.33a) and (D.33b) to get $k_{n,\text{ave}}$, and then substitute $r_{n,\text{real}}$ and $k_{n,\text{ave}}$ into Eqs.(D.26) to (D.29) to reconstruct $f_{1,\text{ave}}(v_n)$ and so on. However, due to the dependence of $r_{n,\text{real}}$ on r_n and $k_{n,\text{ave}}$, it is very complicated to modify even the statistical errors in Eqs.(D.20a) to (D.22d)!

Moreover, this ‘‘average-logarithmic-slope’’ method has also the same ‘‘anti-correlation’’ problem as the method described in the previous section. An upward fluctuation in the n -th Q -bin leads to a too small slope $k_{n-1,n}$ and a too large slope $k_{n,n+1}$, even though the fluctuation of the ‘‘average’’ slope $k_{n,\text{ave}} = (k_{n-1,n} + k_{n,n+1})/2$ could be more or less decreased and the value of $k_{n,\text{ave}}$ should be not very bad.

Furthermore, as shown in e.g., Eqs.(D.18), (D.24a), and (D.30), from B bins one can get $B - 1$ $k_{n,\text{ave}}$, $r_{n,\text{ave}}(Q)$, and $r_{n,\text{real}}$. Then, after one replaces r_n in Eq.(D.18) by $r_{n,\text{real}}$ and runs the whole process from Eq.(D.18) to Eq.(D.29), one can have only $B - 2$ $f_{1,\text{ave}}(v_n)$ given by Eq.(D.26). However, as shown in Figs. 4.2, with 500 (or even 5000) events, one has only 4 (or 8) bins to use.¹ Hence, it can not be allowed to lose 2 bins (points) more!

D.4 Linear approximations of $(dQ/dR)_{Q \simeq Q_n}$

As noted in the beginning of Sec. 4.2, according to the expression in Eq.(4.8), one needs not only an estimator for dR/dQ at $Q = Q_n$ but also one for the *slope* of the recoil spectrum to reconstruct the velocity distribution. A rather crude estimator of this slope is

$$s_{1,n} \equiv \left[\frac{d}{dQ} \left(\frac{dR}{dQ} \right) \right]_{Q=Q_n} = \frac{N_{n,Q>Q_n} - N_{n,Q<Q_n}}{(b_n/2)^2}, \quad (\text{D.34})$$

where $N_{n,Q>Q_n}$ and $N_{n,Q<Q_n}$ are the numbers of events in bin n which have measured recoil energy Q larger and smaller than Q_n , respectively. This estimator is rather crude, since it only uses the information in which half of its bin a given event falls.

It is clear intuitively that an estimator that makes use of the exact Q -value of each event should be better. This can e.g., be obtained from the average Q -value in a given bin. Taylor-expanding dR/dQ around $Q = Q_n$, keeping terms up to linear order, gives

$$\left(\frac{dR}{dQ} \right)_{Q \simeq Q_n} \simeq \left(\frac{dR}{dQ} \right)_{Q=Q_n} + (Q - Q_n) \left[\frac{d}{dQ} \left(\frac{dR}{dQ} \right) \right]_{Q=Q_n} = r_n + (Q - Q_n)s_n. \quad (\text{D.35})$$

Using this linear approximation for the recoil spectrum, one can find

$$N_n = \int_{Q_n - b_n/2}^{Q_n + b_n/2} [r_n + (Q - Q_n)s_n] dQ = r_n b_n, \quad (\text{D.36})$$

(of course, this reproduces the standard estimator in Eq.(4.15)) and the average value of the recoil energies in the n -th Q -bin:

$$\overline{Q - Q_n}|_n = \frac{1}{N_n} \int_{Q_n - b_n/2}^{Q_n + b_n/2} (Q - Q_n) [r_n + (Q - Q_n)s_n] dQ = \left(\frac{b_n^2}{12r_n} \right) s_n. \quad (\text{D.37})$$

Hence, an improved estimator of the slope of dR/dQ at $Q = Q_n$ is

$$s_{2,n} = \frac{12r_n \overline{Q - Q_n}|_n}{b_n^2}. \quad (\text{D.38})$$

¹Not 5 or 10 bins, because the last one or two bin are almost empty, see the discussion in Subsec. 4.2.3.

According to the definition of $s_{1,n}$ in Eq.(D.34) it can be found that

$$\begin{aligned}\sigma^2(s_{1,n}) &= \left[\frac{1}{(b_n/2)^2} \right]^2 \left[\sigma^2(N_{n,Q>Q_n}) + \sigma^2(N_{n,Q<Q_n}) \right] \\ &= \frac{16}{b_n^4} (N_{n,Q>Q_n} + N_{n,Q<Q_n}) \\ &= \frac{16r_n}{b_n^3},\end{aligned}\tag{D.39}$$

where I have used Eqs.(4.17) and (4.15). On the other hand, according to the expression of $s_{2,n}$ in Eq.(D.38), and treating the number of events and the average Q -value in a given bin as two independent variables, one can obtain that

$$\sigma^2(s_{2,n}) = \left(\frac{12\overline{Q} - Q_n|_n}{b_n^2} \right)^2 \sigma^2(r_n) + \left(\frac{12r_n}{b_n^2} \right)^2 \sigma^2(\overline{Q} - Q_n|_n) = \frac{12r_n}{b_n^3}.\tag{D.40}$$

Here I have used Eq.(4.16), the definition in Eq.(4.24) with the linear approximation in Eq.(D.35),

$$\overline{(Q - Q_n)^2}|_n = \frac{1}{N_n} \int_{Q_n - b_n/2}^{Q_n + b_n/2} (Q - Q_n)^2 [r_n + (Q - Q_n)s_n] dQ = \frac{b_n^2}{12},\tag{D.41}$$

and ²

$$\sigma^2(\overline{Q} - Q_n|_n) = \frac{1}{N_n} \left[\overline{(Q - Q_n)^2}|_n - \overline{Q - Q_n|_n}^2 \right].\tag{D.42}$$

This simple calculation shows that the estimator $s_{2,n}$ given in Eq.(D.38) indeed has a smaller statistical error than the crude estimator $s_{1,n}$ in Eq.(D.34) by a factor of $\sqrt{3/4}$.

D.5 Using the exponential ansatz in Eq.(4.18)

In App. D.3 I have used an exponential approximation with the standard estimator r_n to reconstruct the recoil spectrum. A correction due to the approximately exponential form of the recoil spectrum has also been discussed. The use of the average logarithmic slope $k_{n,\text{ave}}$ combined with the correction is very complicated, especially for the error analysis. However, it is clear that an exponential approximation can approximate the recoil spectrum much better than a linear one. On the other hand, in the previous section I have introduced the use of the exact Q -value of each event. The analysis done with two linear approximations has shown that the statistical error can be strongly reduced. Hence, it is pretty straightforwardly to combine these two techniques and their advantages together.

By using an exponential ansatz for the recoil spectrum in each Q -bin, combining with a prefactor which can be adjusted by the event number in this bin, and then estimating the logarithmic slope by the average value of the recoil energies measured in this bin,

²Strictly speaking, the denominator should be $N_n - 1$ as I used in Eq.(4.32).

one can already obtain the expressions given in Subsec. 4.2.1. Substituting the first expression of the exponential ansatz in Eq.(4.18) into Eq.(4.8) with the logarithmic slope k_n estimated by Eq.(4.23), the velocity distribution function can be reconstructed as

$$f_{1,\bar{Q}}(v_n) = \mathcal{N}_{\bar{Q}} \left[\frac{2Q_n \tilde{r}_n}{F^2(Q_n)} \right] \left[\frac{d}{dQ} \ln F^2(Q) \Big|_{Q=Q_n} - k_n \right], \quad (\text{D.43})$$

where v_n is given in Eq.(D.9). This expression is already almost the same as the expression given in Eq.(4.46), except the central point Q_n in the n -th Q -bin has been used here instead of the shifted point $Q_{s,\mu}$ in the μ -th Q -window, and thus I have used \tilde{r}_n instead of r_μ here. Moreover, I have to determine the normalization constant $\mathcal{N}_{\bar{Q}}$ here. It can be done by Eq.(D.27) with replacing $r_{i,\text{ave}}(Q)$ by $\tilde{r}_n e^{k_n(Q-Q_n)}$:

$$\mathcal{N}_{\bar{Q}} = \frac{2}{\alpha} \left\{ \sum_{i=1}^B \int_{Q_{i-}}^{Q_{i+}} \frac{1}{\sqrt{Q}} \left[\frac{\tilde{r}_n e^{k_n(Q-Q_n)}}{F^2(Q)} \right] dQ \right\}^{-1}, \quad (\text{D.44})$$

where $Q_{n\pm}$ have been given as

$$Q_n - \frac{b_n}{2} \equiv Q_{n-} \leq Q \leq Q_{n+} \equiv Q_n + \frac{b_n}{2}. \quad (\text{D.45})$$

However, in order to estimate the statistical error of $f_{1,\bar{Q}}(v_n)$ in Eq.(D.43) more easily, I have defined

$$f_{1,n,\bar{Q}}(v) \equiv \mathcal{N}_{\bar{Q}} \left\{ \frac{2Q \tilde{r}_n e^{k_n(Q-Q_n)}}{F^2(Q)} \left[\frac{d \ln F^2(Q)}{dQ} - k_n \right] \right\}_{Q=v^2/\alpha^2}, \quad (\text{D.46})$$

and

$$\tilde{f}_{1,n,\bar{Q}}(v) \equiv 2 \left\{ \frac{Q \tilde{r}_n e^{k_n(Q-Q_n)}}{F^2(Q)} \left[\frac{d \ln F^2(Q)}{dQ} - k_n \right] \right\}_{Q=v^2/\alpha^2} = \frac{f_{1,n,\bar{Q}}(v)}{\mathcal{N}_{\bar{Q}}}, \quad (\text{D.47})$$

in the n -th v -bin:

$$\alpha \sqrt{Q_{n-}} \equiv v_{n-} \leq v \leq v_{n+} \equiv \alpha \sqrt{Q_{n+}}, \quad (\text{D.48})$$

for $n = 1, 2, 3, \dots, B$. The normalization condition in Eq.(4.7) can be rewritten as

$$\sum_{i=1}^B \int_{v_{i-}}^{v_{i+}} f_{1,i,\bar{Q}}(v) dv = \mathcal{N}_{\bar{Q}} \left[\sum_{i=1}^B \int_{v_{i-}}^{v_{i+}} \tilde{f}_{1,i,\bar{Q}}(v) dv \right] = 1. \quad (\text{D.49})$$

Then the normalization constant can be obtained directly by

$$\mathcal{N}_{\bar{Q}} = \left[\sum_{i=1}^B \int_{v_{i-}}^{v_{i+}} \tilde{f}_{1,i,\bar{Q}}(v) dv \right]^{-1}, \quad (\text{D.50})$$

and $f_{1,n,\bar{Q}}(v)$ in Eq.(D.46) can be rewritten as

$$f_{1,n,\bar{Q}}(v) = \left[\sum_{i=1}^B \int_{v_{i-}}^{v_{i+}} \tilde{f}_{1,i,\bar{Q}}(v) dv \right]^{-1} \tilde{f}_{1,n,\bar{Q}}(v) = \frac{\tilde{f}_{1,n,\bar{Q}}(v)}{S_0}. \quad (\text{D.51})$$

Here I have defined

$$S_\lambda \equiv \sum_{i=1}^B \int_{v_{i-}}^{v_{i+}} v^\lambda \tilde{f}_{1,i,\bar{Q}}(v) dv. \quad (\text{D.52})$$

Moreover, it is reasonable to define the n -th moment of $f_{1,n,\bar{Q}}(v)$ as

$$\langle v^n \rangle_{\bar{Q}} \equiv \sum_{i=1}^B \int_{v_{i-}}^{v_{i+}} v^n f_{1,i,\bar{Q}}(v) dv = \frac{S_n}{S_0}. \quad (\text{D.53})$$

Furthermore, in order to estimate the statistical errors of $f_{1,n,\bar{Q}}(v)$ and $\langle v^n \rangle_{\bar{Q}}$ given in Eqs.(D.51) and (D.53), I have denoted first the independent variables of $\tilde{f}_{1,n,\bar{Q}}(v)$ defined in Eq.(D.47) as $x_{\nu,j}$, where the subscript ν stands for different species of variable, and $j = 1, 2, 3, \dots, B$ stands for the bins. Meanwhile, I have assumed that, in the j -th Q -bin (and then also in the j -th v -bin), the error of each of these variables $x_{\nu,j}$ is approximately equal. Hence, I can use its value at the point $Q = Q_j$, defined as $\delta x_{\nu,j}$, for the whole j -th Q - or v -bin. From the expression of $f_{1,n,\bar{Q}}(v)$ in Eq.(D.51), its statistical error can be found directly as

$$\begin{aligned} \sigma^2(f_{1,n,\bar{Q}}(v)) &= \sum_{\nu} \sum_{j=1}^B \left[\frac{\partial f_{1,n,\bar{Q}}(v)}{\partial x_{\nu,j}} \right]^2 \sigma^2(x_{\nu,j}) \\ &= \frac{1}{S_0^4} \sum_{\nu} \sum_{j=1}^B \left[S_0 (\partial_{\nu,j} \tilde{f}_{1,n,\bar{Q}}(v)) - S_{\nu,j;0} \tilde{f}_{1,n,\bar{Q}}(v) \right]^2 \sigma^2(x_{\nu,j}). \end{aligned} \quad (\text{D.54})$$

Here I have defined

$$\partial_{\nu,j} \tilde{f}_{1,n,\bar{Q}}(v) \equiv \frac{\partial \tilde{f}_{1,n,\bar{Q}}(v)}{\partial x_{\nu,j}}, \quad (\text{D.55})$$

and

$$S_{\nu,j;\lambda} \equiv \sum_{i=1}^B \int_{v_{i-}}^{v_{i+}} v^\lambda [\partial_{\nu,j} \tilde{f}_{1,i,\bar{Q}}(v)] dv. \quad (\text{D.56})$$

Similarly, from the definition of $\langle v^n \rangle_{\bar{Q}}$ in Eq.(D.53), it can be found that

$$\begin{aligned} \sigma^2(\langle v^n \rangle_{\bar{Q}}) &= \sum_{\nu} \sum_{j=1}^B \left(\frac{\partial \langle v^n \rangle_{\bar{Q}}}{\partial x_{\nu,j}} \right)^2 \sigma^2(x_{\nu,j}) \\ &= \frac{1}{S_0^4} \sum_{\nu} \sum_{j=1}^B (S_0 S_{\nu,j;n} - S_n S_{\nu,j;0})^2 \sigma^2(x_{\nu,j}). \end{aligned} \quad (\text{D.57})$$

According to the expression of $\tilde{f}_{1,n,\bar{Q}}(v)$ in Eq.(D.47) and \tilde{r}_n and k_n given in Eqs.(4.22) and (4.23), the independent variables of $\tilde{f}_{1,n,\bar{Q}}(v)$ should be chosen as

$$x_{1,n} = N_n, \quad x_{2,n} = k_n, \quad (\text{D.58})$$

with $\sigma^2(N_n)$ and $\sigma^2(k_n)$ given in Eqs.(4.17) and (4.29). Since $\tilde{f}_{1,n,\bar{Q}}(v)$ depends only on N_n and k_n , Eqs.(D.54) and (D.57) can be reduced to

$$\sigma^2(f_{1,n,\bar{Q}}(v)) = \frac{1}{S_0^4} \sum_{\nu} \sum_{j=1}^B \left[\delta_{n_j} S_0 \left(\partial_{\nu} \tilde{f}_{1,\bar{Q},n}(v) \right) - I_{\nu,j;0} \tilde{f}_{1,\bar{Q},n}(v) \right]^2 \sigma^2(x_{\nu,j}), \quad (\text{D.59})$$

and

$$\sigma^2(\langle v^n \rangle_{\bar{Q}}) = \frac{1}{S_0^4} \sum_{\nu} \sum_{j=1}^B \left(S_0 I_{\nu,j;n} - S_n I_{\nu,j;0} \right)^2 \sigma^2(x_{\nu,j}). \quad (\text{D.60})$$

Here I have defined

$$\partial_N \tilde{f}_{1,n,\bar{Q}}(v) \equiv \frac{\partial \tilde{f}_{1,n,\bar{Q}}(v)}{\partial N_n} = \frac{\tilde{f}_{1,n,\bar{Q}}(v)}{N_n}, \quad (\text{D.61})$$

$$\begin{aligned} \partial_k \tilde{f}_{1,n,\bar{Q}}(v) &\equiv \frac{\partial \tilde{f}_{1,n,\bar{Q}}(v)}{\partial k_n} \\ &= -\tilde{f}_{1,n,\bar{Q}}(v) \left\{ \overline{Q - Q_n|_n} + \left[\frac{d \ln F^2(Q)}{dQ} - k_n \right]^{-1} \right\}_{Q=v^2/\alpha^2}, \end{aligned} \quad (\text{D.62})$$

and, from Eq.(D.56),

$$I_{\nu,j;\lambda} \equiv \int_{v_{j-}}^{v_{j+}} v^{\lambda} \left[\partial_{\nu} \tilde{f}_{1,j,\bar{Q}}(v) \right] dv. \quad (\text{D.63})$$

D.6 Introducing the average value of $Q^{\lambda}/F^2(Q)$

The method presented in the previous section has two disadvantages. First, the estimator of $\mathcal{N}_{\bar{Q}}$ in Eq.(D.50) is the sum of several *integrals*, this makes the estimation complicated. Second, and also the worse disadvantage, by using $\langle v^n \rangle_{\bar{Q}}$ given in Eq.(D.53) with S_{λ} defined in Eq.(D.52), one has to know $\tilde{f}_{1,n,\bar{Q}}(v)$ defined in Eq.(D.47), i.e., $f_{1,n,\bar{Q}}(v)$ defined in Eq.(D.46). It is not only complicated but also loses the advantage of the expressions in Eqs.(4.11) and (4.12), by which one can evaluate the moments of $f_1(v)$ without knowing the functional form of $f_1(v)$. This problem comes essentially from the estimator of $\mathcal{N}_{\bar{Q}}$ in Eq.(D.50) obtained from the normalization condition in Eq.(4.7). Hence, one needs a new estimator for the normalization constant.

Similar to the use of the moments of the recoil spectrum in Eqs.(4.23) and (4.24), I have defined an average value of $Q^{\lambda}/F^2(Q)$ for all events in the n -th Q -bin:

$$\frac{1}{N_n} \int_{Q_n-b_n/2}^{Q_n+b_n/2} \frac{Q^{\lambda}}{F^2(Q)} \left(\frac{dR}{dQ} \right) dQ = \frac{1}{N_n} \sum_{i=1}^{N_n} \frac{Q_{n,i}^{\lambda}}{F^2(Q_{n,i})} \equiv \overline{S_{2,\lambda,n}}. \quad (\text{D.64})$$

Then, for all recorded events in the sample, I can use

$$\int_0^{\infty} \frac{Q^{\lambda}}{F^2(Q)} \left(\frac{dR}{dQ} \right) dQ \rightarrow \sum_{n=1}^B \sum_{i=1}^{N_n} \frac{Q_{n,i}^{\lambda}}{F^2(Q_{n,i})} = \sum_{n=1}^B N_n \overline{S_{2,\lambda,n}} \equiv S_{2,\lambda,\text{tot}}. \quad (\text{D.65})$$

Note that the recoil spectrum dR/dQ here is not specified to the exponential ansatz $(dR/dQ)_n$ in Eq.(4.18). Using the definition in Eq.(D.65), \mathcal{N} in Eq.(4.9) and I_n in Eq.(4.12) can be estimated by

$$\mathcal{N} = \frac{2}{\alpha} \left(\frac{1}{S_{2,-1/2,\text{tot}}} \right) = \frac{2}{\alpha} \left(\sum_{n=1}^B N_n \overline{S_{2,-1/2,n}} \right)^{-1}, \quad (\text{D.66})$$

and

$$I_n = S_{2,(n-1)/2,\text{tot}} = \sum_{n=1}^B N_n \overline{S_{2,(n-1)/2,n}}. \quad (\text{D.67})$$

The expressions in Eqs.(D.66) and (D.67) are already essentially the same as the expressions given in Eqs.(4.48) and (4.54), respectively.

Now replacing $\mathcal{N}_{\overline{Q}}$ in Eq.(D.43) by \mathcal{N} given in Eq.(D.66), the reconstructed velocity distribution function at point $v = v_n$, $f_{1,n,\overline{Q}}(v_n)$, in Eq.(D.43) can be expressed simply as

$$f_1(v_n) = \mathcal{N} \left[\frac{2Q_n \tilde{r}_n}{F^2(Q_n)} \right] \left[\frac{d}{dQ} \ln F^2(Q) \Big|_{Q=Q_n} - k_n \right] = \frac{2}{\alpha} \left(\frac{\tilde{f}_{1,n}}{S_{2,-1/2,\text{tot}}} \right). \quad (\text{D.68})$$

Here, similar to $\tilde{f}_{1,n,\overline{Q}}(v)$ defined in Eq.(D.47), I have defined

$$\tilde{f}_{1,n} \equiv \frac{2Q_n \tilde{r}_n}{F^2(Q_n)} \left[\frac{d}{dQ} \ln F^2(Q) \Big|_{Q=Q_n} - k_n \right]. \quad (\text{D.69})$$

Moreover, the n -th moment of the velocity distribution function, $\langle v^n \rangle$, determined by Eq.(4.11) can now be expressed as (with $Q_{\text{thre}} = 0$)

$$\langle v^n \rangle = \alpha^n (n+1) \left(\frac{S_{2,(n-1)/2,\text{tot}}}{S_{2,-1/2,\text{tot}}} \right). \quad (\text{D.70})$$

By means of this expression, one can finally estimate the moments of the velocity distribution function directly from the experimental data given in Eq.(4.14) without knowing the exact form of $f_1(v_n)$. Actually, according to Eq.(D.67), the expression of $\langle v^n \rangle$ given in Eq.(D.70) is exactly the same as that given in Eq.(4.66), or the general form in Eq.(4.52) with $Q_{\text{thre}} = 0$.

On the other hand, before beginning to calculate the statistical errors of $f_1(v_n)$ and $\langle v^n \rangle$ in Eqs.(D.68) and (D.70), one must pay some special attention with the variables involved in their expressions. According to the expression of $\tilde{f}_{1,n}$ in Eq.(D.69) and of \tilde{r}_n and k_n in Eqs.(4.22) and (4.23), $\tilde{f}_{1,n}$ is a function of only two variables: N_n and $\overline{Q - Q_n|_n}$; while, according to the definition in Eq.(D.67), $S_{2,\lambda,\text{tot}}$ is a function of $2B$ variables: N_n and $\overline{S_{2,\lambda,n}}$ for all $n = 1, 2, \dots, B$. Hence, $f_1(v_n)$ and $\langle v^n \rangle$ depend on $2B + 2$ and $3B$ variables, respectively,

Then, from Eq.(D.68), it can be found that

$$\frac{\partial f_1(v_n)}{\partial \overline{Q - Q_n|_n}} = -f_1(v_n) \left(\overline{Q - Q_n|_n} + K_n \right) \left[\frac{k_n^2}{g(\kappa_n)} \right], \quad (\text{D.71a})$$

where K_n has been defined in Eq.(5.31) and I have used $d\overline{Q - Q_n}|_n/dk_n$ in Eq.(4.30); for $m = 1, 2, \dots, B$, one has

$$\frac{\partial f_1(v_n)}{\partial N_m} = f_1(v_n) \left(\frac{\delta_{nm}}{N_m} - \frac{\overline{S_{2,-1/2,m}}}{S_{2,-1/2,\text{tot}}} \right), \quad (\text{D.71b})$$

and

$$\frac{\partial f_1(v_n)}{\partial \overline{S_{2,-1/2,m}}} = -f_1(v_n) \left(\frac{N_m}{S_{2,-1/2,\text{tot}}} \right). \quad (\text{D.71c})$$

Then the statistical error of $f_1(v_n)$ estimated in Eq.(D.68) can be expressed as

$$\begin{aligned} \sigma^2(f_1(v_n)) = f_1^2(v_n) \left\{ \left[\frac{(\overline{Q - Q_n}|_n + K_n) k_n^2}{g(\kappa_n)} \right]^2 \sigma^2(\overline{Q - Q_n}|_n) + \frac{1}{N_n} \right. \\ \left. + 2 \left[\frac{(\overline{Q - Q_n}|_n + K_n) k_n^2}{g(\kappa_n)} \right] \left(\frac{\overline{S_{2,1/2,n}} - Q_n \overline{S_{2,-1/2,n}}}{S_{2,-1/2,\text{tot}}} \right) \right. \\ \left. + \frac{S_{4,-1,\text{tot}}}{S_{2,-1/2,\text{tot}}^2} - \frac{2\overline{S_{2,-1/2,n}}}{S_{2,-1/2,\text{tot}}} \right\}. \quad (\text{D.72}) \end{aligned}$$

Here I have used Eq.(4.17) for $\sigma^2(N_n)$, and, for simplicity, set $N_m \gg 1$ for all m in order to use

$$\text{cov}(\overline{Q - Q_n}|_n, \overline{S_{2,\lambda,n}}) = \frac{1}{N_n} (\overline{S_{2,\lambda+1,n}} - Q_n \overline{S_{2,\lambda,n}}), \quad (\text{D.73})$$

and

$$\text{cov}(\overline{S_{2,\lambda,n}}, \overline{S_{2,\rho,n}}) = \frac{1}{N_n} (\overline{S_{4,\lambda+\rho,n}} - \overline{S_{2,\lambda,n}} \overline{S_{2,\rho,n}}), \quad (\text{D.74})$$

with the definition

$$\overline{S_{4,\lambda,n}} \equiv \frac{1}{N_n} \sum_{i=1}^{N_n} \frac{Q_{n,i}^\lambda}{F^4(Q_{n,i})}, \quad (\text{D.75})$$

and then

$$S_{4,\lambda,\text{tot}} \equiv \sum_{n=1}^B N_n \overline{S_{4,\lambda,n}}, \quad (\text{D.76})$$

see Eqs.(D.64) and (D.65). Meanwhile, from the expression of $\langle v^n \rangle$ given in Eq.(D.70), it can be found that

$$\frac{\partial \langle v^n \rangle}{\partial \overline{S_{2,(n-1)/2,m}}} = \langle v^n \rangle \left(\frac{N_m}{S_{2,(n-1)/2,\text{tot}}} \right), \quad (\text{D.77a})$$

$$\frac{\partial \langle v^n \rangle}{\partial \overline{S_{2,-1/2,m}}} = -\langle v^n \rangle \left(\frac{N_m}{S_{2,-1/2,\text{tot}}} \right), \quad (\text{D.77b})$$

and

$$\frac{\partial \langle v^n \rangle}{\partial N_m} = \langle v^n \rangle \left(\frac{\overline{S_{2,(n-1)/2,m}}}{S_{2,(n-1)/2,\text{tot}}} - \frac{\overline{S_{2,-1/2,m}}}{S_{2,-1/2,\text{tot}}} \right). \quad (\text{D.77c})$$

Hence, the statistical error of $\langle v^n \rangle$ can be expressed as

$$\sigma^2(\langle v^n \rangle) = \langle v^n \rangle^2 \left(\frac{S_{4,n-1,\text{tot}}}{S_{2,(n-1)/2,\text{tot}}^2} + \frac{S_{4,-1,\text{tot}}}{S_{2,-1/2,\text{tot}}^2} - \frac{2S_{4,(n-2)/2,\text{tot}}}{S_{2,(n-1)/2,\text{tot}} S_{2,-1/2,\text{tot}}} \right), \quad (\text{D.78})$$

where I have used Eq.(D.74).

Finally, if one considers the reconstruction only in bins, the diagonal entries of the covariance matrix in Eq.(4.49) can be reduced to

$$\begin{aligned} \sigma^2(f_{1,r}^2(v_{s,n})) &= \frac{f_{1,r}^2(v_{s,n})}{N_n} + \mathcal{N}^2 \left[\frac{2Q_{s,n}r_n}{F^2(Q_{s,n})} \right]^2 \sigma^2(k_n) \\ &= f_{1,r}^2(v_{s,n}) \left[\frac{1}{N_n} + K_{s,n}^2 \sigma^2(k_n) \right], \end{aligned} \quad (\text{D.79})$$

since r_n and k_n are now two independent variables, and, similar to Eq.(5.31), I have defined here

$$K_{s,n} \equiv \left[\frac{d}{dQ} \ln F^2(Q) \Big|_{Q=Q_{s,n}} - k_n \right]^{-1}. \quad (\text{D.80})$$

The expression in Eq.(D.79) is essentially the same as that in Eq.(D.72) without the last three terms involving $S_{2,-1/2,\text{tot}}$, which correspond to the statistical error of the estimator for \mathcal{N} and have been neglected in Eq.(4.49). Note that $f_1(v_n)$ in Eq.(D.68) is obtained from the first expression of the exponential ansatz in Eq.(4.18) and estimated at $v = v_n$, while $f_{1,r}^2(v_{s,\mu})$ in Eq.(4.46) is obtained from the second expression in Eq.(4.18) and estimated at $v = v_{s,\mu}$, which is not a fixed value like v_n but actually depends on k_n through Eqs.(4.28). Hence, since the two expressions in Eq.(4.18) are equivalent, when one takes into account the uncertainty of the determination of $Q_{s,\mu}$ by Eq.(4.28), the statistical error of $f_{1,r}^2(v_{s,\mu})$ will be identical to the first two terms of $\sigma^2(f_1(v_n))$ in Eq.(D.72).

Similarly, if one neglects Q_{thre} and thus all terms involving r_{thre} , the diagonal entries of the general form of the covariance matrix given in Eq.(4.61) can be reduced to

$$\begin{aligned} \sigma^2(\langle v^n \rangle) &= \frac{1}{I_0^2} \left[\langle v^n \rangle^2 \sigma^2(I_0) + \alpha^{2n} (n+1)^2 \sigma^2(I_n) - 2\alpha^n (n+1) \langle v^n \rangle \text{cov}(I_0, I_n) \right] \\ &= \langle v^n \rangle^2 \left[\frac{\sigma^2(I_0)}{I_0^2} + \frac{\sigma^2(I_n)}{I_n^2} - \frac{2\text{cov}(I_n, I_0)}{I_n I_0} \right], \end{aligned} \quad (\text{D.81})$$

where I have used $\langle v^n \rangle$ in Eq.(4.66). Comparing the definition of $S_{4,\lambda,\text{tot}}$ in Eq.(D.76) with the expression of $\text{cov}(I_n, I_m)$ in Eq.(4.54) and using Eq.(D.67), the expression given in Eq.(D.78) is exactly identical to that in Eq.(D.81).

Appendix E

Some Detailed Calculations

In this chapter I give some detailed derivations.

E.1 Derivations of covariances in Sec. 4.2

E.1.1 Covariances in Subsec. 4.2.2

From Eq.(4.37), one has

$$\frac{\partial N_\mu}{\partial N_{n^*}} = 1, \quad (\text{E.1})$$

where n^* denotes a given bin between the $n_{\mu-}$ -th and the $n_{\mu+}$ -th bins. Then, from (4.38), one has

$$\frac{\partial \overline{Q - Q_\mu |_\mu}}{\partial N_{n^*}} = \frac{\overline{Q |_{n^*}}}{N_\mu} - \frac{1}{N_\mu^2} \left(\sum_{n=n_{\mu-}}^{n_{\mu+}} N_n \overline{Q |}_n \right) = \frac{\overline{Q |_{n^*}} - \overline{Q |}_\mu}{N_\mu}, \quad (\text{E.2})$$

and

$$\frac{\partial \overline{Q - Q_\mu |_\mu}}{\partial \overline{Q |_{n^*}}} = \frac{N_{n^*}}{N_\mu}. \quad (\text{E.3})$$

Combining Eqs.(E.1) to (E.3), it can be found that

$$\begin{aligned} & \text{cov} \left(\overline{Q - Q_\mu |_\mu}, \overline{Q - Q_\nu |_\nu} \right) \\ &= \sum_{n^*} \left[\left(\frac{\partial \overline{Q - Q_\mu |_\mu}}{\partial N_{n^*}} \right) \left(\frac{\partial \overline{Q - Q_\nu |_\nu}}{\partial N_{n^*}} \right) \sigma^2(N_{n^*}) \right. \\ & \quad \left. + \left(\frac{\partial \overline{Q - Q_\mu |_\mu}}{\partial \overline{Q |_{n^*}}} \right) \left(\frac{\partial \overline{Q - Q_\nu |_\nu}}{\partial \overline{Q |_{n^*}}} \right) \sigma^2(\overline{Q |_{n^*}}) \right] \\ &= \frac{1}{N_\mu N_\nu} \sum_{n^*} \left[N_{n^*} (\overline{Q |_{n^*}} - \overline{Q |}_\mu) (\overline{Q |_{n^*}} - \overline{Q |}_\nu) + N_{n^*}^2 \sigma^2(\overline{Q |_{n^*}}) \right]. \end{aligned} \quad (\text{4.39})$$

Meanwhile, from Eqs.(4.37) and (4.40), one has

$$r_\mu = \frac{1}{w_\mu} \sum_{n=n_{\mu-}}^{n_{\mu+}} N_n. \quad (\text{E.4})$$

Thus,

$$\frac{\partial r_\mu}{\partial N_{n^*}} = \frac{1}{w_\mu}, \quad (\text{E.5})$$

and then

$$\text{cov}(r_\mu, r_\nu) = \sum_{n^*} \left(\frac{\partial r_\mu}{\partial N_{n^*}} \right) \left(\frac{\partial r_\nu}{\partial N_{n^*}} \right) \sigma^2(N_{n^*}) = \frac{1}{w_\mu w_\nu} \sum_{n^*} N_{n^*}, \quad (\text{4.41})$$

Combining Eqs.(E.2) and (E.5), it can be found that

$$\begin{aligned} \text{cov}(r_\mu, \overline{Q - Q_\nu|_\nu}) &= \sum_{n^*} \left(\frac{\partial r_\mu}{\partial N_{n^*}} \right) \left(\frac{\partial \overline{Q - Q_\nu|_\nu}}{\partial N_{n^*}} \right) \sigma^2(N_{n^*}) \\ &= \frac{1}{w_\mu N_\nu} \sum_{n^*} N_{n^*} (\overline{Q|_{n^*}} - \overline{Q|_\nu}). \end{aligned} \quad (\text{4.42})$$

E.1.2 Covariance in Eq.(4.61)

The expression of $\langle v^n \rangle$ in Eq.(4.52) can be rewritten as

$$\langle v^n \rangle = \alpha^n \mathcal{N}_m \left[\frac{2Q_{\text{thre}}^{(n+1)/2} r_{\text{thre}}}{F^2(Q_{\text{thre}})} + (n+1)I_n \right], \quad (\text{4.52}')$$

with

$$\mathcal{N}_m = \left[\frac{2Q_{\text{thre}}^{1/2} r_{\text{thre}}}{F^2(Q_{\text{thre}})} + I_0 \right]^{-1}. \quad (\text{4.62}')$$

Hence, it can be found that

$$\frac{\partial \langle v^n \rangle}{\partial I_n} = \mathcal{N}_m \alpha^n (n+1), \quad (\text{E.6})$$

and

$$\frac{\partial \langle v^n \rangle}{\partial I_0} = -\alpha^n \mathcal{N}_m^2 \left[\frac{2Q_{\text{thre}}^{(n+1)/2} r_{\text{thre}}}{F^2(Q_{\text{thre}})} + (n+1)I_n \right] = -\mathcal{N}_m \langle v^n \rangle. \quad (\text{E.7})$$

Moreover,

$$\begin{aligned} \frac{\partial \langle v^n \rangle}{\partial r_{\text{thre}}} &= \alpha^n \mathcal{N}_m \left[\frac{2Q_{\text{thre}}^{(n+1)/2}}{F^2(Q_{\text{thre}})} \right] - \alpha^n \mathcal{N}_m^2 \left[\frac{2Q_{\text{thre}}^{(n+1)/2} r_{\text{thre}}}{F^2(Q_{\text{thre}})} + (n+1)I_n \right] \left[\frac{2Q_{\text{thre}}^{1/2}}{F^2(Q_{\text{thre}})} \right] \\ &= \mathcal{N}_m \left[\frac{2}{F^2(Q_{\text{thre}})} \right] \left(\alpha^n Q_{\text{thre}}^{(n+1)/2} - \sqrt{Q_{\text{thre}}} \langle v^n \rangle \right). \end{aligned} \quad (\text{E.8})$$

This leads to the definition of D_n in Eq.(4.63). Combining Eqs.(E.6), (E.7), and (4.63), Eq.(4.61) can be obtained directly.

E.2 Derivation of the correction terms in Eq.(4.64)

Starting point is the observation that we wish to compute the ratio of two integrals,

$$\frac{G_1}{G_2} = \frac{\int g_1(x) dx}{\int g_2(x) dx} \rightarrow \frac{\sum_i n_i g_1(x_i)}{\sum_j n_j g_2(x_j)}. \quad (\text{E.9})$$

In the second step the integrals have been discretized, i.e., replaced by sums over bins i with n_i events per bin. n_i can be written as sum of average value \bar{n}_i and fluctuation δn_i :

$$\frac{G_1}{G_2} = \frac{\sum_i (\bar{n}_i + \delta n_i) g_1(x_i)}{\sum_j \bar{n}_j g_2(x_j) + \sum_j \delta n_j g_2(x_j)}. \quad (\text{E.10})$$

Introducing the notation

$$\bar{G}_a = \sum_i \bar{n}_i g_a(x_i), \quad (\text{E.11})$$

for $a = 1, 2$, and expanding up to second order in the δn_i , one has

$$\begin{aligned} \frac{G_1}{G_2} &\simeq \frac{\bar{G}_1 + \sum_i \delta n_i g_1(x_i)}{\bar{G}_2} \left[1 - \frac{\sum_j \delta n_j g_2(x_j)}{\bar{G}_2} + \left(\frac{\sum_j \delta n_j g_2(x_j)}{\bar{G}_2} \right)^2 \right] \\ &\simeq \frac{\bar{G}_1}{\bar{G}_2} + \frac{1}{\bar{G}_2} \left(\sum_i \delta n_i g_1(x_i) \right) - \frac{\bar{G}_1}{\bar{G}_2^2} \left(\sum_i \delta n_i g_2(x_i) \right) \\ &\quad - \frac{1}{\bar{G}_2^2} \left(\sum_i \delta n_i g_1(x_i) \right) \left(\sum_j \delta n_j g_2(x_j) \right) + \frac{\bar{G}_1}{\bar{G}_2^3} \left(\sum_i \delta n_i g_2(x_i) \right)^2. \end{aligned} \quad (\text{E.12})$$

Now consider the average over many experiments. Of course, δn_i averages to zero, but the product $\delta n_i \delta n_j$ averages to $\bar{n}_i \delta_{ij}$, i.e., it is non-zero for $i = j$. Hence:

$$\left\langle \frac{G_1}{G_2} \right\rangle \simeq \frac{\bar{G}_1}{\bar{G}_2} - \frac{1}{\bar{G}_2^2} \left(\sum_i \bar{n}_i g_1(x_i) g_2(x_i) \right) + \frac{\bar{G}_1}{\bar{G}_2^3} \left(\sum_i \bar{n}_i g_2^2(x_i) \right). \quad (\text{E.13})$$

The sums appearing in the two correction terms also appear in the definition of the covariance matrix between G_1 and G_2 . Note that we wish to compute the first term on the right-hand side, since in this case the estimators for G_1 and G_2 indeed average to the correct values. This then leads to the final result

$$\frac{\bar{G}_1}{\bar{G}_2} - \left\langle \frac{G_1}{G_2} \right\rangle = \left(\frac{1}{\bar{G}_2^2} \right) \text{cov}(G_1, G_2) - \left(\frac{\bar{G}_1}{\bar{G}_2^3} \right) \text{cov}(G_2, G_2). \quad (\text{E.14})$$

Applying this result to Eq.(4.52) then immediately leads to Eq.(4.64).

E.3 Statistical error of $\mathcal{R}_n(Q_{\text{thre}})$ in Eq.(4.72)

From Eq.(4.72), it can be found directly that

$$\begin{aligned} \frac{\partial \mathcal{R}_n(Q_{\text{thre}})}{\partial r_{\text{thre},X}} &= \frac{2}{n} \left[\frac{Q_{\text{thre},X}^{(n+1)/2} I_{0,X} - (n+1) Q_{\text{thre},X}^{1/2} I_{n,X}}{2Q_{\text{thre},X}^{(n+1)/2} r_{\text{thre},X} + (n+1) I_{n,X} F_X^2(Q_{\text{thre},X})} \right] \\ &\quad \times \left[\frac{F_X^2(Q_{\text{thre},X})}{2Q_{\text{thre},X}^{1/2} r_{\text{thre},X} + I_{0,X} F_X^2(Q_{\text{thre},X})} \right] \mathcal{R}_n(Q_{\text{thre}}), \end{aligned} \quad (\text{E.15a})$$

$$\frac{\partial \mathcal{R}_n(Q_{\text{thre}})}{\partial I_{n,X}} = \frac{n+1}{n} \left[\frac{F_X^2(Q_{\text{thre},X})}{2Q_{\text{thre},X}^{(n+1)/2} r_{\text{thre},X} + (n+1)I_{n,X} F_X^2(Q_{\text{thre},X})} \right] \mathcal{R}_n(Q_{\text{thre}}), \quad (\text{E.15b})$$

and

$$\frac{\partial \mathcal{R}_n(Q_{\text{thre}})}{\partial I_{0,X}} = -\frac{1}{n} \left[\frac{F_X^2(Q_{\text{thre},X})}{2Q_{\text{thre},X}^{1/2} r_{\text{thre},X} + I_{0,X} F_X^2(Q_{\text{thre},X})} \right] \mathcal{R}_n(Q_{\text{thre}}). \quad (\text{E.15c})$$

By first exchanging $Q_{\text{thre},X}^{(n+1)/2}$ and $(n+1)I_{n,X}$ with $Q_{\text{thre},X}^{1/2}$ and $I_{0,X}$, respectively, and then replacing X by Y , one can get

$$\begin{aligned} \frac{\partial \mathcal{R}_n(Q_{\text{thre}})}{\partial r_{\text{thre},Y}} = & -\frac{2}{n} \left[\frac{Q_{\text{thre},Y}^{(n+1)/2} I_{0,Y} - (n+1)Q_{\text{thre},Y}^{1/2} I_{n,Y}}{2Q_{\text{thre},Y}^{(n+1)/2} r_{\text{thre},Y} + (n+1)I_{n,Y} F_Y^2(Q_{\text{thre},Y})} \right] \\ & \times \left[\frac{F_Y^2(Q_{\text{thre},Y})}{2Q_{\text{thre},Y}^{1/2} r_{\text{thre},Y} + I_{0,Y} F_Y^2(Q_{\text{thre},Y})} \right] \mathcal{R}_n(Q_{\text{thre}}), \quad (\text{E.16a}) \end{aligned}$$

$$\frac{\partial \mathcal{R}_n(Q_{\text{thre}})}{\partial I_{n,Y}} = -\frac{n+1}{n} \left[\frac{F_Y^2(Q_{\text{thre},Y})}{2Q_{\text{thre},Y}^{(n+1)/2} r_{\text{thre},Y} + (n+1)I_{n,Y} F_Y^2(Q_{\text{thre},Y})} \right] \mathcal{R}_n(Q_{\text{thre}}), \quad (\text{E.16b})$$

and

$$\frac{\partial \mathcal{R}_n(Q_{\text{thre}})}{\partial I_{0,Y}} = \frac{1}{n} \left[\frac{F_Y^2(Q_{\text{thre},Y})}{2Q_{\text{thre},Y}^{1/2} r_{\text{thre},Y} + I_{0,Y} F_Y^2(Q_{\text{thre},Y})} \right] \mathcal{R}_n(Q_{\text{thre}}). \quad (\text{E.16c})$$

By setting $Q_{\text{thre}} = 0$, the above expressions can be reduced to $\sigma(m_\chi)$ given in Eq.(4.70) directly.

E.4 Derivation of η_n in Eq.(5.24)

From Eq.(5.22), I have

$$\frac{f_{1,(m)}(Q)}{2\mathcal{N}} = \frac{Q}{F^2(Q)} \left(\frac{dR}{dQ} \right)_{(m)} \left\{ \frac{2}{F(Q)} \left(\frac{dF}{dQ} \right) - \frac{1}{(dR/dQ)_{(m)}} \left[\frac{d}{dQ} \left(\frac{dR}{dQ} \right)_{(m)} \right] \right\}. \quad (\text{E.17})$$

Substituting the ansatz for $(dR/dQ)_{(1),n}$ in Eq.(5.13), it can be found that

$$\begin{aligned} & \frac{1}{(dR/dQ)_{(1),n}} \left[\frac{d}{dQ} \left(\frac{dR}{dQ} \right)_{(1),n} \right] \\ = & \frac{1}{(dR/dQ)_{(0)}} \left[\frac{d}{dQ} \left(\frac{dR}{dQ} \right)_{(0)} \right] + \frac{l_n}{l_n(Q - Q_n) + h_n}. \quad (\text{E.18}) \end{aligned}$$

Thus I can obtain that

$$\begin{aligned}
& \frac{f_{1,(m)}(Q)}{2\mathcal{N}} \\
&= \frac{Q}{F^2(Q)} \left(\frac{dR}{dQ} \right)_{(0)} [l_n(Q - Q_n) + h_n] \\
&\quad \times \left\{ \frac{2}{F(Q)} \left(\frac{dF}{dQ} \right) - \frac{1}{(dR/dQ)_{(0)}} \left[\frac{d}{dQ} \left(\frac{dR}{dQ} \right)_{(0)} \right] - \frac{l_n}{l_n(Q - Q_n) + h_n} \right\} \\
&= \frac{f_{1,(0)}(Q)}{2\mathcal{N}} [l_n(Q - Q_n) + h_n] - l_n \left[\frac{Q}{F^2(Q)} \left(\frac{dR}{dQ} \right)_{(0)} \right], \tag{E.19}
\end{aligned}$$

namely,

$$\begin{aligned}
& \frac{f_{1,(1),n}(Q)}{f_{1,(0)}(Q)} \\
&= [l_n(Q - Q_n) + h_n] - l_n \left\{ \frac{2}{F(Q)} \left(\frac{dF}{dQ} \right) - \frac{1}{(dR/dQ)_{(0)}} \left[\frac{d}{dQ} \left(\frac{dR}{dQ} \right)_{(0)} \right] \right\}^{-1}. \tag{E.20}
\end{aligned}$$

Now I use the ansatz for $(dR/dQ)_{(0),n}$ in Eq.(4.18) to get

$$\frac{f_{1,(1),n}(Q)}{f_{1,(0),n}(Q)} = [l_n(Q - Q_n) + h_n] - l_n \left[\frac{2}{F(Q)} \left(\frac{dF}{dQ} \right) - k_n \right]^{-1}. \tag{E.21}$$

Let $Q = Q_n$, the expression of η_n in Eq.(5.24) can be obtained directly.

Bibliography

- [1] G. Jungman, M. Kamionkowski, and K. Griest, *Phys. Rep.* **267**, 195 (1996).
- [2] F. Zwicky, *Helv. Phys. Acta* **6**, 110 (1933).
- [3] S. Smith, *Astrophys. J.* **83**, 23 (1936).
- [4] V. C. Rubin and W. K. Ford, *Astrophys. J.* **159**, 379 (1970).
- [5] S. M. Faber and J. S. Gallagher, *Annu. Rev. Astron. Astrophys.* **17**, 135 (1979).
- [6] V. C. Rubin, W. K. Ford, and N. Thonnard, *Astrophys. J.* **238**, 471 (1980).
- [7] K. G. Begeman, A. H. Broeils, and R. H. Sanders, *Mon. Not. R. Astron. Soc.* **249**, 523 (1991).
- [8] R. P. Olling and M. R. Merrifield, *Mon. Not. R. Astron. Soc.* **311**, 361 (2000).
- [9] M. Fich and S. Tremaine, *Annu. Rev. Astron. Astrophys.* **29**, 409 (1991).
- [10] H. Stöcker, *Taschenbuch der Physik*, Harri Deutsch (2005).
- [11] Review of Particle Physics, *J. Phys. G: Nucl. Part. Phys.* **33**, 2. Astrophysical Constants and Parameters (2006).
- [12] O. Lahav and A. R. Lindle, Review of Particle Physics, *J. Phys. G: Nucl. Part. Phys.* **33**, 21. The Cosmological Parameters (2006).
- [13] WMAP Collab., D. N. Spergel *et al.*, [arXiv:astro-ph/0603449](https://arxiv.org/abs/astro-ph/0603449) (2006).
- [14] E. W. Kolb and M. S. Turner, *The Early Universe*, Addison-Wesley (1990).
- [15] M. S. Turner, [arXiv:astro-ph/9904051](https://arxiv.org/abs/astro-ph/9904051) (1999).
- [16] K. A. Olive and J. A. Peacock, Review of Particle Physics, *J. Phys. G: Nucl. Part. Phys.* **33**, 19. Big-Bang Cosmology (2006).
- [17] B. D. Fields and S. Sarkar, Review of Particle Physics, *J. Phys. G: Nucl. Part. Phys.* **33**, 20. Big-Bang Nucleosynthesis (2006).

- [18] D. Scott and G. F. Smoot, Review of Particle Physics, *J. Phys. G: Nucl. Part. Phys.* **33**, 23. Cosmic Microwave Background (2006).
- [19] J. R. Primack, *Nucl. Phys. Proc. Suppl.* **124**, 3 (2003).
- [20] J. A. Tyson, *Phys. Scr.* **T 85**, 259 (2000).
- [21] P. J. E. Peebles, *Rev. Mod. Phys.* **75**, 559 (2003).
- [22] M. de Jesus, *Int. J. Mod. Phys. A* **19**, 1142 (2004).
- [23] C. S. Frenk, *Phil. Trans. Roy. Soc. Lond.* **300**, 1277 (2002).
- [24] M. Kamionkowski and A. Kinkhabwala, *Phys. Rev. D* **57**, 3256 (1998).
- [25] Review of Particle Physics, *J. Phys. G: Nucl. Part. Phys.* **33**, 1. Physical Constants (2006).
- [26] A. M. Green, *Phys. Rev. D* **63**, 043005 (2001).
- [27] P. D. Sackett *et al.*, *Astrophys. J.* **436**, 629 (1994).
- [28] N. W. Evans, *Mon. Not. R. Astron. Soc.* **267**, 333 (1994).
- [29] J. J. Binney, *Mon. Not. R. Astron. Soc.* **196**, 455 (1981).
- [30] N. W. Evans, *Mon. Not. R. Astron. Soc.* **260**, 191 (1993).
- [31] J. F. Navarro, C. S. Frenk, and S. D. M. White, *Astrophys. J.* **462**, 563 (1996).
- [32] A. Burkert and J. Silk, [arXiv:astro-ph/9904159](https://arxiv.org/abs/astro-ph/9904159) (1999).
- [33] G. Gentile, C. Tonini, and P. Salucci, [arXiv:astro-ph/0701550](https://arxiv.org/abs/astro-ph/0701550) (2007).
- [34] E. L. Lokas, *Mon. Not. R. Astron. Soc.* **311**, 423 (2000).
- [35] T. Kuwabara, A. Taruya, and Y. Suto, *Publ. Astron. Soc. Jap.* **54**, 503 (2002).
- [36] L. Hernquist, *Astrophys. J.* **356**, 359 (1990).
- [37] M. Drees and G. Gerbier, Review of Particle Physics, *J. Phys. G: Nucl. Part. Phys.* **33**, 22. Dark Matter (2006).
- [38] M. W. Goodman and E. Witten, *Phys. Rev. D* **31**, 3059 (1985).
- [39] I. Wassermann, *Phys. Rev. D* **33**, 2071 (1986).
- [40] K. Griest, *Phys. Rev. D* **38**, 2357 (1988).
- [41] A. K. Drukier, K. Freese, and D. N. Spergel, *Phys. Rev. D* **33**, 3495 (1986).

- [42] K. Freese, J. Frieman, and A. Gould, *Phys. Rev. D* **37**, 3388 (1988).
- [43] D. N. Spergel, *Phys. Rev. D* **37**, 1353 (1988).
- [44] P. F. Smith and J. D. Lewin, *Astropart. Phys.* **6**, 87 (1996).
- [45] Y. Ramachers, *Nucl. Phys. Proc. Suppl.* **118**, 341 (2003).
- [46] CDMS Collab., D. S. Akerib *et al.*, [arXiv:astro-ph/0609189](https://arxiv.org/abs/astro-ph/0609189) (2006).
- [47] EDELWEISS Collab., V. Sanglard *et al.*, *Phys. Rev. D* **71**, 122002 (2005).
- [48] See <http://people.roma2.infn.it/~dama/web/home.html>.
- [49] S. P. Ahlen *et al.*, *Phys. Lett. B* **195**, 603 (1987).
- [50] J. Engel, *Phys. Lett. B* **264**, 114 (1991).
- [51] J. Gascon, [arXiv:astro-ph/0504241](https://arxiv.org/abs/astro-ph/0504241) (2005).
- [52] DAMA Collab., R. Bernabei *et al.*, *Phys. Lett. B* **480**, 23 (2000).
- [53] DAMA Collab., R. Bernabei *et al.*, [arXiv:astro-ph/0305542](https://arxiv.org/abs/astro-ph/0305542) (2003).
- [54] DAMA Collab., R. Bernabei *et al.*, [arXiv:astro-ph/0311046](https://arxiv.org/abs/astro-ph/0311046) (2003).
- [55] See <http://hepwww.rl.ac.uk/UKDMC/project/project.html>.
- [56] See <http://www.cresst.de/>.
- [57] CRESST Collab., M. Altmann *et al.*, [arXiv:astro-ph/0106314](https://arxiv.org/abs/astro-ph/0106314) (2001).
- [58] See http://www.mpi-hd.mpg.de/non_acc/dm.html.
- [59] See <http://cdms.berkeley.edu/>.
- [60] See http://edelweiss.in2p3.fr/index_newe.html.
- [61] L. Kaufmann and A. Rubbia, *J. Phys. Conf. Ser.* **60**, 264 (2007).
- [62] R. W. Schnee, *AIP Conf. Proc.* **903**, 8 (2007).
- [63] CDMS Collab., D. S. Akerib *et al.*, *Phys. Rev. D* **72**, 052009 (2005).
- [64] CDMS Collab., P. L. Brink *et al.*, [arXiv:astro-ph/0503583](https://arxiv.org/abs/astro-ph/0503583) (2005).
- [65] CDMS Collab., D. S. Akerib *et al.*, *Phys. Rev. Lett.* **96**, 011302 (2006).
- [66] CDMS Collab., D. S. Akerib *et al.*, *Phys. Rev. D* **73**, 011102 (2006).
- [67] CRESST Collab., G. Angloher *et al.*, *Astropart. Phys.* **23**, 325 (2005).

- [68] CDMS Collab., R. Abusaidi *et al.*, *Phys. Rev. Lett.* **84**, 5699 (2000).
- [69] P. Gondolo and G. Gelmini, *Phys. Rev. D* **71**, 123520 (2005).
- [70] D. Tucker-Smith and N. Weiner, *Phys. Rev. D* **72**, 063509 (2005).
- [71] V. Sanglard, for EDELWEISS Collab., [arXiv:astro-ph/0612207](https://arxiv.org/abs/astro-ph/0612207) (2006).
- [72] See <http://dmrc.snu.ac.kr/>.
- [73] KIMS Collab., H. S. Lee *et al.*, [arXiv:0704.0423](https://arxiv.org/abs/astro-ph/0704.0423) [astro-ph] (2007).
- [74] PICO-LON Collab., K. Fushimi *et al.*, *J. Phys. Soc. Jap.* **74**, 3117 (2005).
- [75] PICO-LON Collab., K. Fushimi *et al.*, [arXiv:astro-ph/0611700](https://arxiv.org/abs/astro-ph/0611700) (2006).
- [76] PICO-LON Collab., K. Fushimi *et al.*, *J. Phys. Soc. Jap.* **75**, 064201 (2006).
- [77] WARP Collab., P. Benetti *et al.*, [arXiv:astro-ph/0701286](https://arxiv.org/abs/astro-ph/0701286) (2007).
- [78] ZEPLIN Collab., G. J. Alner *et al.*, [arXiv:astro-ph/0701858](https://arxiv.org/abs/astro-ph/0701858) (2007).
- [79] See <http://neutrino.ethz.ch/ArDM/>.
- [80] A. Rubbia, *J. Phys. Conf. Ser.* **39**, 129 (2006).
- [81] L. Kaufmann and A. Rubbia, [arXiv:hep-ph/0612056](https://arxiv.org/abs/hep-ph/0612056) (2006).
- [82] See <http://warp.lngs.infn.it/>.
- [83] See <http://xenon.astro.columbia.edu/>.
- [84] K. Ni and L. Baudis, [arXiv:astro-ph/0611124](https://arxiv.org/abs/astro-ph/0611124) (2006).
- [85] XENON Collab., J. Angle *et al.*, [arXiv:0706.0039](https://arxiv.org/abs/astro-ph/0706.0039) [astro-ph] (2007).
- [86] L. Baudis, [arXiv:astro-ph/0703183](https://arxiv.org/abs/astro-ph/0703183) (2007).
- [87] N. Spooner, [arXiv:0705.3345](https://arxiv.org/abs/astro-ph/0705.3345) [astro-ph] (2007).
- [88] See <http://lpsc.in2p3.fr/mimache3/>.
- [89] E. Moulin and D. Santos, [arXiv:astro-ph/0505458](https://arxiv.org/abs/astro-ph/0505458) (2005).
- [90] D. Santos *et al.*, [arXiv:astro-ph/0701230](https://arxiv.org/abs/astro-ph/0701230) (2007).
- [91] SIMPLE Collab., T. Girard *et al.*, [arXiv:hep-ex/0504022](https://arxiv.org/abs/hep-ex/0504022) (2005).
- [92] SIMPLE Collab., T. Morlet *et al.*, [arXiv:0704.2037](https://arxiv.org/abs/astro-ph/0704.2037) [astro-ph] (2007).
- [93] SIMPLE Collab., T. Girard *et al.*, *Phys. Lett. B* **621**, 233 (2005).

- [94] Review of Particle Physics, *J. Phys. G: Nucl. Part. Phys.* **33**, 3. International System of Units (SI) (2006).
- [95] F. S. Ling, P. Sikivie, and S. Wick, *Phys. Rev. D* **70**, 123503 (2004).
- [96] M. Drees and C. L. Shan, *J. Cosmol. Astropart. Phys.* **0706**, 011 (2007), [arXiv:astro-ph/0703651](#).
- [97] A. M. Green, [arXiv:hep-ph/0703217](#) (2007).